Université de Lille

Numéro d'ordre:

Thèse

Université de Lille – Sciences et Technologies

Ecole doctorale Sciences de la Matière, du Rayonnement et de l'Environnement

Pour obtenir le grade de

DOCTEUR DE L'UNIVERSITE

Spécialité: Sciences des Matériaux

Présentée par

Billy C. NZOGANG

Caractérisation avancée de la plasticité des minéraux par microscopie électronique en transmission

Soutenance prévue le 19 juin 2019, devant le jury composé de

Prof. Alexandre DIMANOV	Ecole polytechnique	Rapporteur
Prof. Muriel VERON	Université Grenoble Alpes, INP	Rapporteur
Prof. David MAINPRICE	Université de Montpellier	Examinateur
Prof. Patrick CORDIER	Université de Lille	Directeur de thèse
Dr. Alexandre MUSSI	Université de Lille	Co-encadrant de thèse

Order number:

PhD Thesis

Université de Lille – Sciences et Technologies

Ecole doctorale Sciences de la Matière, du Rayonnement et de l'Environnement

To obtain the degree of

DOCTOR

In Materials Sciences

Presented by

Billy C. NZOGANG

Advanced characterization of mineral plasticity using transmission electron microscopy

Defense scheduled on 19 June 2019, before the jury composed of

Prof. Alexandre DIMANOV	Ecole polytechnique	Reviewer
Prof. Muriel VERON	Université Grenoble Alpes, INP	Reviewer
Prof. David MAINPRICE	Université de Montpellier	Examiner
Prof. Patrick CORDIER	Université de Lille	Co-supervisor
Dr. Alexandre MUSSI	Université de Lille	supervisor

Résumé

Caractérisation avancée de la plasticité des minéraux par microscopie électronique en transmission

L'activité interne de notre planète se manifeste en surface par des phénomènes géologiques tels que le volcanisme ou les séismes. Cette activité résulte de la convection mantellique qui vise à transporter vers la surface la chaleur interne de la Terre. Ces vastes mouvements convectifs impliquent l'écoulement en profondeur des roches à l'état solide. Comprendre les mécanismes élémentaires qui permettent aux roches et à leurs minéraux de subir ces grandes déformations est donc un enjeu majeur en géophysique. Le microscope électronique en transmission (MET) est traditionnellement l'outil de choix pour étudier les mécanismes de plasticité des minéraux. De nouvelles techniques basées sur la microscopie électronique à balayage permettent également de visualiser les orientations préférentielles de réseau ainsi que les désorientations intracristallines (EBSD).

Le dispositif ACOM-TEM (Automated Crystal Orientation Mapping in Transmission Electron Microscopy) permet aujourd'hui de réaliser des cartes d'orientations cristallines à l'échelle du MET. Dans cette thèse, nous explorons les possibilités de cette technique appliquée à la déformation des minéraux. Nous montrons en particulier que la technique ACOM-TEM peut être appliquée sur des échantillons sensibles à l'irradiation électronique comme le quartz ou des phases de haute pression. L'emploi de cartographies à haute résolution (pas d'acquisition de 2 nm) fournit une alternative à l'imagerie conventionnelle en contraste de diffraction, applicable aux minéraux sensibles. Nous montrons également la robustesse de la technique ACOM-TEM vis-à-vis d'échantillons contenant des densités de dislocations élevées, ce qui en fait une technique attractive pour l'étude de matériaux très déformés comme dans le cas d'expériences de déformations sous hautes pressions. Nous présentons également des applications à l'étude de phénomènes de restauration, et de recristallisation.

Abstract

Advanced characterization of minerals plasticity using transmission electron microscopy

The internal activity of our planet is manifested on the surface by some geological phenomena such as volcanism or earthquakes. This activity results from mantle convection, which aims to transport the internal heat of the Earth to the surface. These vast convective movements involve in deep the flow of rocks in the solid state. Understanding the basic mechanisms that allow rocks and their minerals to undergo these large deformations is therefore a major issue in geophysics. The Transmission Electron Microscope (TEM) is traditionally the tool used for studying the mechanisms of plasticity of minerals. However, new techniques based on scanning electron microscopy now make it possible to visualize preferential orientations as well as intracrystalline disorientations (EBSD).

The ACOM-TEM (Automated Crystal Orientation Mapping in Transmission Electron Microscopy) device makes it possible today to produce crystal orientation maps at the MET scale. In this thesis, we explore the possibilities of this technique applied to the deformation of minerals. In particular, we show that the ACOM-TEM technique can be applied to samples sensitive to electron irradiation such as quartz or high pressure phases. The use of high resolution mapping (2 nm as step size) provides an alternative to conventional diffraction contrast imaging, applicable to sensitive minerals. We also show the robustness of the ACOM-TEM technique with respect to samples containing high dislocation densities, which makes it an attractive technique for the study of highly deformed materials as in the case of deformation experiments under high pressures. We also present some applications to the study of recovery phenomena, and recrystallization.

Table des matières

Introduction générale

Notre planète, la Terre, évacue sa chaleur interne à travers de lents mouvements de convection dans le manteau. Ce manteau est pourtant constitué de roches solides jusqu'environ 3000 km de profondeur. Appréhender les mécanismes par lesquels ces roches solides se déforment est une étape importante dans la compréhension des processus dynamiques qui animent l'intérieur de notre planète. A l'échelle microscopique, les défauts et les imperfections structurales sont omniprésents dans les minéraux et les roches ; leurs dynamiques collectives, déterminent les propriétés plastiques de ces roches. Depuis de nombreuses années, la microscopie électronique en transmission a permis d'étudier la structure cristalline de la matière jusqu'à une échelle nanométrique ; c'est donc un outil de choix (MET) pour l'étude et la caractérisation de ces défauts, responsables de la déformation. Etudier les mécanismes fondamentaux de la déformation plastique nécessite donc de comprendre le comportement de ces défauts. Parmi ceux-ci, nous distinguons les dislocations, principaux agents de déformation ; leur comportement est étudié par les physiciens depuis de nombreuses décennies. L'une des limitations dans l'étude mécanique des minéraux est la difficulté d'accès aux échantillons de la Terre profonde. La modélisation numérique et le développement des dispositifs de déformations permettent d'approcher les conditions qui règnent dans les profondeurs terrestres. Les récents développements des dispositifs de déformation sous pression et des modélisations numériques de la plasticité ont jeté une lumière nouvelle sur la déformation des minéraux; ce qui appelle des caractérisations plus poussées des microstructures de déformations.

Cette thèse vise à exploiter les nouvelles possibilités qui sont offertes à ce domaine suite à l'émergence des dispositifs de cartographie d'orientation cristalline automatique dans le microscope électronique en transmission (ACOM-TEM). Notre étude vise à développer de nouvelles approches dans la caractérisation de la déformation des minéraux, et la réalisation d'un couplage entre techniques d'imagerie au MET et cartographie des orientations. Les techniques de post traitement des cartes d'orientations, employées dans le cadre de la diffraction des électrons rétrodiffusés (EBSD) seront utilisées pour mettre en évidence les mécanismes de déformation plastique mis en jeu. Le manuscrit est subdivisé en trois grands chapitres :

Dans le premier chapitre, nous allons présenter les éléments de contexte et les outils qui seront utilisés dans l'ensemble du manuscrit.

Le deuxième chapitre sera consacré essentiellement à la caractérisation des défauts. Nous montrerons, dans ce chapitre, qu'à l'aide de la diffraction électronique à balayage avec un faisceau en mode précession (SPED), nous pouvons imager et caractériser les microstructures de dislocations (jusqu'à la détermination des vecteurs de Burgers) dans des phases sensibles à l'irradiation électronique.

Nous avons rassemblé, dans le troisième chapitre, quatre articles publiés ou en cours de publication qui décrivent les résultats issus de diverses collaborations avec des équipes extérieures au laboratoire. Ces études ont en commun l'application de la SPED à des échantillons déformés expérimentalement. Ces échantillons vont du manteau supérieur au manteau inférieur, en passant

par la zone de transition. Dans ce chapitre, nous montrons comment notre dispositif a permis d'outre passer certaines limitations liées à la nature de ces échantillons (densité des défauts et à la sensibilité à l'irradiation).

Chapitre I. Cartographies d'orientation et cartographies de phase au microscope électronique en transmission

Dans ce chapitre, nous allons, après avoir décrit les méthodes, présenter les outils qui seront utilisés par la suite dans cette thèse. Certains développements qui en seront absents vont être donnés sous forme de références. L'objectif de ce chapitre est triple :

- *Présenter les deux modes de travail que nous utiliserons, à savoir l'imagerie et la diffraction*
- *Présenter la cartographie d'orientation au Microscope Electronique en Transmission (MET) ; de l'acquisition des piles de clichés de diffraction jusqu'à l'indexation, en passant par la technique de dépouillement utilisée.*
- *Appliquer les deux points précédents à l'étude de la plasticité, après un bref rappel des généralités sur la théorie élastique des dislocations et leurs observations au MET.*

I.1 Présentation du Microscope Electronique en Transmission (MET)

Le premier microscope électronique fut fabriqué en 1933, grâce à Ernst Ruska, qui mit au point pour la première fois des lentilles électromagnétiques (Prix Nobel 1986). De la même manière qu'il est possible d'usiner des lentilles optiques pour faire converger de la lumière, nous pouvons utiliser le champ magnétique généré par une bobine électromagnétique pour agir sur un faisceau d'électrons et le focaliser. En se servant de l'optique géométrique de Descartes, il est possible d'associer plusieurs lentilles entre elles pour obtenir une image agrandie de l'objet étudié. Le MET se subdivise en quatre grandes parties (figure 1-1), soumis à différents niveaux de vides :

- La source d'où sont extraits les électrons (canon) : Nous avons travaillé au cours de cette thèse sur deux microscopes en transmission, le FEI® Tecnaï $G^2$20Twin qui fonctionne à 200 kV, et un FEI® CM30 à 300 kV. Ces deux microscopes ont comme source thermo-ionique un filament de LaB_6. Après extraction, les électrons sont accélérés ce qui a pour effet de diminuer leur longueur d'onde. Elle est donnée par l'équation ci-dessous (Williams & Carter, 2009) :

$$\lambda = \frac{h}{\sqrt{[2m_0 eV(1+\frac{eV}{2m_0 c^2})]}} \quad (1)$$

où : e est la charge de l'électron, h est la constante de Planck, V la tension d'accélération et m_0 la masse de l'électron.
En utilisant cette équation nous obtenons pour une tension de 200 kV une longueur d'onde $\lambda = 2{,}51$ pm et à 300 kV $\lambda = 1{,}97$ pm.
- Le condenseur, où est mis en forme le faisceau qui interagit avec l'échantillon : Les lentilles condenseurs (C_1, C_2) contrôlent les conditions d'illumination de l'échantillon et l'angle de convergence du faisceau.
- Etage objectif (zone grisée sur la figure 1-1) : après avoir traversé l'objet, et suite aux différentes interactions électrons-matière (élastiques et inélastiques), le faisceau arrive au niveau de la lentille objectif. Elle est constituée de bobines électromagnétiques qui permettent de dévier les électrons ; l'image de l'objet se forme dans son plan image et la figure de diffraction dans le plan focal.
- Partie projection : le rôle majeur de cet ensemble est d'agrandir et de projeter l'image sur un écran fluorescent ou une caméra CCD. L'écran fluorescent est constitué d'une couche de sulfure de zinc dopée émettant dans le visible.

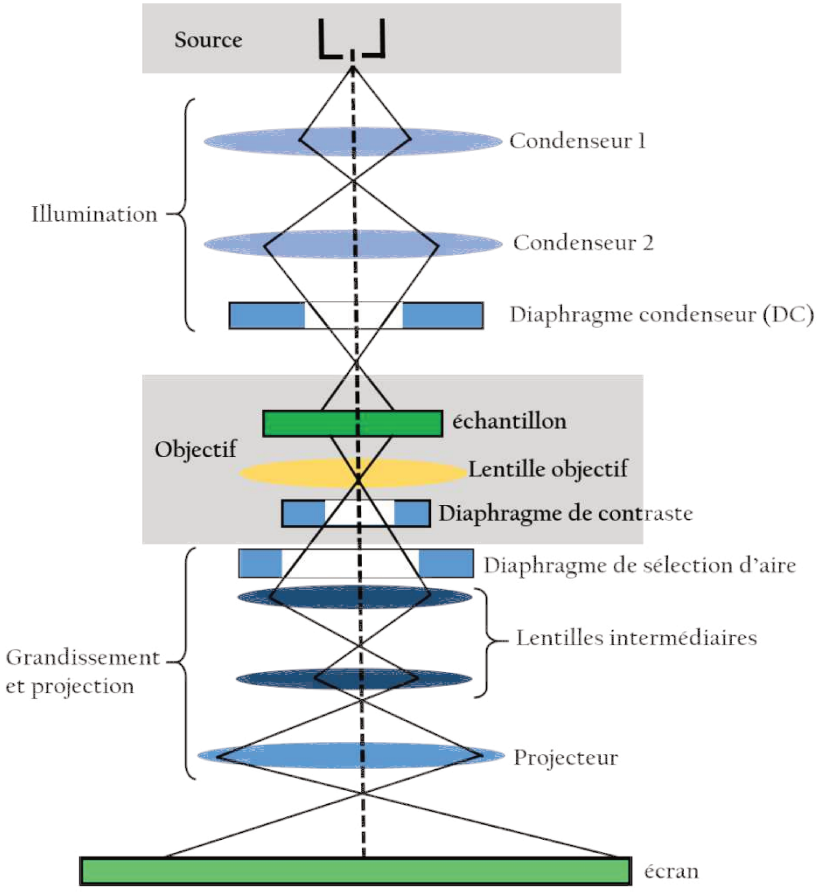

Figure 1-1 : Schéma simplifié d'un microscope électronique en transmission

I.1.1 Formation d'une image contrastée

I.1.1.1 Origine du contraste au microscope

L'interaction électrons-matière donne lieu, dans les cristaux, à plusieurs faisceaux diffractés. Ces faisceaux diffractés sont focalisés ensuite par la lentille objectif du microscope pour former le cliché de diffraction dans son plan focal image. Une image plus contrastée peut alors être produite en sélectionnant une ou plusieurs ondes par insertion du diaphragme de contraste (appelé diaphragme objectif car situé à proximité de la lentille objectif). Le contraste que nous avons alors sur l'image provient des variations locales de l'intensité des faisceaux diffractés par l'échantillon.

I.1.1.2 Champ clair et champ sombre

Au microscope, il est possible de travailler soit en mode image, soit en mode diffraction. En mode image, nous pouvons utiliser le diaphragme de contraste pour ne sélectionner qu'une partie des électrons, après interaction avec l'échantillon. Selon la position du diaphragme il existe deux modes d'imagerie :

- Le diaphragme objectif ne sélectionne que le faisceau transmis (figure 1-2a), les zones de l'échantillon qui contribuent à des événements de diffraction (plans (*hkl*) en position de Bragg) apparaissent alors sombres sur une image en fond clair (les zones sont parfaitement blanches dans le trou car les électrons n'y sont pas diffractés).
- Le diaphragme se positionne sur un faisceau diffracté (figure 1-2b). Sur l'image, les zones en position de Bragg apparaissent en clair sur une image en fond noir (les zones sont parfaitement noires dans le trou car les électrons sont tous transmis).

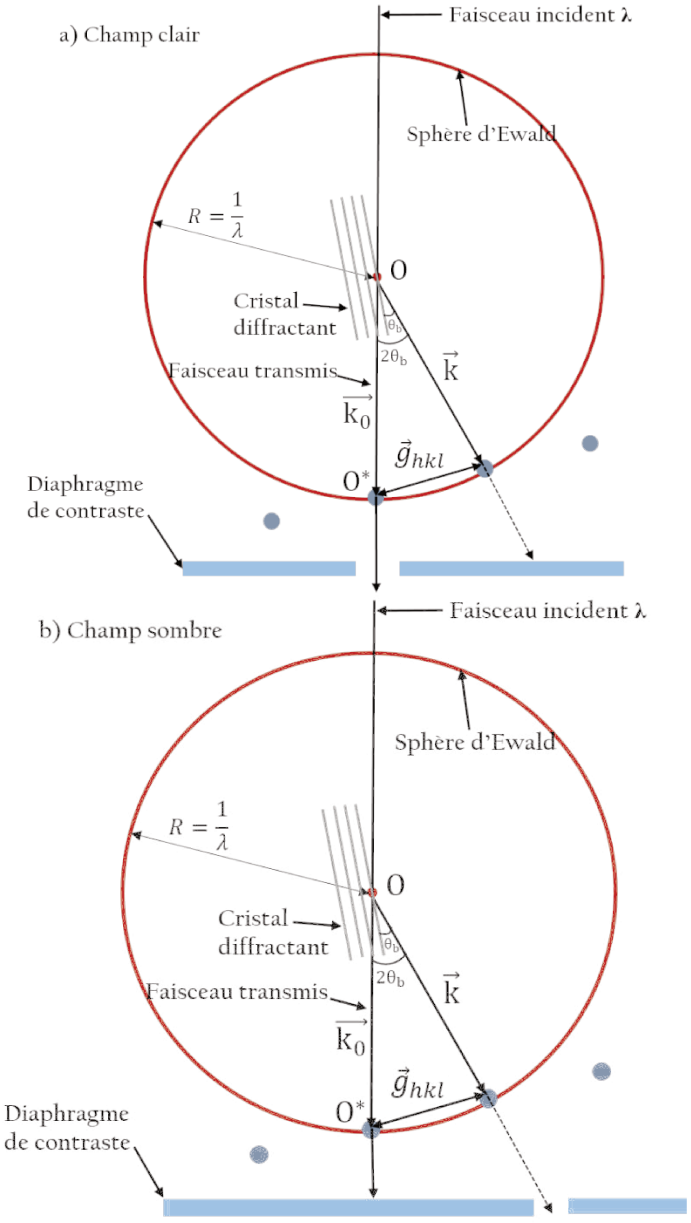

Figure 1-2 : a) Champ clair : le diaphragme objectif permet de sélectionner le faisceau transmis pour former l'image. b) Champ sombre : le diaphragme objectif sélectionne le faisceau diffracté.

I.1.2 Cliché de diffraction dans le plan focal image

I.1.2.1 Construction d'Ewald

Paul Ewald (1888-1985), est un physicien allemand qui fut le pionnier dans l'étude de la diffraction des rayons X. La sphère qui porte son nom permet de déterminer graphiquement les points du réseau réciproque, c'est-à-dire les familles de plans cristallins, donnant lieu à la diffraction. Elle couple le réseau direct (cristal diffractant) et le réseau réciproque (cliché de diffraction). Une façon de formuler la loi de Bragg consiste à dire qu'un faisceau incident dirigé suivant $\vec{k}_0$ n'est diffracté suivant la direction $\vec{k}$ que si le vecteur de diffusion $\vec{k} - \vec{k}_0$ correspond à un vecteur du réseau réciproque, c'est-à-dire $\vec{k} - \vec{k}_0 = \vec{g}_{hkl}$.

Le cristal est au centre d'une sphère en O, et de rayon $1/\lambda$ (figure 1-3). Le réseau réciproque a pour origine O^*.

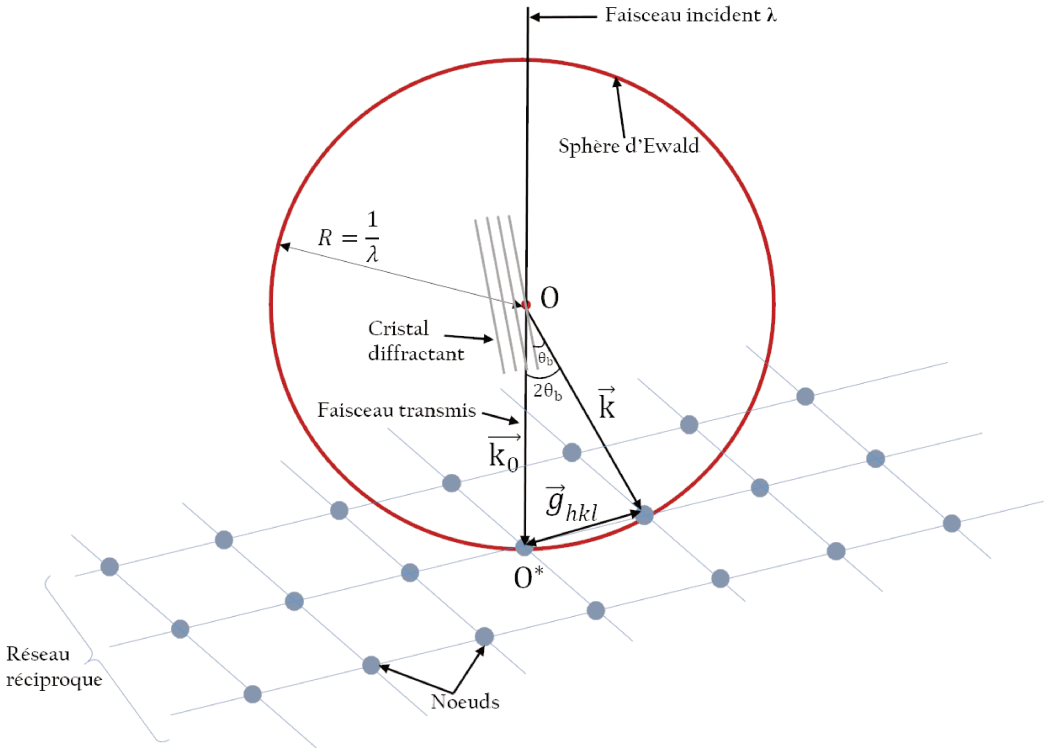

Figure 1-3: Schéma illustrant la construction d'Ewald ; lorsqu'un nœud du réseau réciproque est situé sur la sphère, la loi de Bragg est vérifiée (il y a diffraction).

Au MET, la longueur d'onde étant petite (2.51 pm à 200 kV), nous avons $\frac{1}{\lambda} \gg \|\vec{g}_{hkl}\|$. La sphère d'Ewald coupe le réseau réciproque en sections pratiquement planes. Donc, en première approximation (faibles angles de diffraction notamment), la figure de diffraction électronique peut être considérée comme un plan du réseau réciproque. Mais, il est également possible d'observer

plusieurs strates du réseau réciproque. En effet, d'après la figure 1-5, si nous nous plaçons aux grands angles de diffraction, avec un faisceau parallèle à une rangée [*uvw*] de forte symétrie, nous pouvons considérer que les nœuds du réseau réciproque sont disposés selon des strates (*uvw*)* d'indice n parallèles entre elles et équidistantes. Le cliché de diffraction correspondant est constitué de zones de Laue. Pour les échantillons ayant une très petite épaisseur (~100 nm) selon la direction du faisceau incident, nous observons un allongement des nœuds parallèlement à cette direction, conséquence du fait que la transformée de Fourier (réseau réciproque) inverse les dimensions. Nous avons un relâchement de la condition de Bragg qui devient :

$$\vec{k} - \vec{k}_0 = \vec{g}_{hkl} + \vec{s} \qquad (2)$$

où $\vec{s}$ est le vecteur excitation, ou écart à Bragg (figure 1-4).

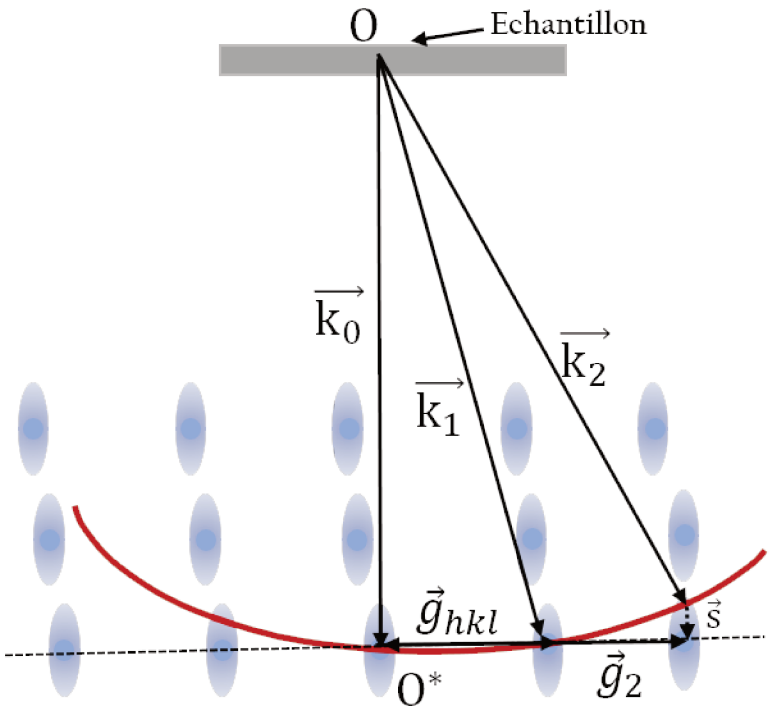

$$\vec{k}_1 - \vec{k}_0 = \vec{g}_{hkl} \quad , \quad \vec{k}_2 - \vec{k}_0 = \vec{g}_2 - \vec{s}$$

Figure 1-4 : Ecart à Bragg = l'allongement des nœuds est dû à la faible épaisseur de l'échantillon

$\vec{s}$ est considéré comme positif lorsqu'il est dans le même sens que le faisceau incident et négatif lorsqu'il est dans le sens contraire.

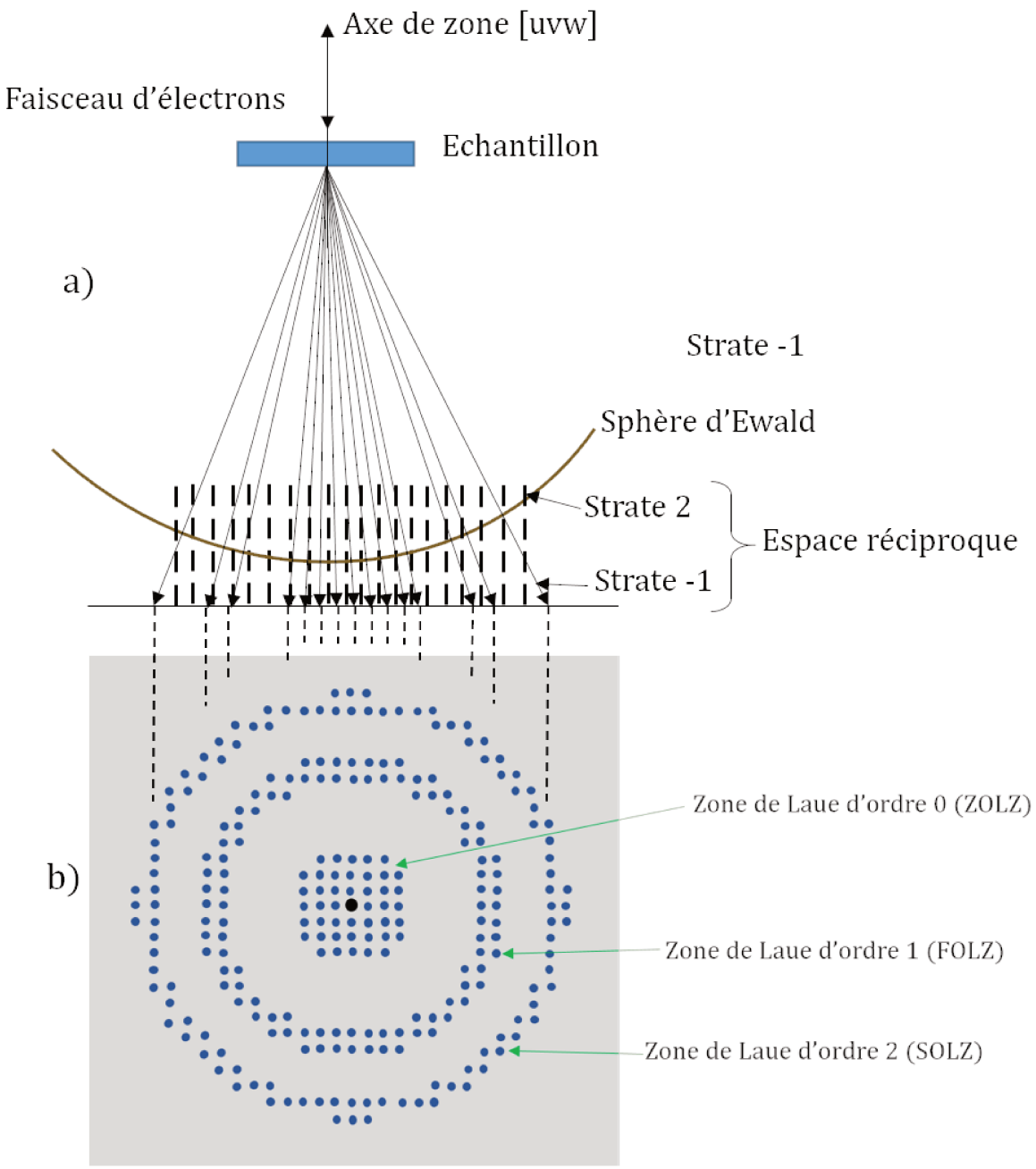

Figure 1-5 : Construction d'Ewald dans le cas d'un cliché de diffraction en axe de zone [uvw]
a-) Construction d'Ewald. Le réseau réciproque est constitué de strates parallèles et équidistantes. Des bâtonnets situés dans les différentes strates coupent la sphère et donnent des faisceaux diffractés.
b-) Cliché de diffraction correspondant formé de zones de Laue. Schéma tiré de Morniroli (1998)

I.1.2.2 Précession électronique

La technique de précession électronique a été mise au point au début des années 90 par Vincent & Midgley, 1994. La précession permet de réduire le caractère dynamique de l'intensité diffractée (la distribution de l'intensité obtenue sur le cliché de diffraction est qualifiée de quasi-cinématique). Elle réduit le phénomène de double diffraction, et augmente le nombre de réflexions ; dont leurs intensités sont approximativement proportionnelles au facteur de structure (figure 1-6). Depuis sa mise au point, elle a été utilisée pour plusieurs applications : La cristallographie électronique (détermination des structures), la caractérisation des défauts, et surtout celle qui nous va nous intéresser tout au long de cette thèse, l'orientation cristallographique par la technique ASTAR®. En précession, un mouvement de rotation est imposé au faisceau d'électrons grâce aux bobines déflectrices qui sont situées au-dessus de l'échantillon. Le faisceau dans son mouvement autour de l'axe optique décrit un cône de demi angle au somment ϕ (avec une fréquence généralement proche de 100 Hz), appelé angle de précession (figure 1-7). Plus cet angle est élevé, plus les phénomènes de diffraction dynamiques sont atténués. Au cours de cette thèse ϕ a pris des valeurs comprises entre 0 et 2 °. Grâces aux bobines déflectrices situées sous l'échantillon, les faisceaux transmis et diffractés subissent un mouvement synchrone et opposé afin d'avoir un cliché de diffraction semblable à celui obtenu avec un faisceau statique.

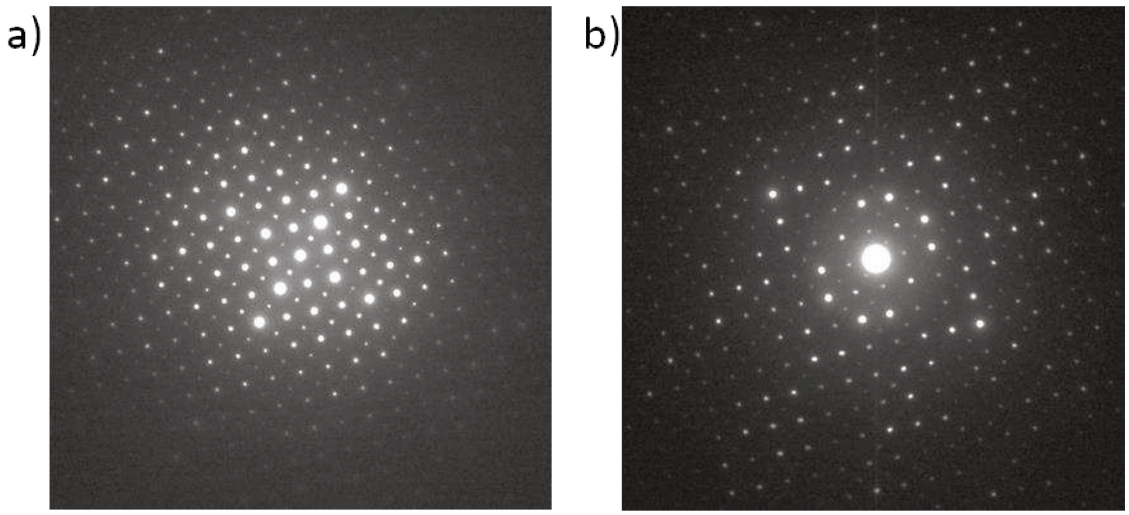

Figure 1-6 : Clichés de diffraction selon l'axe de zone [001] dans l'enstatite. a) Sans précession. b) Avec 2,8° d'angle de précession : Nous remarquons l'absence de certaines réflexions présentes sur le cliché sans précession (il y a eu réduction d'effets dynamiques). ***Crédit : Damien Jacob***

Les intensités observées sur le cliché de diffraction sont des intensités intégrées le long des nœuds du réseau réciproque. En utilisant la précession, l'intensité des réflexions n'est pas seulement celle obtenue pour une seule valeur de s mais le profil en partie intégré $I = f(s)$ (figure 1-8).

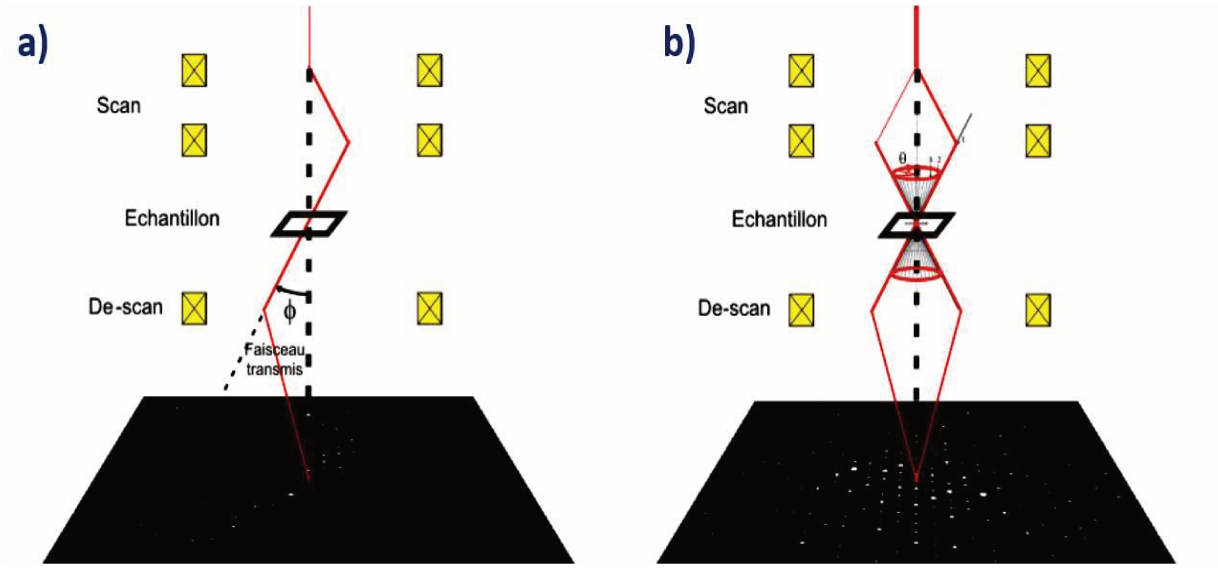

Figure 1-7 : Trajet du faisceau en précession électronique : a) Les bobines déflectrices dévient le faisceau pour le faire pivoter autour de l'axe optique du microscope. b) Les bobines situées sous l'échantillon font subir aux faisceaux transmis et diffractés le même mouvement de façon synchrone et dans le sens opposé (Own, 2005).

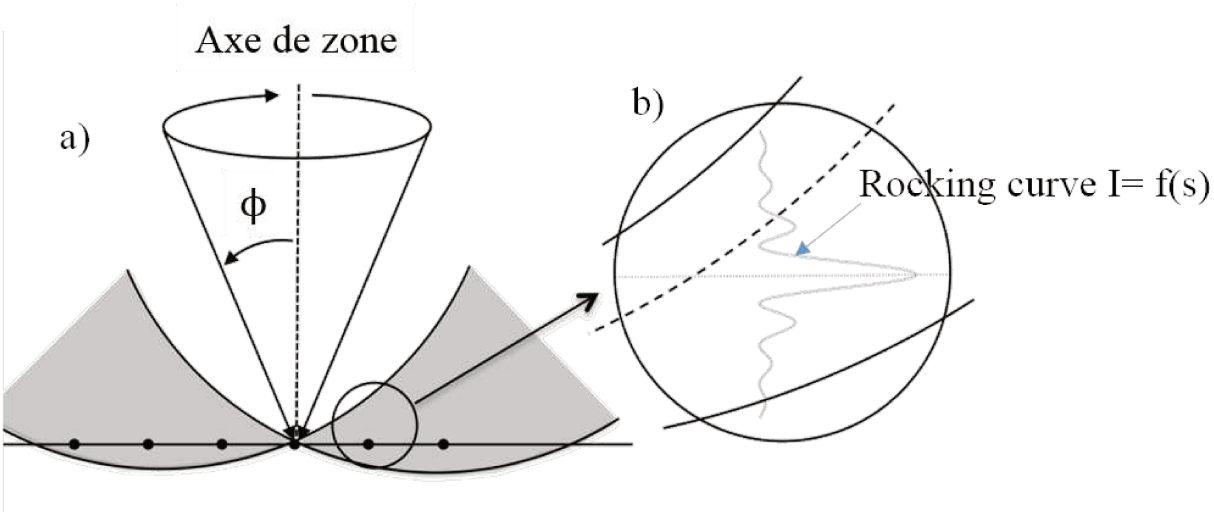

Figure 1-8 : Principe de la précession électronique. a) La précession d'un angle ϕ fait interagir uniquement les réflexions proches, et situées sur la sphère d'Ewald ; le cliché de diffraction est construit séquentiellement grâce au faisceau tournant. b) Zoom sur le profil d'intensité d'une réflexion : la rocking curve est complètement intégrée par le circuit de précession (pour cette réflexion particulière).

I.1.2.3 Diffraction électronique en aire sélectionnée (Selected area electron diffraction : SAED) et en faisceau convergent

a- SAED

La diffraction électronique en aire sélectionnée est une technique très utilisée en MET (identification des phases, indexation des orientations, recherche de symétries cristallines…). Le faisceau incident d'électrons étant parallèle à l'axe optique (figure 1-9), le diaphragme de sélection d'aire est utilisé pour choisir la zone de l'échantillon qui contribue au cliché de diffraction. La taille minimale du diaphragme étant 500 nm, la zone sélectionnée peut comporter des variations d'épaisseur et d'orientation, ce qui fait du cliché obtenu un cliché moyenné. Etant donné que le rayon de la sphère d'Ewald est très grand devant les dimensions du réseau réciproque, de nombreux bâtonnets sont interceptés par la sphère, ce qui donne lieu à de multiples tâches de diffractions pour une seule et même orientation.

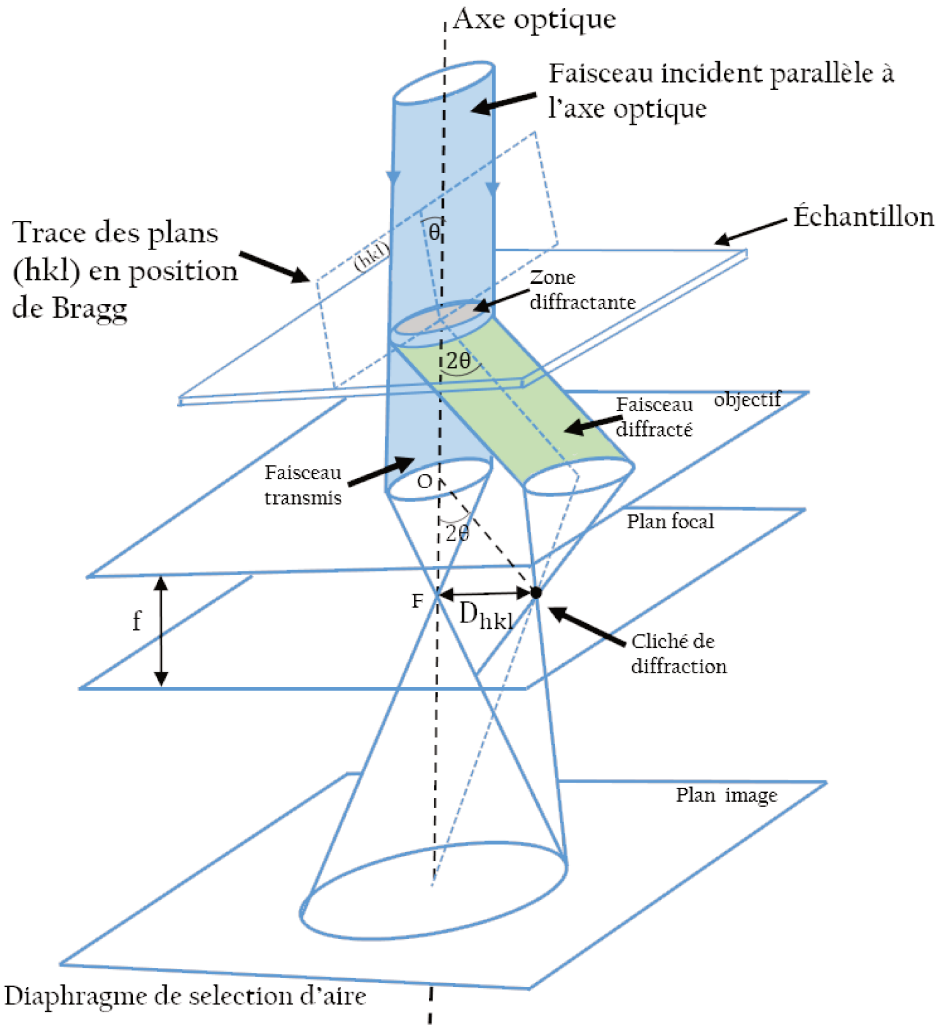

Figure 1-9: Diffraction électronique en faisceau parallèle et en conditions deux ondes ; dans le cas où une famille (hkl) est en position de Bragg. Schéma tiré de Morniroli (1998).

b- Indexation d'un cliché de diffraction

Sur la figure 1-9 ci-dessus la distance D_{hkl} entre la réflexion diffractée et le faisceau transmis dans le plan focal est liée à l'angle de Bragg θ par :

$$D_{hkl} = f.\tan(2\theta) \quad (3)$$

θ étant petit, nous avons $D_{hkl} = 2f\theta$ et sur l'écran, $D_{hkl} = 2L\theta$ ou L est la longueur de caméra. D'après la loi de Bragg, $\theta = \frac{\lambda}{2d_{hkl}}$, soit $D_{hkl} = \frac{L\lambda}{d_{hkl}}$, c'est-à-dire :

$$D_{hkl}.d_{hkl} = L\lambda = C \quad (4)$$

Le terme $L\lambda$ ne dépend que des conditions expérimentales, il est appelé « constante de diffraction ». Nous pouvons donc, en mesurant la distance inter-réticulaire et les angles entres les plans, déduire les familles de plans (*hkl*) correspondants.

I.1.2.4 Cliché de diffraction produit par un faisceau incident convergent

En reprenant les mêmes conditions que la figure 1-9 et en remplaçant le faisceau incident parallèle par un faisceau convergent de demi-angle au sommet α, nous obtenons dans le plan focal un cliché de diffraction constitué de disques (figure 1-10). La taille de ces disques est directement liée à l'angle de convergence. Vu que tous les faisceaux qui sortent de l'échantillon avec la même orientation convergent tous au même point du plan focal, il est possible de réduire ou d'augmenter la taille de la zone qui diffracte sans changer le trajet des électrons dans ce plan. Nous aurons donc un cliché de disques qui ne dépend pas de la taille de la zone (en supposant bien sûr constants l'épaisseur et l'orientation des plans (hkl) dans cette zone) comme dans le cas de la diffraction en faisceau parallèle. La figure 1-10 montre la trajectoire du faisceau qui forme le cliché de diffraction.

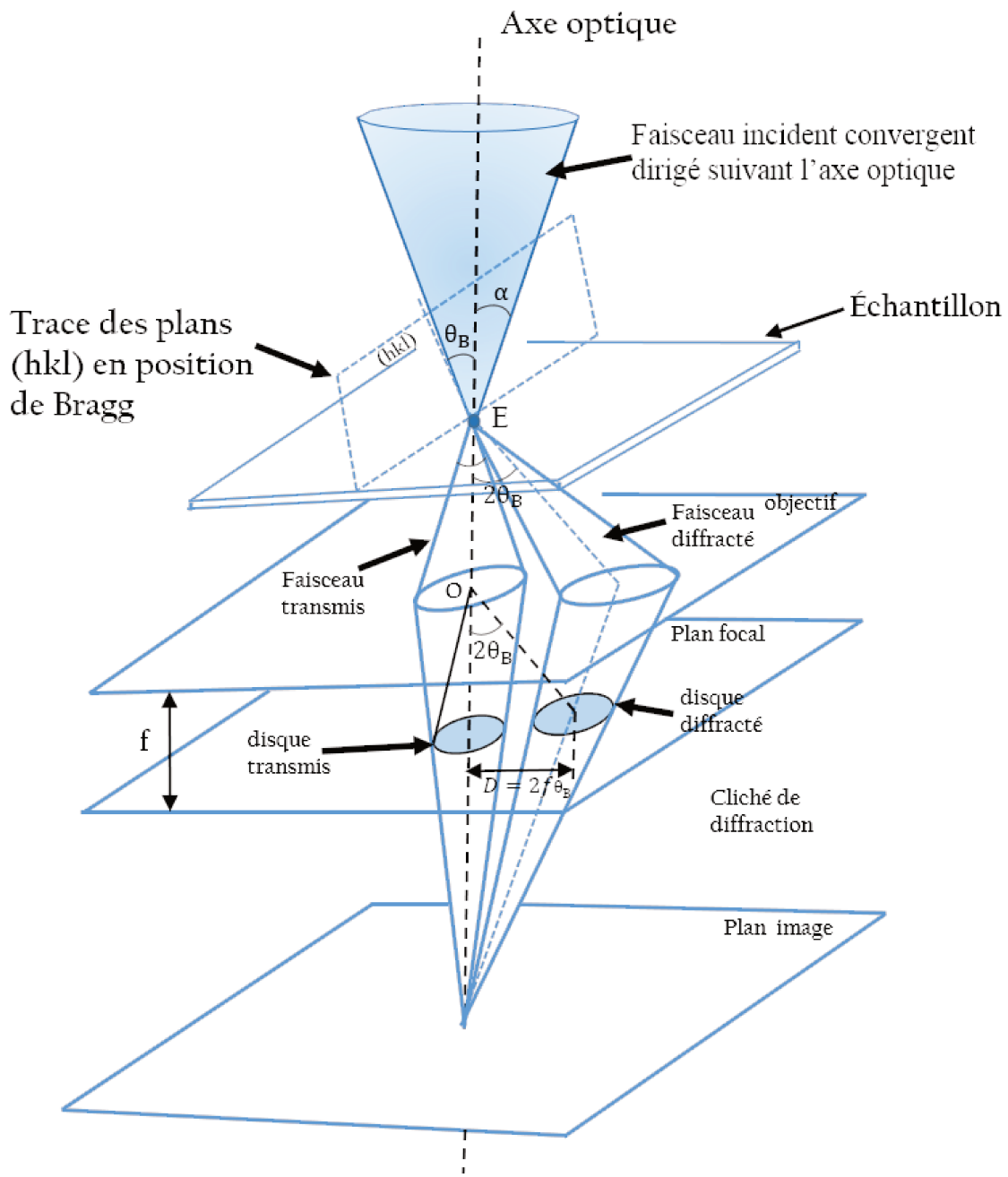

Figure 1-10 : Formation du Cliché de diffraction en faisceau convergent en conditions deux ondes. Le cliché de diffraction, situé dans le plan focal de l'objectif est constitué d'un disque transmis et d'un disque diffracté (hkl) (Morniroli, 1998)

I.2 Cartographie des orientations cristallographiques au microscope électronique

I.2.1 Introduction

Nous allons décrire ici quelques techniques qui à notre connaissance permettent de déterminer les orientations d'un polycristal au MET. Dès lors que les clichés de diffraction d'un matériau cristallin sont associés à l'ensemble de ses informations structurales, il est possible (comme en diffraction des électrons rétrodiffusés en MEB) de développer des techniques permettant d'indexer ces clichés et de remonter aux orientations cristallines. Les lignes de Kikuchi et les clichés de diffraction peuvent être utilisés simultanément (Schwarzer & Sukkau, 1998) pour extraire les informations sur les phases et les orientations. Fundenberger et ses collaborateurs (Fundenberger et al., 2003) proposent cinq ans plus tard une indexation automatique de clichés Kikuchi au MET, avec une résolution spatiale de 10 nm et une résolution angulaire de 0.1°. Néanmoins ces techniques présentent quelques difficultés pour analyser les clichés de diffraction issues d'échantillons avec une forte variation d'épaisseur (effets dynamiques) et très fortement déformés (épaississement des lignes de Kikuchi).

En 2005, Rauch & Dupuy ont proposé un algorithme de corrélation croisée afin de comparer des clichés de diffraction acquis au microscope à des clichés de diffraction pré-calculés. Cet algorithme permet de sélectionner l'orientation cristalline et la phase à partir d'une banque de clichés de diffraction théoriques (dénommés templates par la suite). L'ACOM (Automated Crystal Orientation Mapping) est une technique basée donc sur l'analyse des clichés de diffraction, produit et commercialisé par la société NANOMEGAS® sous le nom d'ASTAR. La résolution angulaire obtenue est de l'ordre de 0.3° (Rauch & Véron, 2014). L'outil ASTAR est constitué de quatre logiciels qui remplissent chacun des tâches bien précises : acquisition des clichés de diffraction, génération des templates, indexation avec l'algorithme de corrélation croisée et exploitation des résultats

I.2.2 Acquisition des clichés de diffraction et calcul des orientations

Nous allons, dans cette partie, décrire les différentes étapes entre l'acquisition d'un ensemble de clichés de diffraction et la cartographie d'orientations (et/ou de phases) associée. Tout au long de cette thèse nous utiliserons ASTAR pour caractériser la microstructure et les mécanismes de déformation des minéraux.

I.2.2.1 Dispositif d'acquisition

Le dispositif d'acquisition est constitué d'un système appelé DigiSTAR qui est relié au microscope (connecté à un ordinateur), et d'une caméra externe CCD. Le logiciel TEM dpa permet de contrôler la taille de la zone à balayer, le pas d'acquisition, le temps d'exposition, entre autres. Le système DigiSTAR contrôle les bobines de déflexion du microscope et permet ainsi la précession du faisceau. Le faisceau d'électrons est focalisé sur l'échantillon en mode « microsonde ». Dans ce mode où l'échantillon est illuminé par un faisceau convergent le cliché de diffraction est constitué de disques (cf. paragraphe 1.2.1). En utilisant le plus petit condenseur, ces disques de diffractions

se réduisent à des taches de diffraction que nous pouvons indexer comme un cliché obtenu avec un faisceau parallèle. Le faisceau balaie la surface de l'échantillon et en chaque point nous obtenons un cliché de points qui est projeté sur un écran phosphorescent. Nous utiliserons donc par la suite, lorsque la précession est employée, l'acronyme SPED (Scanning Precession Electron Diffraction) pour désigner cette technique d'acquisition. Les clichés de diffraction sont ensuite collectés par une caméra externe et stockés dans un Blockfile pour pouvoir être traité ultérieurement. Les acquisitions sont faites avec une caméra Stingray dont la résolution standard est de 144 par 144 pixels.

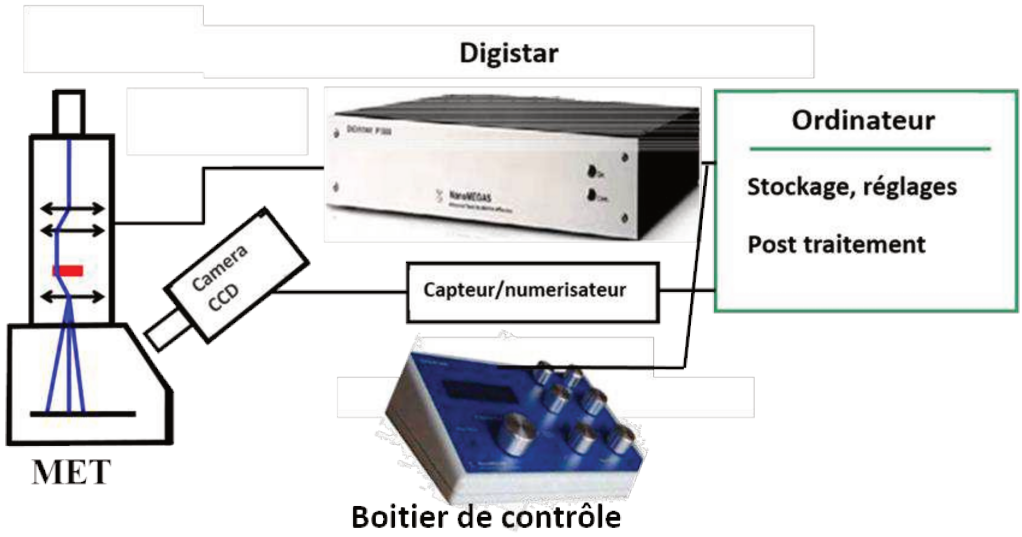

Figure 1-11 : Dispositif d'acquisition des clichés de diffraction

I.2.2.2 Création des banques de clichés de diffraction théoriques

A partir des données de la structure cristalline des constituants de l'échantillon (paramètres de maille, positions atomiques…), le logiciel Diffraction Generator (DiffGen) peut générer en conditions cinématiques (avec une résolution angulaire de l'ordre du degré) des banques de clichés de diffraction (quelques milliers, en fonction de la structure étudiée). La tension du microscope utilisée pour l'acquisition, l'angle maximum de Bragg, ainsi que l'excitation (écart aux conditions de Bragg), peuvent être modifiés afin d'obtenir des clichés simulés qui se rapprochent le plus des clichés de diffraction expérimentaux. Générer des templates adéquats est la principale difficulté que rencontrent les utilisateurs du système ASTAR. Lorsque nous avons un matériau monoatomique (cuivre, fer …) ou certains aciers, la génération est assez simple compte tenu du fait que DiffGen possède des valeurs prédéfinis de paramètres (écart a Bragg, taille de sonde …) pour avoir des templates raisonnables. Lorsque l'on travaille avec une phase qui contient plusieurs atomes, par exemple l'olivine, (((Mg, Fe)$_2$ SiO$_4$), Pbnm) la base est polyatomique et nous obtenons donc un template très dense (figure ci-dessous).

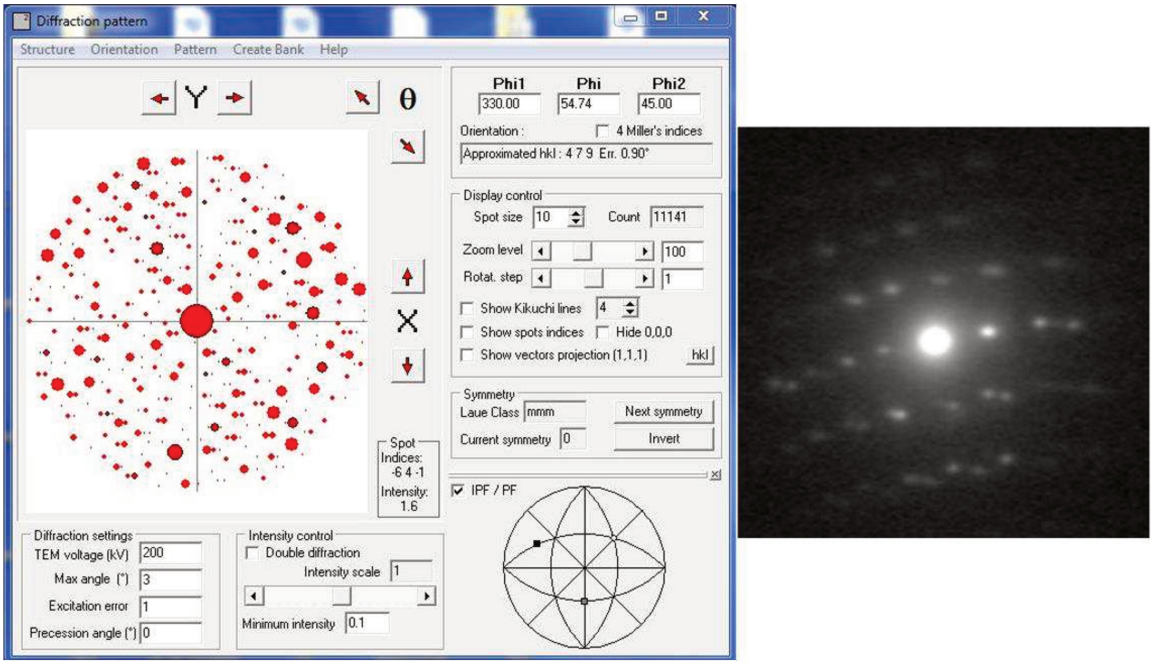

Figure 1-12 : A gauche : cliché simulé de l'olivine à 200 kV avec un écart à Bragg de 1 nm^{-1}. A droite cliché de diffraction à indexer obtenu au microscope.

- Ecart à Bragg :

Un ensemble de plans en conditions de Bragg donne lieu à une réflexion. Même lorsque ces conditions ne sont pas totalement respectées, la tâche apparaît toujours mais avec une intensité plus faible. Pour la génération des templates, cette diminution d'intensité est obtenue en réduisant l'écart aux conditions de Bragg s. La valeur entrée par l'opérateur représente l'écart à Bragg maximum (figure 1-13 ci-dessous).

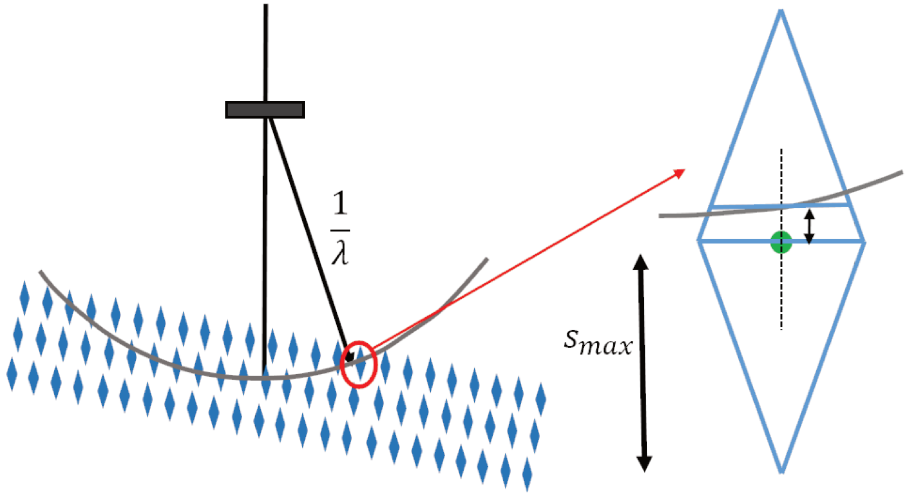

Figure 1-13 : Construction d'Ewald, plusieurs nœuds du réseau réciproque sont proches des conditions de Bragg. L'intensité varie en fonction de la position du nœud par rapport à la sphère.

Pour des structures à grand paramètres de mailles (olivine par exemple) la distance entre plans dans le réseau réciproque diminue et il faut donc diminuer s_{max}.

- Pas angulaire et nombre de pas (Step count)

Les templates sont générés avec un pas angulaire de l'ordre du degré. Lorsque l'écart à Bragg est réduit, il semble naturel d'augmenter le nombre de pas, car l'espace réciproque est sondé par la sphère d'Ewald dans un nombre limité de positions (angles d'Euler successifs). Lorsque l'écart à Bragg est réduit, le degré de chevauchement de deux templates successifs est diminué (cela se traduit par moins de solution dans l'index map (figure 1-15)). Cette tendance est compensée par l'augmentation du nombre de pas. La possibilité est toutefois limitée par la taille des banques (environ 40 Mo pour 150 pas dans la calcite) et le taux d'indexation.

- Echelle d'intensité

C'est un paramètre important qui permet de contrôler le ratio d'intensité entre les différentes taches de diffraction. Elle est non linéaire et son augmentation réduit la différence d'intensité entre les réflexions. La valeur minimale par défaut est 1 et la valeur maximale 100 correspond au cas où toutes les réflexions ont des intensités similaires quelles que soient les conditions de diffraction (à éviter donc !).

I.2.2.1 Comparaison des clichés

Le logiciel « *Index* » est conçu pour rechercher aussi bien l'orientation d'un cliché de diffraction qu'une série de clichés. En d'autres termes ce logiciel compare les clichés collectés au microscope (clichés enregistrés dans un fichier nommé blockfile) à la base de templates générés. Il reçoit donc en entrée la série de clichés stockés dans le blockfile et la banque de clichés théorique. Un certain nombre de paramètres peuvent être modifiés (blockfile et banque) afin d'optimiser la qualité du processus de comparaison. Puisque les clichés de diffraction sont projetés sur un petit écran incliné d'un angle α (dont la valeur dépend du microscope), il devient nécessaire de corriger la distorsion ; douze variétés de distorsion sont ajustables, deux exemples sont donnés sur la figure 1-14 ci-dessous. Aussi, dans le but d'améliorer la qualité des images (diminuer le bruit de fond, augmenter le contraste des taches de diffraction…) plusieurs outils de traitement d'images sont disponibles (distorsion, centrage, pixels d'une réflexion …). La valeur de l'index pour un cliché de diffraction peut être visualisée en niveaux de gris, sur une figure de pôle inverse contenant les indices de corrélation croisée (équation 5) de tous les templates de la banque. L'unicité de la solution peut alors être vérifiée (cf. figure 1-15).

La position de la tâche centrale (faisceau transmis) est un paramètre important de la procédure, puisqu'elle est le centre de rotation de toutes les orientations possibles des clichés générés. Il est important donc de bien la centrer pour avoir une bonne superposition entre les templates et les clichés de points. La longueur de caméra utilisée pour l'acquisition au microscope doit être en accord avec celle de la banque, le programme dispose d'un outil permettant de déterminer la longueur de caméra qui correspond au mieux au blockfile. Concrètement, il balaye un template

avec une gamme de longueurs de caméra proches de celle utilisée lors de l'acquisition, dans le même temps une indexation automatique donne pour chacune des longueurs de caméra un indice de fiabilité. C'est ainsi qu'on choisit la bonne longueur de caméra (correspondant au plus grand indice de fiabilité). Il faut dans certains cas répéter l'opération à différents endroits de la carte pour obtenir la longueur de caméra idéale.

Après le traitement d'image (filtrage, bruit de fond…), le centrage, le choix de la longueur de caméra, le traitement de la distorsion et l'ajustement de paramètres de diffraction, il faut procéder au calcul des orientations. Selon la symétrie du cristal, nous pouvons travailler en « *full matching* » ou en « *fast matching* ». Dans le premier cas, pour chaque template, toutes les rotations azimutales sont testées et la solution est celle qui correspond à l'indice de corrélation le plus grand. Dans le second, uniquement les n templates ayant au moins une réflexion (à fort facteur de structure) en commun avec le cliché de diffraction sont testés, la valeur de n étant définie par l'utilisateur.

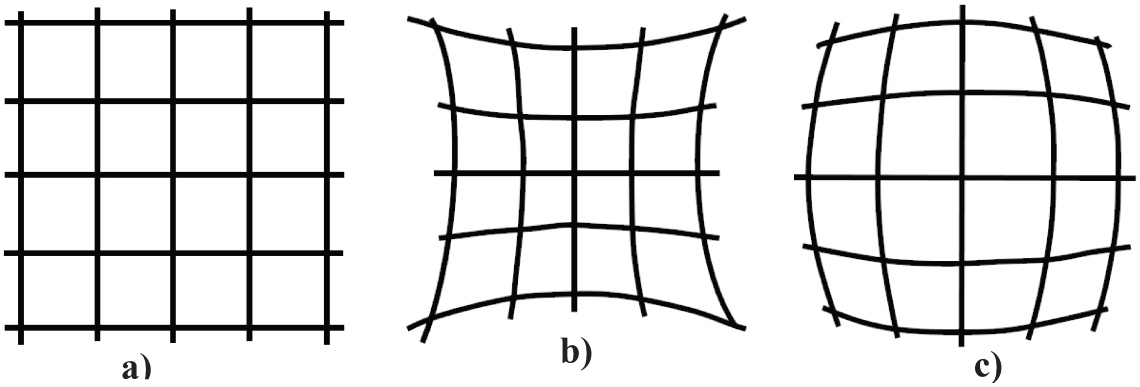

Figure 1-14 : Exemples de distorsions corrigées sur l'image ; a) Image sans distorsion. b) distorsion en coussinet. c) distorsion en barillet.

- Indice de corrélation

Le degré de correspondance entre le cliché de diffraction et le template est quantifié par la grandeur Q. Pour chaque template *i*, nous avons :

$$Q(i) = \frac{\sum_{j=1}^{n} P(x_j, y_j)\, T_i(x_j, y_j)}{\sqrt{\sum_{j=1}^{n} P^2(x_j, y_j)}\ \sqrt{\sum_{j=1}^{n} T^2(x_j, y_j)}} \qquad (5)$$

où $P(x_i,y_j)$ représentent les clichés de diffraction, $T(x_i,y_j)$ les templates, et x_i et y_j sont les coordonnées spatiales des pixels (Rauch, & Dupuy, 2005)
Pour l'unicité de la solution nous définissons la grandeur *R* (pour Reliability ou fiabilité en français), qui mesure le ratio entre les deux meilleures solutions Q_1 et Q_2 ;

$$R = 100(1 - \frac{Q_1}{Q_2}) \quad (6)$$

Généralement la solution est considérée comme étant acceptable à partir de $R = 15$. Dans le cas où nous avons plusieurs solutions qui ont des index proches, nous avons des valeurs de R faibles (figure 1-15)

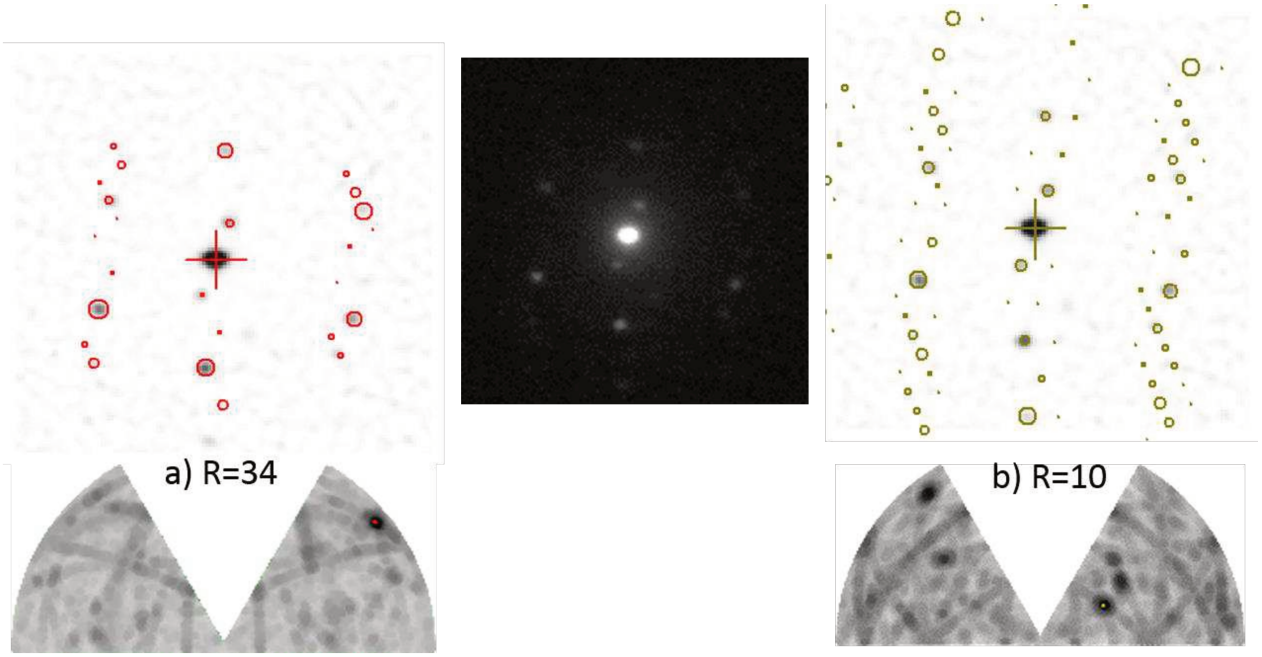

Figure 1-15 : Indexation avec une bonne fiabilité (a) et une mauvaise (b)

I.2.3 Cartographies d'orientation

a) Définition d'une orientation

Afin de définir l'orientation individuelle d'un cristal au sein d'un matériau, considérons deux repères K_A et K_B (figure 1-16). K_B est le repère cristallin lié au grain, dont les axes sont choisis suivant la symétrie cristalline du réseau, et K_A le repère macroscopique lié à l'échantillon. Dans le cas du système cubique par exemple les axes du repère K_B coïncident avec les directions cristallographiques [100], [010] et [001].

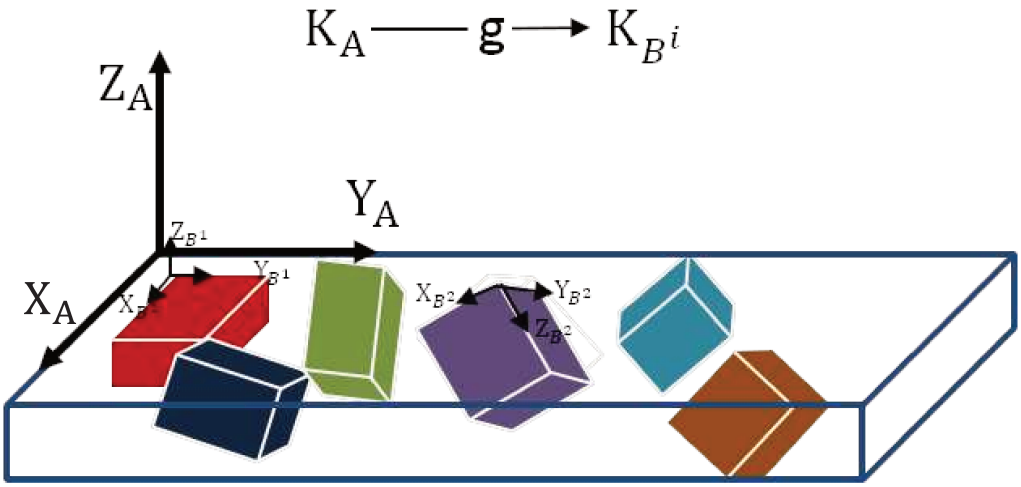

Figure 1-16 : Repère macroscopique et individuel, permettant de décrire les orientations des grains

L'orientation d'un cristal est définie par la matrice de rotation $\underline{g}$ qui permet de faire tourner le repère macroscopique K_A pour le faire coïncider avec le repère K_B, abstraction faite de toute translation. Cette rotation peut être décrite de différentes manières, il est possible d'utiliser soit une représentation graphique, soit une représentation matricielle, soit les angles d'Euler. Les angles d'Euler $\varphi_1, \phi \; et \; \varphi_2$ (convention de Bunge (1993)) sont généralement utilisés pour décrire cette rotation (figure 1-17).

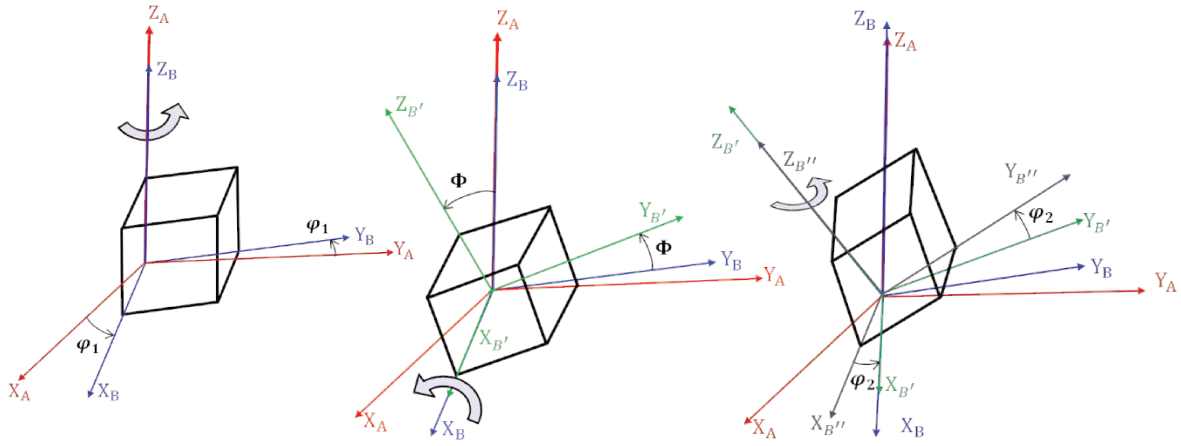

Figure 1-17 : Définition des angles d'Euler, d'après (Bunge, 1993).

Les figures de pôles permettent de représenter, en deux dimensions, des rotations dans un espace à trois dimensions. L'orientation d'un plan est repérée par son pôle (c'est-à-dire la normale au plan cristallographique). Dans le système cubique, par exemple, les plans sont orthogonaux aux

directions. La figure 1-18 ci-dessous montre comment obtenir un pôle <100> dans une structure cubique. Durant cette thèse, nous avons surtout utilisé les angles d'Euler pour déterminer les paramètres des défauts cristallins (et notamment des joints et sous-joints de grains).

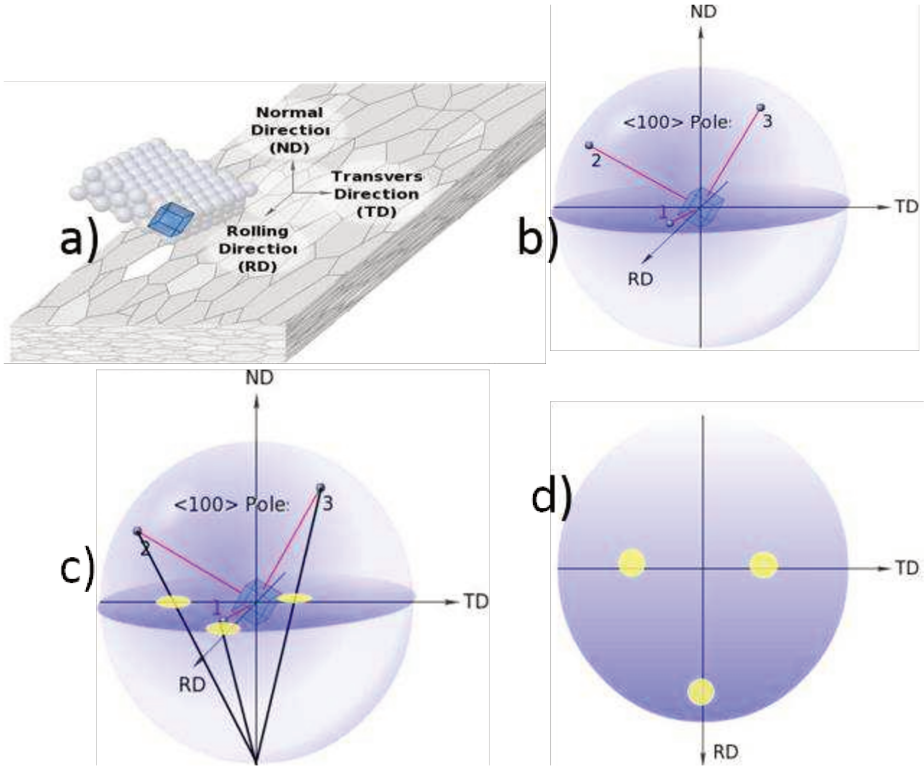

Figure 1-18 : Pôles <100> dans une structure cubique. a) Grain de structure cubique dans un échantillon déformé, b) orientation des pôles [100], [010], [001] : pôles <100>, c) intersection avec le plan équatorial (en violet), d) vue depuis le pôle Nord : figure de pôle <100>

En plus des cartographies d'orientations et de phases, différentes cartographies peuvent être produites et visualisées avec le dernier logiciel nommé « Mapviewer ». Nous pouvons par exemple utiliser l'intensité de la tâche transmise (en utilisant un diaphragme virtuel, de diamètre ajustable) en chacun des points et constituer une image en champ clair virtuelle ou Virtual Bright Field (VBF) en anglais qui ressemble trait pour trait au champ clair en microscopie conventionnelle. Chaque pixel de l'image représente, en niveau de gris (8 bits), l'intensité du faisceau transmis en ce point. Le VBF permet de mettre en évidence certains défauts dans la structure des matériaux cristallins (dislocations, joints de grains, macles, …). Nous pouvons également construire des Virtual Dark Field (VDF) en ne sélectionnant que les taches diffractées ; ce qui permettrait ainsi, après avoir au préalable indexé les clichés de diffraction, de caractériser certains défauts (déterminer les vecteurs de Burgers des dislocations par exemple).

Nous pouvons construire également des cartographies représentant respectivement la qualité de l'indexation et le niveau de fiabilité (figure 1-19). Les clichés de diffraction situés sur les joints de grains sont généralement constitués d'une association de deux clichés de diffraction (superposition de deux grains). Par conséquent, la fiabilité au niveau des joints est faible. Les cartographies de fiabilité permettent donc de distinguer les joints des grains (joints sombres par rapport aux grains

clairs). Le logiciel Mapviewer offre aussi la possibilité de faire une première analyse de la microstructure de l'échantillon (distribution de tailles de grains, figures de pôles et figures inverse de pôles …). Généralement pour des analyses plus poussées, nous pouvons exporter le résultat du calcul en fichier d'extention.ctf (Channel Text File) ou .ang afin de l'étudier avec des logiciels utilisés habituellement par la communauté EBSD. Nous pouvons dans certains cas combiner plusieurs cartes (figure 1.19d ci-dessous).

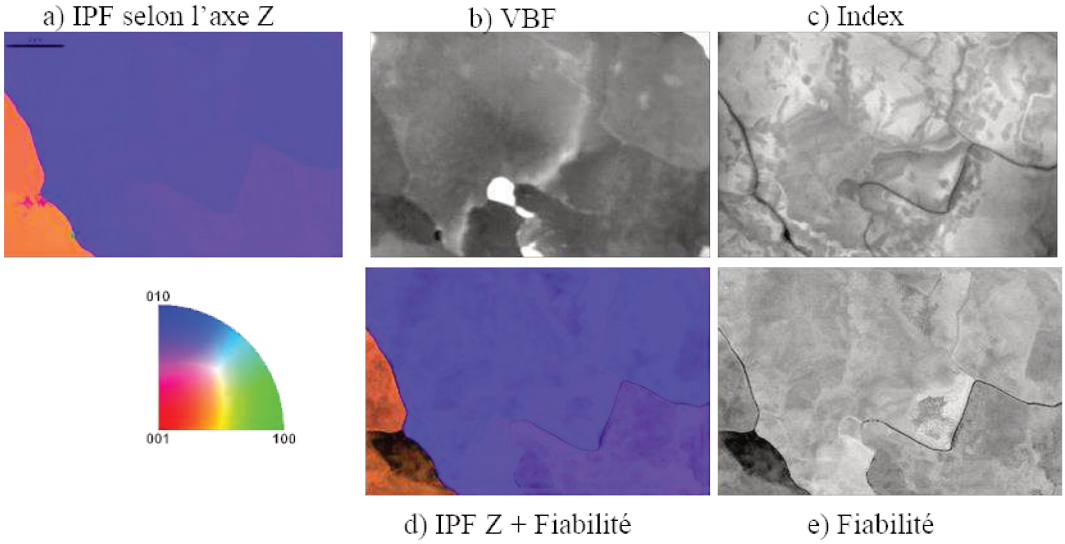

Figure 1-19 : Quelques exemples de cartes issues du logiciel Mapviewer.
a-) Figure inverse de pôle dans l'olivine selon l'axe Z (repère associé à la lame mince). b-) Virtual Bright Field (VBF), c-) index: l'intensité de chaque pixel est rattachée à une valeur d'index, d-) fiabilité. e) figure inverse de pôle + fiabilité

I.3 Plasticité et défauts cristallins

I.3.1 Généralités sur les dislocations

Les matériaux cristallins peuvent se déformer par propagation d'un cisaillement le long de certaines directions spécifiques $< uvw >$ contenues dans des plans {hkl}. La limite entre la partie cisaillée et celle d'origine est appelée « dislocation » (figure 1-20).

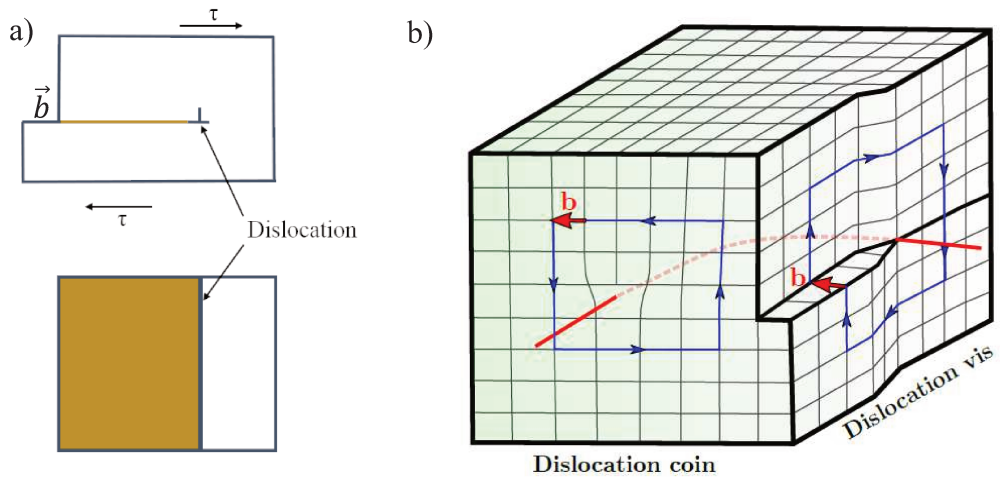

Figure 1-20 : a) Vue de côté et vue de dessus d'un solide soumis à un cisaillement plastique, la dislocation matérialise la limite entre la zone cisaillée et celle qui ne l'est pas. $\vec{b}$ est le vecteur de Burgers.
b) Dislocation coin, mixte et vis. Le vecteur de Burgers et la ligne de dislocation sont représentés en rouge. La portion de la ligne de dislocation en pointillés correspond à une dislocation mixte.

$\vec{b}$ est appelé vecteur de Burgers ; c'est le vecteur qui exprime la discontinuité du champ de déplacement au travers de la ligne. Il peut s'exprimer à l'aide des indices de Miller $< uvw >$. Il représente le cisaillement élémentaire propagé par le déplacement de la ligne de dislocation, laquelle est portée localement par le vecteur $\vec{u}$(M). Dès lors que la dislocation est décrite par deux vecteurs, le vecteur de ligne $\vec{u}$(M) et celui de Burgers $\vec{b}$ nous pouvons distinguer deux cas de figures :

- Le cas où $\vec{b} \perp \vec{u}$(M), la dislocation est de type coin
- Le cas où $\vec{b} \,//\, \vec{u}$(M), la dislocation est de type vis

Il est possible d'avoir des cas où la dislocation n'est pas uniquement coin, ni vis (Figure 1-20b). Nous parlons dans ce cas de dislocation mixte. C'est le cas des dislocations courbées (en rouge sur le schéma ci-dessus) et des boucles de dislocations. Une dislocation étant une singularité linéaire, elle distord localement le réseau et donc introduit des contraintes internes. De façon générale, le champ de déplacement $\vec{R}$(M) d'une dislocation pour un solide homogène et isotrope, de coefficient de poisson ν, est donnée en coordonnées polaires par :

$$\vec{R}(M) = \frac{1}{2\pi}[\vec{b}.\theta + \frac{1}{4(1-\nu)}\{\vec{b}_e + \vec{b}\Lambda\vec{u}(M)\,(1-2\nu)\ln r + \cos 2\theta)\}] \qquad (7)$$

où $\vec{b}_e$ est la composante coin du vecteur de Burgers $\vec{b}$.

Dans le cas d'une dislocation vis, $\vec{b}_e = \vec{0}$ et $\vec{b} // \vec{u}$(M), donc $\vec{b}\Lambda\vec{u}(M) = \vec{0}$ le champ de déplacement se réduit à

$$\vec{\mathrm{R}} = \frac{\theta}{2\pi}\vec{b} \qquad (8)$$

Dans le cas d'une dislocation coin, les composantes du champ de déplacement s'écrivent :

$$\begin{aligned} \mathrm{R}_r &= \frac{b}{2\pi}\left[-\frac{(1-2\nu)}{2(1-\nu)}\sin\theta \ln r + \frac{\sin\theta}{4(1-\nu)} + \theta\cos\theta\right] \\ \mathrm{R}_\theta &= \frac{b}{2\pi}\left[-\frac{(1-2\nu)}{2(1-\nu)}\cos\theta \ln r + \frac{\cos\theta}{4(1-\nu)} - \theta\sin\theta\right] \end{aligned} \qquad (9)$$

Ce champ de déplacement est à l'origine des désorientations qui seront analysées dans la partie 1.3.3.

I.3.1.1 Densité de dislocations géométriquement nécessaires

- Tenseur des dislocations

Le vecteur de Burgers $\vec{b}$ est relié au vecteur normal $\vec{t}$ du plan d'aire unité contenant, dans le cristal non déformé, le circuit de burgers *C* par la relation :

$$b_i = \alpha_{ij}.t_j \qquad (10)$$

Ou α_{ij} est le tenseur introduit par Nye (1953).

Cette relation ne permet pas de remonter à la densité des dislocations. Pour relier le tenseur des dislocations à la densité des dislocations, Nye propose la méthode qui suit (Nye, 1953) : considérons un ensemble de dislocations toutes de même caractère et rectilignes, de vecteurs ligne unitaire $\vec{u}$ et de vecteurs de Burgers $\vec{b}$. Soit *n* le nombre de dislocations traversant l'unité d'aire normale à $\vec{u}$. Le nombre de dislocations traversant une unité de surface normale à $\vec{t}$ est alors $n\,\vec{u}.\vec{t}$. Le vecteur de Burgers associé à ces *n* dislocations est alors :

$$B_i = b_i(n\,u_j t_j) \qquad (11)$$

En injectant la relation (10) dans (11) Nye arrive à :

$$\alpha_{ij} = n\,b_i u_j \qquad (12)$$

Arsenlis et Parks (Arsenlis & Parks, 1999) ont généralisé cette relation pour N configurations différentes de dislocations, en considérant une densité de dislocations ρ^s sur chaque système de glissement :

$$\alpha_{ij} = \sum_{s=1}^{\mathrm{N}} \rho^s b_i^s u_j^s \qquad (13)$$

L'équation ci-dessus montre que les contributions de deux lignes de dislocations (appartenant au même système de glissement) appariées sont égales et opposées. La somme de leurs contributions

est donc nulle et ces dislocations n'ont aucune incidence sur le tenseur des dislocations de Nye ainsi que sur la courbure du réseau. L'analyse de la densité des dislocations par le biais du tenseur de dislocations ne permet donc pas d'avoir accès à la densité totale dans le volume élémentaire. Il faut donc différencier les dislocations qui contribuent à cette expression, des autres, localement appariées.

- Notion de dislocations géométriquement nécessaires

Des dislocations seront donc dites géométriquement nécessaires (GND) ou polaires (dislocations en excès) lorsqu'elles contribuent à l'expression du tenseur des dislocations de Nye, par opposition aux dislocations statistiquement stockées (SSD), qui sont toutes appariées.

Ashby a lui aussi introduit en 1970 le concept de GND (Ashby, 1970). Il s'est basé sur le fait que le stockage des dislocations responsables du durcissement plastique a deux origines : la nécessité de rendre compatible la déformation des différentes parties du matériau d'une part, et le phénomène de la forêt d'autre part. Ashby appelle ainsi donc GND, les dislocations stockées sous l'effet du premier phénomène et SSD les dislocations résultant du phénomène de la forêt.

Plusieurs auteurs (Arsenlis & Parks, 1999; Pantleon, 2008) ont ensuite complété cette définition à l'ensemble des dislocations induisant une distorsion dans un volume élémentaire de référence. Les SSD sont ces dislocations qui, considérées collectivement ne produisent pas d'incompatibilité de réseau.

Un ensemble de dislocations de vecteurs de Burgers non nul dans un volume donné et donnant donc lieu aux dislocations géométriquement nécessaires, peut en outre comporter des SSD (figure 1-21b ci-dessous). Une dislocation isolée est géométriquement nécessaire.

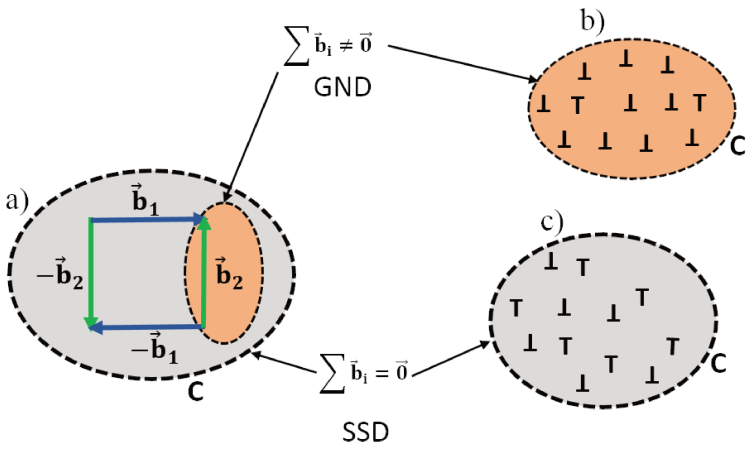

Figure 1-21 : Illustration des concepts de GND et SSD : a) et c): Volume contenant des dislocations toutes appariées, elles ne contribuent pas à la distorsion du volume. b) dislocation en excès.

- Courbure du réseau cristallin

La courbure du réseau cristallin est définie par le tenseur κ_{ij} qui représente le gradient spatial de l'orientation cristalline, donné par la relation :

$$\kappa_{ij} = \frac{\partial \theta_i}{\partial x_j} \qquad (14)$$

où θ_i est le vecteur rotation représentant l'orientation cristalline. En pratique, les cartes que nous obtenons par SPED fournissent une mesure discrète de l'orientation cristalline et nous pouvons à partir d'elles, calculer le tenseur des courbures élastiques. La différence entre deux orientations O_1 et O_2 est équivalente à la rotation permettant de passer du cristal en O_1 au cristal en O_2. Cette rotation peut être définie par un angle $\Delta\theta$ et un axe $\vec{r}$. Le vecteur des désorientations s'écrit alors $\Delta\theta_i = \Delta\theta . r_i$. Le tenseur des courbures élastique entre deux orientations O_1 et O_2 séparées de Δx s'écrit:

$$\kappa_{ij} = \frac{\Delta \theta_i}{\Delta x_j} \qquad (15)$$

- Relation entre courbure du réseau cristallin et tenseur de la densité des dislocations

Le tenseur de la densité des dislocations α_e se défini comme le rotationnel du tenseur des distorsions élastiques U_e.

$$\alpha_e = rot\ (U_e) \qquad (16)$$

Si α_e est non nul, alors U_e se décompose en une partie symétrique ε_e (déformations élastiques) et une partie antisymétrique ω_e (tenseur des rotations élastiques). La partie antisymétrique ω_e s'exprime en fonction du tenseur de courbure élastique par $\kappa_e = grad\ (\Omega_e)$, où Ω_e est le vecteur de rotation élastique. L'équation 16 devient donc :

$$\alpha_e = rot\ (\varepsilon_e) + tr(\kappa_e) I - {\kappa_e}^t \qquad (17)$$

où $tr(\kappa_e)$ et ${\kappa_e}^t$ représentent respectivement la trace et la transposée de κ_e (de composantes κ_{ij}).

En EBSD classique le tenseur des déformations élastiques ne peut être déterminé et il est très généralement négligé (Beausir & Fressengeas, 2013; Field et al., 2005; Pantleon, 2008). Il existe cependant de plus en plus de techniques (Villert et al., 2009; Wilkinson et al., 2006) permettant d'y avoir accès (EBSD-Haute Résolution, en mesurant le déplacement entre 2 clichés de Kikuchi).

Si nous négligeons les déformations élastiques, nous avons :

$$\alpha_e \simeq tr(\kappa_e) I - {\kappa_e}^t \qquad (18)$$

Les cartes 2D d'orientations que nous obtenons par SPED permettent d'avoir six composantes du tenseur des courbures élastiques (i=1, 2, 3 ; et j=1, 2), et à partir des six composantes du tenseur des courbures élastiques, nous pouvons déterminer 5 composantes du tenseur de Nye.

$$\begin{aligned} \alpha_{12} &= \kappa_{21} \\ \alpha_{13} &= \kappa_{31} \\ \alpha_{21} &= \kappa_{12} \\ \alpha_{23} &= \kappa_{32} \\ \alpha_{33} &= -\kappa_{11} - \kappa_{22} \end{aligned} \qquad (19)$$

Il faut noter que cet outil dépend du pas de mesure ; il faut donc, par la suite, faire très attention à comparer des mesures faites avec la même résolution spatiale.

I.3.2 Observations en MET

I.3.2.1 Imagerie des dislocations

Le champ de déplacement d'une dislocation décrit dans la partie précédente est responsable du contraste observé au MET. Lorsqu'une onde, diffusée par une colonne de l'échantillon dans la direction du faisceau, traverse une dislocation caractérisée par son champ de déplacement $\vec{R}(M)$, elle subit un déphasage $\alpha = 2\pi\vec{g}_{hkl}.\vec{R}(M)$. L'amplitude du faisceau diffracté s'écrit alors :

$$\Phi_g = \frac{i\pi}{\xi_g}\Phi_0 \int_0^t \exp 2i\pi(\vec{g}_{hkl}.\vec{R} + s_g z)dz \qquad (20)$$

où t est l'épaisseur de l'échantillon (hauteur de la colonne), s_g la projection suivant la colonne de l'écart à Bragg, son sens positif étant celui du faisceau transmis ; z est la coordonnée dans la direction de l'onde transmise, ξ_g la distance d'extinction des électrons, et Φ_0 l'amplitude du faisceau incident.

Une dislocation produira donc un contraste si et seulement $\vec{g}_{hkl}.\vec{R}(M) \neq 0$.

Dans les conditions réelles d'observation (dites dynamiques) plusieurs faisceaux sont diffractés et chaque faisceau, y compris le faisceau transmis, interagit avec les autres. Il semble donc, de prime abord, difficile d'interpréter l'information provenant d'un seul faisceau sélectionné car son intensité est fonction de tous les autres. Cette ambiguïté peut être diminuée en pivotant l'échantillon de façon à ce que seuls le faisceau transmis et un faisceau diffracté $\vec{g}_{hkl}$ aient une intensité significative : nous parlons alors de conditions « deux ondes ». Puisque les deux ondes recueillent toute l'information ($I_T + I_g = 1$), l'image est essentiellement dépendante du $\vec{g}_{hkl}$ choisi. En théorie il est difficile obtenir les conditions « deux ondes » parfaitement, mais en pratique au microscope il suffit que les autres ondes soient très faiblement excités pour considérer cet approximation comme valable.

I.3.2.1 Critère d'invisibilité

L'une des applications, parmi les plus importantes de la théorie du contraste, est la détermination du vecteur de Burgers d'une dislocation. Comme décrit au paragraphe précédent, le contraste des dislocations est lié au produit $\vec{g}_{hkl}.\vec{R}(M)$, c'est-à-dire au produit $\vec{g}.\vec{b}$ (cf. équation 7). D'après les travaux de Hirsch et al. (1960), le contraste d'une dislocation augmente avec le produit $\vec{g}.\vec{b}$. A contrario, la dislocation devient invisible lorsque $\vec{g}.\vec{b} = 0$ (exemple : figure 1-22 dislocation B). L'absence de contraste lorsque le vecteur de Burgers est perpendiculaire au vecteur diffractant peut être utilisée comme critère pour la caractérisation du vecteur de Burgers d'une dislocation.

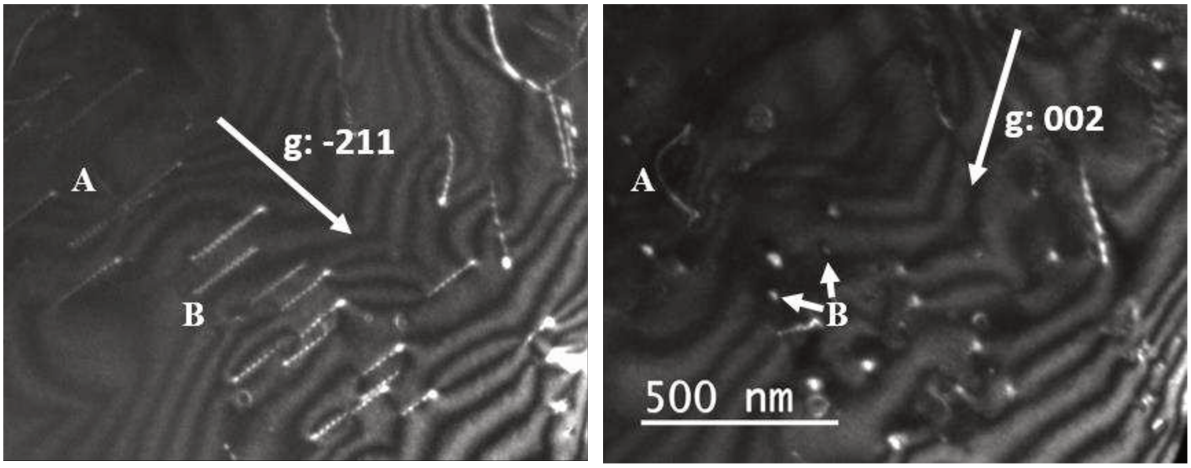

Figure 1-22 : Exemple de dislocation hors contraste dans la cémentite : à gauche, la dislocation B est en contraste et A est hors contraste ; à droite la dislocation courbée A est parfaitement en contraste et B est éteinte. Nous apercevons un contraste résiduel en A qui peut provenir de la composante coin de la dislocation. En B, le contraste résiduel représente les points où la dislocation débouche à la surface de l'échantillon (A. Mussi et al., 2016)

Notons que ce critère ne donne que la direction du vecteur de Burgers, et non pas sa norme. Habituellement les vecteurs de Burgers correspondent aux plus petites translations du réseau.

Le critère d'extinction $\vec{g}.\vec{b}$=0 représente une approximation, car le contraste est dû à un changement de phase $\alpha = 2\pi\vec{g}_{hkl}.\vec{R}$. Dans le cas d'une dislocation vis le critère d'invisibilité se réduit à $\vec{g}.\vec{b} = 0$. Dans le cas de la dislocation coin le champ de déplacement comporte un second terme proportionnel à $\vec{b}\wedge\vec{u}$. Le critère d'invisibilité est donc par conséquent: $\vec{g}.\vec{b} = 0$ et $\vec{g}.(\vec{b}\wedge\vec{u}) = 0$. Lorsque cette dernière condition n'est pas remplie, nous observons sur l'image un léger contraste résiduel (figure 1-22 ci-dessus). Rappelons que toutes ces conditions sont basées sur l'expression du champ de déplacement obtenu dans l'approximation d'un milieu élastique et isotrope donnée au paragraphe 1.3.1.

I.3.2.2 Imagerie des dislocations en Weak-Beam Dark-Field (WBDF)

Cockayne, Ray et Whelan, suite aux travaux de Hirsch (Hirsch et al., 1960) ont proposé en 1969 une nouvelle technique d'imagerie des dislocations (Cockayne et al., 1969), présentant des

contrastes plus fins qu'en microscopie électronique classique (champ clair et champ sombre) (figure 1-23).

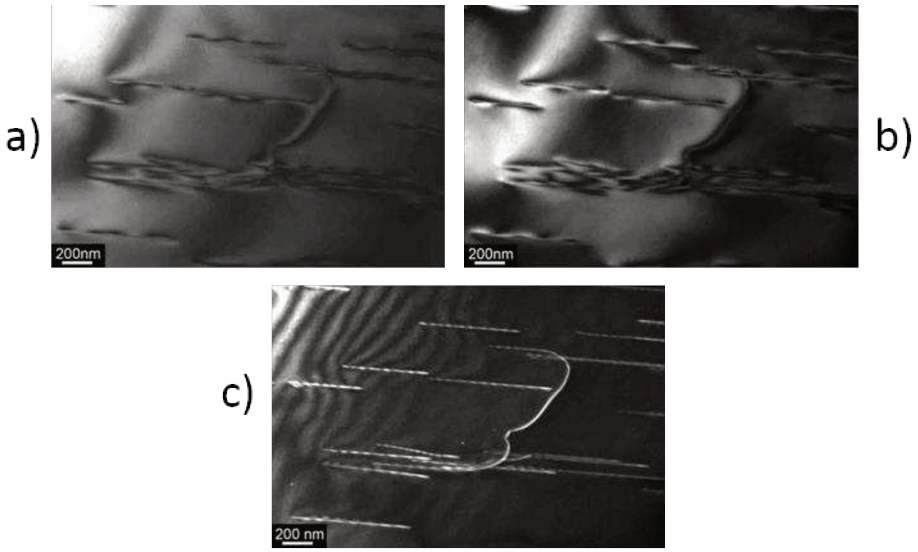

Figure 1-23 : Images de dislocations [001] dans l'olivine obtenues avec $\vec{g}$: 222 (monocristal d'olivine déformé par Sylvie Demouchy à 850°C et sous une pression de confinement de 300 MPa.) a) champ clair, b) champ sombre c) champ sombre faisceau faible. ***Crédit : P. Cordier, travaux non publiés.***

En conditions cinématiques, la demi largeur de l'image de la dislocation (à partir du cœur) avec $n = 2$ est d'environ $1/\pi s$ ($n = \vec{g}.\vec{b}$). En augmentant donc la valeur de s, l'on produit des images beaucoup plus fines, qui se rapprochent de la position réelle de la dislocation (cœur). Pour s = 0,2 nm^{-1}, la demi largeur d'environ 1,6 nm.

Pour se mettre dans ces conditions, nous nous plaçons en mode « deux ondes » (figure1-24a), en sollicitant le faisceau diffracté d'intérêt $\vec{g}$. Ensuite, nous utilisons le diaphragme objectif pour sélectionner ce faisceau, puis nous pivotons l'échantillon de façon à mettre en position exacte de Bragg ($s = 0$) les réflexions d'ordre supérieure $m\vec{g}$, m n'étant pas nécessairement un nombre entier (exemple figure 1-24b, cas où m=3).

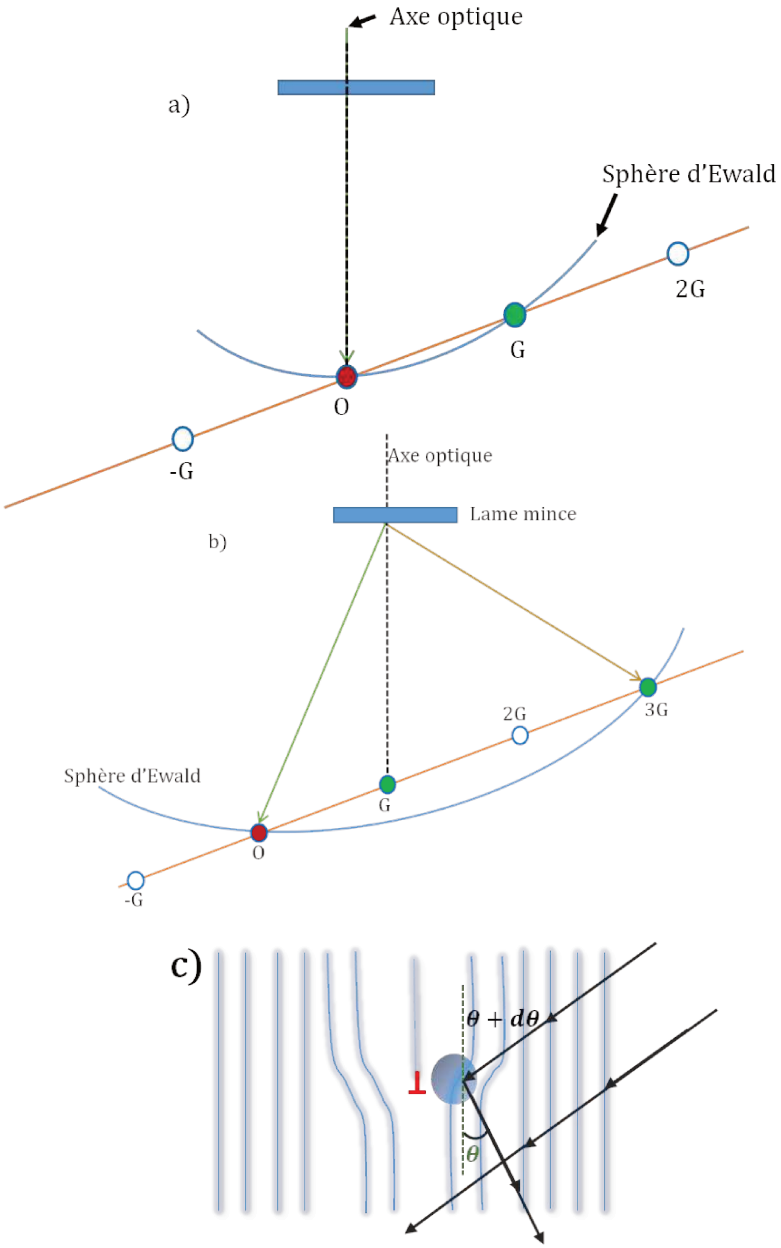

Figure 1-24 :a) Conditions « deux ondes », les intensités des ondes O et G sont les plus importantes. b) Construction d'Ewald montrant les conditions de diffraction utilisées pour obtenir des conditions de WBDF. c)Trajet du faisceau lors du WBDF, le contraste est créé par les plans distordus proches su cœur de la dislocation.

Le contraste d'une dislocation en WBDF est créé en pivotant la lame mince d'un angle donné de façon à ce que le faisceau incident soit loin des conditions de Bragg (figure 1-24c), ceci aboutit donc à un grand écart à Bragg. Les plans qui avoisinent le cœur de la dislocation (zone grisée figure 1-24c) sont en conditions de Bragg. C'est là que réside la principale différence avec le champ sombre, où tout le cristal est proche des conditions de Bragg.

I.3.3 Désorientations locales : techniques d'analyses issues de l'EBSD

L'EBSD dispose de plusieurs outils pour analyser la microstructure d'échantillons déformés. Les variations locales de désorientation sont un bon indicateur de déformation. Il existe deux types d'analyses : celles basées sur le grain et celles basées sur un noyau. On distingue :

- Le KAM (Kernel Average Misorientation) : c'est une mesure de la désorientation locale. Il est calculé en faisant la moyenne de désorientation entre un pixel de référence et les pixels voisins (figure 1-25). Etant donné que la présence des défauts induit des distorsions et crée de la désorientation, le KAM va nous permettre de mettre en évidence les zones où elles sont localisées. Cet outil peut ainsi révéler des gradients locaux de désorientations.

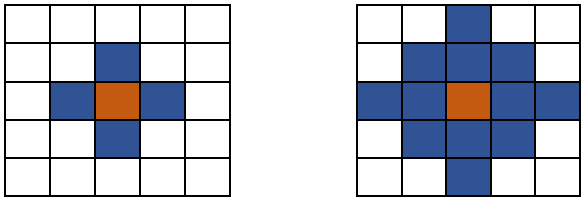

$$\boldsymbol{KAM(j) = \frac{1}{N}\sum_{i=1}^{N} \omega(g_i, g_j)}$$

Figure 1-25 : Principe du calcul du KAM, à gauche premier voisins, à droite seconds voisins. Le pixel de référence, d'orientation g_j est en orange. $g = (\varphi_1, \phi, \varphi_2)$

Le KAM est généralement compris entre 0 et 3°. Il est représenté parfois sur une échelle allant du bleu (0°) au rouge (3°). Il dépend très fortement du pas d'acquisition et sert d'approximant à la densité des GND (cf. paragraphe 1.3.2). Pour son calcul, il est possible d'utiliser soit les pixels autour du périmètre du Kernel, soit tous les pixels de celui-ci.

- Le GROD (Grain Reference Orientation Déviation) : permet de mettre en évidence le gradient de désorientation dans un grain. A partir du calcul de l'orientation moyenne du grain, nous faisons soit la différence entre l'orientation de chaque pixel et l'orientation moyenne (mis2mean, sous MTEX), soit la différence entre l'orientation de chaque pixel et celui du point de plus petit KAM dans le grain. Nous utiliserons le mis2mean dans la suite car le point correspondant au plus petit KAM peut parfois être le résultat d'une erreur de mesure.

- Le GOS (Grain Orientation Spread) : C'est la moyenne des désorientations dans un grain par rapport à l'orientation moyenne (donc la moyenne du mis2mean). Cependant le GOS donne lieu souvent à de fausses interprétations, il faut donc s'en méfier. Il est par exemple possible pour deux grains différents, d'avoir un même GOS pour deux distributions de GND différentes. Il est aussi possible d'avoir deux GOS différents pour deux grains avec la même quantité de GND (figure 1-26).

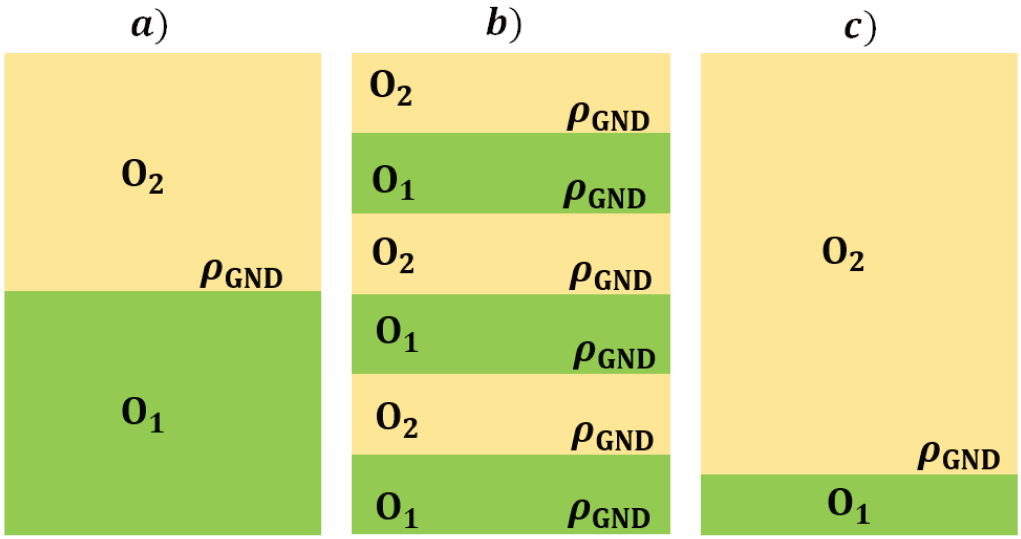

Figure 1-26 : Particularités du GOS : trois grains de tailles identiques présentant des sous structures différentes. O_1 *et* O_2 *sont deux orientations différentes dont l'interface nécessite* ρ_{GND}. *Les cas a) et b) ont la même valeur du GOS mais une densité de GND différente ; alors que les cas a) et c) ont une valeur différente du GOS mais la même densité de GND.*

Ces différents paramètres (KAM, GOS, GROD …) développés en EBSD pour exploiter des données d'orientations, sont accessibles dans un certain nombre de logiciels disponibles sur le marché, en libre accès (MTEX) ou non (TSL OIM, HKL channel 5…). MTEX est surtout utilisé pour un travail quantitatif sur les textures, pour les figures de pôles et le calcul tensoriel (F. Bachmann et al., 2010, 2011; Mainprice et al., 2015).

Chapitre II. Imagerie des défauts dans les minéraux par Scanning Precession Electron Diffraction (SPED)

Dans ce chapitre, après avoir rappelé le contexte, nous présenterons un article publié qui décrit l'apport de la SED dans la caractérisation des défauts dans les minéraux.

II.1 Contexte

La caractérisation par microscopie en transmission des minéraux sensibles à l'irradiation est un problème important en physique des minéraux. En effet, les phases de hautes pressions, des zones de subduction froide (silicates hydratés tels que phase A, phase D, etc.) mais aussi du manteau (bridgmanite, stishovite, coésite…) instables à température et pression ambiante ; s'amorphisent rapidement sous l'influence des bombardements électroniques occasionnés par les observations au MET. C'est également le cas de minéraux comme le quartz bien qu'il soit observé dans son champ de stabilité thermodynamique. Comme nous l'avons montré au chapitre précédent, le dispositif d'acquisition ASTAR nous permet de balayer rapidement la surface de l'échantillon en des temps d'exposition très court (jusqu'à 10 ms). La pile de clichés de diffraction stockée peut être ensuite utilisée de différentes manières.

Nous avons profité des opportunités que nous offre la SED (Kiss et al., 2016; Rauch & Véron, 2014) pour caractériser les défauts dans l'olivine, le quartz et la phase A. Le premier échantillon est une olivine naturelle qui a été déformé à Montpellier par M. Thieme et S. Demouchy à 1273 K (CMT16-8), et à 1,07% de taux de déformation macroscopique (Thieme et al., 2018). Cet échantillon a fait l'objet d'une autre étude qui sera détaillée au prochain chapitre. Le second échantillon, le quartz, est l'un des constituants majeurs de la croûte terrestre. De nombreuses études ont été faites sur le rôle des défauts dans les propriétés mécaniques du quartz, mais elles avaient toutes en commun le fait que les échantillons s'amorphisaient rapidement sous le faisceau. Le troisième échantillon, la phase A, est un silicate de magnésium hydraté de haute pression qui a été synthétisé, puis déformé à 11 GPa et 973 K en cellules multi-enclumes à Bayreuth, en Allemagne (A. Mussi et al., 2012). La caractérisation des défauts dans cet échantillon, a montré qu'il était très sensible au faisceau d'électrons ; cette étude n'a pu être réalisée qu'à l'aide d'un porte objet froid, sous faible illumination électronique.

Pour déterminer le vecteur de Burgers d'une dislocation, nous avons montré au chapitre précédent qu'il fallait acquérir des images en champ sombre (et/ou clair) avec des vecteurs de diffraction différents. En cartographiant (en niveau de gris) l'intensité de la tâche transmise sur l'ensemble des clichés de diffraction stockés par SED, nous obtenons un champ clair virtuel. En faisant de même avec les taches diffractées nous obtenons des champs sombres virtuels. Dans l'exemple de l'olivine (orthorhombique, groupe d'espace *Pbnm*), en indexant un cliché en axe de zone [021] nous avons pu obtenir de la pile de clichés de diffraction des images virtuelles permettant d'identifier les dislocations de vecteurs de Burgers [100] et [001]. Nous avons montré que la résolution était comparable à celle obtenue en champ sombre en faisceau faible, malgré la faible qualité des clichés de diffraction (144 X 144 pixels). Une limitation majeure de la méthode est reliée au fait que l'ensemble des champs sombres virtuels sont produits avec une même orientation de la lame, quand il est bien connu que l'ajustement du contraste nécessite généralement de petits pivotements de l'échantillon. Ceci fait donc qu'en un point nous ne pouvons pas toujours comparer les contrastes, d'une image à l'autre puisqu'ils correspondent à des écarts à Bragg légèrement différents. Malgré

cette limitation, la SED s'avère être une technique puissante d'analyse qui ouvre un champ d'applications attractif en minéralogie.

II.2 Article

Ces résultats sont décrits dans l'article qui est reproduit dans les pages suivantes :

B. Nzogang, A. Mussi & P. Cordier (2019) Application of Scanning Electron Diffraction in the Transmission Electron Microscope for the characterization of dislocations in minerals Mineralogical Magazine, 83, 71-79. https://doi.org/10.1180/mgm.2018.144

Mineralogical Magazine (2019), **83**, 71–79
doi:10.1180/mgm.2018.144

CAMBRIDGE UNIVERSITY PRESS

Article

Application of scanning electron diffraction in the transmission electron microscope for the characterisation of dislocations in minerals

Billy C. Nzogang, Alexandre Mussi and Patrick Cordier*

Université de Lille, CNRS, INRA, ENSCL, UMR 8207 – UMET – Unité Matériaux et Transformations, F-59000 Lille, France

Abstract

We present an application of scanning electron diffraction for the characterisation of crystal defects in olivine, quartz and phase A (a high pressure hydrated phase). In this mode, which takes advantage of the ASTAR™ module from NanoMEGAS, a slightly convergent probe is scanned over the sample with a short acquisition time (a few tens of ms) and the spot patterns are acquired and stored for further post-processing. Originally, orientation maps were constructed from automatic indexing at each probe location. Here we present another application where images are reconstructed from the intensity of diffraction spots, producing either so-called 'virtual' bright- or dark-field images. We show that these images present all the characteristics of contrast (perfect crystal or defects) of conventional transmission electron microscopy images. Data are acquired with a very short time per probe location (a few tens of milliseconds), this technique appears very attractive for the characterisation of beam-sensitive materials. However, as the acquisition is done at a given orientation, fine tuning of the diffraction conditions at a given location for each reflection is not possible. This might present a difficulty for some precise, quantitative contrast analysis.

Keywords: transmission electron microscopy, scanning electron diffraction, dislocations

(Received 5 April 2018; accepted 18 June 2018)

Introduction

The concept of crystal dislocation as a topological defect able to account for plastic deformation of solids was proposed independently in 1934 by Egon Orowan, Michael Polanyi and Geoffrey I. Taylor (Orowan, 1934; Polanyi, 1934; Taylor, 1934). The first direct observation of those defects in a transmission electron microscope (TEM) by Hirsch *et al.* (1956) had a great influence in the development of the subject with applications to mechanical properties and other fields such as crystal growth phenomena. In a series of papers, McLaren and Phakey (1965*a*,*b*,*c*), showed the first TEM characterisations of defects (including dislocations) in an important rock-forming mineral: quartz. From the beginning, the development of the diffraction contrast technique was central, and it is still more widely used than, for instance, the high-resolution imaging of the dislocation cores. The so-called conventional TEM, which is based on diffraction contrast, has the major advantage of providing information at the mesoscale of dislocation arrangements and patterning, which plays a key role in plasticity. The diffraction pattern, which forms in the back focal plane of a transmission electron microscope, is used to guide specimen tilting so as to orientate a chosen diffracting plane in the Bragg position (Fig. 1). Due to the elastic distortions, these diffraction conditions are altered locally close to the dislocation lines giving rise to a strong contrast in bright- or dark-field images (Hirsch *et al.*, 1956). Cockayne *et al.* (1969) showed that tilting slightly away from exact Bragg conditions (so as for instance, to excite higher order reflections) dramatically increases the resolution of the image of the dislocation lines, this is the so-called weak-beam dark-field (WBDF) mode. A major further development was to show that these strict diffracting conditions could be preserved along a wide range of tilt angles to allow electron tomography of dislocations to be performed (Barnard *et al.*, 2006*a*,*b*, 2010; Mussi *et al.*, 2014) to obtain a true three-dimensional (3D) reconstruction of a dislocation network. In all these techniques, image formations, as well as most operations, are performed at the microscope, and final images are captured by a detector conjugate to the image plate. For beam-sensitive materials, the time necessary for adjustments and image optimisation might be detrimental and lead to sample damage before the characterisations are fulfilled. Quartz, as originally pointed out by McLaren and Phakey (1965*b*), is the archetypal case of a beam-sensitive mineral, but this behaviour is exhibited by several other important rock-forming minerals (e.g. topaz, albite, nepheline and phyllosilicates) and is a problem for the study of most high-pressure phases which are metastable under ambient conditions.

Here, following the proposition of Rauch and Véron (2014*a*) and Kiss *et al.* (2016) we present an alternative technique for dislocation imaging and characterisation in the TEM based on scanning electron diffraction (SED), which consists of recording a data

***Author for correspondence:** Patrick Cordier, Email: patrick.cordier@univ-lille.fr
Associate Editor: Giancarlo Della Ventura
Cite this article: Nzogang B.C., Mussi A. and Cordier P. (2019) Application of scanning electron diffraction in the transmission electron microscope for the characterisation of dislocations in minerals. *Mineralogical Magazine*, **83**, 71–79. https://doi.org/10.1180/mgm.2018.144

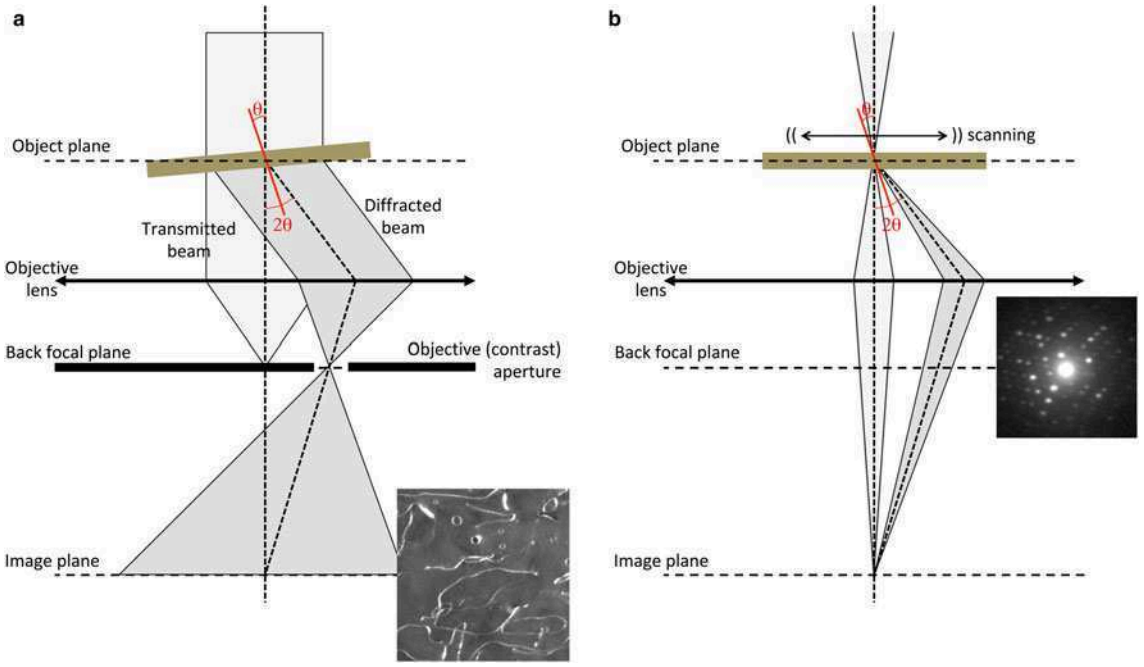

Fig. 1. Microscope settings. (*a*) Conventional TEM dark-field. The electron beam is parallel. The sample is tilted to orientate a given diffraction plane close to Bragg conditions. A contrast aperture is used in the back focal plane so as to select the diffracted beam to form the image that is recorded. To perform using weak-beam dark-field mode the specimen is slightly tilted away from the exact Bragg conditions. (*b*) Scanning electron diffraction. The microscope is set in microprobe mode (the electron beam has a small convergence) and the spot is scanned over the sample. Only the diffraction patterns are recorded and stored.

cube of diffraction patterns from which imaging is extracted off-line by post-treatment. Application of this method to two important rock-forming minerals, olivine and quartz, and on a high-pressure hydrated phase (phase A) are presented.

Experimental

Three samples have been used in this study. One is natural olivine ($(Mg, Fe)_2SiO_4$) deformed experimentally by M. Thieme and S. Demouchy (Geosciences Montpellier, France) at 1030°C (CMT16-8) in a gas-medium apparatus (Thieme *et al.*, 2018). The second is natural quartz from a granulite (Bohemian massif). The third is a synthetic sample of a dense hydrous magnesium silicate (DHMS), phase A. For all samples, thin sections have been cut and mechanically polished to a thickness of ~30 µm. In order to reach electron transparency, the sample foils were Ar-ion sputtered with a Gatan® DuoMill™ model 600. Carbon films were deposited on the thin foils to ensure electron conduction.

Transmission electron microscope investigations were performed with a FEI® Tecnaï $G^2$20Twin microscope, operating at 200 kV and with a Philips CM30 microscope operating at 300 kV, both equipped with a LaB_6 filament and using a double tilt sample-holder.

Orientation maps were acquired with a step size of 2 nm using SED in the TEM with the ASTAR™ tool from NanoMEGAS (Rauch and Véron, 2014*b*). The TEM is set in micro-beam mode (spot size 1 nm, fluence rate 3.5×10^5 electrons.nm^{-2}.s^{-1}) and the incident electron beam, which is focused on the sample, is scanned over the area as a result of the dedicated hardware control system of the TEM deflecting coils (Fig. 1*b*). In this mode where the sample is illuminated by a convergent beam, the diffraction pattern consists of discs. Using the smallest condenser aperture (50 µm) the diffraction patterns are made of very small spot-like discs (Fig. 1*b*) that can be indexed as spot patterns. The individual exposure time at each location is a few tens of milliseconds. Diffraction patterns are collected with an external Stingray CCD camera that points on the TEM phosphorous screen and are stored in the computer memory for further indexation and post processing. The diffraction patterns are collected as 144×144 pixels at a camera length of 105, 135 or 175 mm. In the ASTAR™ system, electron diffraction spot patterns are indexed (providing the local crystal orientations) by comparing individually obtained patterns via cross-correlation matching techniques with pre-calculated electron diffraction templates (Rauch and Dupuy, 2005) generated every 1° (orientation resolution). From this indexation, one usually obtains an orientation map which displays, with a colour coding, the most probable orientation at each scanned beam position. Here we present another use of diffraction data cubes. From experimental spot patterns, virtual bright-field (VBF) maps can be generated, which represents the fluctuation of the central beam intensity of diffraction patterns. This builds up a scanning-TEM-like bright-field contrast directly related to the orientation maps. Virtual dark-field (VDF) images can also be generated by reproducing the same operation with a selected diffracting spot.

Observations and discussion

Olivine

Olivine is the major component of the Earth's mantle down to 410 km depth. This phase is stable at ambient pressure and also quite stable under the electron beam. In Fig. 2, we present ten VDF images reconstructed from the 002, 00$\bar{2}$, 004, 00$\bar{4}$, 2$\bar{4}$0, $\bar{2}$40, 1$\bar{2}\bar{2}$, $\bar{1}$22, 1$\bar{2}$2 and $\bar{1}$2$\bar{2}$ diffraction spots present in the 1,440,000 diffraction patterns of the data cube, which are close to the [210] zone axis (in the *Pbnm* space group). All images

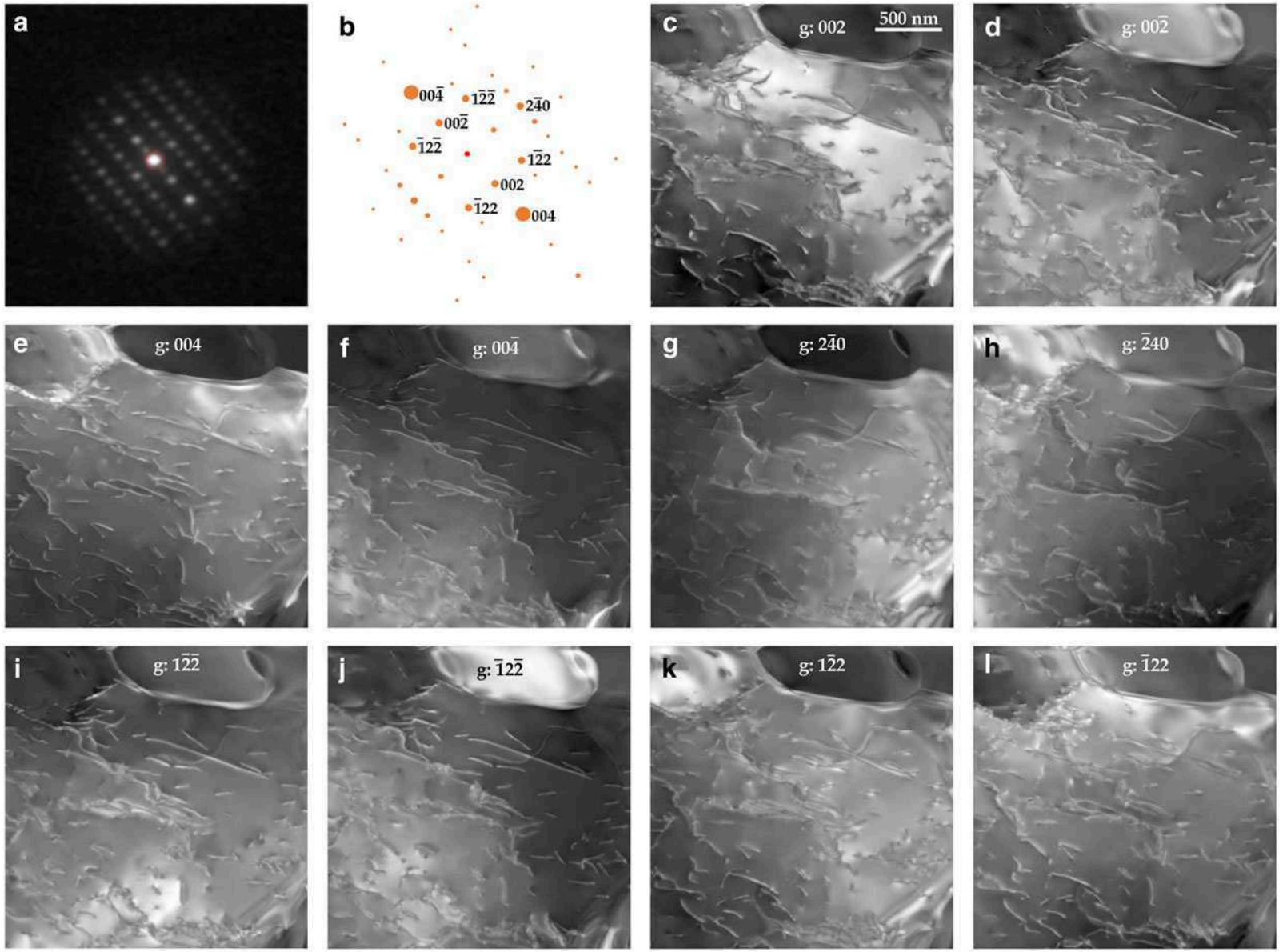

Fig. 2. Olivine. Acquisition parameters: spot size = 1 nm; step size = 2 nm; acquisition time = 10 ms; and 1200 × 1200 points. (*a*) Diffraction pattern. The sample is oriented close to the [210] zone axis. (*b*) Simulation of the diffraction pattern with electron diffraction. The spot diameter indicates the intensity. (*c–l*) Virtual dark-field images: the diffraction vector is indicated on the images.

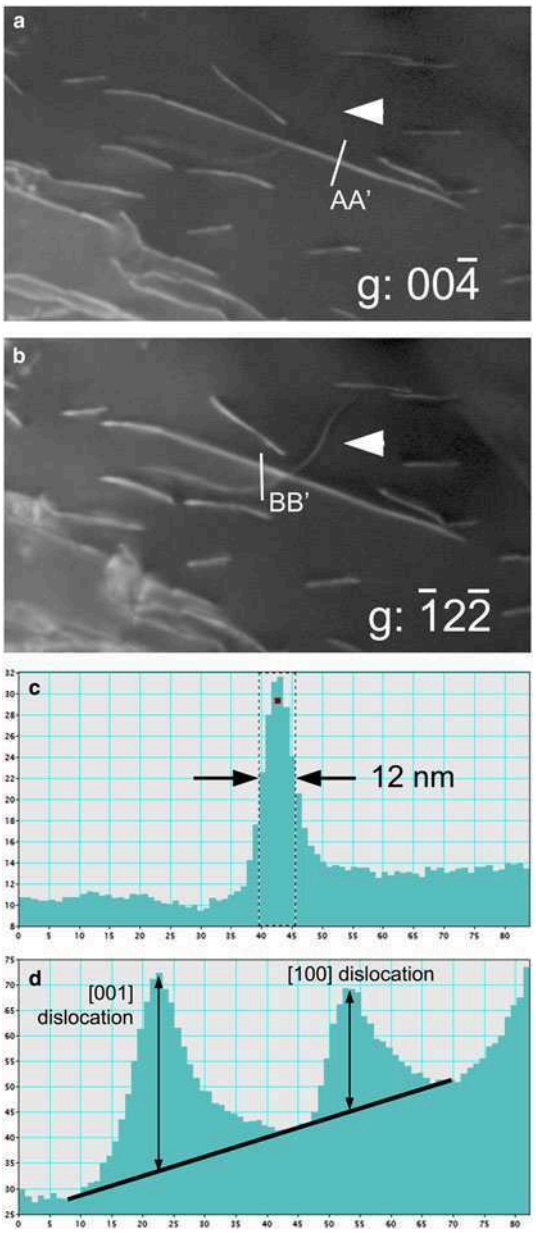

Fig. 3. Olivine. Burgers vectors determinations on enlargements of Fig. 2. (*a*) With 00$\bar{4}$, only [001] dislocations are in contrast. (*b*) With $\bar{1}2\bar{2}$, all dislocations are visible. (*c*) Intensity profile along the AA' line from Fig 3a. The width of the dislocation image is ~12 nm. (*d*) Intensity profile along the BB' line (top-down direction on the line corresponds to left-right direction on the profile) from Fig 3b showing the respective intensity of [100] and [001] dislocations.

are extracted from the same set of diffraction patterns recorded under steady state conditions, in particular at a constant orientation of the specimen in the microscope. One can see, however, that local diffraction conditions are different for each VDF image. For instance, with 002, exact Bragg conditions ($s = 0$) are fulfilled within a wide band towards the top of the image (Fig. 2*c*) which corresponds to larger Bragg deviation (hence to higher resolution WBDF image) with 00$\bar{2}$ (Fig. 2*d*). In the latter image, the best conditions for observation are found in the right and upper parts. Figures 2*e* and 2*f* present VDF reconstructed with 004 and 00$\bar{4}$. These reflections have a larger structure factor than 002 (1384 *vs.* 373). The information gained are in principle the same but the quality of the images is higher. The location of exact Bragg position $s = 0$ is also slightly different on each image. The following images are reconstructed with 240 and 122 reflections. Their structure factors are comparable in olivine (328 and 312 respectively). These images allow the dislocations present to be identified. Indeed, in orthorhombic olivine, only two different dislocation types exist with [100] and [001] Burgers vectors (in the *Pbnm* space group). Dislocation identification could be performed by comparing images reconstructed with 004 (which images only [001] dislocations) and with 240 (which images only [100] dislocations). However, on VDF reconstructed with 2$\bar{4}$0 and $\bar{2}$40, deviation from exact Bragg position is not sufficient to reach weak-beam conditions, and residual contrasts on [001] dislocations give ambiguous information. Identification can be performed however by comparing images reconstructed with 00$\bar{4}$ and $\bar{1}2\bar{2}$ reflections. Figure 3 displays enlargements of Fig. 2 which allow the clear identification of [001] dislocations (seen on Fig. 3a and 3*b*) from a [100] dislocation (visible on Fig. 3*b* only). Figure 3*c* shows the intensity profile of a [001] dislocation in Fig. 3. The full width at half maximum is ~12 nm demonstrating that resolution comparable to WBDF can be attained by SED. With $\bar{1}2\bar{2}$, images of [100] and [001] dislocations correspond to ***g.b*** products (scalar product of the diffraction vector and the Burgers vector) of 1 and 2 respectively. The intensity profile of Fig. 3*d* across two dislocations shows that indeed, the intensity of the [001] dislocation is larger, but only by a factor of 1.63 which is lower than the 2:1 ratio expected. The SED is thus able to lead to dislocation Burgers vectors characterisations through a single data acquisition only.

Quartz

In its low-temperature form (α-quartz) quartz is the most common silica phase. It is ubiquitous in the Earth's crust where it is, after feldspars, the most abundant phase. From the sixties, numerous studies have addressed the role of defects in the mechanical properties of quartz, however, the detailed characterisation of crystal defects were always limited by the rapid amorphisation of the samples under the electron beam (McLaren and Phakey, 1965*b*). Some alternative TEM techniques like large-angle convergent-beam electron diffraction (Cordier *et al.*, 1995) now offer the possibility to carry out detailed characterisations, but the operating conditions are detrimental to observation in the real space.

Reconstructions of a VBF and two VDF images with two {1$\bar{1}$01} reflections present in a [11$\bar{2}$0] zone axis are shown in Fig. 4. These images are compared with a conventional bright-field image of the same area which was recorded after the SED acquisition. It is seen that the 30 ms acquisition time (electron dose 10,500 electrons.nm^{-2}) per pixel does not introduce any significant damage. One can see in Fig. 4 that all characteristic diffraction contrasts of conventional TEM are well reproduced. This shows that, regardless of the diffraction patterns being recorded with a rather low resolution (144 × 144 pixels) to optimise the acquisition, their quality is sufficient to reconstruct images that carry the most important features. In particular, one can clearly see the thickness contours (upper part of Fig. 4*c*–*d*) and how they interact and terminate on dislocations (black arrows) as described by Ishida *et al.* (1980). This contrast helps in recognising that the dislocation arrowed with a star is out of contrast: thickness contour fringes do not interact with it and cross its line. Its Burgers vector is thus $\pm\frac{1}{3}[\bar{1}\bar{1}20]$. The

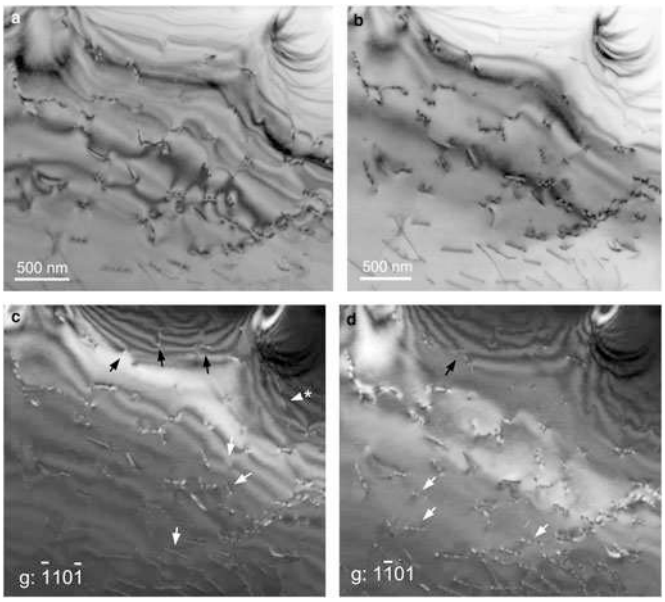

Fig. 4. Quartz. Acquisition parameters: spot size = 1 nm; step size = 2 nm; acquisition time = 30 ms; and 1500 × 1500 points. The sample is oriented close to the $[\bar{1}\bar{1}20]$ zone axis. (*a*) Conventional TEM bright-field image. (*b*) Virtual bright-field image. (*c–d*) Virtual dark-field images with $\{1\bar{1}01\}$ (for explanation of arrowed features, see text).

oscillatory contrast of dislocation lines inclined with respect to the foil mean plane is also clearly recognised (white arrows).

The results from another acquisition in the same thin foil, again with an orientation close to the $[11\bar{2}0]$ zone axis is shown in Fig. 5. From this acquisition, eight VDF could be reconstructed from $1\bar{1}00$, $\bar{1}100$, $2\bar{2}00$, $\bar{2}200$, $1\bar{1}01$, $\bar{1}10\bar{1}$, $3\bar{3}01$ and $\bar{3}30\bar{1}$ diffraction spots. This area displays numerous perfect dislocations which exhibit the same diffraction contrasts as discussed above. One also notices the presence of tiny dislocation loops (as commonly observed in wet quartz, either synthetic or natural, see Cordier *et al.*, 1988). When the diameter of a dislocation loop is much larger than the extinction distance ξ_g, the loop appears as a closed dislocation line (Hirsch *et al.*, 1960). Otherwise, it usually appears as a strain contrast characterised by a pair of black and white lobes (see examples arrowed on Figs 5*c* and *f*; enlargements of loop α are displayed in Figs 6*a* and *b*). For cases with a symmetrical dilation centre (coherent precipitate for instance), the line of no contrast which separates the black and white lobes is always perpendicular to the diffraction vector (Rühle *et al.*, 1965). For tiny dislocation loops, the strain field is not symmetrical and the orientation of the line of no contrast is determined by one of the Burgers vectors (Hirsch *et al.*, 1960; Rühle *et al.*, 1965). This situation is illustrated by the defect labelled α (labelled in Figs 5*c* and *f* and for which enlargements are presented Figs 6*a* and *b*): its contrast is reversed between Figs 6*a* and *b*, but the line of no contrast keeps the same orientation although different diffraction vectors are involved. Further evidence is provided by Fig. 5*i* where the defect (black-and-white contrast) previously arrowed at the centre of Fig. 5*f* (labelled β) now clearly appears as a dislocation loop with a diameter of 20 nm (see enlargements in Figs 6*c* and *d*). Quite high resolutions are obtained, as on Fig. 5*e*, the dislocation loop arrowed exhibits a diameter of 16 nm. It is to be remembered that this is the size of the image and not of the loop itself as the contrast of a dislocation line does not coincide with its actual position. This is illustrated when $+\boldsymbol{g}$ is reversed to $-\boldsymbol{g}$ as in Figs 5*g* and *h* (enlargements in Figs 6*e* and *f*) where the loop arrowed (γ) exhibits an apparent diameter of 30 and 18 nm respectively. All these observations reproduce the contrasts expected in conventional TEM very well.

Some distinctive fringe contrasts which are commonly observed in quartz in relation to plastic deformation and microtwinning are shown in Fig. 5. The two most common types of microtwins observed in quartz are related to the Dauphiné and Brazil twin laws. The Dauphiné twin corresponds to a rotation of 180° about the *c* axis whereas Brazil twins are linked to the enantiomorphism of quartz which can belong to the $P3_121$ (where SiO_4 tetrahedra on the three-fold axes form a left-handed-helix) or to the $P3_221$ (right-handed helix) space groups. Brazil twins correspond to alternating left-handed and right-handed domains. Twin boundaries are usually made visible through fringes which arise because a phase shift occurs across the boundary. The kinematic theory describing this contrast was developed originally by Hirsch *et al.* (1960). It has been further extended to account for dynamical effects (van Landuyt *et al.*, 1964, 1965) and applied specifically to microtwins in quartz by McLaren and Phakey (1966, 1969). In case of Dauphiné twinning, the phase shift is null across the boundary for g: $\{1\bar{1}00\}$ and g: $\{1\bar{1}01\}$ and no diffraction contrast fringes are expected at the boundary (McLaren and Phakey, 1966). Hence, Fig. 5 rather suggests boundaries corresponding to Brazil microtwins. Indeed, the displacement vector across a Brazil microtwin is of the $\frac{1}{6}[11\bar{2}0]$ type also involved in the dissociation of $\frac{1}{3}[11\bar{2}0]$ dislocations as discussed by Trépied and Doukhan (1978) and Doukhan (1995). The microstructure shown in Fig. 5 with multiple overlapping stacking faults and the presence of dislocations is consistent with this interpretation.

The interpretation of diffraction contrast fringes is more straightforward at exact Bragg conditions $s = 0$ (van Landuyt *et al.*, 1964). In that case, for fringes corresponding to $\alpha = \pi$ (which is the case for Brazil microtwins imaged with g : $\{1\bar{1}00\}$ see McLaren and Phakey, 1966), the fringe profiles are expected to be symmetrical with respect to the centre of the foil, and the bright- and dark-field images are complementary. This analysis is not very conclusive here. The (virtual) bright-field image does not correspond to two-beam conditions and it is difficult to infer which reflection influences the contrast more. Concerning the dark-field images, as already underlined above, the fact that data acquisitions are performed at a constant tilt excludes a fine control of the Bragg deviation vectors. Given the local bending of the foils, it varies from place to place and from a virtual dark-field to another. Indeed, van Landuyt *et al.* (1964) have shown that deviation from the exact Bragg orientation can destroy the symmetry of the dark-field image. This may be the reason of the asymmetry of the fringes observed in Fig. 5d.

Phase A

Phase A ($Mg_7Si_2O_8(OH)_6$) is a dense hydrous magnesium silicate (DHMS) phase which is supposed to form in cold hydrous parts of subducting slabs, between depths of 200 and 350 km, by destabilisation of Mg-phyllosilicates. Because of its composition, phase A is probably the main water carrier at these depths and is viewed as a key phase for water transfer down to the transition zone in cold environments (e.g. Poli and Schmidt, 1997). The sample investigated here was synthesised and deformed in the multianvil

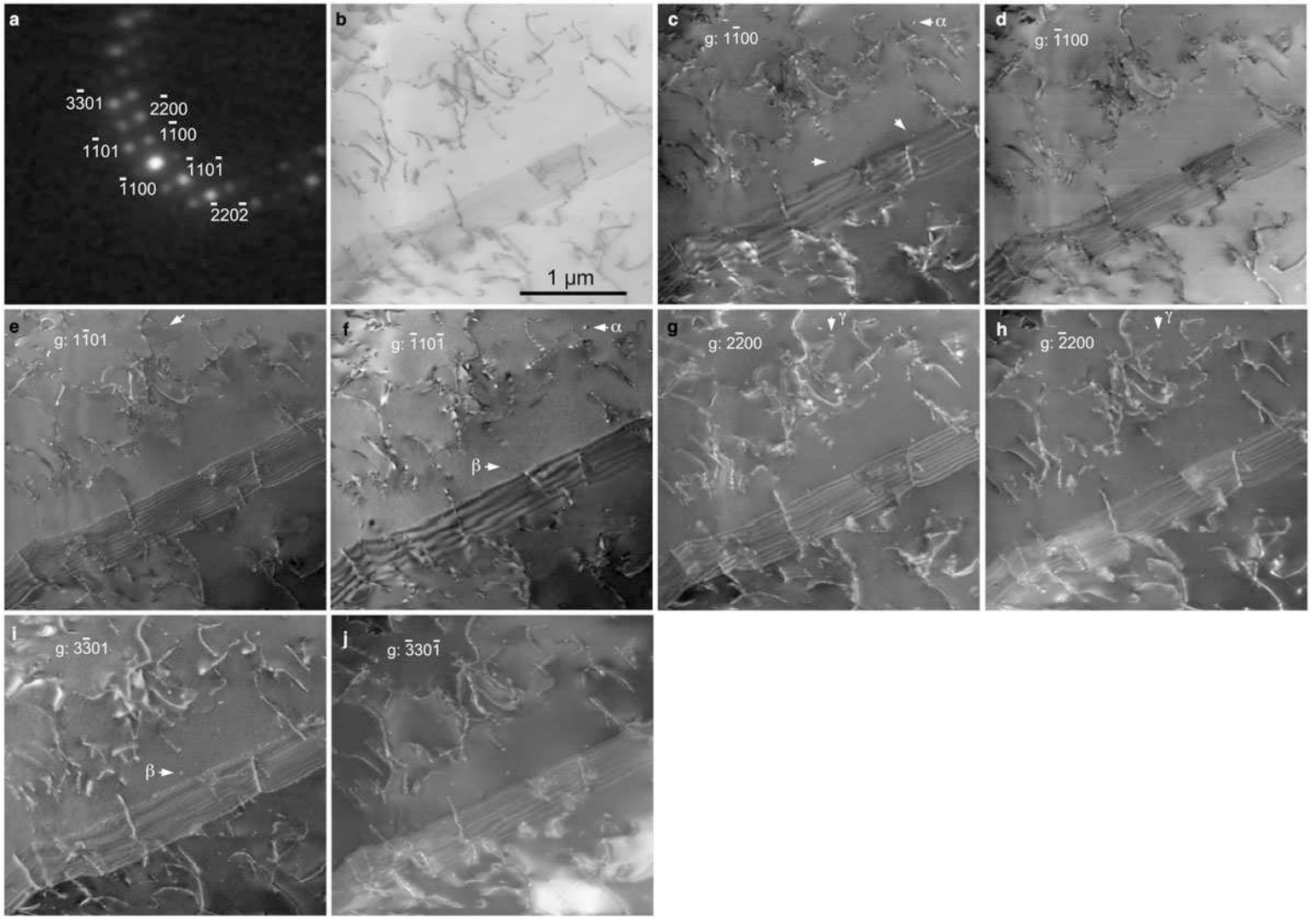

Fig. 5. Quartz. Acquisition parameters: spot size 1 nm; step size 2 nm; acquisition time 30 ms; 1500 × 1500 points. (*a*) Diffraction pattern. The sample is oriented close to the $[\bar{1}\bar{1}20]$ zone axis. (*b*) Virtual bright-field image. (*c–j*) Virtual dark-field images: the diffraction vector is indicated on the pictures.

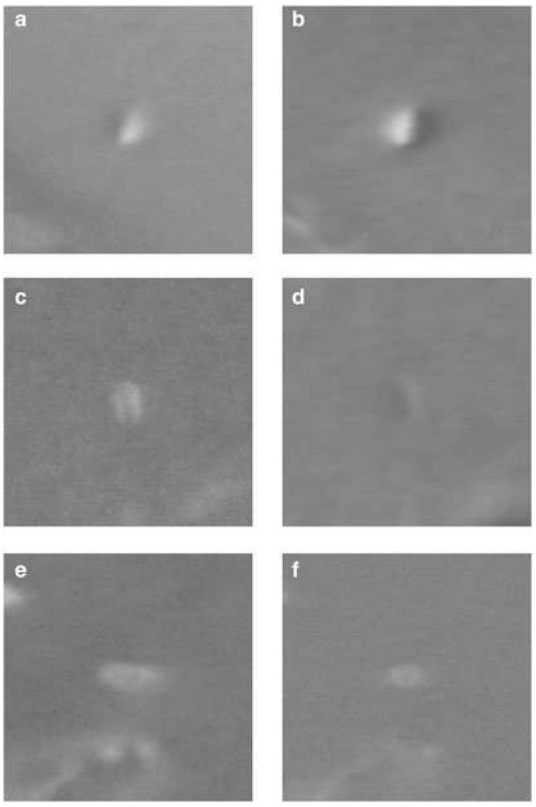

Fig. 6. Quartz. Enlargements of Fig. 5 showing some dislocation loops. All pictures are 100 × 100 pixels, i.e. 200 nm wide. (*a*) Loop α from Fig. 5c, g: $1\bar{1}00$; (*b*) same loop as (*a*), i.e. loop α from Fig. 5f, g: $\bar{1}10\bar{1}$; (*c*) loop β from Fig. 5i, g: $3\bar{3}01$; (*d*) same loop as (*c*), i.e. loop β from Fig. 5f, g: $\bar{1}10\bar{1}$; (*e*) loop γ from Fig. 5g, g: $2\bar{2}00$; (*f*) same loop as (*e*), i.e. loop γ from Fig. 5h, g: $\bar{2}200$.

apparatus at the Bayerisches Geoinstitut, Bayreuth, Germany (Mussi *et al.*, 2012). Phase A was synthesised from high purity oxides at 11 GPa (nominal pressure) and 900°C. The recovered samples were further deformed at 11 GPa and 700°C (run H3008). The first characterisations of crystal defects in phase A, performed by Mussi *et al.* (2012) has shown that phase A was very sensitive to electron beam damage and TEM characterisation could only be performed under conditions adjusted to slow down beam damage, in particular using a liquid nitrogen cooling TEM holder. The structure of phase A is hexagonal, space group $P6_3$, with $a = 7.8603$ Å and $c = 9.5730$ Å (Horiuchi *et al.*, 1979). These larger unit-cell parameters put strong constraints on the dislocation Burgers vectors (see a computational study in Gouriet *et al.*, 2015). So far, perfect dislocations observed exhibit Burgers vectors of the $\frac{1}{3}[11\bar{2}0]$ (so-called <a>) and $\frac{1}{3}[11\bar{2}3]$ (so-called <c + a>) types (Mussi *et al.*, 2012). To perform these characterisations, the dislocations must be imaged with different diffraction vectors. This requires keeping the beam on the same area for some time to adjust several diffracting conditions. Figure 7 demonstrates that even when maximum care is taken to minimise beam damage, like using a cold stage and low illumination (experimental conditions are detailed in the figure caption), beam damage occurs very rapidly with this phase. This is shown by the spotty aspect of the background (clearly visible on the thickness fringes at the top left of Fig. 7*c*) or more severely by the many dislocation loops which grow on the dislocations (white arrows on Fig. 7*c*), which form probably by condensation of point defects resulting from electron irradiation. Figure 8, obtained on the same foil, shows that SED represents an attractive alternative for those phases. Here a standard sample holder is used (not cooled). The foil was oriented purely for the grain under study to be oriented close to a convenient zone axis.

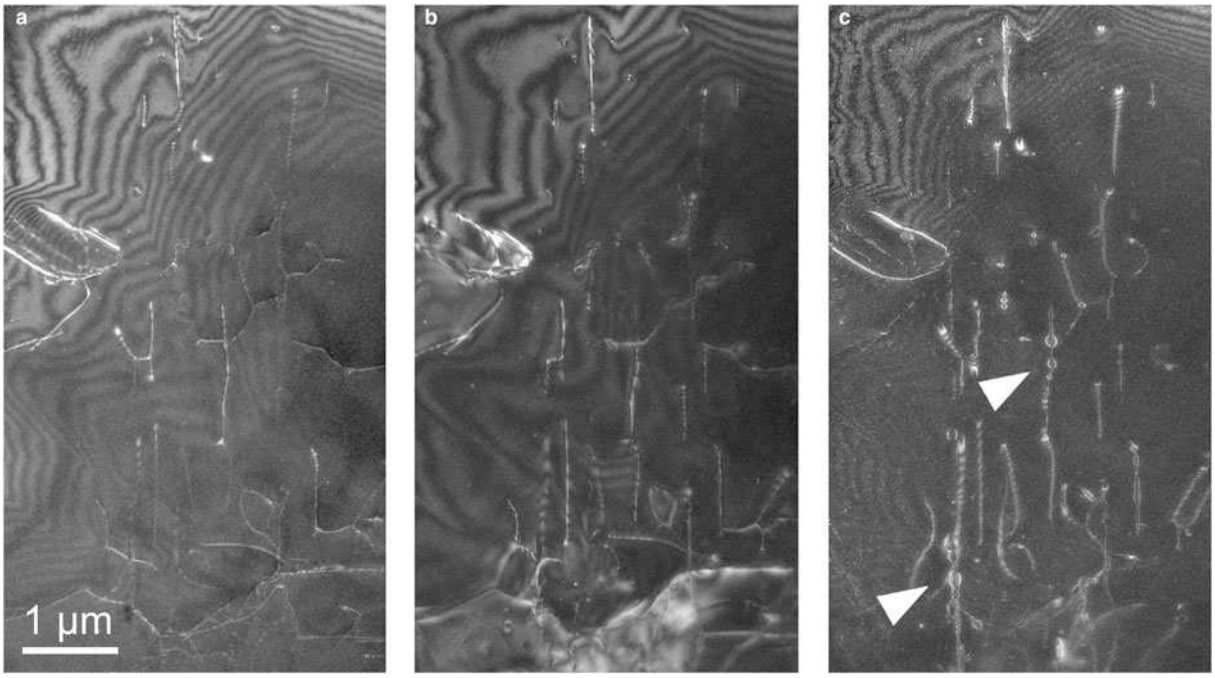

Fig. 7. Phase A. Conventional TEM weak-beam dark-field images. The sample is oriented close to the $[11\bar{2}0]$ zone axis. Observation conditions were performed to minimise beam damage, i.e. by using a small condenser aperture (100 µm), a small spot size (300 nm), a low magnification (M = 3900 × using photographic plates for further enlargement) and a Gatan® cooling TEM holder operated with liquid nitrogen ($T \approx -160$°C near the thin foil). Acquisition time is ~10 s for each micrograph. (*a*) g: $\bar{2}20\bar{2}$; (*b*) g: $2\bar{2}0\bar{2}$; and (*c*) g: $000\bar{8}$. Note the spotty background and the formation of tiny loops on the dislocation lines (arrowed) due to beam damage after *ca.* 3 min of observation on this area.

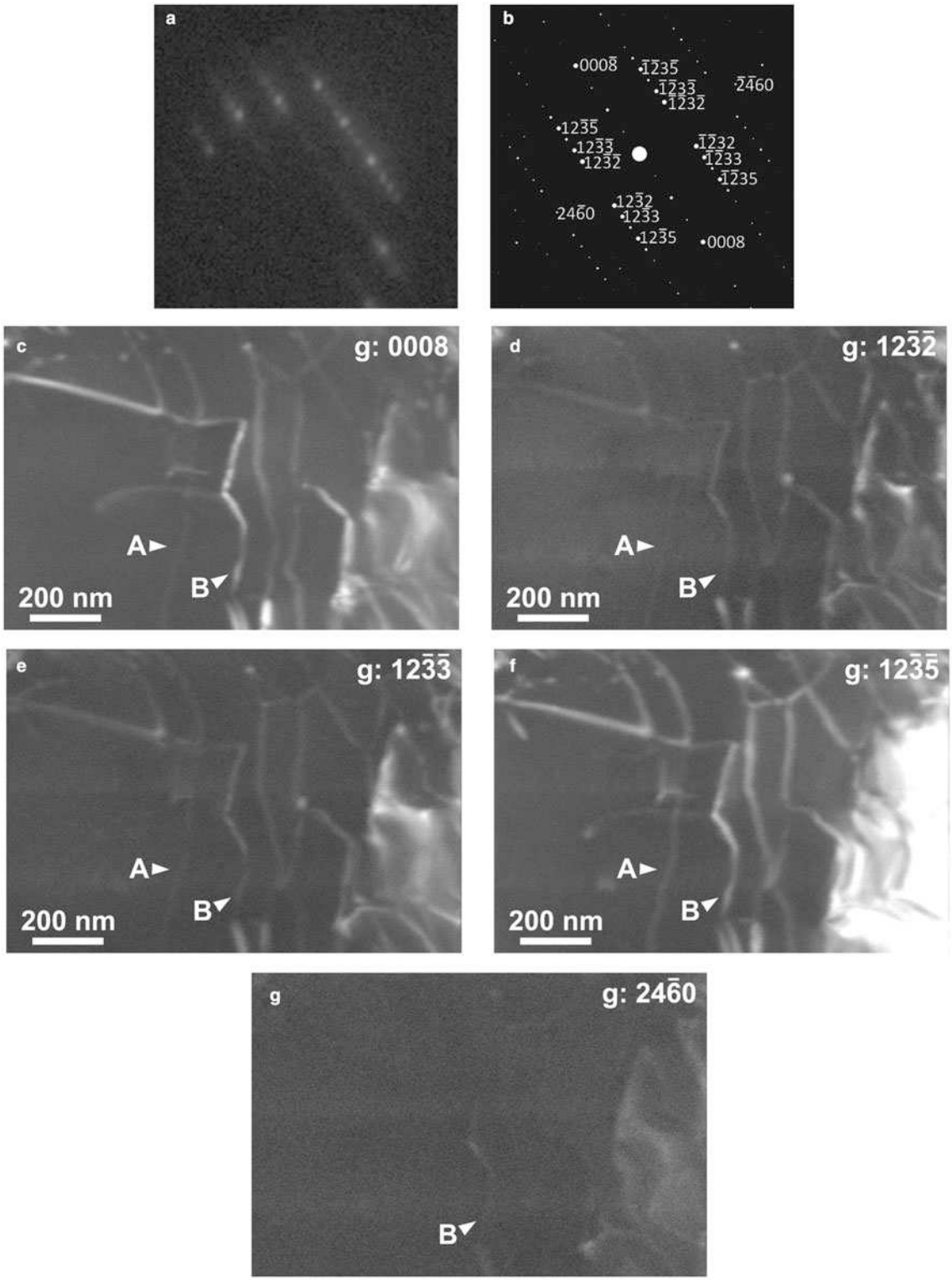

Fig. 8. Phase A. Acquisition parameters: spot size 1 nm; fluence rate 3.5×10^5 electrons.nm^{-2}.s^{-1}; step size 2 nm; and acquisition time 60 ms. The images presented are cropped from a map recorded with 700 × 700 points. (*a*) Diffraction pattern. The sample is oriented close to the [5$\bar{4}\bar{1}$0] zone axis. (*b*) Indexation of the diffraction pattern highlighting the diffraction vectors used. (*c–g*) Virtual dark-fields: the diffraction vector is indicated on the images.

Here [5$\bar{4}\bar{1}$0] is chosen which contains reflections with high structure factors (1395 for 0008; 1057 for 12$\bar{3}$5; 12$\bar{3}$2 and 12$\bar{3}$3 exhibit values of 350 and 163, respectively; the lowest structure factor among those presented is 49 for 24$\bar{6}$0) which are adapted for Burgers vectors characterisation. With the sole acquisition leading to the five VDF presented in Fig. 8, it is possible from the intensity profiles to identify (see Supplementary materials) a $\frac{1}{3}$[1$\bar{2}$10] dislocation (labelled A on Fig. 8) and a $\frac{1}{3}$[11$\bar{2}$3] dislocation (labelled B on Fig. 8). No evidence for beam damage was observed on the mapped area after acquisition.

Conclusions

Images presenting all characteristics of bright- and dark-field images from conventional TEM can be reconstructed from the data cube of diffraction patterns obtained from SED. The image quality and resolution of dislocations (diffraction contrast of strain fields) are comparable with those obtained from conventional TEM. The main advantage is the possibility of extracting a large number of images from different diffraction vectors on the basis of a single acquisition with a very short exposure time per pixel. This possibility is very attractive for investigating beam-sensitive materials as illustrated here with quartz and phase A.

The technique has however some drawbacks. The acquisition of images with a high spatial resolution (here 2 nm) is long (for quartz, 1500×1500 images with an acquisition time of 30 ms correspond to more than 18 hours and for phase A, 700×700 images with an acquisition time of 60 ms correspond to more than eight hours). However, a major limitation is related to the fact that all VDF correspond to a single orientation. In diffraction contrast, very small tilt adjustments are always necessary to adjust precisely the Bragg deviations in order to optimise the contrast. This is not possible here and our examples show that, at a given location, the diffraction conditions are not precisely comparable from one image to another. This might be a limitation for precise contrast interpretation (as shown with dislocations and fringe contrasts related to interfaces).

Regardless of these limitations, we consider that SED represents a very powerful technique which complements our possibilities for characterising defects in beam-sensitive materials.

Acknowledgements. This work was supported by funding from the European Research Council under the Seventh Framework Programme (FP7), ERC grant N°290424 – RheoMan to P. Cordier. The TEM facility in Lille (France) is supported by the Conseil Regional du Nord-Pas de Calais, and the European Regional Development Fund (ERDF). We thank the reviewers and the Associate Editor for their useful comments on the manuscript.

Supplementary material

To view supplementary material for this article, please visit https://doi.org/10.1180/mgm.2018.144

References

Barnard J.S., Sharp J., Tong J.R. and Midgley P.A. (2006*a*) High-resolution three-dimensional imaging of dislocations. *Science*, **313**, 319.

Barnard JS, Sharp J, Tong JR and Midgley PA (2006*b*) Three dimensional analysis of dislocation networks in GaN using weak-beam dark-field electron tomography. *Philosophical Magazine*, **86**, 4901–4922.

Barnard J.S., Eggeman A.S., Sharp J., White T.A. and Midgley P.A. (2010) Dislocation electron tomography and precession electron diffraction – minimising the effects of dynamical interactions in real and reciprocal space. *Philosophical Magazine*, **90**, 4711–4730.

Cockayne D.J.H., Ray I.L.F. and Whelan M.J. (1969) Investigation of dislocation strain fields using weak beams. *Philosophical Magazine*, **20**, 1265–1270.

Cordier P., Boulogne B. and Doukhan J.C. (1988) Water precipitation and diffusion in wet quartz and wet berlinite $AlPO_4$. *Bulletin de Minéralogie*, **111**, 113–137

Cordier P., Morniroli J.P. and Cherns D. (1995) Characterization of crystal defects in quartz by large-angle convergent-beam electron diffraction. *Philosophical Magazine*, **72**, 1421–1430.

Doukhan J.C. (1995) Lattice defects and mechanical behaviour of quartz SiO_2. *Journal de Physique III*, **5**, 1809–1832.

Gouriet K., Hilairet N., Amiguet E., Bolfan-Casanova N., Wang J., Reynard B. and Cordier P. (2015) Plasticity of the dense hydrous magnesium silicate Phase A at subduction zones conditions. *Physics of the Earth and Planetary Interiors*, **248**, 1–11.

Hirsch P.B., Horne R.W. and Whelan M.J. (1956) Direct observation of the arrangement and motion of dislocations in aluminium. *Philosophical Magazine*, **1**, 677–684.

Hirsch P.B., Howie A. and Whelan M.J. (1960) A kinematical theory of diffraction contrast of electron transmission microscope images of dislocations and other defects. *Philosophical Transactions of the Royal Society*, **A252**, 499–529.

Horiuchi H., Morimoto N., Yamamoto K. and Akimoto S.I. (1979) Crystal-structure of $2Mg_2SiO_4{\cdot}3Mg(OH)_2$, a new high-pressure structure type. *American Minereralogist*, **64**, 593–598.

Ishida Y., Ishida H., Kohra K. and Ichinose H. (1980) Determination of the Burgers vector of a dislocation by weak-beam imaging in a HVEM. *Philosophical Magazine*, **42**, 453–462.

Kiss A.K., Rauch E.F. and Lábár J.L. (2016) Highlighting material structure with transmission electron diffraction correlation coefficient maps. *Ultramicroscopy*, **163**, 31–37.

McLaren A.C. and Phakey P.P. (1965*a*) Dislocations in quartz observed by Transmission Electron Microscopy. *Journal of Applied Physics*, **36**, 3244–3246.

McLaren A.C. and Phakey P.P. (1965*b*) A transmission electron microscope study of amethyst and citrine. *Australian* Journal of Physics, **18**, 135–141.

McLaren A.C. and Phakey P.P. (1966) Electron microscope study of Brazil twin boundaries in amethyst quartz. *Physica Status Solidi*, **13**, 413–422.

McLaren A.C. and Phakey P.P. (1969) Diffraction contrast from Dauphiné twin boundaries in quartz. *Physica Status Solidi*, **31**, 723–737.

Mussi A., Cordier P. and Frost D.J. (2012) Crystal defects in dense hydrous magnesium silicate phase A deformed at high pressure: characterization by transmission electron microscopy. *European Journal of Mineralogy*, **24**, 429–438.

Mussi A., Cordier P., Demouchy S. and Vanmansart C. (2014) Characterization of the glide planes of the [001] screw dislocations in olivine using electron tomography. *Physics and Chemistry of Minerals*, **41**, 537–545.

Orowan E. (1934) Zur Kristallplastizität. III. Über den Mechanismus des Gleitvorganges [To crystal plasticity III. About the mechanism of glide]. *Zeitschrift für Physik*, **89**, 634.

Polanyi M. (1934) Über eine Art Gitterstörung, die einen Kristall plastisch machen könnte [About a kind of lattice distortion that could render a crystal plastic]. *Zeitschrift für Physik*, **89**, 660.

Poli S. and Schmidt M. (1997) The high-pressure stability of hydrous phases in orogenic belts: an experimental approach on eclogite-forming processes. *Tectonophysics*, **273**, 169–184

Rauch E.F. and Dupuy L. (2005) Rapid spot diffraction patterns identification through template matching, *Archives of Metallurgy and Materials*, **50**, 87–99.

Rauch E.F. and Véron M. (2014*a*) Analyzing dislocations with virtual dark field images reconstructed from electron diffraction patterns. *Microscopy and Microanalysis*, **20**(Suppl 3), 1456–1457.

Rauch E.F. and Véron M. (2014*b*) Automated crystal orientation and phase mapping in TEM. *Materials Characterization*, **98**, 1–9.

Rühle M, Wilkens M. and Essmann U. (1965) Zur deutung des elecktronenmikroskopischen kontrasterscheinungen an fehlstellenagglomeraten in neutronenbestrahltem kupfer. *Physica Status Solidi*, **11**, 819–829.

Taylor G.I. (1934) The mechanisms of plastic deformation of crystals. Part I – Theoretical; Part II – Comparison with observation. *Proceedings Royal Society, Series A*, **145**, 362–415.

Thieme M., Demouchy S., Mainprice D., Barou F. and Cordier P. (2018) Stress evolution and associated microstructure during transient creep of olivine at 1000–1200°C. *Physics of the Earth and Planetary Interiors*, **278**, 34–46.

Trépied L. and Doukhan J.C. (1978) Dissociated 'a' dislocations in quartz. *Journal of Materials Science*, **13**, 492–498.

Van Landuyt J., Gevers R. and Amelinckx S. (1964) Fringe patterns at antiphase boundaries with $\alpha = \pi$ observed in the electron microscope. *Physica Status Solidi*, **7**, 519–546.

Van Landuyt J., Gevers R. and Amelinckx S. (1965) Dynamical theory of the images of microtwins as observed in the electron microscope I. Overlapping twins. *Physica Status Solidi*, **9**, 135–165.

Chapitre III. Caractérisation de la déformation des minéraux par SPED

Sont rassemblés dans ce chapitre trois articles publiés et un article soumis qui décrivent les résultats issus de collaboration avec des équipes extérieures au laboratoire. Ces études ont en commun l'application de la SPED sur des échantillons déformés expérimentalement.

III.1 Introduction

La tectonique des plaques est aujourd'hui le cadre conceptuel dans lequel sont décrites les grandes manifestations géologiques qui animent la surface du globe. Ce n'est pourtant que l'expression en surface d'un phénomène plus global, la convection mantellique, par lequel le transport vers la surface de la chaleur interne de la Terre est assuré par des transports de matière. Ce modèle suppose que le manteau, composé de roches solides, puisse se déformer à l'échelle des temps géologiques. Quelques observables accessibles en surface, par exemple, les mesures du géoïde[1] et du rebond postglaciaire indiquent que la viscosité moyenne du manteau est de l'ordre de 10^{21} Pa.s (Milne et al., 1998; Mitrovica & Forte, 2004). Les vitesses de déformation associées sont de l'ordre de 10^{-15} s^{-1} (Carter, 1976; Pfiffner & Ramsay, 1982) ce qui est bien plus lent que les vitesses de deformation accessibles aux essais en laboratoire. La compréhension des mécanismes de déformation est le seul indicateur de confiance qui permet de relier les lois de comportement mesurées en laboratoire et celles à l'œuvre dans la nature. Il existe aujourd'hui différentes techniques expérimentales qui permettent de caractériser les échantillons déformés. La microscopie électronique en transmission reste cependant un outil de choix, principalement lorsqu'il s'agit d'étudier la plasticité par mouvement de dislocations. Ces défauts présentent, comme nous l'avons vu, des contrastes caractéristiques qui permettent leurs études et leurs caractérisations. Ces types de caractérisation ont permis par le passé, d'identifier les systèmes de glissement responsables de l'anisotropie plastique des minéraux. L'application de la SPED nous permet ici de proposer une approche légèrement différente, plus proche de celle développée en EBSD, par laquelle nous caractérisons la déformation au travers des désorientations internes des cristaux.

Les deux premiers articles décrivent des caractérisations d'échantillons qui sont constitués de phases de hautes pressions de la zone de transition et du manteau inférieur de la Terre. Ces phases ne sont pas stables thermodynamiquement dans les conditions où nous les caractérisons. Comme nous le suggérons dans le chapitre précédent, le balayage rapide associé à la SPED permet de minimiser les dégâts d'irradiation subis par les matériaux et nous permettent des caractériser ces phases.

Les deux articles suivants portent sur la déformation de l'olivine dans des conditions de manteau lithosphérique. Un nombre croissant d'études suggèrent que les joints de grains sont un acteur important de la plasticité de l'olivine (Hansen et al., 2011). La mise en évidence de ce rôle reste difficile et les évidences microstructurales sont peu nombreuses (Bollinger et al., 2019). Nous montrons dans ces deux articles comment la SPED a permis de mettre en évidence le rôle possible des joints et sous-joints de grains dans la restauration de l'olivine déformée à 1273-1473K.

[1] Un géoïde est une surface équipotentielle de pesanteur. L'inégale répartition des masses à l'intérieur de la Terre et à sa surface créé une déformation de la surface du géoïde

III.2 Caractérisation par SPED d'un agrégat de bridgmanite et de ferropericlase déformé à haute température et haute pression.

III.2.1 Contexte

Cette étude est le fruit d'un partenariat entre l'équipe du professeur Shun Karato, du département de géologie et géophysique de l'université de Yale, et notre équipe à Lille. L'un des axes de recherche majeurs du groupe de Yale est l'étude de la rhéologie des minéraux dans les conditions de la Terre profonde et le développement d'appareils de déformation sous haute pression. On distingue notamment parmi ceux-ci une machine de déformation en torsion appelée le « rotational Drickamer apparatus» (RDA). Son couplage aux sources de rayonnement synchrotron permet de réaliser des mesures *in situ* de contraintes et de déformation. La RDA est constituée de deux enclumes en carbure de tungstène symétriques et opposées, disposées suivant un même axe vertical. L'échantillon à déformer est pris en sandwich entre ces deux enclumes. La déformation résulte de la rotation d'une enclume par rapport à l'autre. Grâce à une réduction de la charge expérimentale, cet appareil a permis récemment de réaliser les premières expériences de déformation dans les conditions qui règnent dans la partie supérieure du manteau inférieur de la Terre (Girard et al., 2016). Ils ont ainsi pu déformer six échantillons (Gamma21-25 et Béta74). Nous avons eu l'opportunité au cours de cette thèse d'étudier en MET l'un de ces échantillons, Gamma21(G21), déformé à 2130 K et 27 GPa. Il s'agit d'un assemblage de bridgmanite et de ferropériclase (70:30 respectivement en proportion volumique) qui a, au préalable été synthétisé grâce à une presse multi-enclumes de type Kawai. Le matériau de départ était une olivine de type San Carlos, de composition $(Mg_{0.9}, Fe_{0.1})_2SiO_4$. Les premieres caractérisations de ces échantillons montrent que l'essentiel de la déformation est assuré par les grains de ferropériclase. Les données mécaniques obtenues *in situ* montrent bien que les contraintes sont plus faibles dans cette phase.

Pour caractériser cet échantillon, nous avons prélevé trois lames FIB à différentes positions: G21I (au centre), G21M (au milieu), et G21O (à l'extérieur). Cela nous permet de tirer parti du gradient de déformation plastique intrinsèque à un échantillon déformé en torsion pour caractériser l'évolution des microstructures avec ce paramètre. Cet échantillon exceptionnel présentait des difficultés particulières. La première était liée au fait que la bridgmanite est très instable à pression ambiante. La possibilité de préserver la bridgmanite à l'issue de la préparation FIB n'était pas garantie. Une importante fraction de matériau s'est en effet amorphisé lors de ce processus, nous avons cependant bénéficié de la préservation d'une quantité de matière suffisante à l'acquisition de données. Ensuite, conformément aux constatations préalablement effectuées en MEB, le ferropériclase est lui très déformé, présentant des densités de dislocations très élevées qui sont d'ordinaire un obstacle à toute caractérisation en MET.

Notre étude a permis de mettre en avant les points suivants :

- Le ferropericlase, bien que très déformé, peut être caractérisé par SPED. Cela démontre la robustesse de l'acquisition de clichés de microdiffraction dans des échantillons présentant de très fortes densités de dislocations.
- L'analyse des gradients locaux de désorientation (KAM) a permis une mise en évidence semi quantitative du taux de déformation du ferropériclase.
- La bridgmanite est bien déformée bien que l'on y observe quasiment pas de dislocations. Nous montrons que les bandes amorphes présentent dans la bridgmanite sont les lieux où se concentre la déformation, mettant en évidence l'origine mécanique de ces microstructures.

III.2.2 Article

Ces résultats sont décrits dans l'article qui est reproduit dans les pages qui suivent :

B. Nzogang, J. Bouquerel, P. Cordier, A. Mussi, J. Girard & S-I Karato (2018) Characterization by scanning precession electron diffraction of an aggregate of bridgmanite and ferropericlase deformed at HP-HT. Geochemistry, Geophysics, Geosystems, 19, 582-594. https://doi.org/10.1002/2017GC007244

AGU PUBLICATIONS

Geochemistry, Geophysics, Geosystems

RESEARCH ARTICLE

10.1002/2017GC007244

Key Points:
- Microstructures of experimentally deformed bridgmanite and ferropericlase aggregates were studied orientation mapping in the TEM
- Bridgmanite deforms by localized shear deformation lamellae
- Most ferropericlase grains show strain much larger than the bulk strain of the sample without showing clear evidence for recrystallization

Supporting Information:
- Supporting Information S1
- Figure S1

Correspondence to:
P. Cordier,
patrick.cordier@univ-lille1.fr

Citation:
Nzogang, B. C., Bouquerel, J., Cordier, P., Mussi, A., Girard, J., & Karato, S. (2018). Characterization by scanning precession electron diffraction of an aggregate of bridgmanite and ferropericlase deformed at HP-HT. *Geochemistry, Geophysics, Geosystems*, *19*. https://doi.org/10.1002/2017GC007244

Received 18 SEP 2017
Accepted 27 JAN 2018
Accepted article online 1 FEB 2018

Characterization by Scanning Precession Electron Diffraction of an Aggregate of Bridgmanite and Ferropericlase Deformed at HP-HT

B. C. Nzogang[1], J. Bouquerel[1], P. Cordier[1], A. Mussi[1], J. Girard[2], and S. Karato[2]

[1]Univ. Lille, CNRS, INRA, ENSCL, UMR 8207-UMET-Unité Matériaux et Transformations, Lille, France, [2]Department of Geology and Geophysics, Yale University, New Haven, Connecticut, USA

Abstract Scanning precession electron diffraction is an emerging promising technique for mapping phases and crystal orientations with short acquisition times (10–20 ms/pixel) in a transmission electron microscope similarly to the Electron Backscattered Diffraction (EBSD) or Transmission Kikuchi Diffraction (TKD) techniques in a scanning electron microscope. In this study, we apply this technique to the characterization of deformation microstructures in an aggregate of bridgmanite and ferropericlase deformed at 27 GPa and 2,130 K. Such a sample is challenging for microstructural characterization for two reasons: (i) the bridgmanite is very unstable under electron irradiation, (ii) under high stress conditions, the dislocation density is so large that standard characterization by diffraction contrast are limited, or impossible. Here we show that detailed analysis of intracrystalline misorientations sheds some light on the deformation mechanisms of both phases. In bridgmanite, deformation is accommodated by localized, amorphous, shear deformation lamellae whereas ferropericlase undergoes large strains leading to grain elongation in response to intense dislocation activity with no evidence for recrystallization. Plastic strain in ferropericlase can be semiquantitatively assessed by following kernel average misorientation distributions.

Plain Language Summary We present a microstructural characterization of a mineralogical assemblage of the lower mantle deformed in the pressure-temperature conditions of the upper most lower mantle. We show that the magnesium silicate perovskite named bridgmanite is stiffer and deforms only along very localized shear bands. The magnesium oxide ferropericlase is much more ductile and takes most of the plastic strain.

1. Introduction

Deformation-induced microstructures carry critical information on the microscopic processes of deformation, hence on the relevance of deformation experiments for processes operating in the Earth's interior. Such characterizations are critical because the experimental conditions of deformation are vastly different from those in Earth's interior particularly in strain rate. For deformation under the shallow mantle conditions, experimental studies are straightforward (e.g., Karato et al., 1986; Mei & Kohlstedt, 2000), and a comparison of microstructures of experimentally deformed samples with those of naturally deformed rocks provides a guide to justify the extrapolation in strain rate (e.g., Karato & Wu, 1993).

The situation is very different for deformation in Earth's deep interior such as the lower mantle. Quantitative studies on deformation under the lower mantle pressure-temperature conditions and controlled strain rate became possible only recently (Girard et al., 2016). The experimental study by Girard et al. (2016) was conducted under the shallow lower mantle conditions (P = 27 GPa, T = 2,130 K) at a typical laboratory strain rate ($\sim 3 \times 10^{-5}$ s^{-1}). This provides the first opportunity to understand the processes of plastic deformation in the lower mantle. However, common to all experimental studies on plastic deformation, strain rates used are much higher (about 10 orders of magnitude, see, for instance, Paterson, 1987) than those expected in Earth, and stress needed to deform samples in these experiments (1–5 GPa) is substantially higher than those estimated for Earth's interior. Consequently, before applying these results, one needs to understand the microscopic processes of deformation.

Important microstructural observations include grains morphologies and the distribution of grain size, but also the intragranular defects contents: dislocations, their nature, and microstructures. Preliminary observations on grain morphology were reported by Girard et al. (2016) that provide evidence for stronger elongation of ferropericlase grains compared to bridgmanite. However, no characterization of defects microstructures has been performed to constrain active deformation mechanisms. Such a study is challenging because of technical difficulties including the high sensitivity of bridgmanite against electron beam radiation and the large strains involved in these experiments. Here we use a newly developed technique involving orientation and local misorientation mapping in transmission electron microscopy (TEM) to overcome these limitations.

Microstructures that develop as a result of plastic deformation are constituted of patterns of dislocation. Traditionally these features are studied by diffraction contrast in the TEM provided the dislocation density is not too high. For dislocations densities larger than ca. 10^{15} m^{-2}, individual dislocation contrasts overlap and cannot be resolved. Other parameters or proxies must then be found to follow the evolution of the plastic behavior. In 1993, Argon and Haasen (1993) have argued that a square root scaling law would describe the dependence of the mean, intragranular, misorientation angle θ_{mean} on plastic strain due to random fluctuations in the long-range strain field of dislocations:

$$\theta_{mean} \propto \sqrt{\varepsilon} \quad (1)$$

Some studies on microstructural evolution in deformed fcc metals and alloys have confirmed that plastic strain scales with misorientation (Hughes et al., 1997, 1998). Although, so far, these scaling laws have only been tested on metals, it is still interesting to note that they were found to be quite robust being independent of material properties such as stacking fault energy, solute content, etc., and process parameters such as temperature, strain, strain rate, strain paths, etc., suggesting a rather universal behavior. Intragranular misorientations can be detected in the reciprocal space through X-ray peak broadening which can be analyzed to provide average measurements of strain, including dislocation densities (Nyilas et al., 2006) and even information on Burgers vectors and slip systems (Cordier et al., 2004; Nisr et al., 2012). In the real space, scanning electron microscope (SEM)-based Electron Backscattered Electron Diffraction (EBSD) provides a very efficient and largely automated technique to sample long-range and short-range information on misorientations within deformed samples. Within the last decades, misorientations-based approaches have been used by metallurgists to follow the evolution of substructures during static and dynamic deformations (or loadings) (e.g., Schayes et al., 2016; Wright et al., 2011; Zhong et al., 2007).

In this paper, we present an alternative approach to SEM-based EBSD where orientation maps are obtained in the TEM from microbeam spot patterns. Compared to EBSD, this technique has several advantages. Being carried out in a TEM it benefits from the spatial resolution which results from the probe size, but also from the use of a thin foil. Also, TEM uses higher voltages which induce less damage in beam sensitive materials and spot patterns are less sensitive to the defect content and much more adapted to analyze highly deformed materials (see for instance, Figure 4 in Bollinger et al. (2015)). Of course, there are also some disadvantages, such as the need to prepare electron-transparent foils or the size of the sampled area which can be a strong limitation regarding the number of grains analyzed (especially if crystal preferred orientations were to be considered).

Here we apply scanning precession electron diffraction (SPED) to a high-pressure assemblage of bridgmanite and ferropericlase, shear deformed at large strains (of the order of 100%) in conditions of the uppermost lower mantle (Girard et al., 2016). Our goal is to study the defect distribution in bridgmanite and ferropericlase to better understand their deformation mechanisms at high-pressure and high-temperature. This is important to assess the scalability of the laboratory data to natural conditions.

Table 1
Samples Studied: Synthesis and Deformation Conditions

Run number	Pressure (GPa)	Temperature (K)	Strain (%)	Strain rate (s^{-1})
K1481	24	1,873	0	N.A.
Gamma 21 (G21)	27	2,130	100	5×10^{-5}

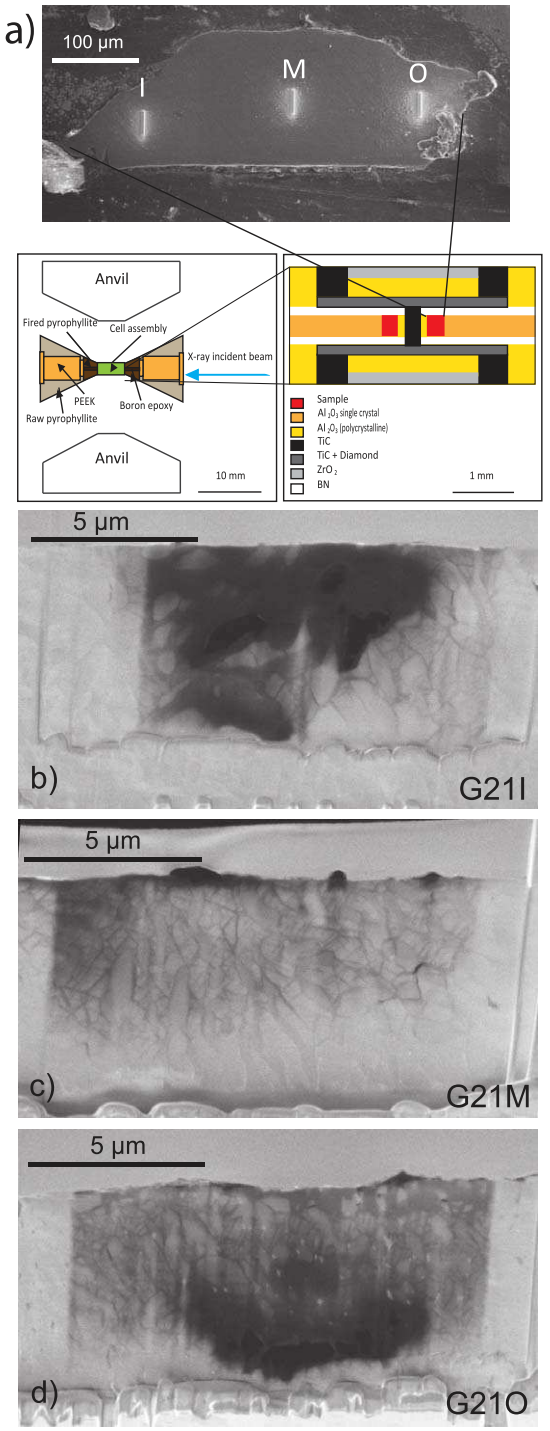

Figure 1. (a) Sketch of the deformation experimental setup with the locations where the three thin foils investigated in this study were extracted from Gamma 21. Their names are given according to their positions inner (I), middle (M), and outer (O): (b) FIB thin section G21I ("I" for inner position: lower strain), (c) FIB thin section G21M from the middle, and (d) FIB thin section G21O ("O" for outer position: higher strain).

2. Experimental Setup

2.1. Samples

Two samples have been investigated in this study. Their conditions of elaborations are summarized in Table 1.

The bridgmanite and ferropericlase assemblage have been synthesized under hydrostatic conditions during run K1481 using a Kawai type multi-anvil at Yale University (Table 1). The starting material, San Carlos olivine $(Mg_{0.9},Fe_{0.1})_2SiO_4$, was loaded in a molybdenum capsule, in an 8/3 cell assembly with a $LaCrO_3$ Furnace. The sample was annealed for 70 min at 24 GPa, 1,873 K. Pressure was estimated using pressure versus load calibration curve and temperature was estimated from power versus temperature calibration curve. The sample was then cut into 200 μm thick discs, and then cut into half ring (ID = 0.45 mm, OD = 1 mm) to be used in the Rotational Drickamer Apparatus (RDA) for deformation experiment (run Gamma 21).

Run Gamma 21 (Table 1) was performed using the RDA at the NSLS synchrotron beamline X17B2. A cross section of the cell assembly used at the beamline is shown in Figure 1. The sample was first compressed, then annealed for 60 min before starting the deformation. Pressure and temperature were estimated by in situ X-ray diffraction data obtained during annealing, using bridgmanite and ferropericlase equation of state (Komabayashi et al., 2010; MaO et al., 1991; Tange et al., 2012). Because the X-ray synchrotron beam has been lost at the beginning of the deformation, total strain was estimated from the angle of rotation of the anvil and the relationship between the angle of rotation and shear strain based on the previous results.

Electron-transparent foils (Figures 1b–1d) for TEM were extracted from the as-transformed (K1481) and HP-deformed (Gamma 21) samples using the focus ion beam technique with a FIB Dual Beam FEI Strata DB 235.

2.2. Transmission Electron Microscopy

TEM investigations were performed with a FEI® Tecnaï $G^2$20Twin microscope, operating at 200 kV and with a FEI CM30 microscope operating at 300 kV, both with a LaB_6 filament and using a double tilt sample-holder.

Orientation maps were acquired with a step size of 5 nm using SPED in the TEM with the ASTAR™ tool from NanoMEGAS (Rauch & Véron, 2014). The TEM is set in microbeam mode (spot size 4 nm) and the incident electron beam is scanned over the area thanks to a dedicated hardware control system of the TEM deflecting coils. The individual exposure time at each location is 10 or 20 ms. The spot patterns are collected with an external Stingray CCD camera that points on the TEM phosphorous screen and stored in the computer memory for further indexation and postprocessing. The diffraction patterns were collected as 144 × 144 pixels at a camera length of 89 mm. Electron diffraction spot patterns are indexed (providing the local crystal orientations) by comparing individually obtained patterns via cross-correlation matching techniques with precalculated electron diffraction templates generated every 1° (orientation resolution). For bridgmanite, templates have been generated from the crystallographic data of Tschauner et al. (2014). All crystallographic data for bridgmanite are presented within the *Pbnm* space

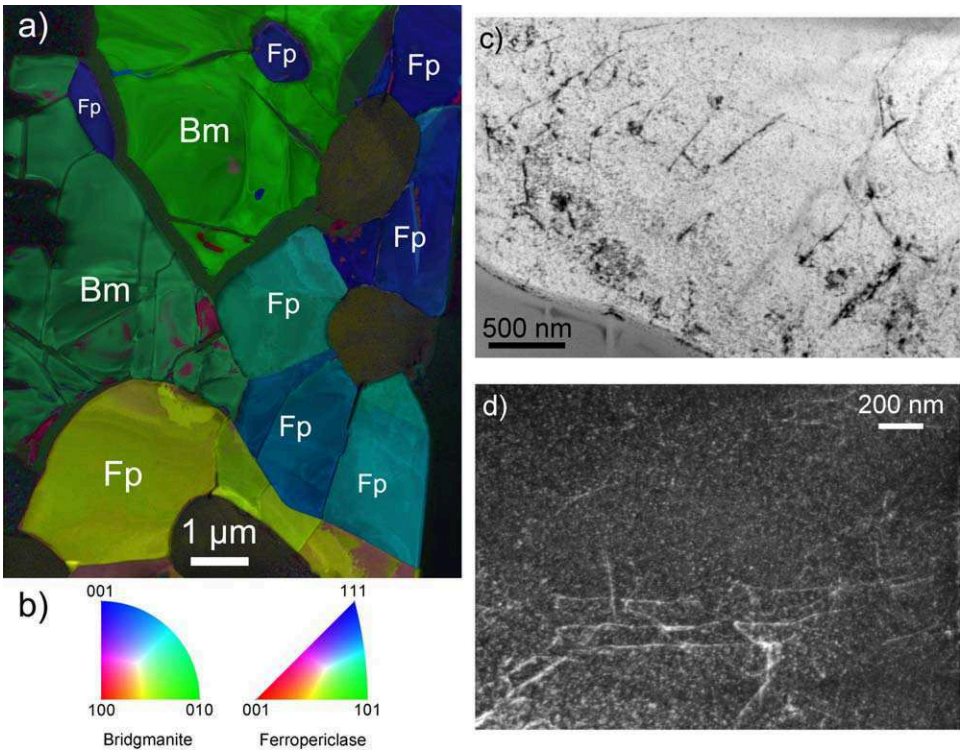

Figure 2. Starting material K1481. (a) Orientation map-spatial resolution 5 nm-1,600 × 2,000 data points—inverse pole figure (IPF). For each phase, the color indicates the crystallographic orientation of the vertical direction. Bm stands for bridgmanite and Fp for ferropericlase. (b) Color code for the crystallographic orientations of the IPF in Figure 2a. Ferropericlase is indexed within the *Fm3m* space group and bridgmanite within the *Pbnm* space group. (c) Ferropericlase: TEM bright field showing dislocations (dark lines) with a density of the order of 10^{12}–10^{13} m^{-2}. The spotty aspect in the background is due to damage induced by ion bombardment. (d) Ferropericlase: TEM dark field showing dislocations (white lines) with a density of the order of 10^{12}–10^{13} m^{-2}.

group (where a = 4.82 Å, b = 5.05 Å, and c = 6.92 Å). Ferropericlase templates were calculated from crystallographic data from Fei et al. (1992).

In this study, we used precession illumination in the TEM. When the precession mode is activated, a hollow-cone illumination is formed with the upper coils and equal and opposite signal is applied to the lower coils to bring the tilted beam back onto the optic axis. The net effect of the double-rocking is equivalent to having a stationary beam and a crystal which would precessed about the optic axis. The great advantage of this technique is that many more reflections are seen in the diffraction pattern and the intensity distribution gets closer to the kinematical diffracting conditions. We used precession angles in the range 0.5–1°. The orientations maps are presented as inverse pole-figures (IPF), where the color at each position represents the crystal orientation, that is, for the shear deformed sample, parallel either to the shear direction (SD), the radial direction (RD), or the compression direction (CD, i.e., parallel to the axis of the anvils). No cleaning procedure was applied to these maps. From the orientation maps, virtual bright field (VBF) maps can be generated which represents the fluctuation of the central beam intensity of the diffraction patterns. This builds up a STEM-like bright field contrast directly related to the orientation maps. The quality of indexation from template matching is quantified by the image correlation index, $Q(i)$, which is calculated for every template (Rauch & Dupuy, 2005):

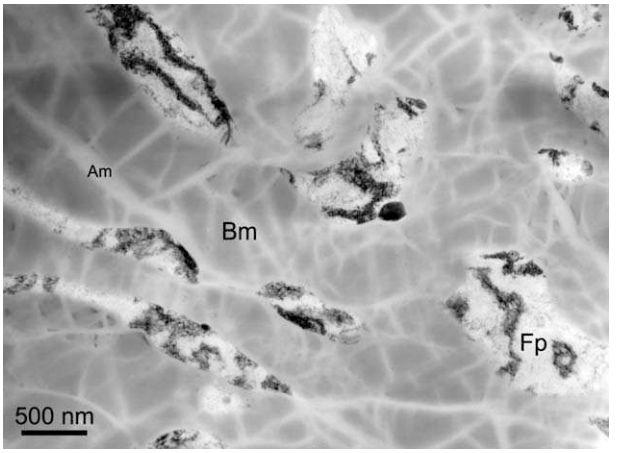

Figure 3. Overall microstructure of G21M (middle position). TEM bright field. Bm stands for bridgmanite, Fp for ferropericlase, and Am for amorphous material. In this sample, bridgmanite is well preserved although the grains contain pervasive amorphous lamellae.

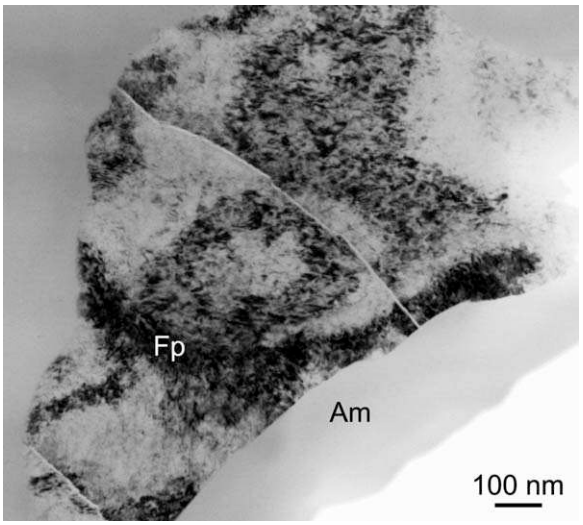

Figure 4. G21I (inner position). TEM bright field. Fp, ferropericlase and Am, amorphous material. All ferropericlase grains contain a very large density of dislocations, which precludes visualizing individual defects.

$$Q(i)=\frac{\sum_{j=1}^{m} P(x_j,y_j)T_i(x_j,y_j)}{\sqrt{\sum_{j=1}^{m} P^2(x_j,y_j)}\sqrt{\sum_{j=1}^{m} T_i^2(x_j,y_j)}} \quad (2)$$

In this expression, the diffraction pattern is represented by the intensity function $P(x,y)$ at each position (x,y) and each template i is described by the function $T_i(x,y)$. The highest Q value corresponds to the solution. The reliability of this solution can be quantified by the ratio of the matching indices for the two best solutions Q_1 and Q_2:

$$R=100\left(1-\frac{Q_1}{Q_2}\right) \quad (3)$$

In reliability maps, the brighter the pixel (i.e., the highest the reliability index) the more reliable is the indexation proposed. On the contrary, the darker is the pixel, the least reliable is the solution. This is typically the case at grain boundaries where two solutions of coexisting grains overlap or when for some reasons, the quality of the diffraction patterns is less. The presence of amorphous material represents an extreme case of that situation.

SPED can be compared with EBSD performed in transmission in an SEM (originally called t-EBSD for transmission EBSD or TKD for transmission Kikuchi diffraction). Both use electron-transparent thin foils and work in transmission. TKD is based on low-energy transmission Kikuchi diffraction in an SEM (Keller & Geiss, 2012; Suzuki, 2013; Trimby, 2012) whereas SPED involves high-energy microdiffraction in the TEM. It is important to highlight that the ASTAR™ algorithm saves all diffraction patterns and that no original data are lost. This is a huge advantage compared to commercial (standard) EBSD techniques which are usually not saving patterns and never perform image matching. Instead, in standard EBSD, indexing is based on Hough-transforms of the pattern for indexing and in most scenarios only the indexing is saved and the original data, namely the Kikuchi patterns, are discarded. From that perspective, SPED performed with ASTAR can be compared to the Dictionary Indexing approach for EBSD indexing, which also saves all patterns and performs image matching for indexing against a library of precomputed patterns (Marquardt et al., 2017; Ram et al., 2017; Singh & De Graef, 2016, 2017). If reliable results in terms of angular resolution (HR-EBSD or HR-KAM, cf. Britton et al., 2010) are needed, high-resolution patterns must be acquired (1,600 × 1,000 pixels). This results in an extremely large set of data to postprocess. In the most common TKD setups (except for Brucker), the EBSD camera is not in the most suitable condition for pattern acquisition and the patterns are generally deformed. This could

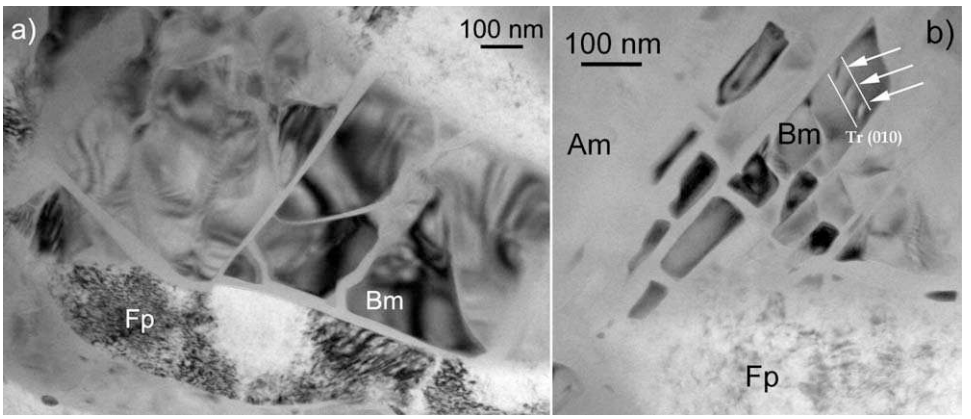

Figure 5. G21M (middle position). TEM bright field (Bm, bridgmanite; Fp, ferropericlase; and Am, amorphous material). The remaining crystalline bridgmanite parts are set in Bragg orientation to promote diffraction contrast. No evidence for defects is found in any grains besides the three dislocations arrowed in Figure 5b. See text for the analysis of the trace of the glide plane.

result in lower angular resolution that conventional EBSD. Still, TKD looks superior to SPED in term of angular resolution, but this advantage disappears with beam sensitive samples. The acquisition rate should be much higher with TKD to avoid beam damage and requires new technology which only becomes available.

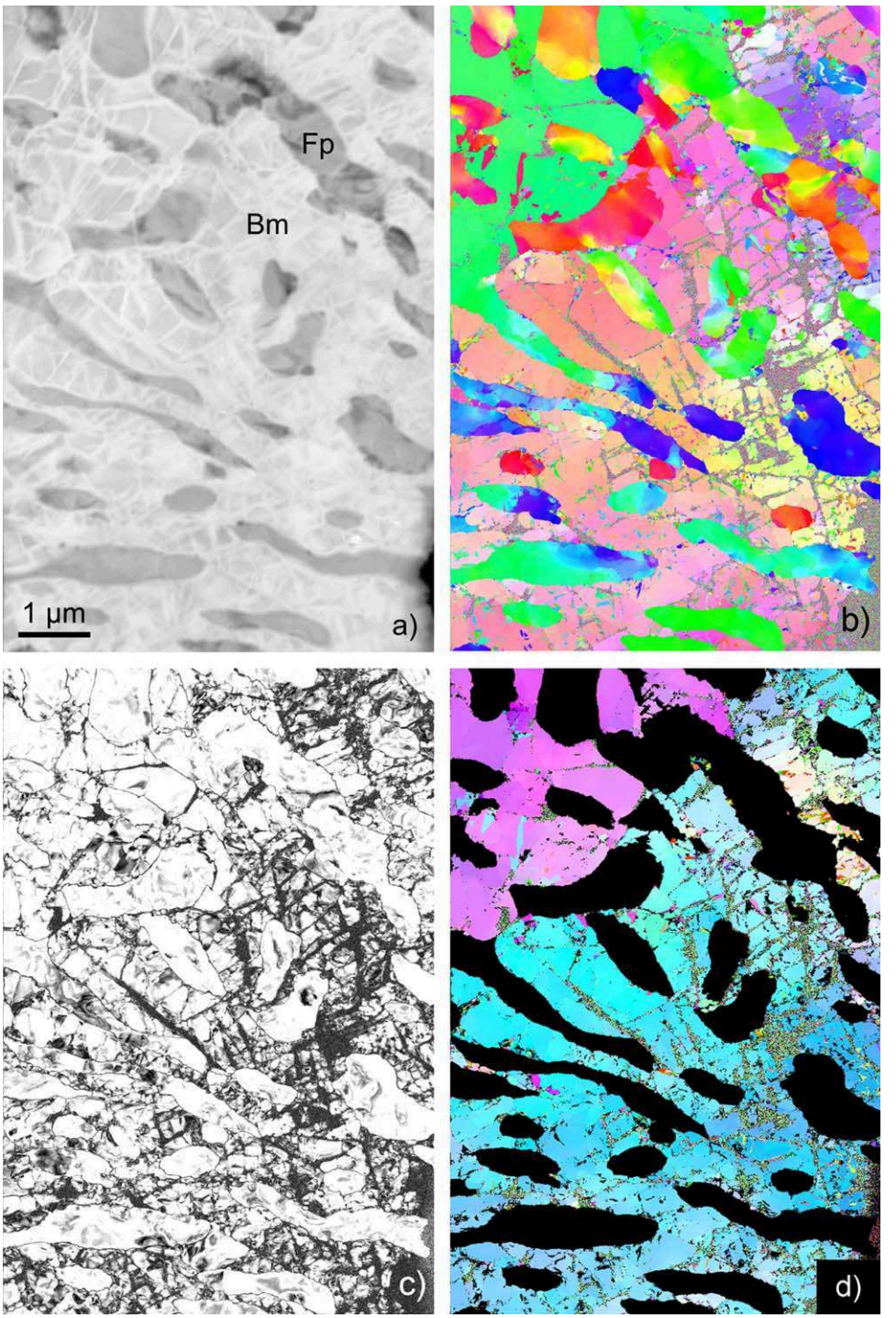

Figure 6. G21M (middle position). (a) SPED-virtual bright field. Spatial resolution 5 nm-1,200 × 1,800 data points. (b) SD-IPF: inverse pole figure map corresponding to the shear direction (horizontal). (c) Reliability map (plotted between 0 and 35). Less reliable places appear dark. (d) RD-IPF: inverse pole figure map of bridgmanite corresponding to the radial direction (perpendicular to the map plane). (e) CD-IPF: inverse pole figure map of ferropericlase corresponding to the compression direction (vertical). (f) IPF color legend. Ferropericlase is indexed within the *Fm3m* space group and bridgmanite within the *Pbnm* space group.

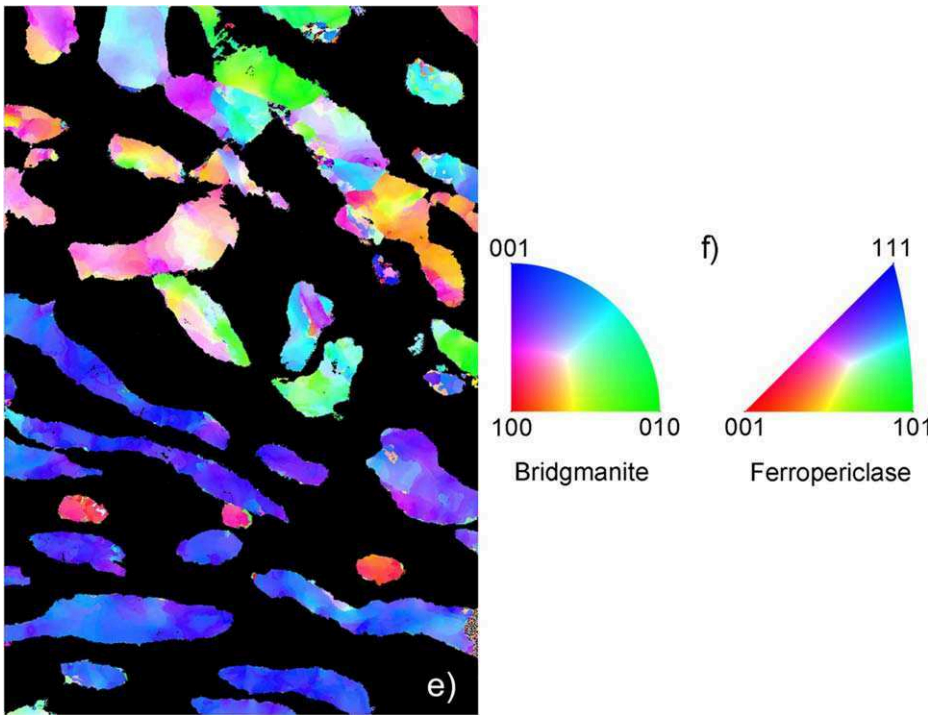

Figure 6. (Continued).

Although Q-maps have been proposed as a first approach to detect residual plastic strain, several parameters can affect this parameter as discussed above (Wright et al., 2011). In this study, we rather focus on the measurements of local misorientations as recently developed in the EBSD community (e.g., Wright et al., 2011). Postprocessing of the orientation maps was performed with the TSL OIM^{TM} Analysis 7 commercial software provided by EDAX. As commonly used in EBSD, several quantities are calculated from the orientation maps:

1. The *Kernel Average Misorientation* (KAM) calculates the average misorientation between a pixel and its neighbors provided that the misorientation does not exceed a predefined threshold value, e.g., 5°, thus the incorporation of well-defined grain boundaries is avoided. If plastic deformation results from dislocation glide and crystal lattice rotation, this approach allows quantitative evaluation of the local plastic strain gradients (Godfrey et al., 2005). A kernel is a set of points of prescribed size surrounding the scan point of interest. The size of the kernel is generally prescribed to the *n*th nearest-neighbors. Hence, this parameter is sensitive to the step size of the measurement grid.
2. The *Grain Orientation Spread* (GOS) is the average deviation in orientation between each point in a grain and the average orientation of the grain. This approach leads to assigning the same value of the GOS to every scan point contained within a grain.
3. The *Grain Reference Orientation Deviation* (GROD) is based on the misorientation between a reference point of that grain and the other points. The reference point can be the mean misorientation of the grain (in that case the GROD is also called *Mis2mean* in MTEX) or the point of the grain where the KAM is the lowest.

KAM, GROD, and GOS approaches appear to be complementary. GROD maps show the orientation field referenced to a fixed point whereas KAM approach shows the magnitude of the gradient, which can be seen as the first derivative of the orientation field.

3. Observations

3.1. Starting Material (K1481)

The microstructure of the starting material is illustrated in Figure 2. As already reported in Girard et al. (2016), it consists in a mixture of bridgmanite and ferropericlase grains which are mostly equiaxed. With

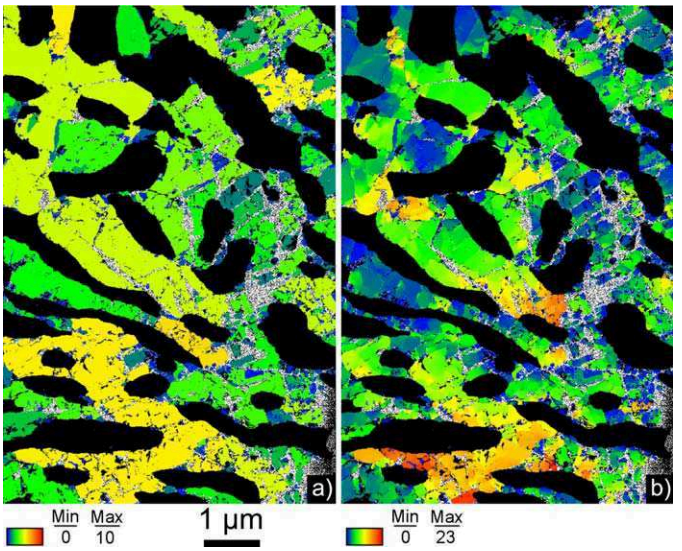

Figure 7. Bridgmanite in G21M (middle position). Same map area as Figure 6. (a) Grain Orientation Spread (GOS) map. Each grain displays a color corresponding to its average internal misorientation. (b) Grain Reference Orientation Deviation (GROD) or Mis2mean map since here, the reference is the mean misorientation in each grain. This representation highlights intragranular misorientations which would correspond to small color changes in Figures 6b, 6d, and 6e.

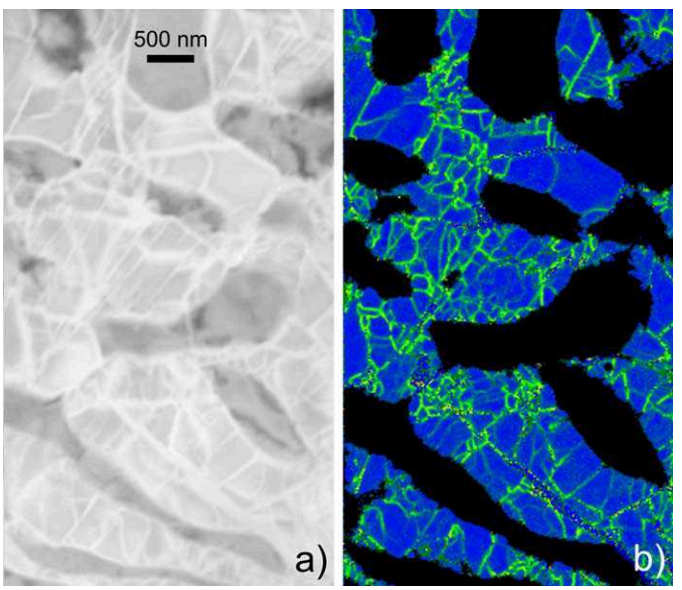

Figure 8. Origin of amorphous lamellae in bridgmanite from G21M (middle position). (a) SPED-virtual bright field where the amorphous lamellae in bridgmanite appear brighter than the crystalline parts (ferropericlase appear even darker). (b) Kernel Average Misorientation (KAM—third neighbor) in bridgmanite. This representation highlights local gradients of orientation. One can see that amorphous lamellae correlate with high KAM, demonstrating that they localize shear and thus have a mechanical origin and do not result from sample preparation.

conventional bright-field TEM analyses, only ferropericlase shows some dislocations, with a density of the order of 10^{12}–10^{13} m^{-2} at the most (Figures 2c and 2d).

3.2. Conventional TEM Observation of Gamma 21

Although ferropericlase is found equally well in the three thin foils, the preservation of bridgmanite after FIB milling is very uneven. In G21M, crystalline bridgmanite has been well preserved everywhere in the thin section although this phase contains systematically numerous amorphous lamellae (Figure 3). In G21I, most bridgmanite has been amorphized in the central part of the thin section. Almost no bridgmanite is preserved in G21O.

The strong plastic strain of ferropericlase is suggested by the elongated shape of most grains (already observed at the SEM: Girard et al., 2016) as seen in Figure 3 (with clearer evidence in Figure 6e) in G21M, but also from the very large dislocation density which prevents further analysis with conventional techniques (Figure 4).

In bridgmanite, rapid amorphization under the electron beam prevents from having an exhaustive characterization of the microstructure. However, the only remaining crystalline areas are remarkably free of dislocations (Figure 5a). Only three dislocations have been observed, they are displayed in Figure 5b. Taking into account the orientation of the grain (close to the zone axis [746]) from the orientation map (see below), the orientation of the trace of the glide plane, and the thickness of the thin foil, one finds that the plane containing the dislocations is compatible with (010). One notes the pervasive occurrence of amorphous lamellae which preexisted observation (but broaden rapidly under the beam). It is worth mentioning that, because of the sensitivity of the samples to the beam, we took care to record the orientation maps described below before any exposure of the samples and that the conventional TEM investigation has been done only at the end of the study.

3.3. Orientation Imaging Mapping on Gamma 21

To gain more information on the deformation, we have acquired orientation maps by SPED with the ASTAR™ system. Figure 6 shows the maps obtained on G21M (which is the sample for which both phases are best preserved). The virtual bright field shows the microstructure of the two phases, and also the amorphous lamellae later imaged in TEM bright field. From the indexation of the diffraction patterns, it is possible to plot the IPF maps either corresponding to the shear direction, to the compression direction or to the radial direction. In Figure 6b, we present the IPF of both phases corresponding to the shear direction (SD). It is possible to separate both phases as shown in Figures 6d and 6e. The indexation is usually very good. This can be assessed from the reliability map (Figure 6c). The reliability drops at the grain boundaries when the diffraction patterns consist in the superposition of those of the two grains. The reliability map thus offers a good visualization of the grain boundaries. The reliability is also poor in thicker areas or when crystallinity is less. Such is the case in some places in bridgmanite, for instance along the thickest amorphous lamellae (Figures 6c and 6d).

3.3.1. Bridgmanite

The orientation map of bridgmanite from Gamma 21 reveals rather large grains (several micrometers) which contain elongated ferropericlase grains. The colors are not perfectly uniform in the IPF suggesting

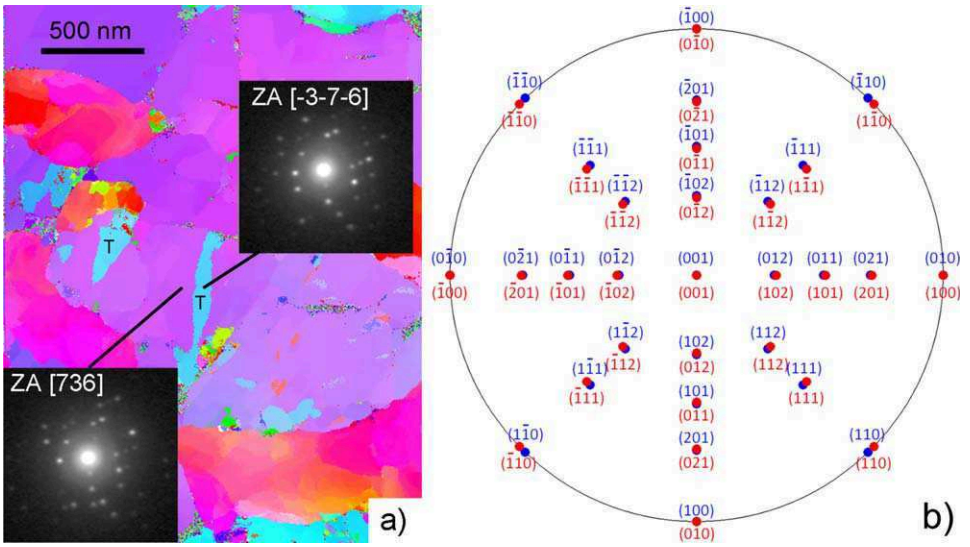

Figure 9. G21M (middle position). (a) CD-IPF (enlargement) showing twinned domains *T* (see text) with corresponding diffraction patterns (indices are given within the *Pbnm* space group). (b) Twin model resulting from the switch of the [100] and [010] axis (*Pbnm* space group) corresponding to an 87.3° rotation around [001].

some misorientation in the bridgmanite grains. The GOS (Figure 7a) is well suited to reveal these variations and quantify them. It shows that all bridgmanite grains (or domains within those grains) exhibit significant internal misorientation. The GROD (Figure 7b) shows that these misorientations are pervasive and rather heterogeneous. The GROD seems to be more pronounced when bridgmanite forms narrow channels between elongated ferropericlase grains suggesting strain resulting from the infiltration process of ferropericlase grains.

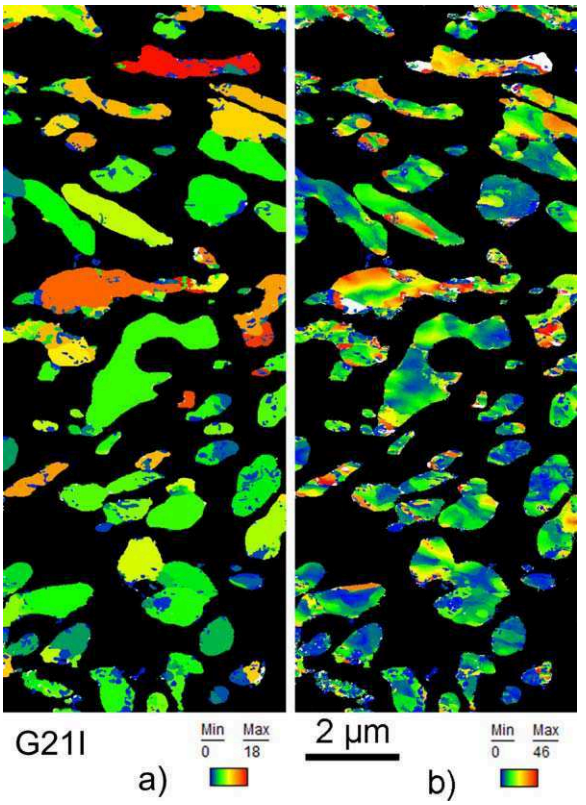

Figure 10. Ferropericlase in G21I (inner position see Figure 1). Total map acquired with a spatial resolution 5 nm-1,200 × 3,000 data points. (a) Grain Orientation Spread (GOS) and (b) Grain Reference Orientation Deviation (GROD) using the average orientation for each grain as the reference (Mis2mean).

Further understanding comes from plotting point to point misorientation profiles across the amorphous lamellae. This shows that these lamellae correspond to jumps of misorientation between largely undeformed regions (supporting information Figure S1). These features appear well on the KAM maps, which highlight places where strong misorientation localizes. Comparison of the KAM with the TEM bright field or the SPED-virtual bright field (Figure 8) demonstrates that misorientation gradients correlate very well with the amorphous lamellae. These lamellae thus appear to be the location where deformation localized in bridgmanite.

In bridgmanite, some domains attract attention (Figure 9a or Figures 6b and 6d (upper left corner)). They exhibit a remarkable misorientation with the surrounding matrix of 87.4 ± 0.1°. The analysis of the diffraction patterns of both domains shows that they correspond to switching the [100] and [010] axis, i.e., to the {110} pseudomerohedral twinning of the *Pbnm* orthorhombic structure already reported (e.g., Wang et al., 1992). Indeed, this model (Figure 9b) predicts a theoretical misorientation of 87.3° between the variants which is in excellent agreement with the value found experimentally.

3.3.2. Ferropericlase

As already mentioned above and in Girard et al. (2016), the morphology of the ferropericlase grains is already a strong indication of large strain in this phase. It seems that from the inner to the outer sample there is a gradient in the microstructure with more elongated (G21M) and then fragmented (G21O) ferropericlase grains as one goes

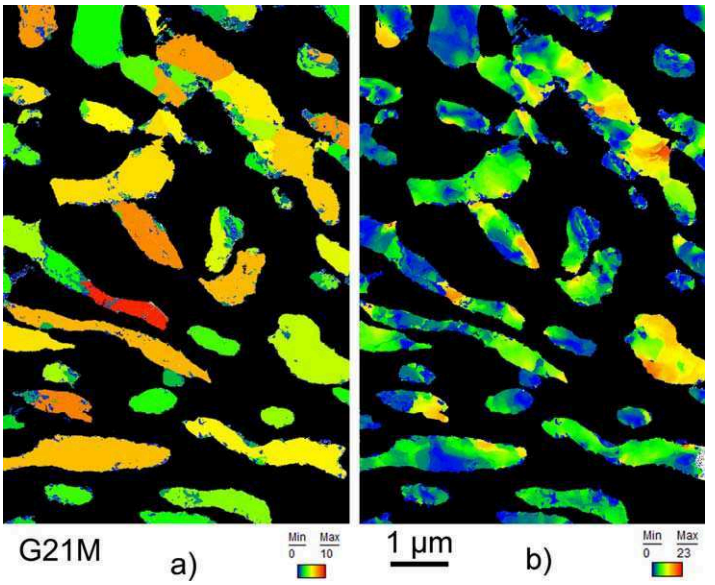

Figure 11. Ferropericlase in G21M (middle position). Same map area as Figure 6. Total map acquired with a spatial resolution 5 nm-1,200 × 1,800 data points. (a) Grain Orientation Spread (GOS) and (b) Grain Reference Orientation Deviation (GROD) using the average orientation for each grain as the reference (Mis2mean).

from inside to outside the deformation sample. The GOS maps (Figures 10a, 11a, and 12a) show that all grains are strongly internally disoriented (i.e., deformed). Comparison is, however, quite difficult since heterogeneities lead to use different scales. The GROD maps (Figures 10b, 11b, and 12b) show that the indistinct, large dislocation densities observed in the TEM bright-fields hide some complex, heterogeneous structures at a very fine scale. One can understand that such strong local heterogeneities can ultimately lead to fractures during foil thinning as seen in Figure 4.

4. Discussion

TEM-based SPED appears as a powerful complement to in situ X-ray diffraction to study the plastic behavior of high-pressure phases, especially in case of samples that include beam sensitive minerals and also aggregates of phases exhibiting a large viscosity contrast. In the present case, in situ X-ray diffraction acquired during deformation provided information on stress against shear strain. Where strain, obtained from a marker or (here) from the rotation of the anvils, could only be assessed on average, in situ X-ray diffraction provides information which can distinguish both phases. Using this technique, Girard et al. (2016) could demonstrate that ferropericlase is much softer than bridgmanite at 27 GPa and 2,130 K, with average flow stress 4–5 times smaller in ferropericlase than in bridgmanite. SEM, backscattering images of the recovered Gamma 21 already showed (Girard et al., 2016) that ferropericlase grains undergone strains much larger than the average value of the sample estimated to 100%.

Our microscopic investigation confirms these observations. Prior to deformation, ferropericlase in K1481 is often larger than 1 μm and rather equiaxed (Figure 2). After deformation (Figures 6 and 10−12), the grains of ferropericlase are strongly stretched, eventually leading to fragmentation into grains of a few hundreds of nanometers in size. These processes have been observed in monomineralic magnesiowüstite deformed in shear for ca. $\gamma = 5$ to ca. $\gamma = 10$ (Heidelbach et al., 2003; see also similar observations in halite deformed under large shear strains: Wenk et al., 2009). We can see in Figure 6e that most grains in the lower part of the map exhibit very close orientations. We can speculate that they result from the stretching and fragmentation of a single larger grain of ferropericlase. It is difficult from a cross section only to decide whether this also corresponds to a three-dimensional interconnectivity in G21M. Conventional TEM observations show further evidence of accumulated strain with very large dislocations densities. In the starting material, the dislocation density was found to be of the order of 10^{12}–10^{13} m^{-2}. In ferropericlase from Gamma 21, the dislocation densities are much larger. They are so large that no measurement of dislocation density is now possible. This illustrates the usual limitation of TEM studies on samples deformed at large strains. Here we show how SPED can overcome this limitation.

Beyond the shape of the grains and without directly imaging the dislocations, the IPF of ferropericlase (Figure 6e) show that grains do not exhibit a single orientation. Indeed misorientation profiles show extremely strong gradients inside every grains. To gain more information on these misorientations, we have applied the standard posttreatments used in EBSD. First, we used the grain-based method to better reveal the presence of intracrystalline misorientations. The GOS affects a single value (taken as the average) for the misorientation to a body identified as a grain.

Figures 10a, 11a, and 12a show that all ferropericlase grains, even the smallest, exhibit average misorientations of several degrees. The spatial distribution of those misorientations is better illustrated using the GROD, which represents at each measurement point the misorientation with a reference value. Here we choose the average misorientation as the reference. The GROD is then usually called the Mis2mean. The Mis2mean maps (Figures 10b, 11b, and 12b) show that deformation in ferropericlase is very heterogeneous at a very small scale. This information could not be withdrawn from standard diffraction contrast imaging (e.g., Figure 4). Being cubic, ferropericlase exhibits a large number of equivalent slip systems which involve dislocations which can interact

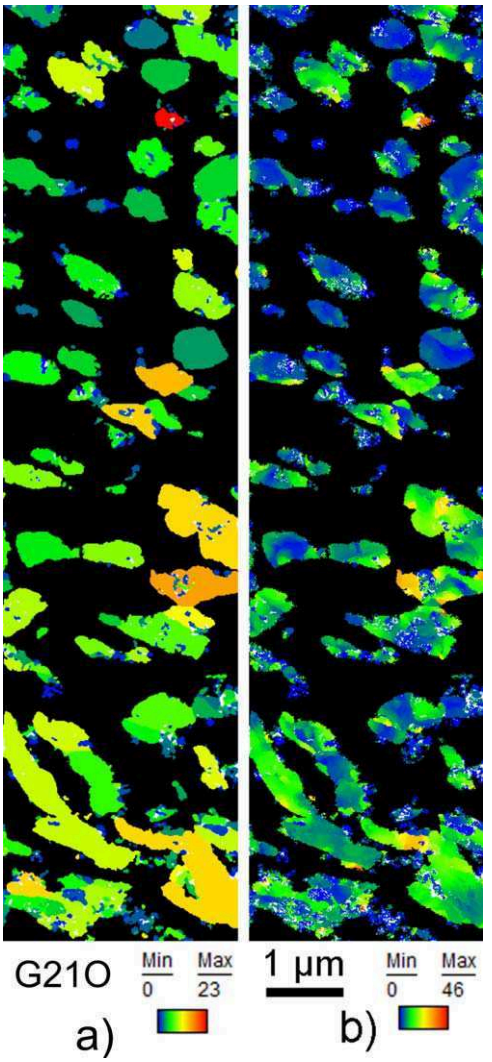

Figure 12. Ferropericlase in G21O (outer position). Total map acquired with a spatial resolution 5 nm-600 × 2,400 data points. (a) Grain Orientation Spread (GOS) and (b) Grain Reference Orientation Deviation (GROD) using the average orientation for each grain as the reference (Mis2mean).

and form various kinds of junctions. This is the origin of strong dislocation storage in this material which can lead to significant strain hardening (Amodeo et al., 2014). Usually, this dislocation storage leads to recrystallization, i.e., to the formation of new grains free of dislocations, even in single crystals (see, for instance, Mariani et al., 2009). Here we find no evidence of dislocation-free grains or domains. Further quantification is difficult. Indeed, the grain grouping algorithms (GOS and GROD) are by definition sensitive to the body considered as a grain. A usual criterion is to consider a limit of misorientation of 15° as a standard limit to discriminate subgrains and grain boundaries. In the present case, ferropericlase grains are strongly deformed and present strong misorientations which challenge the automatic detection of "grains." Hence, we consider that GOS and GROD are useful to highlight the strong strains undergone by the ferropericlase grains, but not well adapted to further quantification. We prefer here to rely on short-range misorientation parameters with a kernel-based algorithm like the KAM. In that case, to provide comparable results, one must compare maps acquired with the same spatial resolution, and the same kernel size must be used. Figure 13 corresponds to maps acquired with a step size of 5 nm and processed with third nearest-neighbor kernels. Figure 13b shows in the case of ferropericlase that KAM distributions can resolve more quantitative information. The KAM distribution in K1481 is clearly distinct from those in Gamma 21. Being much narrower, indicating much less intragranular misorientation, it is clearly consistent with what is expected from the undeformed state. More interestingly, one also observes a consistent evolution of the KAM distribution with the sample position in the experimental setup. From the inner position to the outer position in the sample ring, one finds that (i) the KAM distribution peak shifts to higher values of misorientation, (ii) the peak fractions decrease, and (iii) the distributions broaden. This evolution is characteristic of increasing strain. One can see here that our analysis is able to evidence the radial strain gradient which is expected in a torsion test.

Although preservation of bridgmanite remains a challenging issue, we have been able to gather enough diffraction patterns on this phase to gain information on its deformation mechanisms. From G21M (which is the sample where bridgmanite is best preserved), one can essentially see two large grains with a morphology which cannot be distinguished from those in K1481. The GOS and GROD maps of those grains (Figure 7) show evidence of intragranular misorientation which suggests some deformation. The KAM distributions (Figure 13a) also show that Gamma 21 is clearly distinct from the undeformed state. The difference in the distributions from G21I and G21M is also consistent with a radial strain gradient although it is less conclusive than in ferropericlase. Here we get more information from the KAM map. In Figure 8, one can see an excellent correlation between the KAM spatial distribution and the presence of amorphous lamellae observed in the virtual bright field or in the TEM bright-field images. We interpret that these amorphous lamellae are regions where strain was localized during HP-HT deformation. The only information that we have to further constrain deformation mechanisms that were active at HP-HT comes from the three dislocations observed. Their alignment allows to infer their glide plane which is compatible with (010). Considering the possible slip systems predicted in bridgmanite (Ferré et al., 2007; Hirel et al., 2014; Mainprice et al., 2008), this suggests that the observed dislocation would belong to the [100](010) slip system. Our (single) observation is not compatible with the [001](100) slip system inferred by Tsujino et al. (2016) from crystal preferred orientation developments. We have also observed a few pseudomerohedral twins in bridgmanite. Twinning occurs and can be observed, but it is not pervasive, showing that twinning does not represent a significant deformation mechanism for bridgmanite under those conditions.

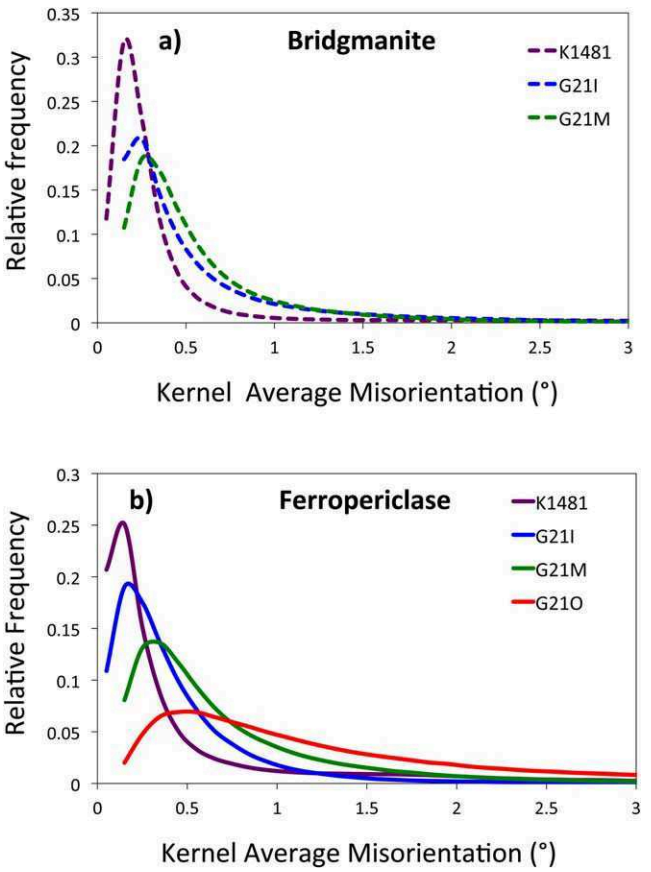

Figure 13. KAM distributions in undeformed and deformed bridgmanite and ferropericlase in each sample investigated here, i.e., for the deformed samples for increasing strains from the inner to the outer positions (see Figure 1). (a) Third nearest-neighbor KAM distributions in bridgmanite, where the starting material is compared with G21I and G21M. Since bridgmanite was completely amorphized in G21O, this sample is not represented here. (b) Third nearest-neighbor KAM distributions in ferropericlase for all samples including the starting material.

5. Conclusions

SPED represents a powerful new technique to analyze samples deformed at HP-HT. Applied to aggregates of bridgmanite and ferropericlase deformed in conditions of the uppermost lower mantle, it provides new information about the plastic behavior of those phases. We see only evidence form intracrystalline plasticity by dislocation motion although the deformed microstructure of bridgmanite and ferropericlase suggest very different mechanisms and plastic behavior. Ferropericlase shows strong evidence for large strains (much larger than the average 100% strain of the aggregate) with intense dislocation activity and storage leading to what we interpret as elongation leading to fragmentation of the grains. Despite these high strains, we observe no evidence for dynamic recrystallization. Evidence of deformation is demonstrated in bridgmanite although clearly less pronounced. It occurs essentially through localized, amorphous, shear deformation lamellae. An evidence for dislocations belonging to the [100](010) slip system is reported.

Acknowledgments
The work in Lille was supported by funding from the European Research Council under the Seventh Framework Programme (FP7), ERC grant 290424—RheoMan to P. Cordier. The TEM facility in Lille (France) is supported by the Conseil Regional du Nord-Pas de Calais, and the European Regional Development Fund (ERDF). We thank D. Troadec (IEMN-Lille) for sample preparation with the FIB. We are grateful to Dr. K. Marquardt and an anonymous reviewer for their comments which helped improving the manuscript. Data are available from https://figshare.com/s/4a19bbda734beef58be1.

References

Amodeo, J., Devincre, B., Carrez, P., & Cordier, P. (2014). Dislocation reactions, plastic anisotropy and forest strengthening in MgO at high temperature. *Mechanics of Materials*, *71*, 62–73.

Argon, A. S., & Haasen, P. (1993). A new mechanism of work hardening in the late stages of large strain plastic flow in F.C.C. and diamond cubic crystals. *Acta Metallurgica et Materialia*, *41*(11), 3289–3306. https://doi.org/10.1016/0956-7151(93)90058-Z

Bollinger, C., Merkel, S., Cordier, P., & Raterron, P. (2015). Deformation of forsterite polycrystals at mantle pressure: Comparison with Fe-bearing olivine and the effect of iron on its plasticity. *Physics of the Earth and Planetary Interiors*, *240*, 95–104. https://doi.org/10.1016/j.pepi.2014.12.002

Britton, T. B., Maurice, C., Fortunier, R., Driver, J. H., Day, A. P., Meaden, G., et al. (2010). Factors affecting the accuracy of high resolution electron backscatter diffraction when using simulated patterns. *Ultramicroscopy*, *110*(12), 1443–1453.

Cordier, P., Ungár, T., Zsoldos, L., & Tichy, G. (2004). Dislocation creep in $MgSiO_3$ perovskite at conditions of the Earth's uppermost lower mantle. *Nature*, *428*(6985), 837–840.
Fei, Y., Mao, H.-K., Shu, J., & Hu, J. (1992). P-V-T equation of state of magnesiowüstite $(Mg_{0.6}Fe_{0.4})O$. *Physics and Chemistry of Minerals*, *18*(7), 416–422.
Ferré, D., Carrez, P., & Cordier, P. (2007). First-principles determination of dislocations properties of $MgSiO_3$ perovskite at 30 GPa based on the Peierls-Nabarro model. *Physics of the Earth and Planetary Interiors*, *163*, 283–291.
Girard, J., Amulele, G., Farla, R., Mohiuddin, A., & Karato, S.-I. (2016). Shear deformation of bridgmanite and magnesiowüstite aggregates at lower mantle conditions. *Science*, *351*(6269), 144–147. https://doi.org/10.1126/science.aad3113
Godfrey, A., Cao, W. Q., Liu, Q., & Hansen, N. (2005). Stored energy, microstructure, and flow stress of deformed metals. *Metallurgical and Materials Transactions A*, *36*, 2371–2378.
Heidelbach, F., Stretton, I., Langenhorst, F., & Mackwell, S. (2003). Fabric evolution during high shear strain deformation of magnesiowüstite $(Mg_{0.8}Fe_{0.2}O)$. *Journal of Geophysical Research: Solid Earth*, *108*(B3), 2154. https://doi.org/10.1029/2001JB001632
Hirel, P., Kraych, A., Carrez, P., & Cordier, P. (2014). Atomic core structure and mobility of [100](010) and [010](100) dislocations in $MgSiO_3$ perovskite. *Acta Materialia*, *79*, 117–125.
Hughes, D. A., Chrzan, D. C., Liu, Q., & Hansen, N. (1998). Scaling of misorientation distributions. *Physical Review Letters*, *81*(21), 4664–4667.
Hughes, D. A., Liu, Q., Chrzan, D. C., & Hansen, N. (1997). Scaling of microstructural parameters: Misorientations of deformed induced boundaries. *Acta Materialia*, *45*(1), 105–112.
Karato, S., Paterson, M. S., & Fitz Gerald, J. D. (1986). Rheology of synthetic olivine aggregates: Influence of grain-size and water. *Journal of Geophysical Research: Solid Earth*, *91*(B8), 8151–8176. https://doi.org/10.1029/JB091iB08p08151
Karato, S., & Wu, P. (1993). Rheology of the upper mantle: A synthesis. *Science*, *260*(5109), 771–778.
Keller, R. R., & Geiss, R. H. (2012). Transmission EBSD from 10 nm domains in a scanning electron microscope. *Journal of Microscopy*, *245*, 245–251.
Komabayashi, T., Hirose, K., Nagaya, Y., Sugimura, E., & Ohishi, Y. (2010). High temperature compression of ferropericlase and the effect of temperature on iron spin transition. *Earth and Planetary Science Letters*, *297*(3–4), 691–699.
Mainprice, D., Tommasi, A., Ferré, D., Carrez, P., & Cordier, P. (2008). Predicted glide systems and crystal preferred orientation of polycrystalline silicate Mg-Perovskite at high pressure: Implications for the seismic anisotropy in the lower mantle. *Earth and Planetary Science Letters*, *271*(1–4), 135–144.
Mao, H. K., Hemley, R. J., Fei, Y., Shu, J. F., Chen, L. C., Jephcoat, A. P., et al. (1991). Effect of pressure, temperature and composition on lattice parameters and density of $(Fe,Mg)SiO_3$-perovskite to 30 GPa. *Journal of Geophysical Research: Solid Earth*, *96*(B5), 8069–8079. https://doi.org/10.1029/91JB00176
Mariani, E., Mecklenburgh, J., Wheeler, J., Prior, D. J., & Heidelbach, F. (2009). Microstructure evolution and recrystallization during creep of MgO single crystals. *Acta Materialia*, *57*, 1886–1898.
Marquardt, K., De Graef, M., Singh, S., Marquardt, H., Rosenthal, A., & Koizuimi, S. (2017). Quantitative electron backscatter diffraction (EBSD) data analyses using the dictionary indexing (DI) approach: Overcoming indexing difficulties on geological materials. *American Mineralogist*, *102*(9), 1843–1855.
Mei, S., & Kohlstedt, D. L. (2000). Influence of water on plastic deformation of olivine aggregates 2. Dislocation creep regime. *Journal of Geophysical Research: Solid Earth*, *105*(B9), 21471–21481. https://doi.org/10.1029/2000JB900180
Nisr, C., Ribárik, G., Ungár, T., Vaughan, G. B. M., Cordier, P., & Merkel, S. (2012). High resolution three-dimensional X-ray diffraction study of dislocations in grains of $MgGeO_3$ post-perovskite at 90 GPa. *Journal of Geophysical Research: Solid Earth*, *117*, B03201. https://doi.org/10.1029/2011JB008401
Nyilas, K., Couvy, H., Cordier, P., & Ungár, T. (2006). The dislocation structure and crystallite-size in forsterite (olivine) deformed at 1400°C by 11 GPa. *Zeitschrift für Kristallographie Supplements*, *2006*(Suppl_23_2006), 135–140.
Paterson, M. S. (1987). Problems in the extrapolation of laboratory rheological data. *Tectonophysics*, *133*(1–2), 33–43.
Ram, F., Wright, S., Singh, S., & De Graef, M. (2017). Error analysis of the crystal orientations obtained by the dictionary approach to EBSD indexing. *Ultramicroscopy*, *181*, 17–26.
Rauch, E. F., & Dupuy, L. (2005). Rapid spot diffraction patterns identification through template matching. *Archives of Metallurgy and Materials*, *50*, 87–99.
Rauch, E. F., & Véron, M. (2014). Automated crystal orientation and phase mapping in TEM. *Materials Characterization*, *98*, 1–9.
Schayes, C., Bouquerel, J., Vogt, J. B., Palleschi, F., & Zaefferer, S. (2016). A comparison of EBSD based strain indicators for the study of Fe-3Si steel subjected to cyclic loading. *Materials Characterization*, *115*, 61–70.
Singh, S., & De Graef, M. (2016). Orientation sampling for dictionary-based diffraction pattern indexing methods. *Modelling and Simulation in Materials Science and Engineering*, *159*, 81–94.
Singh, S., & De Graef, M. (2017). Dictionary indexing of electron channeling patterns. *Microscopy and Microanalysis*, *23*(1), 1–10. https://doi.org/10.1017/S1431927616012769
Suzuki, S. (2013). Features of transmission EBSD and its application. *JOM*, *65*(9), 1254–1263. https://doi.org/10.1007/s11837-013-0700-6
Tange, Y., Kuwayama, Y., Irifune, T., Funakoshi, K.-I., & Ohishi, Y. (2012). V-T equation of state of $MgSiO_3$ perovskite based on the MgO pressure scale: A comprehensive reference for mineralogy of the lower mantle. *Journal of Geophysical Research: Solid Earth*, *117*, B06201. https://doi.org/10.1029/2011JB008988
Trimby, P. W. (2012). Orientation mapping of nanostructured materials using transmission Kikuchi diffraction in the scanning electron microscope. *Ultramicroscopy*, *120*, 16–24.
Tschauner, O., Ma, C., Beckett, J. R., Prescher, C., Prakapenka, V. B., & Rossman, G. R. (2014). Discovery of bridgmanite, the most abundant mineral in Earth, in a shocked meteorite. *Science*, *346*(6213), 1100–1102.
Tsujino, N., Nishihara, Y., Yamazaki, D., Seto, Y., Higo, Y., & Takahashi, E. (2016). Mantle dynamics inferred from the crystallographic preferred orientation of bridgmanite. *Nature*, *539*(7627), 81–85.
Wang, Y., Guyot, F., & Liebermann, R. C. (1992). Electron microscopy of (Mg, Fe)SiO3 Perovskite: Evidence for structural phase transitions and implications for the lower mantle. *Journal of Geophysical Research: Solid Earth*, *97*(B9), 12327–12347. https://doi.org/10.1029/92JB00870
Wenk, H.-R., Armann, M., Burlini, L., Kunze, K., & Bortolotti, M. (2009). Large strain shearing of halite: Experimental and theoretical evidence for dynamic texture changes. *Earth and Planetary Science Letters*, *280*(1–4), 205–210. https://doi.org/10.1016/j.epsl.2009.01.0
Wright, S. I., Nowell, M. M., & Field, D. P. (2011). A review of strain analysis using electron backscatter diffraction. *Microscopy and Microanalysis*, *17*(3), 316–329.
Zhong, Y., Yin, F., Sakaguchi, T., Nagai, K., & Yang, K. (2007). Dislocation structure evolution and characterization in the compression deformed Mn–Cu alloy. *Acta Materialia*, *55*(8), 2747–2756.

III.3 Caractérisation par SPED d'un agrégat de wadsleyite et ringwoodite déformé à haute température et haute pression

III.3.1 Contexte

Ce travail résulte d'une collaboration avec des collègues du BGI (Bavarian Research Institute of Experimental Geochemistry and Geophysics) de l'université de Bayreuth en Allemagne. Là encore, il s'agit d'utiliser notre approche pour caractériser des échantillons déformés à haute pression et haute température. Il s'agit de wadsleyite et de ringwoodite, deux polymorphes de haute pression de l'olivine qui constituent la zone de transition du manteau entre 410 et 670 km de profondeur. Ces échantillons ont été déformés sur une presse de type D-DIA installée sur le synchrotron japonais SPring-8. Le D-DIA est un dispositif développé par (Wang et al., 2003) qui permet, dans un environnement cubique, d'appliquer une déformation contrôlée selon l'axe vertical en maintenant la pression constante en rétractant les quatre enclumes horizontales. Dans l'article de Kawazoe et al., (2016), les auteurs décrivent les résultats de déformation de cinq échantillons déformés à 16-18 GPa et 1300-1700 K. La plupart de ces échantillons sont constitués de ringwoodite. L'un d'entre eux M1219, déformé à 17,3 GPa et 1700 K, se distingue par la présence des deux phases wadsleyite et ringwoodite. Cette microstructure donne l'opportunité de caractériser le contraste éventuel de propriétés mécaniques entre ces deux phases. Cependant, la superposition des pics de diffraction de la wadsleyite et de la ringwoodite n'avait pas permis d'isoler leurs contributions respectives lors de la caractérisation *in situ* au rayonnement synchrotron. Cet échantillon avait été au préalable observé en MET au BGI, montrant l'activation de la plasticité par glissement de dislocations dans les deux minéraux.

Dans l'étude de l'agrégat de bridgmanite et de ferropericlase, nous avions montré que les distributions de gradients locaux de désorientation (KAM) représentent un approximant intéressant de la déformation. Cependant, dans ces échantillons, les mécanismes de déformations étaient très différents dans les deux phases (lamelles amorphes de cisaillement, versus glissement de dislocations). Il ne nous avait donc pas semblé pertinent de comparer les distributions de KAM entre ces deux phases. Dans M1219 en revanche, les mécanismes de déformations semblent assez similaires pour tenter l'approche comparative. Nous observons en effet des profils distincts dans les deux phases avec une distribution assez atypique dans la wadsleyite pour laquelle nous proposons l'interprétation de l'activation de mécanismes de restauration.

III.3.2 Article

Ces résultats sont décrits dans l'article qui est reproduit dans les pages qui suivent :

B. Nzogang, S. Thilliez, A. Mussi, T. Kawazoe, N. Miyajima, J. Bouquerel & P. Cordier (2018) Application of Scanning Precession Electron Diffraction in the Transmission Electron Microscope to the characterization of deformation in wadsleyite and ringwoodite. Minerals, 8, 153; https://doi.org/10.3390/min8040153

minerals

MDPI

Article

Application of Scanning Precession Electron Diffraction in the Transmission Electron Microscope to the Characterization of Deformation in Wadsleyite and Ringwoodite

Billy C. Nzogang [1], Simon Thilliez [1], Alexandre Mussi [1], Takaaki Kawazoe [2,3], Nobuyoshi Miyajima [2], Jérémie Bouquerel [1] and Patrick Cordier [1,*]

1 CNRS, INRA, ENSCL, UMR 8207-UMET-Unité Matériaux et Transformations, University of Lille, F-59000 Lille, France; bc.nzogang@etudiant.univ-lille1.fr (B.C.N.); simon.thilliez@gmail.com (S.T.); alexandre.mussi@univ-lille1.fr (A.M.); jeremie.bouquerel@univ-lille1.fr (J.B.)
2 Bayerisches Geoinstitut, University of Bayreuth, D-95440 Bayreuth, Germany; kawazoe@hiroshima-u.ac.jp (T.K.); nobuyoshi.miyajima@uni-bayreuth.de (N.M.)
3 Department of Earth and Planetary Systems Science, Hiroshima University, Higashi-Hiroshima 739-8526, Japan
* Correspondence: patrick.cordier@univ-lille1.fr; Tel.: +33-320-434-34341

Received: 19 March 2018; Accepted: 10 April 2018; Published: 12 April 2018

Abstract: The mantle transition zone represents an important layer in the interior of the Earth that is characterized by phase transformations of olivine polymorphs. Constraining the rheology difference between wadsleyite and ringwoodite is important in determining the viscosity contrast at a depth of 520 km. In this study, we perform a post-mortem by transmission electron microscopy of a wadsleyite + ringwoodite aggregate, deformed at high-pressure and high-temperature, in a deformation-DIA apparatus. From orientation maps acquired by scanning precession electron diffraction, we calculate local misorientations and misorientation-gradients, which are used as a proxy of plastic strain. We show that at 17.3 GPa, 1700 K, the plastic responses of wadsleyite and ringwoodite are comparable, although recovery by subgrain boundary migration is more easily activated in wadsleyite.

Keywords: mantle transition zone; wadsleyite; ringwoodite; plastic deformation; transmission electron microscopy; scanning precession electron diffraction

1. Introduction

The Earth's mantle is divided into an upper and a lower part, separated by a transition zone (TZ) at a depth of between 520 km and 670 km. The TZ is characterized by phase transitions between polymorphs of olivine: wadsleyite and ringwoodite. The viscosity of the TZ is still a matter of debate. Some studies propose that it represents a weak layer [1,2] although slab stagnation may suggest the opposite [3]. A way of answering this question is to determine experimentally the rheology of the key phases of the TZ: wadsleyite and ringwoodite. Such experiments are very challenging, due to the P, T conditions which prevail in the TZ; however, recent technological developments have made such experiments possible. Two apparatuses can presently perform deformation experiments in the P, T condition of the TZ: the rotational Drickamer apparatus [4], and the D-DIA apparatus [5]. Using these devices, several studies have addressed the rheology of wadsleyite (e.g., [6,7]) and ringwoodite [8,9], including the one describing the sample investigated here [10]. In these experiments, rheological data are obtained by coupling deformation apparatuses with synchrotron X-ray beams. The total plastic strain is usually inferred from X-ray radiography, whereas stress is deduced from

lattice strain measurements from Bragg peaks displacements. The limited availability of synchrotron beamline access represents a strong limitation associated with such investigations. In the present study, we investigate an alternative approach based on the investigation and post-mortem, by transmission electron microscopy (TEM), of samples deformed at high-pressure. Not being performed in situ, our approach cannot be seen as a substitute for synchrotron studies (for instance, in giving access to stress-strain relationships). It can, however, complement in situ experiments and allow exploiting high-pressure deformation experiments to be performed off-line.

Deformed crystals contain defect microstructures which represent a valuable source of information about their mechanical properties. In this study, these defects and dislocations will not be characterized individually (as is commonly done at the TEM; see for instance a preliminary study of this sample in [10]). Dislocations introduce a long-range strain field in their surrounding materials. Each dislocation gives rise to a small increment of misorientation. This effect has been known and used for a long time, since undulatory extinction represents a common criterion for intragranular plasticity without recovery in optical microscopy. With the advent of automated orientation mapping by electron backscatter diffraction (EBSD) in the scanning electron microscope (SEM), the measurement of intragranular misorientation has been used as a proxy for plastic strain [11,12], with applications for severely deformed materials [13,14]. Such measurements are now possible in the TEM with a very high spatial resolution, and we have demonstrated recently the capability of the technique in providing information about deformation mechanisms in a bridgmanite and ferropericlase aggregate deformed at high-pressure and high-temperature [14].

Here we apply a technique called scanning precession electron diffraction (SPED) to the characterization of a sample deformed at 17.3 GPa and 1700 K, which contains both wadsleyite and ringwoodite. This sample represents a unique opportunity to gain information on the relative strength of the two phases, since they bore exactly the same deformation conditions.

2. Materials and Methods

2.1. Sample M1219: Synthesis and Deformation

Deformation of the sample characterized in this study (reference M1219) has been described in [10]. The main information is summarized here. Polycrystalline ringwoodite was synthesized from an olivine (San Carlos origin with composition $(Mg_{0.9}Fe_{0.1})_2SiO_4$) aggregate while increasing temperature to 1700 K at ~17–18 GPa in the D-DIA apparatus at the BL04B1 beamline of SPring-8. The sample was axially deformed with stress-strain measurements by X-ray diffraction and radiography respectively. Ringwoodite partially transformed to wadsleyite after a strain of 14.8% during deformation at 17.3 GPa and 1700 K. The wadsleyite + ringwoodite aggregate was further deformed to a strain of 24.9%. Stresses of coexisting wadsleyite and ringwoodite were not determined because X-ray diffraction peaks of ringwoodite (e.g., 220, 311 and 400) overlaps with those of wadsleyite (e.g., 040 + 200, 141 and 240), due to similarity between their crystal structures.

2.2. TEM Characterization

For the TEM investigation, sample foils were cut from the deformed samples using a dual beam focused ion (FIB) milling machine with Ga ion and electron beams (FEI (Hillsboro, OR, United States), Scios at the Bayerisches Geoinstitut, Bayreuth, Germany). TEM investigations were performed at the University of Lille with a FEI® Tecnaï $G^2$20Twin microscope (FEI, Hillsboro, OR United States), operating at 200 kV, and with a Philips CM30 microscope operating (now FEI, Hillsboro, OR, United States) at 300 kV; both were equipped with a LaB_6 filament and were using a double tilt sample-holder.

Orientation maps were acquired with a step size of 5 nm, using SPED in the TEM with the ASTAR™ tool from NanoMEGAS (Forest, Belgium) [15]. The TEM is set in micro-beam mode (spot size 4 nm), and the incident electron beam, which is focused on the sample, is scanned over the area thanks to a dedicated hardware control system composed of TEM deflecting coils. In this mode, where

the sample is illuminated by a convergent beam, the diffraction pattern consists of discs. Using the smallest condenser aperture (50 μm) the diffraction patterns are made of very small, spot-like discs, and can be indexed as spot patterns. The individual exposure time at each location is 10 ms. In this study, we used precession illumination (with a precession angle of 0.5°) in the TEM, which allows many more reflections to be seen in the diffraction pattern with intensities closer to the kinematical diffraction conditions. Diffraction patterns are collected with an external Stingray CCD camera (Allied Vision Technologies GmbH, Stadtroda, Germany) that points on the TEM phosphorous screen, and stored in the computer memory for further indexation and post processing. The diffraction patterns were collected as 144 × 144 pixel images, at a camera length of 89 mm. In the ASTAR system, electron diffraction spot patterns are indexed (providing the local crystal orientations) by comparing individually obtained patterns via cross-correlation matching techniques with pre-calculated electron diffraction templates generated every 0.5° (orientation resolution). For wadsleyite and ringwoodite, templates have been generated from the crystallographic data of Horiuchi and Sawamoto [16] and Hazen et al. [17] respectively. From this indexation, one obtains an orientation map which displays, with a color coding, the most probable orientation at each scanned beam position.

The quality of indexation from template matching is quantified by the image correlation index, which is calculated for every template [18]:

$$Q(i) = \frac{\sum_{j=1}^{m} P(x_j, y_j) T_i(x_j, y_j)}{\sqrt{\sum_{j=1}^{m} P^2(x_j, y_j)} \sqrt{\sum_{j=1}^{m} T_i^2(x_j, y_j)}} \quad (1)$$

In this expression, the diffraction pattern is represented by the intensity function $P(x, y)$, and every template i is described by the function $T_i(x, y)$. The highest Q value corresponds to the solution retained. The reliability of this solution can be quantified by the ratio of the matching indexes for the two best solutions Q_1 and Q_2:

$$R = 100\left(1 - \frac{Q_1}{Q_2}\right) \quad (2)$$

In reliability maps, the brighter the pixel, the more reliable the indexation proposed is. On the contrary, the darker the pixel, the less the solution is reliable. This is typically the case at grain boundaries where two solutions of co-existing grains overlap, or when for various reasons, the quality of the diffraction patterns is diminished.

In this study we use orientation maps to calculate local misorientations, as recently developed in the EBSD community (e.g., [19]). Post-processing of the orientation maps was performed using HKL Channel 5 software (Oxford Instruments, Abingdon-on-Thames, United Kingdom). As commonly used in EBSD, several quantities are calculated from the orientation maps:

The Kernel Average Misorientation (KAM) calculates the average misorientation between a pixel and its neighbors, provided that the misorientation does not exceed a predefined threshold value, e.g., 5°; thus, the incorporation of well-defined grain boundaries is avoided. If plastic deformation results from dislocation glide and crystal lattice rotation, this approach allows quantitative evaluation of the local plastic strain gradients [20]. A kernel is a set of points of prescribed size surrounding the scan point of interest. The size of the kernel is generally prescribed to the nth nearest-neighbors. Hence this parameter is sensitive to the step size of the measurement grid.

- The Grain Orientation Spread (GOS) is the average deviation in orientation between each point in a grain and the average orientation of the grain. This approach leads to assigning the same value of the GOS to every scan point contained within a grain. The minimum area grain size is set to 100 pixels (ca. 50 nm in diameter assuming quasi-spherical grains), and the grain tolerance angle is set to 15°.
- The Grain Reference Orientation Deviation (GROD) is based on the misorientation between a reference point of that grain and the other points. The reference point can be the mean misorientation of the grain or the point of the grain where the KAM is the lowest.

- KAM, GROD and GOS approaches are complementary. GROD maps show the orientation field referenced to a fixed point, whereas KAM shows the magnitude of the gradient, which can be seen as the first derivative of the orientation field.

3. Results

The FIB thin section investigated in this study is shown on Figure 1a, with the area scanned by SPED appearing in red. It shows a large fraction of open grain boundaries, probably resulting from sample preparation. Hence we will focus on intragranular plasticity mechanisms only. During post-processing, each diffraction pattern at each point is compared to the patterns calculated for wadsleyite and ringwoodite. Phase identification is thus the first outcome of the process. The phase map is shown on Figure 1b. The main phase represented is wadsleyite, which represents 62.2% of the thin section. Wadsleyite also exhibits coarser grains. In the FIB section studies, some wadsleyite grains reach 4–6 µm, whereas grains of ringwoodite are in the range 0.6–2 µm. Figure 1c,d shows the inverse pole figures (IPF) of wadsleyite and ringwoodite respectively. One can already notice on those figures that the color is not completely uniform in each grain. This is more visible on ringwoodite. Slight color changes on the IPF are due to intragranular misorientations, resulting from the population of dislocations inside the grains, which are further analyzed below.

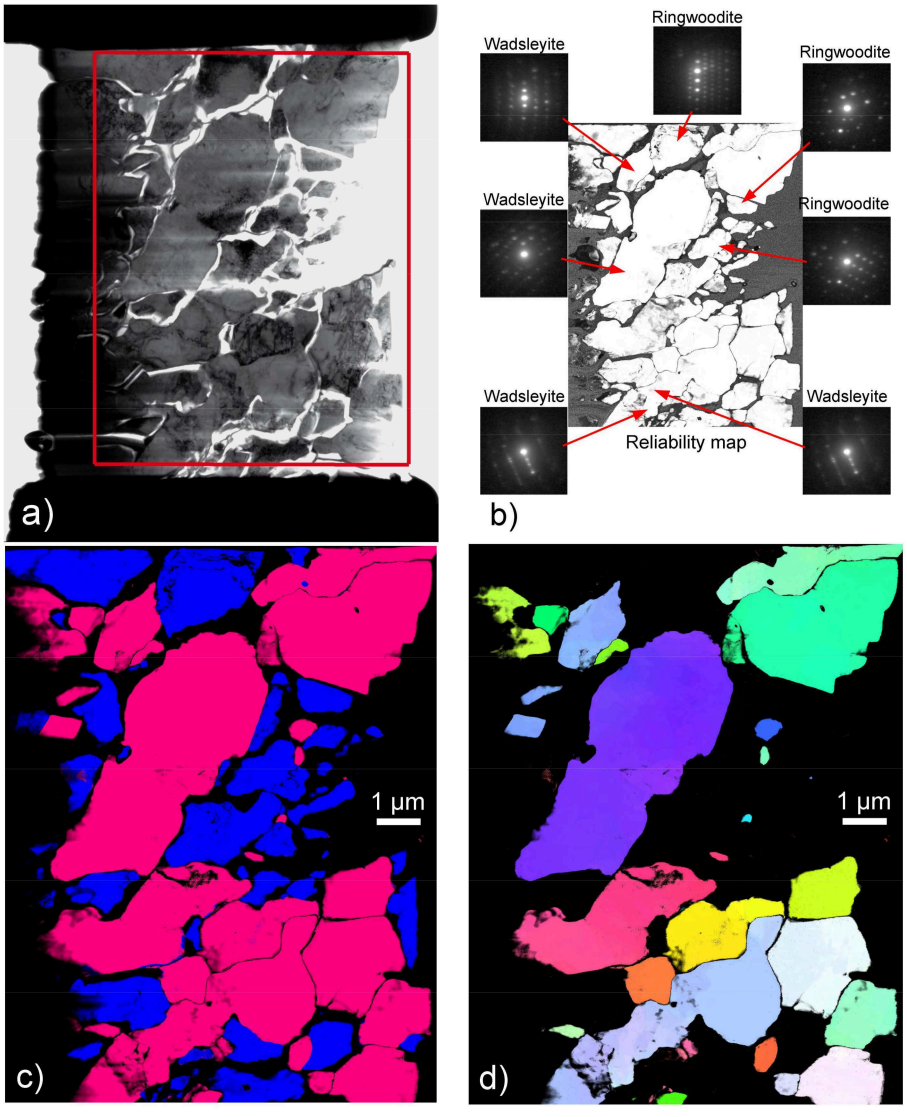

Figure 1. *Cont.*

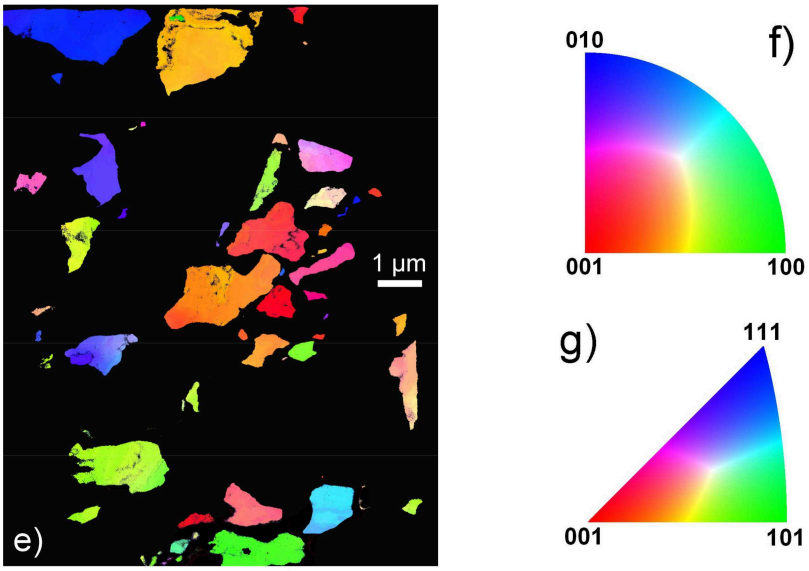

Figure 1. (**a**) General view of the FIB section. The compression direction is vertical; the scanned area (2200 × 2500 grid points) is represented by a red rectangle; (**b**) Reliability map (greyscale between 0 and 61) showing the quality of indexation (see text and Equation (2)), with some examples of diffraction patterns attached; (**c**) Phase map: wadsleyite is in red and ringwoodite is in blue; (**d**) Inverse pole figure (direction normal to the plane of representation) of wadsleyite (color code in **f**); (**e**) Inverse pole figure (direction normal to the plane of representation) of ringwoodite (color code in **g**); (**f**) Color code for the crystallographic orientations of the IPF in wadsleyite indexed within the *Imma* space group; (**g**) Color code for the crystallographic orientations of the IPF in ringwoodite indexed within the *Fd*3*m* space group.

4. Discussion

To emphasize the intragranular misorientations, we applied several post-treatments of the IPF maps which are displayed in Figure 2. Figure 2a,b show the grain orientation spreadings (GOS) of wadsleyite and ringwoodite respectively. This representation gives each grain a uniform color describing the range of misorientation within the grain. One can readily see that almost all grains exhibit significant intragranular misorientations resulting from plastic deformation. It is, however, difficult to exploit this data to compare grains with different sizes, since the GOS is intrinsically grain size dependent. The GROD (Figure 2c,d) allows us to visualize how intragranular misorientations organize themselves spatially within the grains. It represents a potential means to study how plasticity transfers from one grain to another in response to grain to grain interactions (see for instance [21] for a theoretical description of such heterogeneities resulting from plastic strain): see as illustration the strain concentration in-between the two large wadsleyite grains on top of Figure 2c (white arrow). It also gives interesting clues about the processes taking place in the materials. For instance, one can see in Figure 2c a curved boundary separating two parts of a grain of wadsleyite (black arrowed on Figure 2c) which exhibit a misorientation of 6°; this is a subgrain boundary (SGB). It is striking that, across the SGB, very distinct GROD values are observed. The part on the left is almost free of dislocations (see Figure 3, where this part has been imaged by weak-beam dark-field), whereas the part on the right exhibits a high amount of internal misorientation, as shown by the GROD. This grain is thus experiencing recovery by SGB migration, driven by the difference of stored elastic energy well highlighted by the GROD. Indeed, the center of curvature of the SGB (which gives the sense of motion) is located in the part characterized by highest GROD.

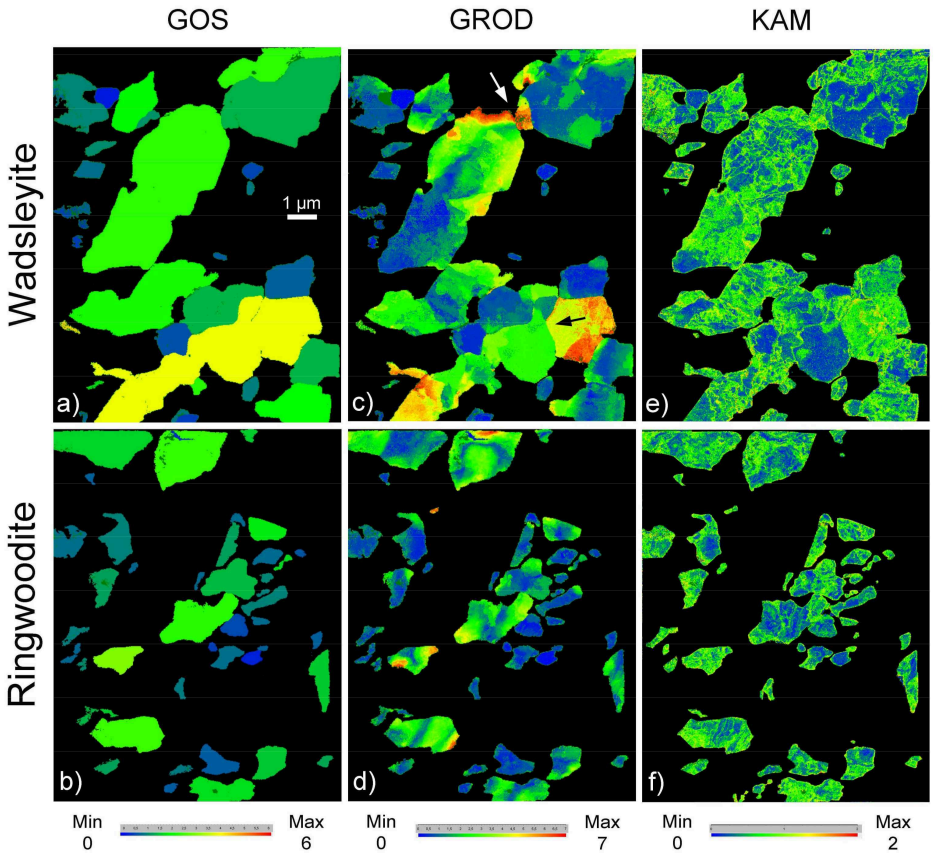

Figure 2. GOS in wadsleyite (**a**) and ringwoodite (grain tolerance angle 15°; minimum area grain size 100 pixels) (**b**); GROD in wadsleyite (**c**) and ringwoodite (**d**); KAM (3rd nearest-neighbor) in wadsleyite (**e**) and ringwoodite (**f**).

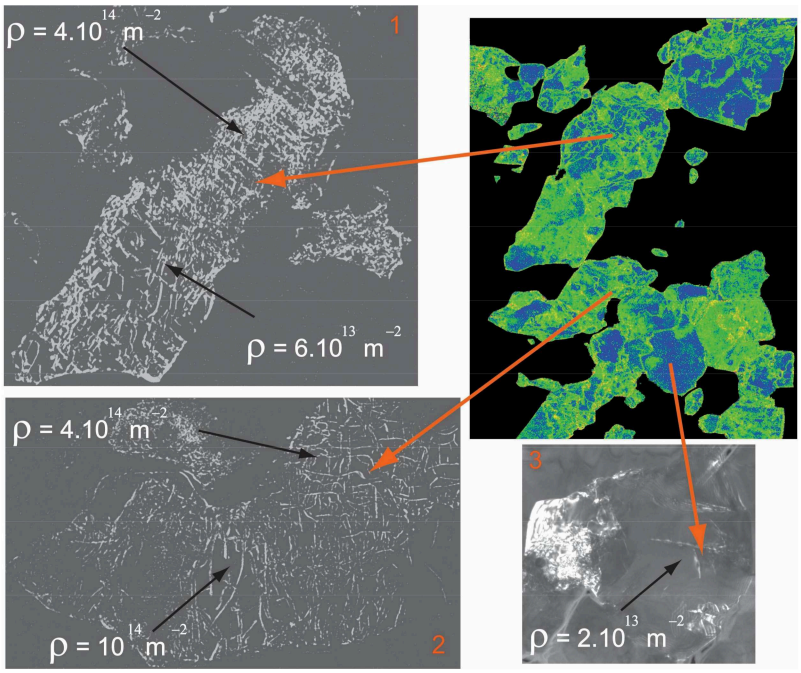

Figure 3. Weak-beam dark field images and dislocation density counts (using the method of [22]) in three grains of wadsleyite located on the KAM map of Figure 2e. Diffraction vectors: for 1, g: 440; for 2, g: 400 and for 3, g: 112.

In EBSD, the angular resolution is such that accurate measurements of geometrically necessary dislocation (GNDs) densities are now possible [23,24]. So far, applications have been mostly shown to apply to metals after severe deformation. The situation is not so favorable in SPED. The actual quantitative determination of dislocation density is indeed facing the angular resolution of SPED which, in a standard mode, is lower than in EBSD. Ghamarian et al. [13] discuss this issue and report that the minimum resolvable GND density relates to the angular resolution and to the step size:

$$\rho_{min}^{GND} = \frac{\text{angular resolution (rad)}}{\text{step size} \times \text{Burge}'\text{s vector length}} \quad (3)$$

With an angular resolution of 0.5° and our step size (5 nm), the minimum dislocation density resolvable would be in the order of 3×10^{15} m^{-2} (in wadsleyite, which is under examination here, the Burgers vectors lengths are 0.569 nm for [100] dislocations and 0.761 nm for $\frac{1}{2}\langle 111 \rangle$ dislocations). We have conducted conventional weak-beam dark-field investigations of some grains of wadsleyite. The results are presented in Figure 3. The dislocation densities measured are in the order of 10^{14} m^{-2}, i.e., slightly below the threshold found from Equation (3). It is also worthy of mention that such measurements face the somehow artificial (or at least experimentally constrained) distinction between geometrically necessary dislocations (GNDs) and statistically stored dislocations (SSDs). In SPED, the spatial resolution is close overcoming this limitation, as shown recently by Rottmann and Hemker [25], who demonstrated that strains from individual dislocations could be mapped. Here, we decide to stay at the level of the KAM mapping. Rollett et al. [26] have shown that local gradients in orientation revealed by the KAM correlate well with plastic strain heterogeneities modeled in the framework of crystal plasticity theory.

Figure 3 shows that if the correlation between KAM maps and images of dislocations patterns is not sufficient to resolve individual dislocations and provide reliable quantitative measurements, the agreement is fair. Note that the KAM map (Figure 2e) also shows the plastic strain gradient driving the mobility of the SGB discussed above. We propose that the KAM represents a proxy of plastic strain which can be used to compare strains in different grains. In a previous study performed on an aggregate of bridgmanite and ferropericlase [14], we avoided making such comparisons, since the two phases were undergoing very different deformation mechanisms (dense shear lamellae for bridgmanite, and homogeneous dislocation glide for ferropericlase). Here, wadsleyite and ringwoodite both deform by dislocation glide, and exhibit very comparable dislocation microstructures. Their Burgers vectors also present comparable lengths, which should not induce any differential bias in the detection (Equation (1)). The results are presented in Figure 4. Beyond 0.8°, the KAM distributions are similar for both phases. For lower misorientations, the curves are slightly different with those of ringwoodite, exhibiting a log-normal profile (whereas the wadsleyite shows a distinct peak at 0.2°).

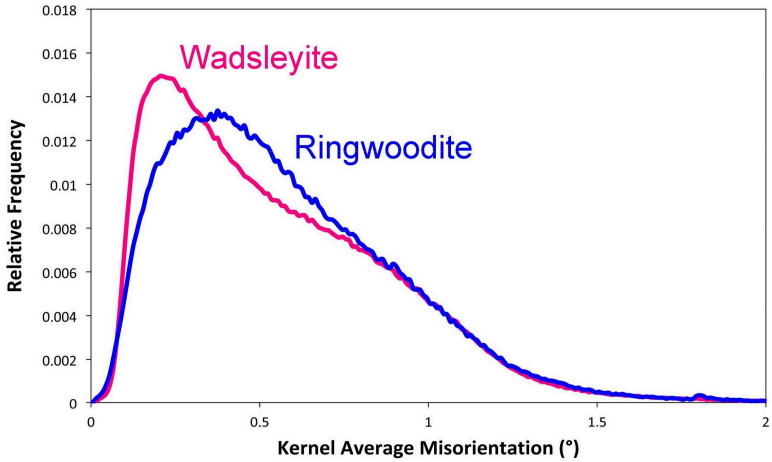

Figure 4. KAM distributions (3rd nearest-neighbor) in wadsleyite and ringwoodite.

The difference between the two minerals is illustrated in Figure 5. In Figure 5a, we show the KAM distributions samples in two regions located on both sides of the SGB already mentioned. The KAM distributions of those two regions reproduce the peaks of the global distribution. We propose that the peculiar shape of the KAM distribution of wadsleyite reflects activation of recovery driven by SGB migration. Apparently, this mechanism is not activated in ringwoodite. One might not exclude the possibility that the difference in behavior is related to the smaller grain size of ringwoodite grains. However, we raise the possibility that this is due to the fact that ringwoodite, being cubic, activates many slip systems with non-perpendicular Burgers vectors, which give rise to profuse interactions (junctions), leading to a dislocation storage which is less favorable to the formation and migration of SGBs.

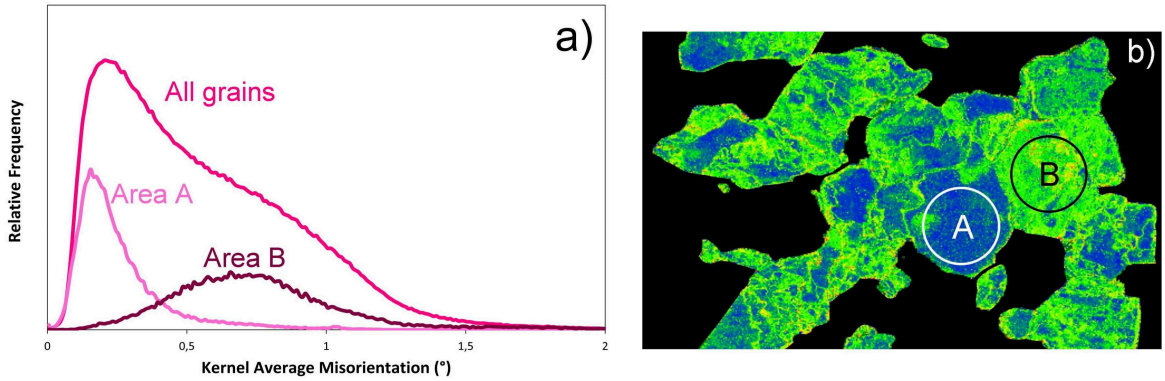

Figure 5. (**a**) KAM distributions (3rd nearest-neighbor) in two subsets A and B located on the KAM map (**b**) extracted from Figure 2e.

5. Conclusions

As previously shown with bridgmanite and ferropericlase [14], we present here a new demonstration that SPED is well adapted to the study of plastic deformation of mantle phases deformed at high-pressure and high-temperature. This is made possible thanks to the short acquisition time at each probe location which preserves beam-sensitive phases. The spot patterns of SPED are also very robust against highly deformed materials, and the technique is well suited to characterize highly deformed phases with dislocation densities which become challenging for standard weak-beam dark-field characterizations. Hence, we suggest that SPED represents an interesting means of studying samples deformed at high-pressure, even without coupling with a synchrotron beamline. Considering the limited availability of synchrotron access, this might open interesting perspectives for high-pressure deformation facilities. Moreover, we show here that even for studies carried out at the synchrotron, SPED can provide complementary information.

In the present case, where the plastic behavior of wadsleyite and ringwoodite at 17.3 GPa, 1700 K was studied, we find no significant contrast in the plastic response of both phases, except that recovery by subgrain boundary migration seems to be more easily activated in wadsleyite.

Acknowledgments: This work was supported by funding from the European Research Council under the Seventh Framework Programme (FP7), ERC grant No. 290424—RheoMan to P. Cordier. The TEM facility in Lille (France) is supported by the Conseil Regional du Nord-Pas de Calais, and the European Regional Development Fund (ERDF). The deformation experiment was supported by the power user program of SPring-8. We acknowledge the DFG for funding of the FIB facility in Bayreuth (grant INST 91/315-1 FUGG).

Author Contributions: P.C. and A.M. conceived the study; T.K. performed the experiments; B.C.N., S.T., A.M., P.C. and N.M. performed TEM studies; S.T. analyzed the data with B.C.N. and J.B.; All authors discussed and interpreted the results. P.C. wrote the paper with contributions of all authors.

Conflicts of Interest: The authors declare no conflict of interest. The founding sponsors had no role in the design of the study; in the collection, analyses, or interpretation of data; in the writing of the manuscript, and in the decision to publish the results.

References

1. Mitrovica, J.X.; Forte, A.M. A new inference of mantle viscosity based upon joint inversion of convection and glacial isostatic adjustment data. *Earth Planet. Sci. Lett.* **2004**, *225*, 177–189. [CrossRef]
2. Liu, X.; Zhong, S. Constraining mantle viscosity structure for a thermochemical mantle using the geoid observation. *Geochem. Geophys. Geosyst.* **2016**, *17*, 895–913. [CrossRef]
3. Fukao, Y.; Obayashi, M.; Nakakuki, T.; the Deep Slab Project Group. Stagnant Slab: A Review. *Annu. Rev. Earth Planet. Sci.* **2009**, *37*, 19–46. [CrossRef]
4. Yamazaki, D.; Karato, S. High-pressure rotational deformation apparatus to 15 GPa. *Rev. Sci. Instrum.* **2001**, *72*, 4207. [CrossRef]
5. Wang, Y.; Durham, W.B.; Getting, I.C.; Weidner, D.J. The deformation-DIA: A new apparatus for high temperature triaxial deformation to pressures up to 15 GPa. *Rev. Sci. Instrum.* **2003**, *74*, 3002. [CrossRef]
6. Kawazoe, T.; Karato, S.-I.; Ando, J.-I.; Jing, Z.; Otsuka, K.; Hustoft, J.W. Shear deformation of polycrystalline wadsleyite up to 2100 K at 14–17GPa using a rotational Drickamer apparatus (RDA). *J. Geophys. Res.* **2010**, *115*, B08208. [CrossRef]
7. Kawazoe, T.; Nishihara, Y.; Ohuchi, T.; Nishiyama, N.; Higo, Y.; Funakoshi, K.; Irifune, T. In situ stress–strain measurements in a deformation–DIA apparatus at P–T conditions of the upper part of the mantle transition zone. *Am. Mineral.* **2011**, *96*, 1665–1672. [CrossRef]
8. Nishiyama, N.; Wang, Y.; Uchida, T.; Irifune, T.; Rivers, M.L.; Sutton, S.R. Pressure and strain dependence of the strength of sintered polycrystalline Mg_2SiO_4 ringwoodite. *Geophys. Res. Lett.* **2005**, *32*, L04307. [CrossRef]
9. Miyagi, L.; Amulele, G.; Otsuka, K.; Du, Z.; Farla, R.; Karato, S.-I. Plastic anisotropy and slip systems in ringwoodite deformed to high shear strain in the Rotational Drickamer Apparatus. *Phys. Earth Planet. Inter.* **2014**, *228*, 244–253. [CrossRef]
10. Kawazoe, T.; Nishihara, Y.; Ohuchi, T.; Miyajima, N.; Maruyama, G.; Higod, Y.; Funakoshi, K.; Irifune, T. Creep strength of ringwoodite measured at pressure–temperature conditions of the lower part of mantle transition zone using a deformation–DIA apparatus. *Earth Planet. Sci. Lett.* **2016**, *454*, 10–19. [CrossRef]
11. Hughes, D.A.; Liu, Q.; Chrzan, D.C.; Hansen, N. Scaling of microstructural parameters: Misorientations of deformed induced boundaries. *Acta Mater.* **1997**, *45*, 105–112. [CrossRef]
12. Hughes, D.A.; Liu, Q.; Chrzan, D.C.; Hansen, N. Scaling of misorientation distributions. *Phys. Rev. Lett.* **1998**, *81*, 4664–4667. [CrossRef]
13. Ghamarian, I.; Liu, Y.; Samimi, P.; Collins, P.C. Development and application of a novel precession electron diffraction technique to quantify and map deformation structures in highly deformed materials—As applied to ultrafine-grained titanium. *Acta Mater.* **2014**, *79*, 203–215. [CrossRef]
14. Nzogang, B.C.; Bouquerel, J.; Cordier, P.; Mussi, A.; Girard, J.; Karato, S. Characterization by scanning precession electron diffraction of an aggregate of bridgmanite and ferropericlase deformed at HP-HT. *Geochem. Geophys. Geosyst.* **2018**, *19*. [CrossRef]
15. Rauch, E.F.; Véron, M. Automated crystal orientation and phase mapping in TEM. *Mater. Charact.* **2014**, *98*, 1–9. [CrossRef]
16. Horiuchi, H.; Sawamoto, H. Beta-Mg_2SiO_4: Single-crystal X-ray diffraction study. *Am. Mineral.* **1981**, *66*, 568–575.
17. Hazen, R.M.; Downs, R.T.; Finger, L.W. Crystal chemistry of ferromagnesian silicate spinels: Evidence for Mg-Si disorder. *Am. Mineral.* **1993**, *78*, 1320–1323.
18. Rauch, E.F.; Dupuy, L. Rapid spot diffraction patterns identification through template matching. *Arch. Metal. Mater.* **2005**, *50*, 87–99.
19. Wright, S.I.; Nowell, M.M.; Field, D.P. A review of strain analysis using electron backscatter diffraction. *Microsc. Microanal.* **2011**, *17*, 316–329. [CrossRef] [PubMed]
20. Godfrey, A.; Cao, W.Q.; Liu, Q.; Hansen, N. Stored energy, microstructure, and flow stress of deformed metals. *Metal. Mater. Trans. A* **2005**, *36*, 2371–2378. [CrossRef]
21. Barbe, F.; Forest, S.; Cailletaud, G. Intergranular and intragranular behavior of polycrystalline aggregates. Part 2: Results. *Int. J. Plast.* **2001**, *17*, 537–563. [CrossRef]
22. Ham, R.K. The determination of dislocation densities in thin films. *Philos. Mag.* **1961**, *6*, 1183–1184. [CrossRef]
23. Littlewood, P.D.; Wilkinson, A.J. Geometrically necessary dislocation density distributions in cyclically deformed Ti–6Al–4V. *Acta Mater.* **2012**, *201260*, 5516–5525. [CrossRef]

24. Zhu, C.; Harrington, T.; Livescu, V.; Gray, G.T., III; Vecchio, K.S. Determination of geometrically necessary dislocations in large shear strain localization in aluminum. *Acta Mater.* **2016**, *118*, e383–e394. [CrossRef]
25. Rottmann, P.F.; Hemker, K.J. Nanoscale elastic strain mapping of polycrystalline materials. *Mater. Res. Lett.* **2018**, *6*, 249–254. [CrossRef]
26. Rollett, A.D.; Wagner, F.; Allain-Bonasso, N.; Field, D.P.; Lebensohn, R.A. Comparison of Gradients in Orientation and Stress between Experiment and Simulation. *Mater. Sci. Forum* **2012**, *702*, 463–468. [CrossRef]

III.4 Evidences microstructurales de migration de joints et de sous-joints de grains dans l'olivine. Recristallisation.

III.4.1 Contexte

Le rôle des joints de grains dans la plasticité des minéraux est encore assez peu compris. Cette question a fait l'objet de plusieurs études ces dernières années dans le cas de l'olivine. Elle se pose en effet de manière particulièrement saillante dans le cas de ce minéral de structure orthorhombique qui ne possède pas assez de systèmes de glissement pour assurer la déformation homogène d'un agrégat polycristallins. Récemment, plusieurs études ont suggéré que le glissement aux joints de grains pouvait apporter une contribution significative à la plasticité de l'olivine (Hansen et al., 2011). Dans un récent article en cours de publication dans American Mineralogist, Caroline Bollinger présente des évidences microstructurales de mobilité aux joints de grains (Bollinger et al., 2019).

Nous avons décidé, avec elle, d'entreprendre une caractérisation d'échantillons d'olivine fortement déformés (25 et 40% de déformation respectivement voir Table 3-1) à 1373 K. Ces échantillons présentent des densités de dislocations qui peuvent être assez élevées rendant les caractérisations en contraste de diffraction difficiles. Une observation préliminaire d'un de ces échantillons à l'aide de la technique de cartographie d'orientation (reproduite ci-dessous) avait montré l'intérêt potentiel de cette approche.

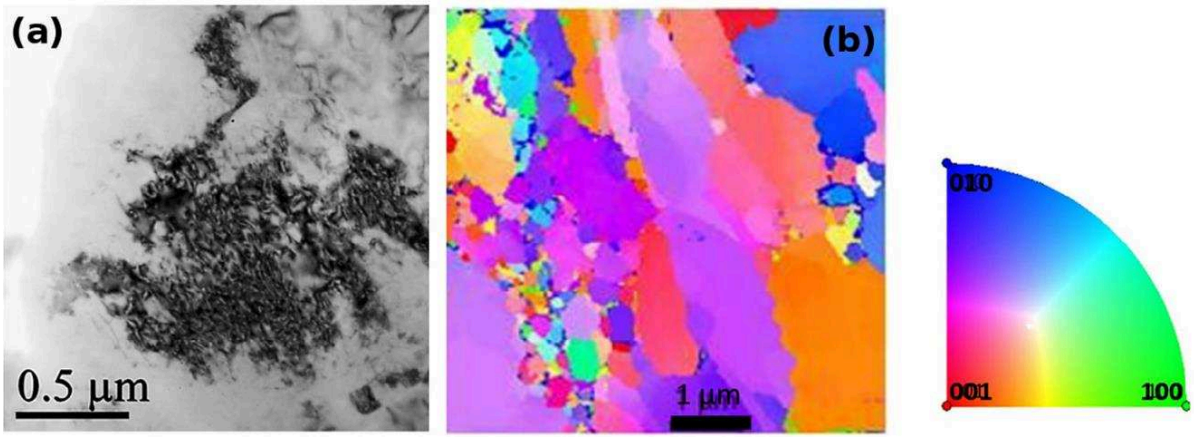

Figure 3-1: For70B (1373 K, 3,7 GPa, et 40% de taux de déformation). a) : Champ clair ; la très forte densité de défauts ne permet pas d'avoir un aperçu de la microstructure. b) figure de pôle inverse décrivant l'orientation des grains dans la direction perpendiculaire au plan observation.

Nos observations ont mis en évidence de nombreuses structures très hors-équilibre de joints et de sous-joints caractérisées par d'importantes sinuosités. Sous l'influence de la tension de surface, ces

courbures représentent une force motrice pour la migration dont nous montrons l'importance. Une autre force motrice résulte du contraste d'énergie élastique emmagasinée de part et d'autre des parois que les gradients de désorientation permettent de révéler. Ces observations nous ont conduits à proposer que la migration de sous-joints de grains soit un mécanisme de restauration actif dans ces échantillons très déformés. Nous mettons en évidence également des microstructures de recristallisation pour lesquelles nous fournissons, ce qui est à notre connaissance les premières évidences microstructurales des mécanismes de formation des nouveaux grains dans la forstérite. Nous suggérons également le rôle possible de la migration des sous-joints dans cette nucléation.

Echantillon	**Déformation (%)**	**Température (K)**	**Pression GPa)**	**Vitesse de déformation (10^{-5} s^{-1})**
For70B	40	1373	3,1	4,5
M642	25	1373	3,5	5,0

Table 3-1: Résumé des conditions de déformation des deux échantillons

III.4.2 Article

Ces résultats sont décrits dans l'article qui est reproduit dans les pages qui suivent :

C. Bollinger, B.C. Nzogang, A. Mussi & P. Cordier (2019) Microstructural evidence for grain boundary migration in experimentally deformed forsterite aggregates. Minerals, 9(1), 17 https://doi.org/10.3390/min9010017

minerals

MDPI

Article

Microstructural Evidence for Grain Boundary Migration and Dynamic Recrystallization in Experimentally Deformed Forsterite Aggregates

Caroline Bollinger [1,2,*], Billy C. Nzogang [3], Alexandre Mussi [3], Jérémie Bouquerel [3], Dmitri A. Molodov [4] and Patrick Cordier [3]

1 Bayerisches Geoinstitut, Universität Bayreuth, D-95445 Bayreuth, Germany
2 Department of Earth and Planetary Sciences, Washington University in Saint Louis, Saint Louis, MO 63117, USA
3 University of Lille, CNRS, INRA, ENSCL, UMR 8207-UMET-Unité Matériaux et Transformations, F-59000 Lille, France; billy-clitton.nzogang@univ-lille.fr (B.C.N.); alexandre.mussi@univ-lille.fr (A.M.); jeremie.bouquerel@univ-lille.fr (J.B.); patrick.cordier@univ-lille.fr (P.C.)
4 Institute of Physical Metallurgy and Metal Physics, RWTH Aachen University, 52074 Aachen, Germany; Molodov@imm.rwth-aachen.de
* Correspondence: c.bollinger@email.wustl.edu

Received: 21 October 2018; Accepted: 21 December 2018; Published: 27 December 2018

Abstract: Plastic deformation of peridotites in the mantle involves large strains. Orthorhombic olivine does not have enough slip systems to satisfy the von Mises criterion, leading to strong hardening when polycrystals are deformed at rather low temperatures (i.e., below 1200 °C). In this study, we focused on the recovery mechanisms involving grain boundaries and recrystallization. We investigated forsterite samples deformed at large strains at 1100 °C. The deformed microstructures were characterized by transmission electron microscopy using orientation mapping techniques (ACOM-TEM). With this technique, we increased the spatial resolution of characterization compared to standard electron backscatter diffraction (EBSD) maps to further decipher the microstructures at nanoscale. After a plastic strain of 25%, we found pervasive evidence for serrated grain and subgrain boundaries. We interpreted these microstructural features as evidence of occurrences of grain boundary migration mechanisms. Evaluating the driving forces for grain/subgrain boundary motion, we found that the surface tension driving forces were often greater than the strain energy driving force. At larger strains (40%), we found pervasive evidence for discontinuous dynamic recrystallization (dDRX), with nucleation of new grains at grain boundaries. The observations reveal that subgrain migration and grain boundary bulging contribute to the nucleation of new grains. These mechanisms are probably critical to allow peridotitic rocks to achieve large strains under a steady-state regime in the lithospheric mantle.

Keywords: olivine; plastic deformation; ACOM-TEM; grain boundary migration; recrystallization; recovery

1. Introduction

As $(Mg, Fe)_2SiO_4$ olivine is the main constituent of the upper mantle, understanding its plastic behavior and deformation mechanisms is important in order to model the rheology of the mantle. From a mineral physics point of view, despite efforts by the research community for more than 50 years, a lot of questions remain unsolved. At a very fundamental level, olivine raises many questions. With only two slip directions, i.e., [100] and [001], this crystal structure does not exhibit enough slip systems to satisfy the von Mises–Taylor criterion [1,2], which states that five independent

slip systems are required to allow homogeneous grain-scale deformation of polycrystalline aggregates. Below ca. 1200 °C, laboratory deformation experiments on olivine rapidly show significant hardening due to the increase in the internal stored energy, which rapidly leads to brittle behavior [3]. Further deformation, especially under steady-state regime, is only possible if the microstructure can evolve to release this stored energy. Recrystallization is a general term that encompasses different mechanisms leading to such evolution of microstructures during deformation [4]. The formation of new grains is one of those mechanisms. Other recovery mechanisms involving dislocation annihilation (by cross-slip or climb) as well as grain boundary migration can also contribute.

Most studies on recrystallization in olivine have addressed its influence on crystal preferred orientations [5–8] and on grain size evolution [8–11]. Recently, Trepmann et al. [12] experimentally addressed the recrystallization of olivine following low-temperature (300–600 °C) deformation episodes followed by annealing at 700–1100 °C, showing some microstructural observations. They suggested that "recrystallization microstructures have a great diagnostic potential for past seismic activity because they are expected to be stable over geological timescales" (cf. p.1 in [12]). Karato et al. [13] showed that, at high temperatures (above 1500 °C), recrystallization can occur in single crystals, provided strains are large enough (40–60%). However, the number of studies documenting the microstructural evolutions of olivine during recrystallization are relatively scarce. The materials science literature [14,15] demonstrates that there is a large variety of mechanisms involved in recrystallization. Further microstructural investigations are thus needed so that reliable criteria can be used to decipher recrystallization processes in naturally deformed rocks.

In this paper, we present a microstructural characterization of forsterite samples that have been deformed to relatively large strains under conditions that promote a strong activity of intragranular deformation by dislocation activity. We used orientation mapping in transmission electron microscopy (TEM) to infer active recovery mechanisms using the morphology of grains, grain boundaries (GB), and determination of intracrystalline misorientations.

2. Materials and Methods

Experimental set up, data analysis, and results for sample For70B have been previously reported in [16–18] for sample M642. The following section is hence limited to the most relevant information regarding the present study.

2.1. Synthesis

2.1.1. Sample M642

Forsterite was synthesized from MgO (99.99% purity with 1.5 µm grain size) and SiO_2 (99.99% purity with ~150 µm grain size) oxide powders from ChemPur. MgO was added in excess to avoid the formation of enstatite during synthesis because MgO powders easily capture humidity from the air during the weighing. This mixture was then sintered in a furnace at 1500 °C for at least 12 h and crushed again. This procedure was repeated five times. The evolution to 100% forsterite was monitored with X-ray diffraction and confirmed later in the study. Once forsterite was formed, the excess MgO was removed using acetic acid at 10% at 60 °C (this process was repeated four times). The resulting forsterite powder was then sent to PNF2 (CIRIMAT, Toulouse, France) to be aggregated and densified by flash sintering [19]. This resulted in pellets that were 2 cm high and 4 cm in diameter.

2.1.2. Sample For70B

The forsterite starting material was prepared by crushing one gem-quality single crystal of Fo_{100} in an alumina mortar and grinded to a fine-grained powder at the optical scale (average grain size of ~10 µm). Forsterite powder was mixed with a small fraction (5 wt. %) of natural enstatite ($En_{84}Fs_{13}Wo_3$) powder [17] in order to buffer the orthopyroxenes (Opx) activity (a_{Opx} = 1) and limit grain growth during the runs. Oxygen fugacity (fO_2) was not controlled during the runs.

2.2. Deformation Experiments

A summary of the experimental conditions is given in Table 1.

Table 1. Conditions of deformation of the samples characterized in this study.

Run #	T (°C)	P (GPa)	$\dot{\varepsilon}$ (10^{-5} s^{-1})	ε (%)	Average Grain Size (μm)	Def.	Deformation Press	Reference Paper
M642	1100	3.5	5.0	~25	20–100	Pure shear	6-ram MAVO press, BGI, Bayreuth, Germany	[18]
For70B	1100	3.1	4.5	40	0.2–3.0	Uniaxial	D-DIA, NSLS, NY, USA	[17]

2.2.1. Sample M642

M642 was deformed within the six second-stage anvils in the six-ram MAVO press [20] at the Bayerisches GeoInstitut (Bayreuth, Germany). The pressurization occurred in approximately 60 min, followed by heating within 30 min by current injection controlled with the power supply. After reaching the pressure–temperature conditions, annealing was performed for ~30 min to let the system adjust before deformation. One pair of rams was then pushed forward by injecting oil at a rate corresponding to an applied strain rate of ~2×10^{-5} s^{-1}. Another pair of rams remained fixed as the last one was pushed backward in response to ensure a constant confining pressure while the sample was deformed in pure shear geometry. The applied pressure was 3.5 GPa with a temperature of 1100 °C. The power-controlled temperature was monitored using a thermocouple. After deformation, the sample was quenched by switching off the power, and pressure was released slowly for 18 h. The applied strain was 40%, corresponding to a deformation duration of 5 h. The measurement of the capsule after the deformation showed that the strain transmitted to the sample was ~25%.

2.2.2. Sample 70B

For70B was uniaxially deformed at 3.1 GPa, 1100 °C, and 4.5×10^{-5} s^{-1} to 40% strain (Table 1) in the deformation-DIA apparatus (D-DIA, [21,22] at the X17B2 beamline of the National Synchrotron Light Source (Upton, NY, USA). The deformation cell containing the forsterite powder was first pressurized at room temperature (T), then brought to high T. Annealing under hydrostatic conditions was performed for ~1 h to allow sintering of pistons and sample and relaxation of cold-compression stresses. Then, axisymmetric deformation was ensured by moving the D-DIA vertical anvils forward at a fixed rate until 5–10% strain was reached at a constant strain rate. At the end of the run, temperature was quenched by turning off the power supply, and both D-DIA vertical anvils were stopped. Pressure (P) was then released (for 1 to 2 h) to room pressure. To preserve specimen deformation microstructures during decompression, the specimen length was maintained constant by adjusting the vertical anvil positions. The grain size distribution in this highly deformed material was found to be bimodal. Grains with the size of 2–3 μm were surrounded by smaller grains with the sizes in the range of 0.2–0.5 μm.

2.3. Orientation Mapping in the Transmission Electron Microscope

After deformation, thin sections (~25 μm thick) from the central part of the deformed specimens were prepared for TEM. Thin slabs were cut and mechanically polished down to a thickness of about 30 μm. In order to reach electron transparency, the sample foils were Ar-ion sputtered with a Gatan® DuoMill™ model 600. Carbon films were deposited on the thin foils to ensure electron conduction. TEM investigations were performed at the university of Lille (France) with a FEI® Tecnai G220Twin microscope (FEI Company, Hillsboro, OR, USA) operating at 200 kV and a Philips CM30 microscope (PHILIPS, Amsterdam, The Netherlands) operating at 300 kV, both equipped with a LaB_6 filament and using a double tilt sample holder.

Automated crystal orientation mapping (ACOM-TEM) was operated in the TEM with the ASTAR™ tool from NanoMEGAS [23]. The TEM was set in microbeam mode (nominal spot size of ~6 nm without precession), and the incident electron beam, which was focused on the sample, was scanned over the area with a step size of 6 nm, thanks to a dedicated hardware control system of the TEM deflecting coils. In this mode, where the sample was illuminated by a convergent beam, the diffraction pattern consisted of discs. Using the smallest condenser aperture (50 µm), the diffraction patterns were made of very small spot-like discs and could be indexed as spot patterns. The individual exposure time at each location was 10–40 ms. In this study, we used precession illumination (with a precession angle of 0.5°–1.0°) in the TEM, which allowed many more reflections to be seen in the diffraction pattern with intensities closer to the kinematical diffraction conditions. Diffraction patterns were collected with an external Stingray CCD camera that was pointed on the TEM phosphorous screen, and they were then stored in the computer memory for further indexation and post-processing. The diffraction patterns were collected at 144 × 144 pixels at a camera length of 89–97 mm (chosen so as to optimize the diffraction pattern for indexation). In the ASTAR system (NanoMEGAS, Forest, Belgium), electron diffraction spot patterns are indexed (providing the local crystal orientations) by comparing individually obtained patterns via cross-correlation matching techniques with precalculated electron diffraction templates generated every 0.5° (orientation resolution). For forsterite, templates were generated from the crystallographic data of Birle et al. [24]. From this indexation, we obtained orientation maps that displayed, with color coding (indexed here within the *Pnma* space group), the most probable orientation at each scanned beam position.

The quality of indexation (IQ in the figures) from template matching was quantified by the image correlation index, which was calculated for every template [25]:

$$IQ(i) = \frac{\sum_{j=1}^{m} P(x_j, y_j) T_i(x_j, y_j)}{\sqrt{\sum_{j=1}^{m} P^2(x_j, y_j)} \sqrt{\sum_{j=1}^{m} T_i^2(x_j, y_j)}} \quad (1)$$

In this expression, the diffraction pattern is represented by the intensity function $P(x, y)$, and every template i is described by the function $T_i(x, y)$. The highest IQ value corresponds to the solution retained. The reliability of this solution can be quantified by the ratio of the matching indexes for the two best solutions IQ_1 and IQ_2:

$$R = 100\left(1 - \frac{IQ_1}{IQ_2}\right) \quad (2)$$

In reliability maps, the brighter the pixel (i.e., the higher the reliability index), the more reliable is the proposed indexation. In contrast, the darker the pixel, the less reliable is the solution. This is typically the case at GB, where two solutions of coexisting grains overlap, or when, for some reasons, the quality of the diffraction patterns is decreased.

The orientation dataset was a square-shaped grid with ASTAR, and it was transformed to channel text file (.ctf) to process the datasets using MTEX (free and open source MATLAB R2014b Toolbox (MathWorks, Natick, MA, USA) [26]. Grain boundaries were identified where the misorientation to the next pixel was higher than 15° [27]. Groups of pixels below a size of 10 points were ignored. To be able to detect deformation details in the microstructure, one must use other tools in addition to the inverse pole figure (IPF) color-coding. In this study, we used orientation maps to calculate local misorientations as developed recently by the electron backscatter diffraction (EBSD) community (e.g., [28]). As commonly used in EBSD, several quantities can be calculated from the orientation maps:

- The kernel average misorientation (KAM) calculates the average misorientation between a pixel and its neighbors, provided that the misorientation does not exceed a predefined threshold value (e.g., 5°, which is the value chosen here for all figures). Hence, the incorporation of well-defined GB is avoided. A kernel is a set of points of prescribed size surrounding the scan point of interest. The size of the kernel is generally prescribed to the nth nearest neighbors. Hence, this parameter is sensitive to the step size of the measurement grid. If plastic deformation results from dislocation

glide and crystal lattice rotation, this approach allows quantitative evaluation of the local plastic strain gradients [29]. KAM is consequently used as a proxy of the local plastic strain.

- The grain orientation spread (GOS) is the average deviation in orientation between each point in a grain and the average orientation of the grain. This approach leads to assigning the same value of the GOS to every scan point contained within a grain.
- The grain reference orientation deviation (GROD) is based on the misorientation between a reference point of that grain and the other points. The reference point can be the mean misorientation of the grain (in this case and in MTEX, the GROD is called the Mis2Mean, as referred in this paper) or the point of the grain where the KAM is the lowest.

KAM, Mis2mean, and GOS approaches are complementary.

3. Results

It is first worth mentioning that the samples chosen for this study corresponded to rather large strains. For70B was deformed up to 40%. As deformation was performed in situ on a synchrotron beamline, the strain could be followed up and measured accurately in situ during deformation. M642 was not deformed at a beamline, and the plastic strain of 25% measured ex situ (Table 1) was an estimation from the measurement of the sample length in the capsule after deformation. In such samples, the dislocation density can be quite high and can give rise to multiple diffraction contrasts, which makes observation difficult on the TEM (Figure 1a). Here, we present an alternative approach based on scanning precession electron diffraction (SPED), which allows the orientation maps to be recorded with high resolution (6 nm in the present case). This technique has already been used by us to characterize highly deformed specimens from high-pressure experiments [30,31]. In those studies, we had shown that the microdiffraction spot patterns were very robust against the defect microstructure and that high-quality orientation maps could be obtained on deformed samples. In this study, the microstructure was imaged with this technique (Figure 1), allowing us to obtain information about intragranular misorientations.

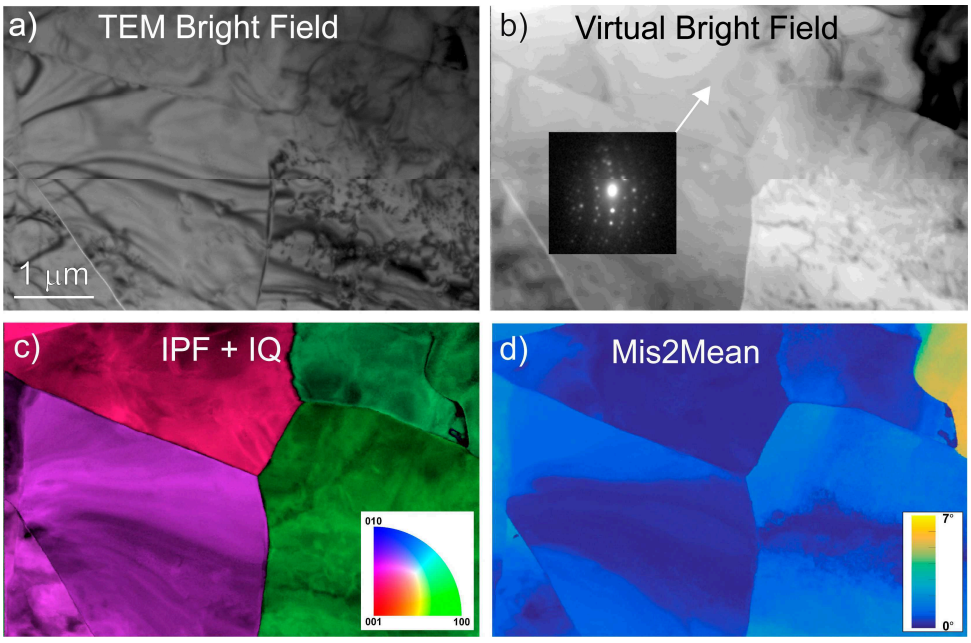

Figure 1. M642. (**a**) Conventional multibeam transmission electron microscopy (TEM) bright field. (**b**) Virtual bright field of the same area reconstructed from the intensity of the transmitted beams of the scanning precession electron diffraction (SPED) dataset (an example of a diffraction pattern acquired is presented). (**c**) Inverse pole figure (IPF) corresponding to the horizontal direction superimposed with the quality of indexation (IQ) (Equation (1)); color code inserted (*Pnma*). (**d**) Mis2Mean map, up to 7°.

Examples of the grain microstructure in M642 characterized by numerous subgrain/low-angle boundaries (SGB) with very curvy shapes are shown in Figures 2 and 3. On the IPF (orientation maps in Figures 2a and 3a), the single color corresponds to a single orientation and hence to a single grain each. However slight changes of colors in a grain indicate local misorientations, which correspond to SGBs (indicated by arrows in Figures 2 and 3). A better visualization is obtained from the Mis2Mean maps, which enhances the contrast of intragranular misorientations (Figures 2b and 3b).

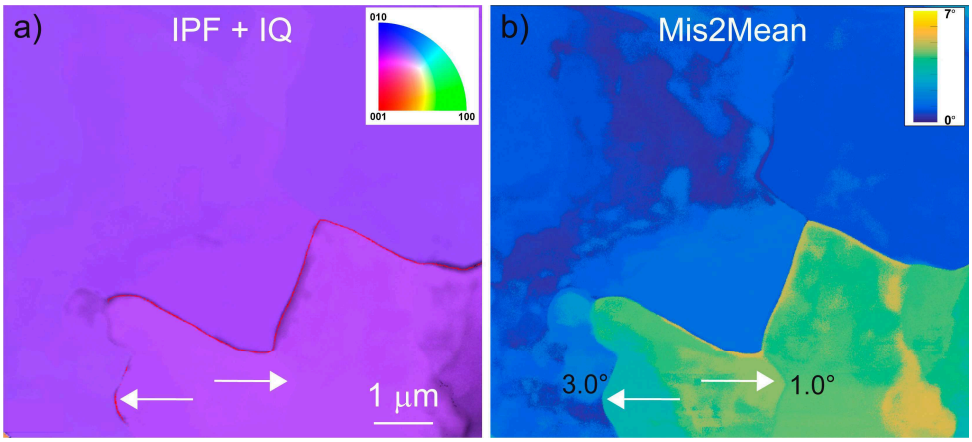

Figure 2. M642 subgrain boundaries (SGB; indicated by white arrows). (**a**) IPF corresponding to the direction perpendicular to the plane of view superimposed with the IQ (Equation (1)); color code inserted (*Pnma*). The subgrain boundary is highlighted by a red line. (**b**) Mis2Mean map corresponding to (**a**), up to 7°. Misorientation angles are indicated next to the boundary arrows.

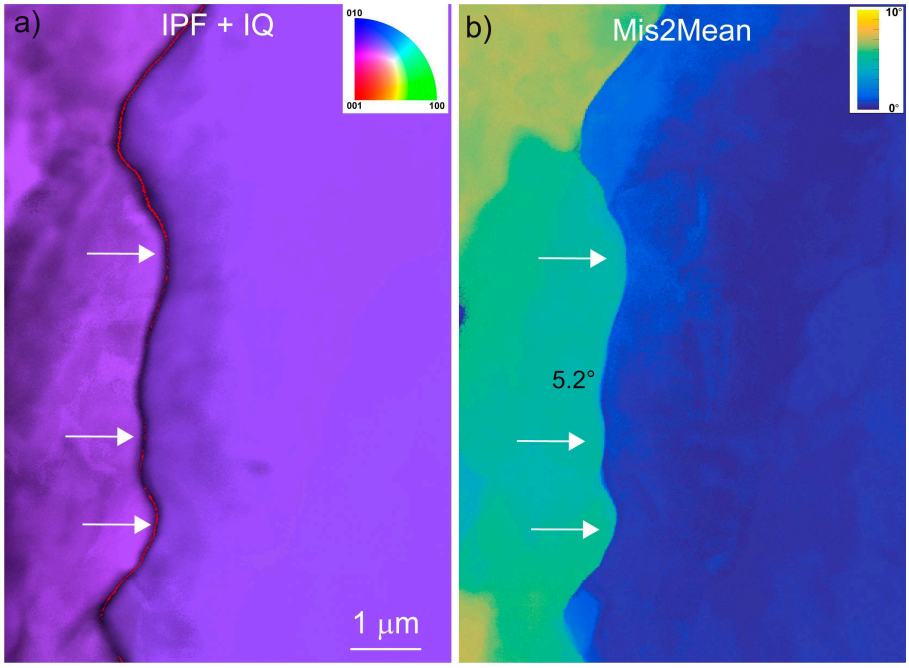

Figure 3. M642 SGB (indicated by white arrows). (**a**) IPF corresponding to the direction perpendicular to the plane of view superimposed with the IQ (Equation (1)); color code inserted (*Pnma*). White arrows point to a SGB (highlighted by a red line) with a misorientation of 5.2°. (**b**) Mis2Mean map corresponding to (**a**), up to 10°.

A curved SGB (arrows in white) and a high angle (90°) grain boundary (arrows in black), which exhibited serration with a much smaller length scale, are presented in Figure 4. This observation

was not unique as many other examples of curved GBs were found in M642. Another example of a curved high-angle GB is shown in Figure 5.

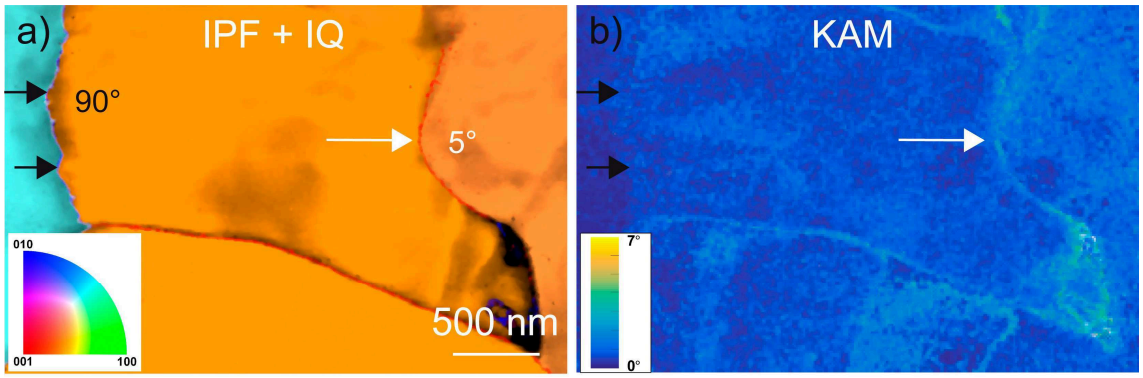

Figure 4. M642 SGB (arrows in white) and GB (arrows in black). (**a**) IPF corresponding to the direction normal to the plane of representation, superimposed with the IQ (Equation (1)); color code inserted (*Pnma*). The SGB arrow in white has a misorientation of 5°, and the GB arrow in black has a misorientation of 90°. (**b**) Kernel average misorientation (KAM) map corresponding to (**a**), up to 7°.

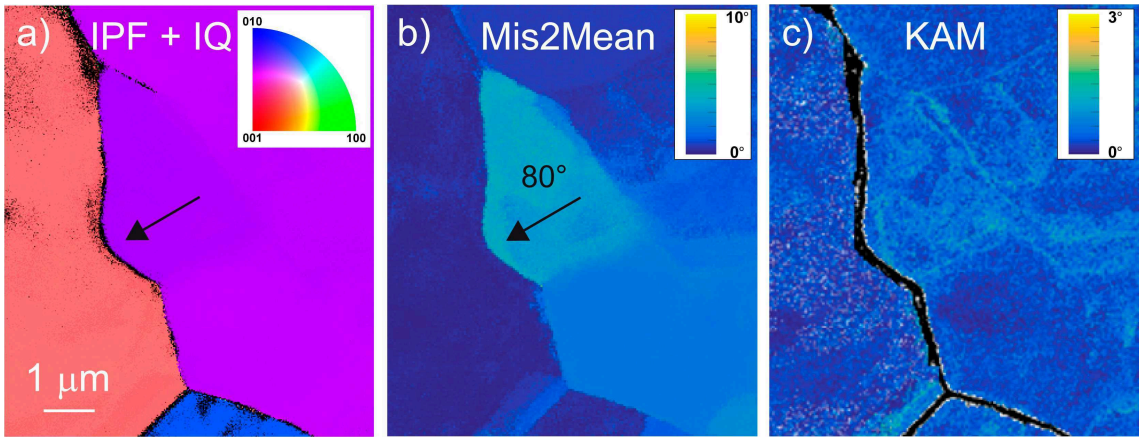

Figure 5. M642 GB. (**a**) IPF corresponding to the direction perpendicular to the plane of view superimposed with the IQ (Equation (1)); color code inserted (*Pnma*). The GB arrow in black has a misorientation of 80°. (**b**) Mis2Mean map corresponding to (**a**), up to 10 °. (**c**) KAM map corresponding to (**a**), up to 3°.

Sample For70B was more strained than M642 (40% strain versus 25%, respectively, as shown in Table 1), with a significantly different microstructure. The characteristic dislocation density was of the order of 10^{15} m^{-2} in For70B, while it was close to 10^{13} m^{-2} in M642 (values obtained from TEM measurement using the method of Ham [32]). However, pervasive occurrences of curved GBs and SGBs were still observed. Several examples can be seen in Figures 6–8. A region where a curved grain boundary (60° misorientation) encloses a domain with a highest GROD, leading to the formation of a low-angle SGB (in red), is presented in Figure 8.

In addition, we found a lot of evidence for recrystallization in this sample (Figures 9 and 10). New grains were found to nucleate at GBs, forming necklaces. The newly nucleated grains generally exhibited rather low GOS values, although some of them started to present some evidence for intragranular deformation (dislocations). To further establish the origin of those grains and decipher the mechanism responsible for the formation of those new grains, we compared their orientations with those of the parent grains (Figure 10c–e).

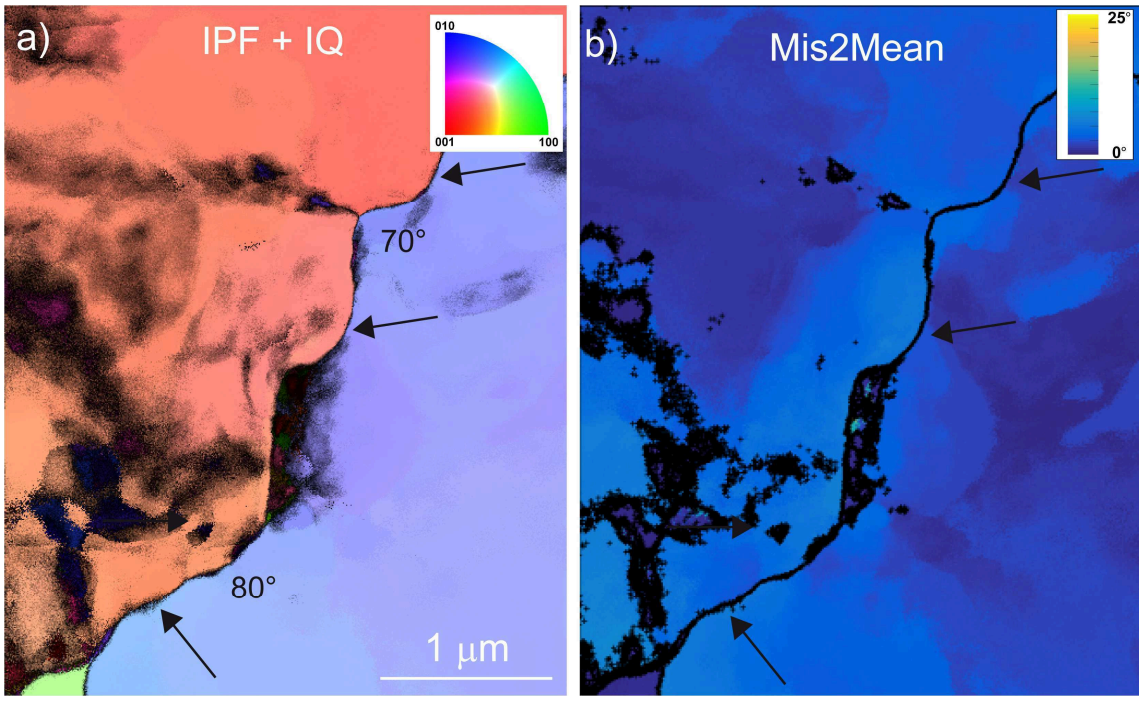

Figure 6. For70B GB. (**a**) IPF corresponding to the direction perpendicular to the plane of view superimposed with the IQ (Equation (1)); color code inserted (*Pnma*). The GB arrow in black has a misorientation of 70°–80°. (**b**) Mis2Mean map corresponding to (**a**), up to 25°.

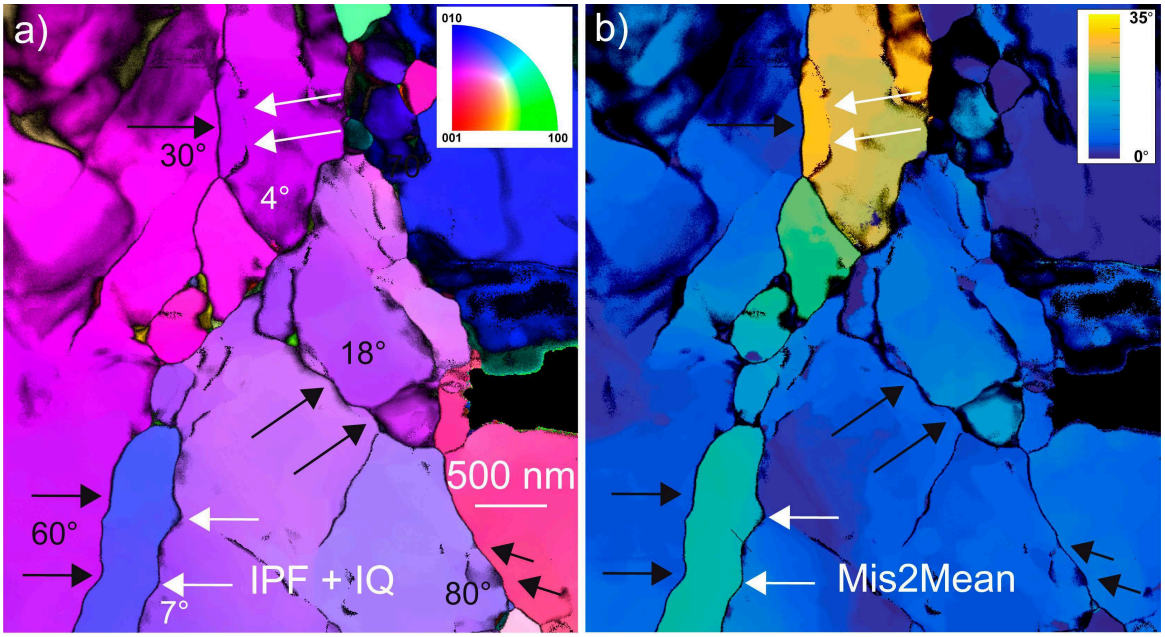

Figure 7. For70B GB (arrows in black), SGB (arrows in white), and small grains. (**a**) IPF corresponding to the direction perpendicular to the plane of view superimposed with the IQ (Equation (1)); color code inserted (*Pnma*). The misorientation of some boundaries are indicated next to them. (**b**) Mis2Mean map corresponding to (**a**), up to 35°.

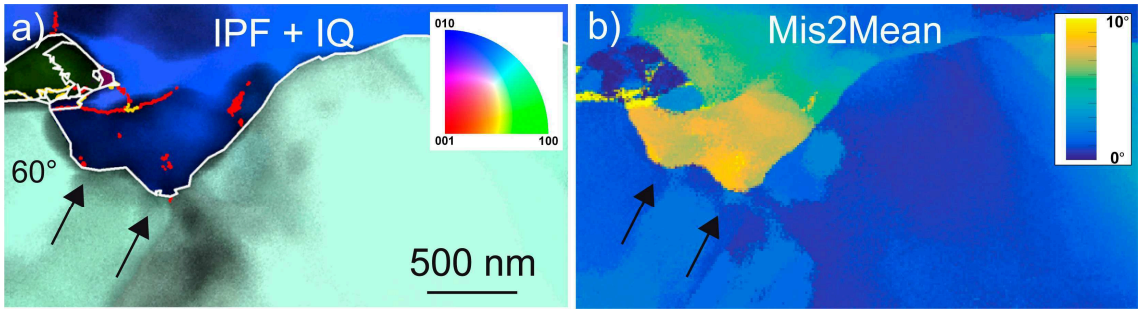

Figure 8. For70B GB bulging. (**a**) IPF corresponding to the direction perpendicular to the plane of view superimposed with the IQ (Equation (1)); color code inserted (*Pnma*). The GB arrowed in black (and highlighted by a white line) has a misorientation of 60°. The SGB in formation is highlighted by a red line. (**b**) Mis2Mean map corresponding to (**a**), up to 10 °.

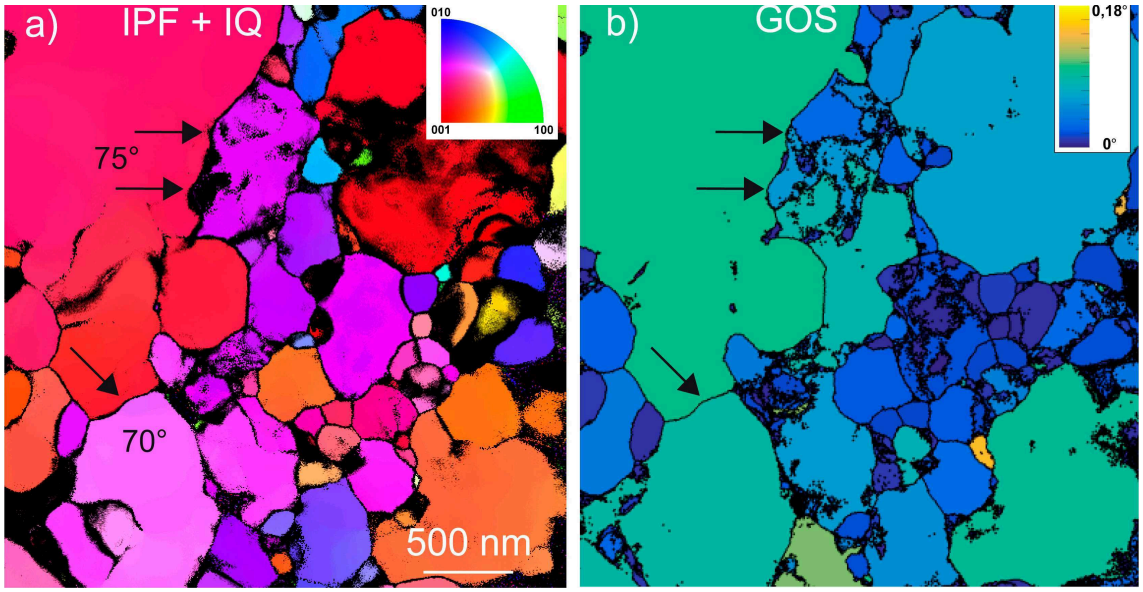

Figure 9. For70B small grains. (**a**) IPF corresponding to the direction perpendicular to the plane of view superimposed with the IQ (Equation (1)); color code inserted (*Pnma*). The misorientation of some boundaries (arrowed in black) are indicated next to them. (**b**) Grain orientation spread (GOS) map corresponding to (**a**).

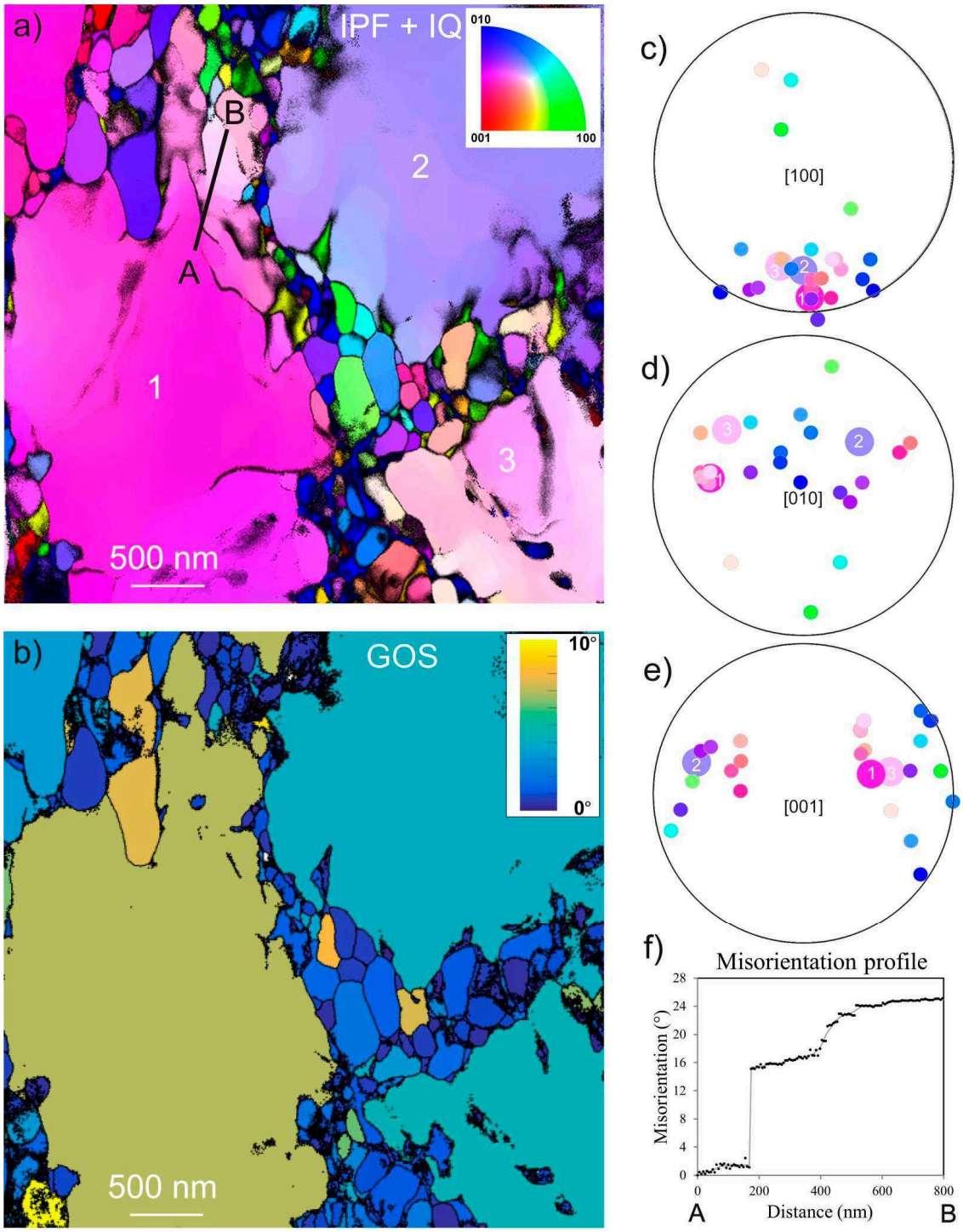

Figure 10. For70B small grains. (**a**) IPF corresponding to the direction perpendicular to the plane of view superimposed with the IQ (Equation (1)); color code inserted (*Pnma*). (**b**) GOS map corresponding to (**a**). (**c**–**e**) Orientations of the recrystallized grains (color coded as in (**a**)) compared to those of the parent grains (labeled 1, 2, and 3 as in (**a**)). (**f**) Misorientation profile along the segment A–B displayed in (**a**).

4. Discussion

The samples characterized here were highly strained at 1100 °C. Hence, they exhibited deformation microstructure with high dislocation density. After ca. 25% strain (M642), the dislocation density was in the order of 10^{13} m^{-2}, which raised no particular problems for TEM observation.

After 40% strain, the dislocation density reached 10^{15} m^{-2}, which rendered TEM characterization more difficult because dislocation contrasts strongly overlap [17]. In this study, we used orientation maps obtained from ACOM-TEM, which is not very much affected by large dislocation densities. We focused our attention on grain and subgrain morphologies as well as on the formation of new grains to shed some light on the recovery and recrystallization mechanisms.

We observed that recrystallization involving the formation of new grains occurred in forsterite aggregates deformed at 1100 °C at 3.0–3.5 GPa confining pressure and a strain rate of ~5×10^{-5} s^{-1} after large strains. Indeed, recrystallized grains were abundant in For70B deformed up to 40% and much less common in M642 deformed up to 25%. The recrystallization origin for the small grains was suggested from their morphology (forming necklaces between highly deformed grains), from their orientations close to the surrounding grains as well as from their rather low internal strains. Trepmann et al. [12] observed microstructures comparable to ours, with necklaces of new grains mostly formed at GB. This suggests that, in olivine, discontinuous dynamic recrystallization (dDRX) dominates, as opposed to continuous dynamic recrystallization (cDRX), where new grains arise from the continuous increase in misorientation due to the continuous accumulation of dislocations in SGBs [15]. It is worth noting that, in dDRX, new grains, originally free of dislocations, nucleate at site of high-strain energy and orientation gradients, most often grain boundaries [14]. Meanwhile, in cDRX, "dislocations organize themselves into low-angle boundaries, leading to formation of subgrains (polygonization). Continuous dislocation accumulation results in progressive increase in the misorientation at the low-angle boundaries, which evolve into high-angle boundaries" [33].

However, the formation of new grains is not the only mechanism involved in dynamic recrystallization; the migration of grain boundaries is another important mechanism [4]. In olivine, this mechanism has been mostly documented at higher temperatures from the mechanical point of view and from rheological data analysis, with only few microstructural evidences reported. Indeed, performing static annealing experiments in olivine at 1240–1500°C, Toriumi [34] determined the average GB migration rates. Lee et al. [6] found clear evidence for modifications of crystal preferred orientations (CPO) by grain boundary migration in samples deformed in simple shear geometry in the temperature range of 1200–1300 °C. Later, Boneh et al. [8] described the effect of annealing at 1 GPa, 1250 °C, on a Fo50 olivine aggregate, which was previously deformed in torsion at a confining pressure of 0.3 GPa and 1200 °C in a Paterson apparatus. From the grain size evolution, they calculated a mean grain boundary mobility of 6.6×10^{-16} $m^3/N{\cdot}s$ at 1250 °C (a value that can be compared to 2×10^{-15} $m^3/N{\cdot}s$, which was the grain mobility value found by Cooper and Kohlstedt [35] during secondary recrystallization after sintering at 1300–1400 °C). The shape of boundaries is usually the main source of post mortem information about grain boundary migration processes. In some cases, fractal analysis has been employed to quantify the serration of GB [36] and to correlate it to the strain rate or temperature. The curvature of boundaries is the most widely used morphological feature to infer GB mobility, especially in naturally deformed rocks [37–39]. Some examples of this can be observed in Figure 11. It is well known that GBs are nonequilibrium defects, and application of any equilibrium thermodynamics must always be done with care (see a careful discussion of these aspects in Gottstein and Shvindlerman [40]). Still, a GB or a SGB are characterized by their surface tension γ, and any increase in the surface area of the boundary will result in an increase in the Gibbs energy of the system. The SGBs observed in Figures 2 and 3 can then hardly be interpreted as recovery features in the sense of dislocations rearranging into SGBs so as to minimize stored strain energy; this is because SGBs have lower long-range stress fields than isolated dislocations. In the absence of strong anisotropy of surface tension, an equilibrium shape of SGBs would correspond to a zero Laplace curvature. In contrast, (S)GB curvature results in a driving force to straighten the boundary. If this driving force is responsible for boundary migration, the boundary is expected to move toward its center of curvature [40,41]. However, in deformed samples, the boundary surface tension is not the only source of driving force for grain boundary motion. During DRX, another driving force comes from the reduction in elastically stored energy, which is strongly controlled by the density

of dislocations. When observing curved SGBs, one can thus expect them to delimitate subgrains with different elastically stored energies. In metallurgy, that strain energy is usually considered the dominant driving force. To a first order and within a mean field approximation, the driving pressure due to stored dislocation produced by the plastic strain $P_{\varepsilon_{plast}}$ can be evaluated from the dislocation density through the following relation [14,40]:

$$P_{\varepsilon_{plast}} = \frac{1}{2}\mu b^2(\rho(\varepsilon) - \rho_0) \approx \frac{1}{2}\mu b^2 \rho(\varepsilon) \quad (3)$$

where $\rho(\varepsilon)$ is the dislocation density caused by the plastic strain (compared to ρ_0, which describes the undeformed state); μ is the shear modulus (65 GPa for olivine); and b the modulus of the Burgers vector (either 4.75 Å for [100] dislocations or 5.97 Å for [001] dislocations in olivine). With a dislocation density of the order of 10^{13} m^{-2}, this gives an order of magnitude for the driving force arising from stored strain energy of 0.1 MPa. For a dislocation density of 10^{15} m^{-2}, this driving force is of the order of 10 MPa (this is an upper bound because, in most cases, a boundary will separate domains that both contain dislocations). This can be compared with the surface tension/curvature driving force. The driving pressure due to boundary energy is given as follows:

$$P_\gamma = \frac{2\gamma}{R} \quad (4)$$

where γ is the surface energy of (sub)grain boundaries, and R is the local radius of curvature of the boundary. This driving force can be evaluated by utilizing the results of the work by Duyster and Stökhert [42]. According to their study, for high-angle GB, the boundary energy amounts to about 1.4 $J{\cdot}m^{-2}$. For subgrain/low-angle boundaries, this value depends, of course, on the misorientation angle. This is ca. 0.5 $J{\cdot}m^{-2}$ when the misorientation is 5° and increases up to ca. 1.3 $J{\cdot}m^{-2}$ when the misorientation reaches 10°. The important parameter, however, is the length scale of boundary bending. The observations presented in the present paper were made using TEM, with a spatial resolution much higher than in EBSD. In Figure 2, for instance, the radius of curvature of the SGB arrows was in the range of 200–500 nm, which led to a surface tension driving force of slightly greater that 2 MPa. Similar values (1–3 MPa) were obtained for the SGB presented in Figures 3 and 4. In Figure 4, it can be seen that the 90° GB exhibited undulations with very short radii of curvature (40–50 nm), leading to higher tension driving force (up to ca. 60 MPa). In Figure 5, the radius of curvature of the 80° grain boundary (200 nm) corresponded to a driving force of the order of 15 MPa. The first conclusion of this analysis is that, in samples deformed at relatively large strains (25–40%) at 1100 °C, GB surface tension represents a major, and probably dominant, driving force for GB migration. In this study, we used the KAM to visualize the local intragranular misorientations gradients as a proxy for the strain energy. Indeed, we can see in Figures 4 and 5 that the boundaries separated domains with contrasting strain energies. Interestingly, in these figures, we can observe that the concave side of the curved boundaries corresponded to a high elastically stored energy. This means that both driving forces (surface tension and strain energies) were acting together in the same direction. Although our observations are static and performed post mortem on deformed samples, we think that they provide convincing evidence that SGB migration is an active process in forsterite deformed at 1100 °C and large strains and that SGB morphology (serrated boundaries) is a good indicator for this process.

Furthermore, we can see a significant evolution between the two samples, i.e., as a function of strain. In M642 (25% strain), GB migration seems to be the major recovery/softening process. Evidence for this mechanism can also be observed in For70B deformed to a higher extent (40%). However, another mechanism involving the formation of new, undeformed grains is now very active.

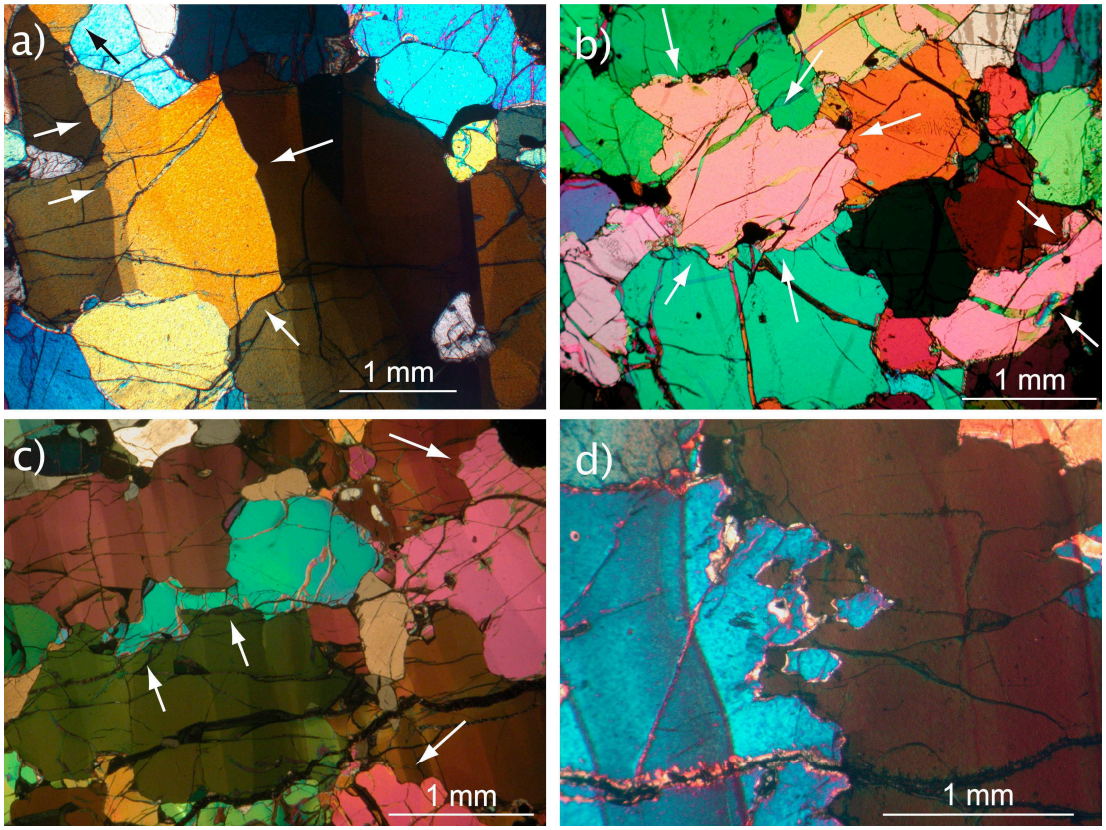

Figure 11. Evidence for GB and SGB migration and GB bulging in natural samples (arrows). (**a**) Olivine grains within a coarse porphyroclastic harzburgite (ET72, see [39]) shown with well-developed (100) SGB and very sinuous GB; courtesy A. Tommasi. (**b**) Olivine grains in a dunite from French Polynesia (RP6, see [38]); courtesy A. Tommasi. (**c**) Olivine grains in a harzburgite from French Polynesia (RPA18A, see [38]); courtesy A. Tommasi. (**d**) Evidence for GB bulging in olivine within a peridotite from a Labait volcano xenolith (Tanzania, [37]); courtesy A. Vauchez.

In copper, Miura and co-workers [43] showed how GB serration resulting from migration could assist nucleation of new grains and recrystallization. In that study, bulging followed by local boundary migration was accompanied by twinning, resulting in a small domain being the nucleus of a new grain. A similar mechanism was observed in ice [44], where, in the absence of twinning, formation of a SGB at the edges of the bulged part of the GB was the mechanism to close the domain. We found evidence for this mechanism in For70B, as illustrated in Figure 8. Here, a 60° GB bulged, leaving behind a misoriented domain that started to close through the formation of a SGB. The bulging mechanism is thus a potential mechanism to account for the nucleation of recrystallized grains. One way to test this hypothesis is to look at the relative misorientation between the recrystallized and the parent grains [44]. Unlike nucleation, which is likely to produce random texture (unless there are some preferential epitaxial relationships), the bulging mechanism is expected to yield orientations that cluster around the parent orientations because new grains are formed by continuous misorientations of domains of the parent grains. The new grain orientations are always in the vicinity of the parent ones, although it is not always the same orientation, which is the closest (Figure 10c–e). However, an alternative mechanism to bulging is suggested with Figure 10. At the top of grain 1, one can see a series of SGB, which locally produced a significant misorientation (along the short segment AB, the misorientation amplitude was 24°). On this observation, we can speculate that, upon further deformation, these misoriented domains could evolve to new grains. We did observe that, in our samples, SGB migration was a very active mechanism. We suggest that when these SGBs pile up at GB, they build up misoriented domains that leads to the formation of new grains as in the case of bulging.

Observation of naturally deformed olivine-rich rocks shows microstructures that are very similar to ours (Figure 11). One can observe much evidence of sinuous GB and interpenetrating olivine–olivine GB, indicating active grain boundary migration [37–39]. Only the length scales are different due to the differences in strain rates and stresses between natural and experimental deformation conditions. We thus conclude that the recovery and recrystallization mechanism evidenced in this study on forsterite also operate in olivine under natural conditions.

5. Conclusions

In this study, using orientation mapping of highly deformed forsterite samples, we carried out a detailed microstructural investigation using ACOM-TEM, which shed new light on the recovery and recrystallization mechanisms in forsterite. At the resolution of the TEM, we found pervasive evidence for wavy (S)GBs with radii of curvature less than a micron, which we interpreted as an indication of boundary migration being an active recovery mechanism. At larger strains (40% in our experimental conditions), we observed ubiquitous dDRX, which resulted from the formation of new, undeformed grains at GBs. The new grains did not exhibit random orientations; rather, they clustered in the vicinity of the orientations of the parent grains, supporting bulging as a potential formation mechanism. Indeed, we found some configurations supporting this hypothesis. However, there were other observations that support an alternative nucleation mechanism based on the accumulation of migrating SGBs at GBs. Thus, some questions remain unanswered. Grain boundary sliding is often invoked as a source of high strain gradients at the GBs. Microstructural evidence for sliding at GBs have indeed been reported in olivine, either deformed in the diffusion creep regime [45,46] or in the dislocation creep regime [18]. However, in the present post mortem study, we did not have a marker to confirm or dismiss the possible contribution of GBs in the nucleation of new grains.

We suggest that the recovery and recrystallization mechanism evidenced in this study on forsterite may also operate in olivine under natural conditions, given comparable observations have been made in naturally deformed olivine-rich rocks samples [37,38], which support our conclusions.

Author Contributions: C.B. and P.C. conceived the study; C.B. performed the deformation experiments; B.C.N., A.M., and P.C. performed TEM studies; B.C.N. and C.B. analyzed the data. All authors discussed and interpreted the results. C.B. and P.C. wrote the paper with contribution from all authors.

Acknowledgments: This work in Lille (France) was supported by funding from the European Research Council under the Seventh Framework Programme (FP7), ERC grant N°290424–RheoMan to P. Cordier. The TEM facility in Lille was supported by the Conseil Regional du Nord-Pas de Calais, and the European Regional Development Fund (ERDF). The deformation of sample M642 at the Bayerisches GeoInstitut was supported by the German Alexander von Humboldt Foundation and the Free State of Bavaria.

Conflicts of Interest: The authors declare no conflict of interest.

References

1. Von Mises, R.V. Mechanik der plastischen Formänderung von Kristallen. *Z. Angew. Math. Mech.* **1928**, *8*, 161–185. [CrossRef]
2. Taylor, G.I. Plastic strain in metals. *J. Inst. Met.* **1938**, *62*, 307–324.
3. Demouchy, S.; Mussi, A.; Barou, F.; Tommasi, A.; Cordier, P. Viscoplasticity of polycrystalline olivine experimentally deformed at high pressure and 900 °C. *Tectonophysics* **2014**, *623*, 123–135. [CrossRef]
4. Drury, M.R.; Urai, J.L. Deformation-related recrystallization processes. *Tectonophysics* **1990**, *3–4*, 235–253. [CrossRef]
5. Wenk, H.R.; Tomé, C.N. Modeling dynamic recrystallization of olivine aggregates deformed in simple shear. *J. Geophys. Res.* **1999**, *104*, 25513–25527. [CrossRef]
6. Lee, K.-H.; Jiang, Z.; Karato, S.-I. A scanning electron microscope study of the effects of dynamic recrystallization on lattice preferred orientation in olivine. *Tectonophysics* **2002**, *351*, 331–341. [CrossRef]
7. Falus, G.; Tommasi, A.; Soustelle, V. The effect of dynamic recrystallization on olivine crystal preferred orientations in mantle xenoliths deformed under varied stress conditions. *J. Struct. Geol.* **2011**, *33*, 1528–1540. [CrossRef]

8. Boneh, Y.; Wallis, D.; Hansen, L.N.; Krawczynski, M.J.; Skemer, P. Oriented grain growth and modification of 'frozen anisotropy' in the lithospheric mantle. *Earth Planet. Sci. Lett.* **2017**, *474*, 368–374. [CrossRef]
9. Austin, N.J.; Evans, B. Paleowattmeters: A scaling relation for dynamically recrystallized grain size. *Geology* **2007**, *35*, 343–346. [CrossRef]
10. Ricard, Y.; Bercovici, D. A continuum theory of grain size evolution and damage. *J. Geophys. Res.* **2009**, *114*, B01204. [CrossRef]
11. Rozel, A.; Ricard, Y.; Bercovici, D. A thermodynamically self-consistent damage equation for grain size evolution during dynamic recrystallization. *Geophys. J. Int.* **2011**, *184*, 719–728. [CrossRef]
12. Trepmann, C.A.; Renner, J.; Druiventak, A. Experimental deformation and recrystallization of olivine–processes and timescales of damage healing during postseismic relaxation at mantle depths. *Solid Earth* **2013**, *4*, 423–450. [CrossRef]
13. Karato, S.; Toriumi, M.; Fuji, T. Dynamic recrystallization of olivine single crystals during high-temperature creep. *Geophys. Res. Lett.* **1980**, *7*, 649–652. [CrossRef]
14. Humphreys, F.J.; Hatherly, M. *Recrystallization and Related Annealing Phenomena*, 2nd ed.; Elsevier: Oxford, UK, 2004; pp. xxi–xxii, ISBN 9780080441641.
15. Sakai, T.; Belyakov, A.; Kaibyshev, R.; Miura, H.; Jonas, J.J. Dynamic and post-dynamic recrystallization under hot, cold and severe plastic deformation conditions. *Prog. Mater. Sci.* **2014**, *60*, 130–207. [CrossRef]
16. Bollinger, C.; Raterron, P.; Cordier, P.; Merkel, S. Polycrystalline olivine rheology in dislocation creep: Revisiting experimental data to 8.1 GPa. *Phys. Earth Planet. Inter.* **2014**, *228*, 211–219. [CrossRef]
17. Bollinger, C.; Merkel, S.; Cordier, P.; Raterron, P. Deformation of forsterite polycrystals at mantle pressure: Comparison with Fe-bearing olivine and the effect of iron on its plasticity. *Phys. Earth Planet. Inter.* **2015**, *240*, 95–104. [CrossRef]
18. Bollinger, C.; Marquardt, K.; Ferreira, F. Intragranular plasticity vs. grain boundary sliding (GBS) in forsterite: Microstructural evidence at high pressures (3.5–5.0 GPa). *Am. Min.* **2018**. [CrossRef]
19. Guignard, J.; Bystricky, M.; Béjina, F. Dense fine-grained aggregates prepared by spark plasma sintering (SPS), an original technique in experimental petrology. *Eur. J. Mineral.* **2011**, *23*, 323–331. [CrossRef]
20. Manthilake, M.A.G.M.; Walter, N.; Frost, D.J. A new multi-anvil press employing six independently acting 8 MN hydraulic rams. *High. Press. Res.* **2012**, *32*, 195–207. [CrossRef]
21. Durham, W.B.; Weidner, D.J.; Karato, S.I.; Wang, Y. New developments in deformation experiments at high pressure. *Rev. Mineral. Geochem.* **2002**, *51*, 21–49. [CrossRef]
22. Wang, Y.; Durham, W.B.; Getting, I.C.; Weidner, D.J. The deformation-DIA: A new apparatus for high temperature triaxial deformation to pressures up to 15 GPa. *Rev. Sci. Instrum.* **2003**, *74*, 3002–3011. [CrossRef]
23. Rauch, E.F.; Véron, M. Automated crystal orientation and phase mapping in TEM. *Mater. Charact.* **2014**, *98*, 1–9. [CrossRef]
24. Birle, J.D.; Gibbs, G.V.; Moore, P.B.; Smith, J.V. Crystal structures of natural olivines. *Am. Mineral.* **1968**, *53*, 807–824.
25. Rauch, E.F.; Dupuy, L. Rapid diffraction patterns identification through template matching. *Arch. Metall. Mater.* **2005**, *50*, 87–99.
26. Hielscher, R.; Schaeben, H. A novel pole figure inversion method: Specification of the MTEX algorithm. *J. Appl. Cryst.* **2008**, *41*, 1024–1037. [CrossRef]
27. Bachmann, F.; Hielscher, R.; Schaeben, H. Grain detection from 2d and 3d EBSD data–Specification of the MTEX algorithm. *Ultramicroscopy* **2011**, *111*, 1720–1733. [CrossRef] [PubMed]
28. Wright, S.I.; Nowell, M.M.; Field, D.P. A review of strain analysis using electron backscatter diffraction. *Microsc. Microanal.* **2011**, *17*, 316–329. [CrossRef]
29. Godfrey, A.; Cao, W.Q.; Hansen, N.; Liu, Q. Stored energy, microstructure, and flow stress of deformed metals. *Metall. Mater. Trans. A* **2005**, *36*, 2371–2378. [CrossRef]
30. Nzogang, B.C.; Bouquerel, J.; Cordier, P.; Mussi, A.; Girard, J.; Karato, S. Characterization by scanning precession electron diffraction of an aggregate of bridgmanite and ferropericlase deformed at HP-HT. *Geochem. Geophys. Geosyst.* **2018**, *19*, 582–594. [CrossRef]
31. Nzogang, B.C.; Thilliez, S.; Mussi, A.; Kawazoe, T.; Miyajima, N.; Bouquerel, J.; Cordier, P. Application of Scanning Precession Electron Diffraction in the Transmission Electron Microscope to the Characterization of Deformation in Wadsleyite and Ringwoodite. *Minerals* **2018**, *8*, 153. [CrossRef]
32. Ham, R.K. The determination of dislocation densities in thin films. *Philos. Mag.* **1961**, *6*, 1183–1184. [CrossRef]

33. Signorelli, J.; Tommasi, A. Modeling the effect of subgrain rotation recrystallization on the evolution of olivine crystal preferred orientations in simple shear. *Earth Planet. Sci. Lett.* **2015**, *430*, 356–366. [CrossRef]
34. Toriumi, M. Grain boundary migration in olivine at atmospheric pressure. *Phys. Earth Planet. Inter.* **1982**, *30*, 26–35. [CrossRef]
35. Cooper, R.F.; Kohlstedt, D.L. Sintering of olivine and olivine-basalt aggregates. *Phys. Chem. Miner.* **1984**, *11*, 5–16. [CrossRef]
36. Takahashi, M.; Nagahama, H.; Masuda, T.; Fujimura, A. Fractal analysis of experimentally, dynamically recrystallized quartz grains and its possible application as a strain rate meter. *J. Struct. Geol.* **1998**, *20*, 269–275. [CrossRef]
37. Vauchez, A.; Dineur, F.; Rudnick, R. Microstructure, texture and seismic anisotropy of the lithospheric mantle above a mantle plume: Insights from the Labait volcano xenoliths (Tanzania). *Earth Planet. Sci. Lett.* **2005**, *232*, 295–314. [CrossRef]
38. Tommasi, M.; Godard, M.; Coromina, G.; Dautria, J.M.; Barsczus, H. Seismic anisotropy and compositionally induced velocity anomalies in the lithosphere above mantle plumes: A petrological and microstructural study of mantle xenoliths from French Polynesia. *Earth Planet. Sci. Lett.* **2004**, *227*, 539–556. [CrossRef]
39. Tommasi, A.; Baptiste, V.; Vauchez, A.; Holtzman, B. Deformation, annealing, reactive melt percolation, and seismic anisotropy in the lithospheric mantle beneath the southeastern Ethiopian rift: Constraints from mantle xenoliths from Mega. *Tectonophysics* **2016**, *682*, 186–205. [CrossRef]
40. Gottstein, G.; Shvindlerman, L.S. *Grain Boundary Migration in Metals*, 2nd ed.; CRC Press, Taylor and Francis group: Boca Raton, FL, USA, 2010; p. 674. ISBN 978-1-4200-5436-1.
41. Mullins, W.W. Two-dimensional motion of idealized grain boundaries. *J. Appl. Phys.* **1956**, *27*, 900–904. [CrossRef]
42. Duyster, J.; Stöckhert, B. Grain boundaries energies in olivine derived from natural microstructures. *Contrib. Mineral. Petrol.* **2001**, *140*, 567–576. [CrossRef]
43. Miura, H.; Sakai, T.; Mogawa, R.; Jonas, J.J. Nucleation of dynamic recrystallization and variant selection in copper bicrystals. *Philos. Mag.* **2007**, *87*, 4197–4209. [CrossRef]
44. Chauve, T.; Montagnat, M.; Barou, F.; Hidas, K.; Tommasi, A.; Mainprice, D. Investigation of nucleation processes during dynamic recrystallization of ice using cryo-EBSD. *Philos. Trans. R. Soc. A* **2017**, 375. [CrossRef] [PubMed]
45. Maruyama, G.; Hiraga, T. Grain- to multiple-grain-scale deformation processes during diffusion creep of forsterite + diopside aggregate: 1. Direct observations. *J. Geophys. Res.* **2017**, *122*, 5890–5915. [CrossRef]
46. Maruyama, G.; Hiraga, T. Grain- to multiple-grain-scale deformation processes during diffusion creep of forsterite + diopside aggregate: 2. Grain boundary sliding-induced grain rotation and its role in crystallographic preferred orientation in rocks. *J. Geophys. Res.* **2017**, *122*, 5916–5934. [CrossRef]

III.5 Caractérisation des mécanismes de restauration par migration des joints et sous-joints de grains dans l'olivine déformée expérimentalement.

III.5.1 Contexte

L'article précédent ayant fait émerger l'idée de l'importance de la mobilité des (sous)joints de grains dans la restauration de l'olivine, nous avons décidé de reconsidérer les échantillons déformés par Manuel. Thieme. Dans sa thèse préparée à Géoscience Montpellier sous la direction de Sylvie. Demouchy, M. Thieme a conduit une série d'expériences de déformation de polycristaux d'olivine de San Carlos ($(Mg_{0.91}Fe_{0.09}Ni_{0.003})_2SiO_4$) en presse Paterson. Dans cette étude, dont les principaux résultats sont publiés dans Thieme et al. (2018), deux températures sont considérées : 1273 et 1473 K. Les courbes contrainte-déformation sont présentées figure 3.2. Nous pouvons constater qu'à 1273 K, les courbes montrent un durcissement important conduisant à la rupture après seulement 1% de déformation. A haute température, les échantillons sont clairement plus ductiles et tendent vers un état stationnaire vers 3% de déformation. Ces échantillons ont déjà donné lieu au préalable à une étude en MET à Lille afin de trouver une signature microstructurale permettant de rendre compte de ces comportements mécaniques si différents. En vain. Une des difficultés est liée à la forte hétérogénéité d'échantillons déformés à de très faibles taux au niveau macroscopique. Au niveau microscopique, on observe, dans les deux lots, des grains vierges de dislocations et des grains clairement déformés sans qu'il soit possible d'extraire une signature microstructurale distinctive. Dans l'article (Thieme et al., 2018), plusieurs hypothèses sont mises en avant sans aboutir à une conclusion. Nous avons donc décidé de reprendre cette étude en acquérant des cartes d'orientation et en portant notre attention sur la morphologie des joints. Les taux de déformation étant nettement plus faibles que dans Bollinger et al. (2019), les caractéristiques sont moins nettes, mais il apparait cependant clairement que dans les échantillons déformés à 1473 K, les joints sont moins rectilignes, morphologie que nous proposons de relayer à une mobilité activée, donc à de la restauration qui pourrait expliquer la ductilité observée.

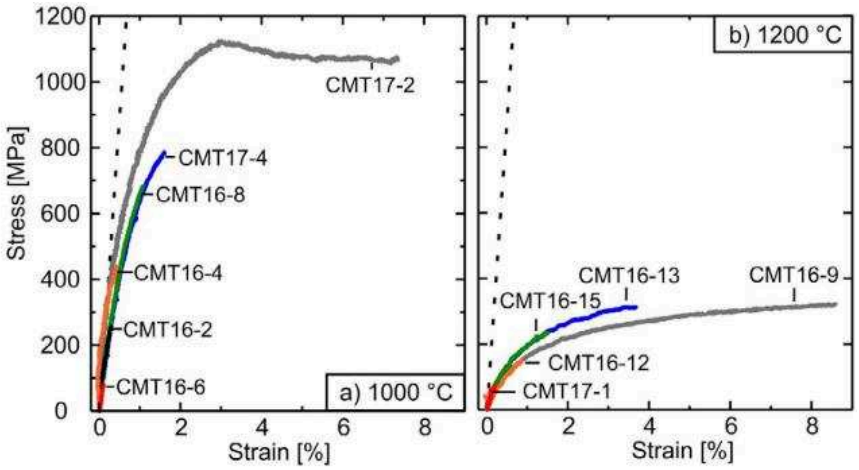

Figure 3-2: Courbes représentant la contrainte différentielle en fonction de la déformation obtenues lors des essais de compression. Le trait interrompu montre la déformation purement élastique basée sur un module Young à 152 GPa (a) et 146 GPa (b).

	Déformation à 1273 K		**Déformation à 1473 K**	
Echantillon	**CMT16-4**	**CMT16-8**	**CMT16-9**	**CMT16-13**
Contrainte différentielle (MPa)	440	684	322	313
Vitesse de déformation $\dot{\varepsilon}$ (s^{-1})	3,6 x 10^{-6}	3,3 x 10^{-6}	1,0 x 10^{-5}	1,0 x 10^{-5}
Durée (min)	42	79	174	84
Deformation ε (%)	0,42	1,07	8,59	3,68

Tableau 3-2: Conditions expérimentales de déformation des échantillons étudiés par SPED.

III.5.2 Article

Ces résultats sont décrits dans l'article en cours d'examen dans EJM (European Journal of Mineralogy), dont le manuscrit est reproduit dans les pages qui suivent :

B.C. Nzogang, M. Thieme, A. Mussi, S. Demouchy & P. Cordier. Characterization of recovery by sub-grain and grain boundary migration in experimentally deformed polycrystalline olivine. En expertise dans EJM.

Title: **Characterization of recovery by sub-grain and grain boundary migration in experimentally deformed polycrystalline olivine**

Running title: **Sub-grain and grain boundary migration in experimentally deformed olivine**

Billy Clitton Nzogang[1], Manuel Thieme[2], Alexandre Mussi[1], Sylvie Demouchy[2], and Patrick Cordier[1]

[1]Univ. Lille, CNRS, INRA, ENSCL, UMR 8207 - UMET - Unité Matériaux et Transformations, F-59000 Lille, France

[2]Univ. Montpellier, CNRS, Geosciences Montpellier, F-34095 Montpellier, France

Manuscript submitted to European Journal of mineralogy (February 2019)

Title: **Characterization of recovery by sub-grain and grain boundary migration in experimentally deformed polycrystalline olivine**

Running title: **Sub-grain and grain boundary migration in experimentally deformed olivine**

Billy Clitton Nzogang[1], Manuel Thieme[2], Alexandre Mussi[1], Sylvie Demouchy[2], and Patrick Cordier[1]

[1]Univ. Lille, CNRS, INRA, ENSCL, UMR 8207 - UMET - Unité Matériaux et Transformations, F-59000 Lille, France

[2]Univ. Montpellier, CNRS, Geosciences Montpellier, F-34095 Montpellier, France

Text statistics: 6571 words

Abstract

To apprehend plate tectonics and the dynamics of the lithosphere-asthenosphere boundary, composed principally of olivine, we need to understand what controls the mechanisms of olivine plastic deformation. After more than fifty years of laboratory studies and investigations on natural rocks, several key parameters controlling polycrystalline olivine plasticity remain difficult to assess. Here, we study four olivine polycrystals, which have been deformed in axial compression, at 300 MPa and at 1273 or 1473 K. Despite significant difference in mechanical properties (stress-strain curves), characterization by scanning (SEM) and transmission electron microscopy (TEM) did not reveal significant difference in microstructures or dislocation densities. Here, we have undertaken automatic crystallographic orientation mapping (ACOM) analyses in TEM to increase the spatial resolution of

characterization compared to previously obtained electron backscatter diffraction maps to further decipher the microstructures at nanoscale. With this novel technique applied on olivine, a noticeable difference in recovery mechanisms has been identified between the four specimens. The microstructures of the olivine polycrystal deformed at 1473 K are composed of numerous curved grain and sub-grain boundaries, advocating for recovery mechanisms by boundary migrations. In contrast, the microstructures of the olivine polycrystal deformed at 1273 K have less sub-grain boundaries, and straighter (*i.e.* closer to equilibrium) boundaries than in the specimen deformed at 1473 K.

Keywords: olivine; grain boundary migration; plastic deformation; earth mantle; polycrystal; ACOM-TEM.

Introduction

Olivine is the most abundant silicate in Earth's upper mantle with 60-80 % in volume. It is the only mineral phase interconnected at centimetric and metric scales in peridotites. Thus, its rheological properties are expected to control the plastic deformation of the upper mantle, including at the base of tectonic plates (*i.e.*, lithosphere-asthenosphere boundary). As such an important mineral, its ductile deformation was intensively characterized by studying natural mantle specimens, from xenoliths of peridotites or tectonic massifs (*e.g.*, Ave'Lallemant *et al.*, 1970; Gueguen, Y., 1979; Ben Ismail *et al.*, 1998; Warren & Hirth, 2006; Le Roux *et al.*, 2007; Drury & Pennock, 2007; Le Roux *et al.*, 2008; Jung, 2009; Drury *et al.*, 2011; Précigout & Hirth, 2014; Satsukawa & Michibayashi, 2014; Behr & Platt, 2014) and by laboratory deformation experiments at high pressure and high temperature on single crystals and polycrystals (*e.g.*, Goetze, 1978; Bai & Kohlstedt, 1992; Hirth & Kohlstedt, 2003; Mainprice *et al.*, 2005; Demouchy *et al.*, 2014). The primary aim of deformation experiments was to provide a generic (semi-empirical) flow law, which can be extrapolated to mantle

strain rates (10^{-13}-10^{-15} s^{-1}) and temperatures (773-1673 K). Over the last 5 decades, laboratory experiments and numerical models have provided a variety of power flow laws (*e.g.*, Hirth & Kohlstedt, 2003; Demouchy *et al.*, 2013; Tielke *et al.*, 2017; Boioli *et al.*, 2015a-b), which can be used to estimate the stress level in the mantle asthenosphere in both the diffusion creep and the dislocation creep regime. However, for the lithospheric mantle, the experiments are facing a challenge as stresses obtained in deformation experiments below 1073 K and at laboratory strain rates (*e.g.*, 10^{-5} s^{-1}) do not reach steady state and consequently make extrapolation to deep Earth's strain rates rather imprecise (*e.g.*, lower bound for stresses only, see for discussion Demouchy *et al.*, 2013 and Tielke *et al.*, 2017).

To investigate the plastic behavior of olivine at lithospheric temperatures (773 -1173 K), where steady state is not reached experimentally, an alternative approach is to use experiments to identify dislocation interactions in glide and/or climb configurations at the microscopic scale to implement interactions as specific rules into 2.5-dimension dislocation dynamics models (*e.g.*, Boioli *et al.*, 2015a-b; Gouriet *et al.*, 2019). With such numerical models, deformation of crystalline solids at the slow strain rates relevant for natural conditions can be reproduced (10^{-13}-10^{-15} s^{-1} and a large temperature range). However so far, 2.5-D models can only be performed for single crystals (*e.g.*, Boioli *et al.*, 2015b).

To continue to constrain how polycrystalline olivine plastically deforms at lithospheric mantle temperatures, a recent study (Thieme *et al.*, 2018) has deformed very fine-grained iron-bearing polycrystalline olivine at two temperatures (1273 and 1473 K) for small finite strains. Nevertheless, this recent study has reported conflicting results on strain hardening: (1) The stress during deformation rises nonlinearly as a function of strain before reaching steady state or brittle failure ; (2) This hardening is dependent on the deformation temperature and must therefore be based on a thermally activated mechanism, and (3) based on electron backscatter diffraction (EBSD) and transmission electron microscopy (TEM) investigations,

92 the increases in stress or finite strain do not lead to a measurable increase in dislocation
93 density in the deformed samples (Thieme *et al.*, 2018). Even at 1473 K, multiple grains
94 remain free of dislocations. Thus, these observations question the transferability of the
95 standard description of strain hardening established in metals (*i.e.*, increase in dislocation
96 density, dislocation forest interactions, (Evans & Goetze, 1979)) to olivine deformed far from
97 its melting temperature (*e.g.*, transient creep at 1273-1473 K relative to melting temperature
98 for Fo90 ≃ 1973 K). In metals, hardening is explained by the contending influence of the
99 grain size reduction (*e.g.*, dynamic recrystallization, see Huang & Logé (2016) for a recent
100 review) and an increasing dislocation density in the newly formed sub-grain boundaries.
101 These high dislocation densities will then act as obstacles and lead to increasing sub-grain
102 boundary misorientation (Estrin *et al.*, 1998; Nes, 1997). Since, the microstructures observed
103 by Thieme *et al.* (2018) were not modified with increasing stress or finite strain, several
104 alternatives were proposed

105 - for hardening at low temperature: (1) Dislocation interactions; (2) temperature
106 dependence of the dislocation mobility, which remains difficult to assess in *post*
107 *mortem* specimens; (3) grain boundaries acting as obstacles, as reported for the Hall-
108 Petch effect (Hansen, 2004) where the formation of pile-ups could cause sufficient
109 back stresses and therefore be the source of the observed hardening;
110 - or for strain softening at higher temperature: (4) grain boundaries, acting as efficient
111 dislocation sources with increasing temperature; or (5) grain boundaries acting as
112 agent of deformation, such as grain boundary sliding, grain boundary migration and
113 bulging and the subsequent dynamic recrystallization (*e.g.*, Drury & Urai, 1990).

114 To be able to discriminate between these hypotheses, it is necessary to change the scale
115 of observation, as compared to previous studies on plastically deformed polycrystalline
116 olivine (*e.g.*, Demouchy *et al.*, 2013-2014; Thieme *et al.*, 2018).

In this study, we use automatic crystallographic orientation mapping in transmission electron microscopy (ACOM-TEM) on experimentally deformed polycrystalline olivine to identify the differential activity of recovery processes during plastic deformation. For the first time, we report evidence of contrasting behavior of subgrain and grain boundaries as a function of temperature in polycrystalline olivine.

Materials and Methods

The samples analyzed here were already the focus of a previously published study (Thieme *et al.*, 2018). We recall briefly the experimental conditions and the main results of the mechanical data and microstructure characterization below. From this study (Thieme *et al.*, 2018), we have selected four fine-grained polycrystalline olivine samples (CMT16-4, CMT16-8, CMT16-9 and CMT16-13) deformed in axial compression at constant displacement rates (see Table 1) with small finite strains (below 9%) under identical confining pressure (300 MPa of Ar), but at different temperatures (1273 K for CMT16-4 and CMT16-8 and 1473 K for CMT16-9 and CMT16-13). The polycrystalline samples were prepared from the same fine-grained powder of San Carlos olivine (Arizona, USA), with an initial grain size of 1.8-2 μm. The polycrystalline powder was first cold pressed (2-20 MPa), then hot pressed for 3 hours at 1473 K and 300 MPa to reduce the porosity to less than 3 % (see also Thieme *et al.*, 2018). The hot-press step was directly followed by axial compression when the targeted temperature was reached for deformation at 1473 K. For deformation at 1273 K (*i.e.* temperature lower than the hot-press) the temperature was decreased at a rate of 6.5 K/min and then kept constant at 1273 K for at least 30 minutes to ensure satisfying stability of the temperature distribution along the samples prior to axial compression. Additional technical details are available in Thieme *et al.* (2018). The deformation experiments were performed using a high-pressure, high-temperature *in situ* deformation apparatus (Paterson, 1990).

Deformation conditions are summarized in Table 1. While the samples were deformed at the same constant displacement rate, CMT 16-4 and CMT 16-8 did not reach steady state (*i.e.*, finite strain ≦ 1 %). Indeed, the strain must be corrected for the ongoing elastic deformation of the vessel (stiffness of 82.5 kN/mm) and elasticity of the olivine (E = 152 GPa at 1273 K and 146 GPa at 1473 K, Liu *et al.*, 2005) since they accommodates part of the imposed displacement rate, resulting in different (slower) strain rates than for quasi-steady-state experiments (*i.e.*, CMT-16-8 and CMT 16-13).

Insert Table I and Fig. 1

As expected from the low finite strain for the four deformation experiments, the mechanical curves displayed in Figure 1 indicate that steady state was not reached, even for the two samples deformed at 1473 K, CMT16-13 and CMT16-9. For these samples, the total finite strain is different (3.68 % and 8.59 % respectively) but the maximum stresses are comparable (313 MPa and 322 MPa respectively). Samples deformed at the lowest temperature, 1273 K have been interrupted in a strongly hardening regime at 0.42 % for sample CMT16-4 and 1.07 % for CMT16-8. The corresponding stresses are 440 MPa and 684 MPa respectively, well above the confining pressure. The difference in stress between the two pair of experiments is very high (> factor of 2) and is expected to induce modification of the microstructure. At the scale of the investigated sample sections (large maps of ≈ 20,000 μm^2 and small maps ≈ 2400 μm^2), the first step of microstructural characterization by scanning electron microscopy (SEM) and electron backscatter diffraction (EBSD) has permitted to establish the following results: from SEM images and EBSD maps, there are no significant differences in grain size (1.6 ± 0.2 μm), aspect ratio (1.5 ± 0.4), internal misorientation from mean orientation (Mis2Mean), grain orientation spread (GOS, 0.58-0.59 °), between the different samples.

After deformation, doubly-polished thin sections (~30 μm thick) parallel to the deformation axis were prepared. The sections were glued on a grid (Cu or Mo) and ion milled

at 5 kV under a low beam angle of 15° with a Gatan® DuoMill™ model 600 until electron transparency was reached. The foils were subsequently covered with a thin layer of carbon. TEM observations were carried out at the University of Lille (France) using a FEI® Tecnai G2-20 twin microscope operating at 200 kV and a Philips CM30 microscope operating at 300 kV, both equipped with a LaB_6 filament and using a double tilt sample-holder.

Conventional TEM investigation had been performed previously (Thieme *et al.*, 2018) and had reported a heterogeneous distribution of dislocations, with some olivine grains containing a high density of dislocations and other grains void of linear defects in the four samples and did not report the formation of dislocation entanglement (*e.g.*, forest hardening) in the high stress sample (CMT16-8), as compared to the low stress samples.

In the present study, ACOM-TEM was operated in the TEM with the ASTAR™ tool from NanoMEGAS (Rauch & Véron, 2014). The TEM was set in micro-beam mode (nominal spot size ~6 nm without precession) and the incident electron beam, which was focused on the sample, was scanned over the area with a step size of 6 nm, thanks to a dedicated hardware control system of the TEM deflecting coils. In this mode, where a convergent beam illuminates the sample, the diffraction pattern consists of discs. Using the smallest condenser aperture (50 µm) the diffraction patterns are made of very small spot-like discs and can be indexed as spot patterns. The individual exposure time at each location was 10 ms. In this study, we used precession illumination (with a precession angle of 0.5°) in the TEM which allows many more reflections to be seen in the diffraction pattern with intensities closer to the kinematical diffraction conditions. Diffraction patterns were collected with an external Stingray CCD camera directed toward the TEM phosphorous screen and are stored in the computer memory for further indexation and post processing. The diffraction patterns were collected as 144×144 pixels at a camera length of 89 mm. This distance was chosen to optimize the diffraction pattern for indexation. Using the ASTAR™ software, electron diffraction spot patterns are indexed

192 (providing the local crystal orientations) by comparing individually obtained patterns via cross-
193 correlation matching techniques with pre-calculated electron diffraction templates which are
194 generated every 0.5 ° (orientation resolution). For iron-bearing olivine, templates have been
195 generated from the crystallographic data of Birle *et al.* (1968) for forsterite. From this
196 indexation within the *Pnma* space group, one obtains crystallographic orientation maps, which
197 display, with a colour coding, the most probable orientation at each scanned beam position.

198 The indexation quality (*IQ*) in the figures 2, 5, 6, 7, 9, 10, 11, 12 and 13 is calculated from
199 template matching and is quantified by the image correlation index (Rauch & Dupuy, 2005):

200 $$IQ(i) = \frac{\sum_{j=1}^{m} P(x_j,y_j) T_i(x_j,y_j)}{\sqrt{\sum_{j=1}^{m} P^2(x_j,y_j)} \sqrt{\sum_{j=1}^{m} T_i^2(x_j,y_j)}} \quad (1)$$

201 In eq. (1), the diffraction pattern is represented by the intensity function $P(x, y)$ and
202 every template *i* is described by the function $T_i(x, y)$. The highest *Q* value corresponds to the
203 retained solution. The reliability of this solution can be quantified by the ratio of the matching
204 indexes for the two best solutions IQ_1 and IQ_2:

205 $$R = 100\left(1 - \frac{IQ_1}{IQ_2}\right) \quad (2)$$

206 In reliability maps, the brighter the pixel (*i.e.* the higher the reliability index) the more
207 reliable is the proposed indexation. On the contrary, darker pixels correspond to less reliable
208 solutions. The latter is typically the case at grain boundaries where two solutions of co-
209 existing grains overlap.

210 The datasets were processed with MTEX (free and open source MATLAB^{TM} Toolbox
211 from Bachmann *et al.*, 2011). Grain boundaries were identified where the misorientation to
212 the next pixel is higher than 15 ° (Bachmann *et al.*, 2011). Groups of pixels below a size of 10
213 points have been ignored.

214 Note that the orientation dataset was a square-shaped grid for ASTAR, and has been
215 converted to a Channel Text File (*i.e.*, .ctf file) for usage in MTEX. To be able to detect

deformation details in the microstructures, one must use other tools than only the inverse pole figure colour-coding. In this study, we use the orientation maps to calculate local misorientations as recently developed in the EBSD community (*e.g.* Wright *et al.*, 2011). As commonly used in EBSD, several quantities can be calculated from the orientation maps:

(1) The kernel average misorientation (KAM) calculates the average misorientation between a pixel and its neighbours, provided that the misorientation does not exceed a predefined threshold value, *e.g.* 5 °, thus the incorporation of well-defined grain boundaries is avoided. If plastic deformation results from dislocation glide and crystal lattice rotation, this approach allows quantitative evaluation of the local plastic strain gradients (Godfrey *et al.*, 2005). Therefore KAM can be seen as proxy for GND dislocation density (Wallis *et al.*, 2016). A kernel is a set of points of prescribed size surrounding the scan point of interest. The size of the kernel is generally prescribed to the n^{th} nearest-neighbours. Hence this parameter is sensitive to the step size of the measurement grid and can be adjusted by the user as well. For that reason, all KAM maps presented in this study have been calculated with a fixed kernel to the 3^{rd} neighbours.

(2) The grain orientation spread (GOS) is the average deviation in orientation between each point in a grain and the average orientation of the grain. This approach leads to assigning the same value of the GOS to every scan point contained within a grain.

(3) The grain reference orientation deviation (GROD) is based on the misorientation between a reference point of the considered grain and the other points. The reference point can be the point of the grain where the KAM is the lowest or the mean misorientation of the considered grain. For the latter specific case, the GROD is called the 'Mis2Mean'. The Mis2Mean shows how the orientation of each pixel deviates from a reference value taken as the mean orientation of a given grain. As for the GOS values, the Mis2Mean values depend not only on the plastic strain, but also on the mapped grain area fraction. Here, since at the

TEM scale many grains are not entirely mapped, the Mis2Mean value should be regarded as a semi-quantitative tool only. The KAM, GROD and GOS approaches provide complementary information.

Results

The deformation microstructures of these samples have already been described based on a conventional TEM investigation (Thieme *et al.*, 2018). Regarding the dislocation microstructure, no clear trend could be distinguished among the investigated samples, including CMT16-13, CMT16-9, CMT16-4 and CMT16-8, largely due to the strong heterogeneity as samples were deformed to rather low plastic strains (0.4-8.6 %). Extensive EBSD characterizations have also been performed to characterize grain morphologies (*e.g.*, shape factor) with representative statistics (Thieme *et al.*, 2018). Here we utilize a comparable technique where orientation maps are acquired in the TEM but with a higher spatial resolution (*e.g.*, 6 nm in TEM, at best 70 nm for EBSD on olivine (Thieme *et al.*, 2018)). As a consequence, the area mapped here are much smaller. We focus then on the morphologies of the grain and their boundaries, and on the intragranular microstructures. Indeed, from orientation maps shown in Figure 2a, the morphologies of the grain boundaries are defined at a higher resolution than in conventional TEM, where images are impacted by the very strong superimposed diffraction contrasts. On these new maps, slight color variations are indicative of misorientations within grains, which are quantified by the GOS.

Insert Fig. 2-5

Samples CMT16-13 and CMT16-9 deformed at 1473 K

From IPF orientation maps and/or GOS maps shown in Figures 2a, 3a, 4a, 5a, 5b, 6b, 6c, 7a and 7b, one can see that in these samples, the grain boundaries are strongly curved, even in case of small grains (Figure 2a, pink grain). Radii of curvature can be locally of the order of a

few tens of nm. Besides a higher spatial resolution, the merit of ACOM-TEM is also to go beyond the statistical average per grain value of the GOS and to map intragranular misorientation at higher resolution than EBSD (see figure 3 in Thieme *et al.* (2018) for comparison). In Figures 3, 4 and 5, one can observe grain division into multiple crystallographic domains. Misorientation profiles across these domain boundaries (highlighted in the Mis2Mean and the KAM maps) show that they are subgrain boundaries and permit the quantification of their individual misorientations. Several examples of angular determinations are presented in Figures 2b, 3c, 4b, 4c, 5c, 5d, 6d, 6e, 7c and 7d. In Figure 6, bulging of the 95° grain boundary is clearly associated with a differential dislocation density across the boundary. In Figure 7, the horizontal 102° grain boundary appears to be pinned by the 2.2° subgrain boundary.

Insert Fig. 6-8

Samples CMT16-4 and CMT16-8 deformed at 1273 K

Orientation maps gathered on samples deformed at lower temperature show a very different morphology as illustrated in Figure 8. Conventional TEM observations in Thieme *et al.* (2018) had already shown heterogeneity, with evidence for intracrystalline plastic deformation resulting from dislocation activity. We found the same results here as shown in Figures 8a, 9a, 10a and 11a. Further evidence for intragranular deformation is provided by misorientations as shown by the GOS maps in Figures 8b, 9b, 10b and 11b and the Mis2Mean maps in Figures 8c, 9c, 10c and 11c. However here, the grain boundaries are significantly less sinuous/curved, and more importantly, the interior of the grains show less misoriented domains and subgrain boundary development.

Insert Fig. 9-11

As already reported in Thieme *et al.* (2018), each microstructure is very heterogeneous, and one can also find some evidence of curved subgrain boundaries in samples deformed at

1273 K (Figure 12a,c,d). Also in figure 12, the 46 ° grain boundary is not fully straight and indeed, the KAM map in Figure 12d shows a difference of intensity across the boundary and hence a difference of stored strain energy which can act as a driving force for migration. Still, the high temperature and low temperature microstructures are different samples.

In sample CMT16-8, one can even find microstructures which can be interpreted as the onset of formation of neograins. For example, two bulges are identified in Figure 13, which are associated with misoriented domains terminated by a subgrain boundary (see the misorientation profiles). Comparable microstructures have been shown in polycrystalline copper (Miura *et al.*, 2007) and ice (Chauve *et al.*, 2017), and interpreted as nuclei for neograins during discontinuous dynamic recrystallization (dDRX). This mechanism has also been identified recently in polycrystalline forsterite deformed at high pressure (3.5-5 GPa) to large strains (25-40 %) (Bollinger *et al.*, 2019).

Insert Fig. 12-13

Discussion

The deformation experiments conducted at 1273 and 1473 K on fine-grained olivine polycrystals by Thieme *et al.* (2018) show markedly contrasted mechanical behaviors, which are well illustrated in Figure 1. At 1273 K, the stress-strain curves exhibit significant strain hardening leading to brittle failure after *ca.* 1% of strain. In contrast, at 1473 K, the sample is fully ductile and approaches mechanical steady state after *ca.* 3% of strain. Despite such markedly different mechanical behaviors and maximum final stress, the dislocation microstructures did not show any clear differences and thus was a call for further investigation by changing the resolution of characterization.

Plastic strain hardening is commonly observed in metals during cold working. Indeed, contrary to silicates and ceramics, metals are significantly ductile at low homologous

316 temperatures. In metals, during low-temperature deformation the dislocation density increases
317 due to mutual trapping of dislocations resulting from long-range and/or short-range junctions.
318 This is facilitated in cubic metals since they, by symmetry, have a large number of slip systems
319 able to lead to numerous configurations of junctions. This dislocation storage capacity leads to
320 an increase of the free energy of the material as dislocations are sources of long-range elastic
321 fields. This increase of free energy is the driving force for an evolution to low energy
322 configurations (see Rollett *et al.* (2004) for a general description of these processes). This
323 evolution is only possible if temperature is high enough (*i.e.*, relative to melting temperature)
324 for specific mechanisms, such as recovery, to operate (*e.g.*, ionic diffusion, recrystallization).
325 In olivine, the situation is different. Being a silicate, dislocation mobility is strongly
326 thermally activated and slower than in cubic metals and alloys. This element has already been
327 reminded in Thieme *et al.* (2018), it is however difficult to assess dislocation mobility
328 quantitatively. Here we focus on another aspect at mesoscopic scale. A major characteristic of
329 olivine is its plastic anisotropy. There exist only two slip directions in olivine (Raleigh, 1968):
330 [100] and [001]. Having orthogonal Burgers vectors, dislocations from these slip systems have
331 a very weak propensity to form junctions (Mussi *et al.*, 2015). Hence the tendency for
332 dislocation storage is lower than in other crystallographic structures and indeed, we did not
333 observe a clear correlation between the total finite plastic strain and the dislocation content.
334 However, since olivine does not exhibit enough independent slip systems to fulfill the von
335 Mises-Taylor criterion (Mises, 1928; Taylor, 1938; Ribe & Yu, 1991), dislocation activity
336 rapidly builds internal stresses due to incompatibilities between grains. This is likely the origin
337 of the strong strain hardening observed at 1273 K (Figure 1) reaching up to twice the confining
338 pressure, and which cannot be compensated by recovery mechanisms.
339 At high temperature (1473 K), the activation of recovery mechanisms is identified as the
340 formation of subgrain boundaries. We observe that unlike well annealed structures commonly

observed in natural samples (*e.g.* Figure 11 of Rauch & Véron (2014) and associated references), subgrain boundaries are very curved or wavy, thus far from equilibrium. This morphology is indicative of driving forces (surface tension) and we proposed it is indicative of recovery by boundary migration as reported previously by Bollinger *et al.*, (2019). Another mechanism which allows relaxing stored strain energy is the formation of new, dislocation-free grains (*i.e.*, dDRX). This mechanism was observed (Bollinger *et al.*, 2019) in polycrystalline olivine, deformed at high pressure and at larger strains (*ca.* 40 %). Here, finite strains are much smaller than in Bollinger *et al.* (2019), however we found indication that locally, heterogeneities could be strong enough to trigger small localized misoriented domains, which lead to the formation of new grains as illustrated by Figure 13. It is important to remember that in an anisotropic structure like olivine, the plastic strains reported in Table 1 represent macroscopic average values, and that at the microscopic scale of our observations, actual local strains and stress can deviate very significantly from these values (see for instance Barbe *et al.*, 2001).

Dynamic recrystallization (DRX) is known to induce strain-softening in olivine in the temperature range between 973 and 1573 K (Drury, 2005) and to involve a wide range of possible mechanisms (Drury & Urai, 1990; Rollett *et al.*, 2004). The formation of new, undeformed grains represents a strong indication of DRX, which usually requires large strain to develop (Bollinger *et al.*, 2019). Here we describe experiments involving low macroscopic strains. Although some evidence for new grains in formation could be postulated (*e.g.*, Figure 13), we propose that boundary migration is an active mechanism in our samples. The role of boundary migration in DRX has already been proposed (Drury & Urai, 1990; Drury & Pennock, 2007) as part as rotation recrystallization mechanisms (Drury & Pennock, 2007).

To conclude, our study using a novel ACOM-TEM technique has permitted to further address the role of grain and subgrain boundaries as agent of recovery at lithospheric temperatures in polycrystalline olivine, and indicates that grain boundary migration and

bulging play a noticeable accommodating and recovering role. It would be interesting to know whether other grain boundary degrees of freedom, namely sliding (*i.e.*, motion restricted to direction parallel to grain interfaces), also contribute to either recovery or strain. It is interesting to note that in Figure 8 one observes a quadruple junction, with a void which could be indicative of the operation of grain boundary sliding (Ashby & Verrall, 1973). It is difficult however to draw firm conclusions from this single observation and we leave this question to further investigation.

Acknowledgments:

This project received funding from the European Research Council under the Seventh Framework Programme (FP7), ERC grant N°290424 – RheoMan, and from the European Union's Horizon 2020 research and innovation program under the Marie Sklodowska-Curie Grant agreement No. 642029 - ITN CREEP. We thank C. Nevado and D. Delmas for providing high-quality thin sections for TEM. The TEM in Lille is supported by the Institut National de Sciences de l'Univers (INSU) du Centre National de la Recherche Scientifique (CNRS, France), and by the Conseil Régional du Hauts-de-France (France).

References

Ashby, M.F. & Verrall, R.A. (1973): Diffusion-accommodated flow and superplasticity. *Acta Met.*, **21**, 149-163. https://doi.org/10.1016/0001-6160(73)90057-6.

Ave'Lallemant, H.G., Carter, N.L. (1970): Syntectonic recrystallization of olivine and modes of flow in the upper mantle. *Geol. Soc. America. Bull.*, **81**, 2203–2220. https://doi.org/10.1130/0016-7606(1970)81[2203:SROOAM]2.0.CO;2.

389 Bachmann, F., Hielscher, R., Schaeben, H. (2011): Grain detection from 2d and 3d EBSD
390 data - Specification of the MTEX algorithm. *Ultramicroscopy*, **111**, 1720-1733.
391 https://doi.org/10.1016/j.ultramic.2011.08.002.

392 Bai, Q. & Kohlstedt, D.L. (1992): High-temperature creep of olivine single crystals III.
393 Mechanical results for unbuffered samples and creep mechanisms. *Philos. Mag. A*, **66**, 1149–
394 1181. https://doi.org/10.1080/01418619208248011.

395 Barbe, F., Forest, S., Cailletaud, G. (2001): Intergranular and intragranular behavior of
396 polycrystalline aggregates. Part 2: Results. *Int. J. Plasticity*, **17**, 537-563.
397 https://doi.org/10.1016/S0749-6419(00)00062-0.

398 Behr, W. M. & Platt, J. P. (2014): Brittle faults are weak, yet the ductile middle crust is
399 strong: Implications for lithospheric mechanics. *Geophys. Res. Lett.*, **41**, 8067–8075.
400 doi:10.1002/2014GL061349.

401 Ben Ismail, W., Mainprice, D. (1998): An olivine fabric database: an overview of
402 uppermantle fabrics and seismic anisotropy. *Tectonophysics*, **296**, 145–158.
403 https://doi.org/10.1016/S0040-1951(98)00141-3.

404 Birle, J.D., Gibbs, G.V., Moore, P.B., Smith, J.V. (1968): Crystal structures of natural
405 olivines, *Am. Mineral.*, **53**, 807-824.

406 Boioli, F., Carrez, P., Cordier, P., Devincre, B., Marquille, M. (2015a): Modeling the creep
407 properties of olivine by 2.5-dimensional dislocation dynamics simulations. *Phys. Rev. B*, **92**,
408 014115. https://doi.org/10.1103/PhysRevB.92.014115.

409 Boioli, F., Tommasi, A., Cordier, P., Demouchy, S., Mussi, A. (2015b): Low steady-state
410 stresses in the cold lithospheric mantle inferred from dislocation dynamics models of
411 dislocation creep in olivine. *Earth Planet. Sci. Lett.*, **432**, 232–242.
412 https://doi.org/10.1016/j.epsl.2015.10.012.

Bollinger, C., Nzogang, B.C., Mussi, A., Bouquerel, J., Molodov, D.A., Cordier, P. (2019): Microstructural evidence for grain boundary migration and dynamic recrystallization in experimentally deformed forsterite aggregates. *Minerals*, **9**, 17. https://doi.org/10.3390/min9010017.

Chauve, T., Montagnat, M., Barou, F., Hidas, K., Tommasi, A., Mainprice, D. (2017): Investigation of nucleation processes during dynamic recrystallization of ice using cryo-EBSD. *Phil. Trans. R. Soc. A*, **375**, 20150345. http://dx.doi.org/10.1098/rsta.2015.0345.

Demouchy, S., Mussi, A., Barou, F., Tommasi, A., Cordier, P. (2014): Viscoplasticity of polycrystalline olivine experimentally deformed at high pressure and 900°C. *Tectonophysics*, **623**, 123–135. https://doi.org/10.1016/j.tecto.2014.03.022.

Demouchy, S., Tommasi, A., Ballaran, T.B., Cordier, P. (2013): Low strength of Earth's uppermost mantle inferred from tri-axial deformation experiments on dry olivine crystals. *Phys. Earth Planet. Inter.*, **220**, 37–49. https://doi.org/10.1016/j.pepi.2013.04.008.

Drury, M.R. (2005): Dynamic recrystallization and strain softening of olivine aggregates in the Laboratory and the Lithosphere. *Geol. Soc. London Special Publications*, **243**, 143-158. https://doi.org/10.1144/GSL.SP.2005.243.01.11.

Drury, M.R., Avé Lallemant, H.G., Pennock, G.M., Palasseac, L.N. (2011): Crystal preferred orientation in peridotite ultramylonites deformed by grain size sensitive creep, Étang de Lers, Pyrenees, France. *J. Struct. Geol.*, **33**, 1776-1789. https://doi.org/10.1016/j.jsg.2011.10.002.

Drury, M.R. & Pennock, G.M. (2007): Subgrain Rotation Recrystallization in Minerals. *Materials Science Forum*, **550**, 95-104. https://doi.org/10.4028/www.scientific.net/MSF.550.95.

Drury, M.R. & Urai, J.L. (1990): Deformation-related recrystallization processes. *Tectonophysics*, **172**, 235-253. https://doi.org/10.1016/0040-1951(90)90033-5.

437 Estrin, Y., Tóth, L.S., Molinari, A., Bréchet, Y. A (1998): dislocation-based model for all
438 hardening stages in large strain deformation. *Acta Mater.*, **46**, 5509–5522.
439 http://dx.doi.org/10.1016/S1359-6454(98)00196-7.

440 Evans, B. & Goetze, C. (1979): The temperature variation of hardness of olivine and its
441 implication for polycrystalline yield stress. *J. Geophys. Res.*, **84**, 5505–5524.
442 https://doi.org/10.1029/JB084iB10p05505.

443 Godfrey, A., Cao, W.Q., Hansen, N., Liu, Q. (2005): Stored energy, microstructure, and flow
444 stress of deformed metals. *Metall. Mater. Trans.* A, **36**, 2371–2378.
445 https://doi.org/10.1007/s11661-005-0109-0.

446 Goetze, C. (1978): The mechanism of creep in olivine. *Phil. Trans. R. Soc. Lond. A*, **288**, 99–
447 119. https://doi.org/10.1098/rsta.1978.0008.

448 Gouriet, K., Cordier, P., Garel, F., Thoraval, C., Demouchy, S., Tommasi, A., Carrez, P.
449 (2019): Dislocation Dynamics modelling of the power-law breakdown in olivine single
450 crystals: toward a unified creep law for the upper mantle. *Earth Planet Sci. Lett.*, **506**, 282-
451 291. https://doi.org/10.1016/j.epsl.2018.10.049.

452 Gueguen, Y. (1979): Dislocation in naturally deformed terrestrial olivine: classification,
453 interpretation, application. *Bull. Minéral*, **102**, 178–183.
454 https://doi.org/10.3406/bulmi.1979.7273.

455 Hansen, N. (2004): Hall-Petch relation and boundary strengthening. *Scripta Mater.*, **51**, 801–
456 806. https://doi.org/10.1016/j.scriptamat.2004.06.002.

457 Hirth, G. & Kohlstedt, D.L. (2003): Rheology of the upper mantle and the mantle wedge: a
458 view from the experimentalists, in: Inside The Subduction Factory. AGU, Washington, 83–
459 105.

Huang, K. & Logé, R.E. (2016): A review of dynamic recrystallization phenomena in metallic materials. *Mater. Des.*, **111**, 548-574. https://doi.org/10.1016/j.matdes.2016.09.012.

Jung, H. (2009): Deformation fabrics of olivine in Val Malenco peridotite found in Italy and implications for the seismic anisotropy in the upper mantle. *Lithos*, **109**, 341–349. https://doi.org/10.1016/j.lithos.2008.06.007.

Le Roux, V., Bodinier, J.L., Tommasi, A., Alard, O., Dautria, J.M., Vauchez, A., Riches, A.J.V. (2007): The Lherz spinel lherzolite: refertilized rather than pristine mantle. *Earth Planet. Sci. Lett.*, **259**, 599–612. https://doi.org/10.1016/j.epsl.2007.05.026.

Le Roux, V., Tommasi, A., Vauchez, A. (2008): Feedback between melt percolation and deformation in an exhumed lithosphere-asthenosphere boundary. *Earth Planet. Sci. Lett.*, **274**, 401–413. https://doi.org/10.1016/j.epsl.2008.07.053.

Liu, W., Kung, J., Li, B. (2005): Elasticity of San Carlos olivine to 8 GPa and 1073 K. *Geophys. Res. Lett.*, 32, L16301. http://dx.doi.org/10.1029/2005GL023453

Mainprice, D., Tommasi, A., Couvy, H., Cordier, P., Frost, D.J. (2005): Pressure sensitivity of olivine slip systems and seismic anisotropy of the Earth's upper mantle. *Nature*, **433**, 731–733. https://doi.org/10.1038/nature03266.

Miura, H., Sakai, T., Mogawa, R., Jonas, J.J. (2007): Nucleation of dynamic recrystallization and variant selection in copper bicrystals. *Philos. Mag.*, **87**, 4197-4209. https://doi.org/10.1080/14786430701532780.

Mises, R.V. (1928): Mechanik der plastischen Formänderung von Kristallen. *Z. Angew. Math. Mech.*, **8**, 161-185. https://doi.org/10.1002/zamm.19280080302.

Mussi, A., Cordier, P., Demouchy, S. (2015): Characterization of dislocation interactions in olivine using electron tomography. *Philos. Mag.*, **95**, 335–345. http://dx.doi.org/10.1080/14786435.2014.1000996.

Nes, E. (1997): Modelling of work hardening and stress saturation in FCC metals. *Prog. Mater. Sci.*, **41**, 129–193. http://dx.doi.org/10.1016/S0079-6425(97)00032-7.

Paterson, M.S. (1990): Rock deformation experimentation. in ‘‘The Brittle-Ductile transition in rocks: the Heard volume’’, A.G. Duba, W.B. Durham, J.W. Handin and H.F. Wang, eds. Geophysical Monograph Series. AGU, Washington, 187–194.

Précigout, J. & Hirth, G. (2014): B-type olivine fabric induced by grain boundary sliding. *Earth Planet. Sci. Lett.*, **395**, 231–240. https://doi.org/10.1016/j.epsl.2014.03.052.

Raleigh, C.B. (1968): Mechanisms of plastic deformation of olivine. *J. Geophys. Res.*, **73**, 5391-5406. https://doi.org/10.1029/JB073i016p05391.

Rauch, E.F. & Véron, M. (2014): Automated crystal orientation and phase mapping in TEM, *Mater. Charact.*, **98**, 1-9. https://doi.org/10.1016/j.matchar.2014.08.010.

Rauch, E.F. & Dupuy, L. (2005): Rapid spot diffraction patterns identification through template matching, *Arch. Metall. Mater.*, **50**, 87–99.

Ribe, N. & Yu, Y. (1991): A theory for plastic deformation and textural evolution of olivine polycrystals. *J. Geophys. Res.*, **96**, 8325-8335. https://doi-org /10.1029/90JB02721.

Rollett, A., Humphreys, F.J., Rohrer, G.S., Hatherly, M. (2004): Recrystallization and Related Annealing Phenomena, 2nd edition. Elsevier: Oxford, UK, 658 pp., ISBN 9780080441641.

Satsukawa, T. & Michibayashi, K. (2014): Flow in the uppermost mantle during back-arc spreading revealed by Ichinomegata peridotite xenoliths, NE Japan. *Lithos*, **189**, 89–104. https://doi.org/10.1016/j.lithos.2013.10.035.

504 Taylor, G.I. (1938): Plastic strain in metals. *J. lnst. Met.*, **62**, 307-324.

505 Tielke, J.A., Zimmerman, M.E., Kohlstedt, D.L. (2017): Hydrolytic weakening in olivine
506 single crystals. *J. Geophys. Res.*, **122**, 3465-3479. https://doi.org/10.1002/2017JB014004.

507 Thieme, M., Demouchy, S., Mainprice, D., Barou, F., Cordier, P. (2018): Stress evolution and
508 associated microstructure during transient creep of olivine at 1000–1200 °C. *Phys. Earth*
509 *Planet. Inter.*, **278**, 34–46. https://doi.org/10.1016/j.pepi.2018.03.002.

510 Wallis, D., Hansen, L.N., Ben Britton, T., Wilkinson, A.J. (2016): Geometrically necessary
511 dislocation densities in olivine obtained using high-angular resolution electron backscatter
512 diffraction. *Ultramicroscopy*, **168**, 34-45. https://doi.org/10.1016/j.ultramic.2016.06.002.

513 Warren, J.M. & Hirth, G. (2006): Grain size sensitive deformation mechanisms in naturally
514 deformed peridotites. *Earth Planet. Sci. Lett.*, **248**, 438-450.
515 https://doi.org/10.1016/j.epsl.2006.06.006.

516 Wright, S.I., Nowell, M.M., Field, D.P. (2011): A review of strain analysis using electron
517 backscatter diffraction, *Microsc. Microanal.*, **17**, 316-329. doi:10.1017/S1431927611000055.

518 **Tables**

519 **Table 1.** Experimental deformation conditions.

Sample	Temp.(K)	Strain rate $\dot{\varepsilon}$ (s^{-1})	Finite strain ε (%)	Diff stress σ_{max} (MPa)	Duration (min)
CMT 16-4	1273	3.4×10^{-6}	0.42	440	42
CMT 16-8	1273	3.3×10^{-6}	1.07	684	79
CMT 16-9	1473	1.0×10^{-5}	8.59	322	174
CMT 16-13	1473	1.0×10^{-5}	3.68	313	84

520

521 **Figures captions**

522 Figure 1. Differential stress versus strain curves for the four deformation experiments in axial
523 compression investigated in this study from (Thieme *et al.*, 2018).

524

525 Figure 2. Morphology of the grains and grain boundaries in CMT16-13 deformed at 1473 K.
526 (**a**) Inverse pole figure (IPF) corresponding to the direction normal to the figure superimposed
527 with the indexation quality (see eq. (1) and main text for details). Colour code inserted refers
528 to *Pnma* (**b**) Mis2Mean distribution, from 0° to 15°. (**c**) KAM distribution (3rd neighbours),
529 from 0° to 2°.

530

531 Figure 3. Morphology of the grains and grain boundaries in CMT16-13 deformed at 1473 K.
532 (**a**) GOS distribution; (**b**) Mis2Mean distribution, from 0° to 8°; (**c**) KAM distribution (3rd
533 neighbours), from 0° to 2°.

534

535 Figure 4. Morphology of the grains and grain boundaries in CMT16-13 deformed at 1473 K.
536 (**a**) GOS map (**b**) Mis2Mean map, from 0° to 15°. (**c**) KAM map (3rd neighbours), from 0° to
537 2°. GROD and KAM maps permit to identify numerous subgrain boundaries; the
538 misorientation of some of them is indicated on the figure.

539

540 Figure 5. Morphology of the grains and grain boundaries in CMT16-13 deformed at 1473 K.
541 (**a**) Inverse pole figure (IPF) corresponding to the direction normal to the figure superimposed
542 with the indexation quality IQ (see eq. (1) and main text). (**b**) GOS map (**c**) Mis2Mean map,
543 from 0° to 7°. (**d**) KAM map (3rd neighbours), from 0° to 2°. GROD and KAM maps permit
544 to identify numerous subgrain boundaries; the misorientation of some of them is indicated on
545 the figure.

Figure 6. Morphology of the grains and grain boundaries in CMT16-9 deformed at 1473 K. (**a**) Conventional multi-beam TEM bright-field. (**b**) Inverse pole figure (IPF) corresponding to the direction normal to the figure superimposed with the indexation quality IQ (see eq. (1) and main text). (**c**) GOS map (**d**) Mis2Mean map, from 0° to 10°. (**c**) KAM map (3rd neighbours), from 0° to 2°. Mis2Mean and KAM maps are consistent in indicating stored elastic energy where dislocation density is larger.

Figure 7. Morphology of the grains and grain boundaries in CMT16-9 deformed at 1473 K. (**a**) Inverse pole figure (IPF) corresponding to the direction normal to the figure superimposed with the indexation quality IQ (see eq. (1) and main text). (**b**) GOS map (**c**) Mis2Mean map, from 0° to 10°. (**d**) KAM map (3rd neighbours), from 0° to 3°. The pinning effect of the 2.2° subgrain boundary on the 102-103° grain boundary is clearly visible.

Figure 8. Morphology of the grains and grain boundaries in CMT16-8 deformed at 1273 K. **(a)** Conventional multi-beam TEM bright-field (**b**) GOS map (**c**) Mis2Mean map, from 0° to 7°. (**d**) KAM map (3rd neighbours), from 0° to 2°.

Figure 9. Morphology of the grains and grain boundaries in CMT16-4 deformed at 1273 K. (**a**) Conventional multi-beam TEM bright-field. (**b**) Inverse pole figure (IPF) corresponding to the direction normal to the figure superimposed with the indexation quality IQ (see eq. (1) and main text). (**c**) GOS map (**d**) Mis2Mean map, from 0° to 10°. (**e**) KAM map (3rd neighbours), from 0° to 3°.

570 Figure 10. Morphology of the grains and grain boundaries in CMT16-4 deformed at 1473 K.
571 (**a**) Conventional multi-beam TEM bright-field. (**b**) Inverse pole figure (IPF) corresponding to
572 the direction normal to the figure superimposed with the indexation quality IQ (see eq. (1) and
573 main text). (**c**) GOS map (**d**) Mis2Mean map, from 0° to 10°. (**e**) KAM map (3rd neighbours),
574 from 0° to 3°.
575
576 Figure 11. Morphology of the grains and grain boundaries in CMT16-4 deformed at 1473 K.
577 (**a**) Conventional multi-beam TEM bright-field. (**b**) Inverse pole figure (IPF) corresponding to
578 the direction normal to the figure superimposed with the indexation quality IQ (see eq. (1) and
579 main text). (**c**) GOS map (**d**) Mis2Mean map, from 0° to 10°. (**e**) KAM map (3rd neighbours),
580 from 0° to 2°.
581
582 Figure 12. Morphology of the grains and grain boundaries in CMT16-8 deformed at 1273 K.
583 (**a**) Inverse pole figure (IPF) corresponding to the vertical direction superimposed with the
584 indexation quality IQ (see eq (1) and main text).; (**b**) GOS map ; (**c**) Mis2Mean map, from 0°
585 to 15°, and (**d**) KAM map (3rd neighbours), from 0° to 2°.
586
587 Figure 13. Morphology of the grains and grain boundaries in CMT16-8 deformed at 1273 K.
588 (**a**) Inverse pole figure (IPF) corresponding to the direction normal to the figure superimposed
589 with the indexation quality IQ (equation (1)); (**b**) Mis2Mean map, from 0° to 12°; (**c**) KAM
590 map (3rd neighbours), from 0° to 1.2°; (d) and (e) show misorientation profiles across subgrain
591 boundaries from (b).
592

Figures

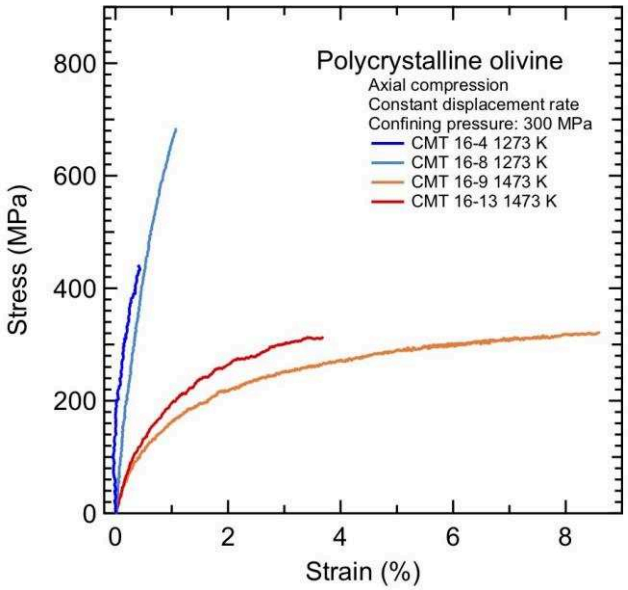

Figure 1. Differential stress versus strain curves for the four deformation experiments in axial compression investigated in this study from (Thieme *et al.*, 2018).

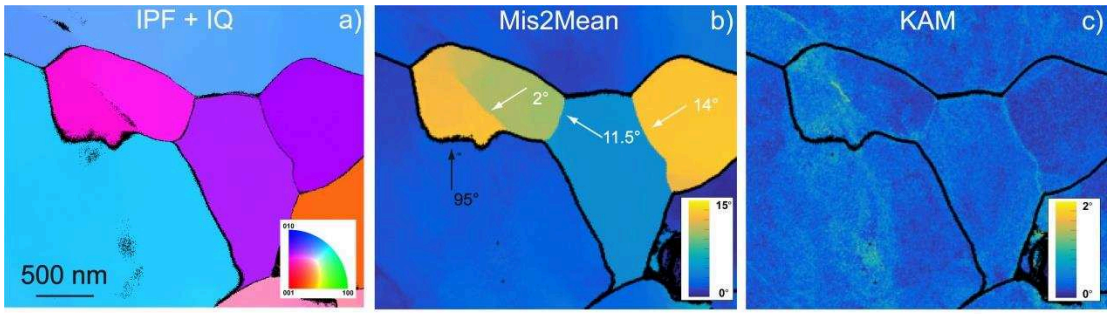

Figure 2. Morphology of the grains and grain boundaries in CMT16-13 deformed at 1473 K. (**a**) Inverse pole figure (IPF) corresponding to the direction normal to the figure superimposed with the indexation quality (see eq. (1) and main text for details). Colour code inserted refers to *Pnma* (**b**) Mis2Mean distribution, from 0° to 15°. (**c**) KAM distribution (3rd neighbours), from 0° to 2°.

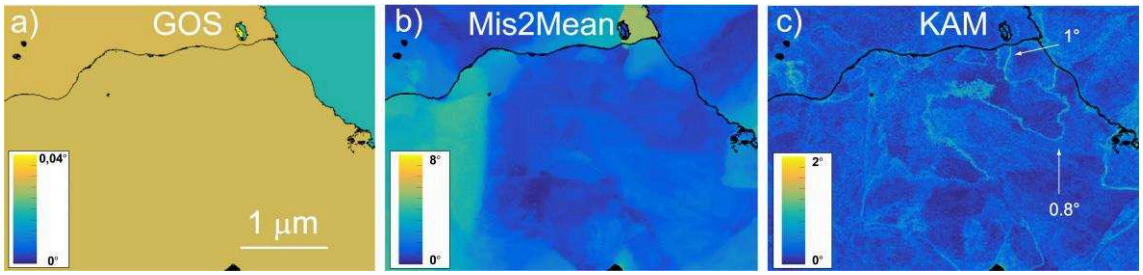

603 **Figure 3.** Morphology of the grains and grain boundaries in CMT16-13 deformed at 1473
604 K. (**a**) GOS distribution; (**b**) Mis2Mean distribution, from 0° to 8°; (**c**) KAM distribution
605 (3rd neighbours), from 0° to 2°.

606

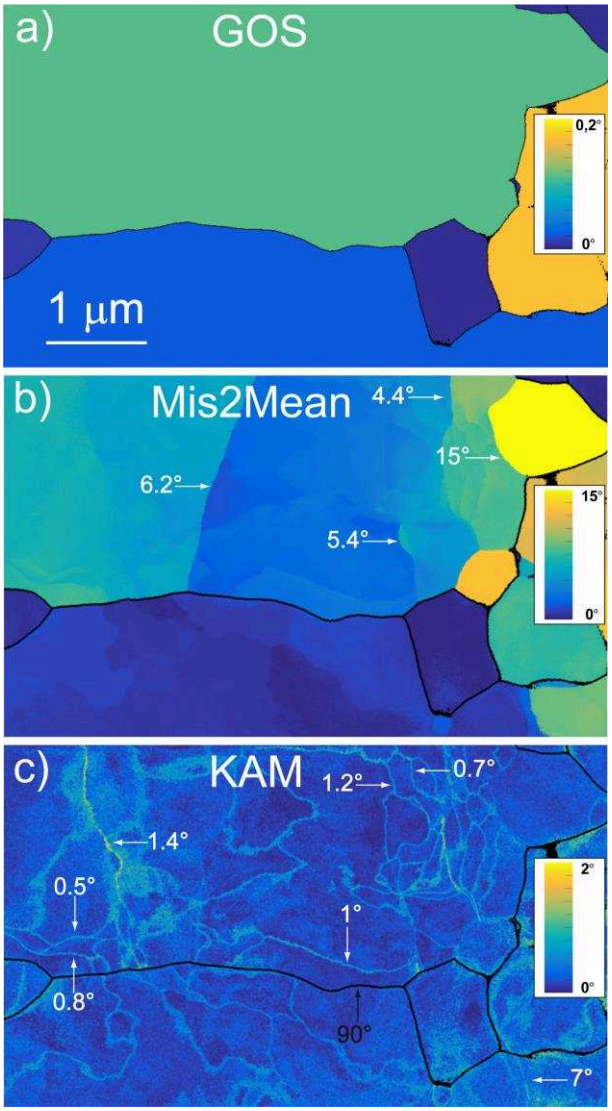

607 **Figure 4.** Morphology of the grains and grain boundaries in CMT16-13 deformed at 1473
608 K. (**a**) GOS map (**b**) Mis2Mean map, from 0° to 15°. (**c**) KAM map (3rd neighbours), from

0° to 2°. GROD and KAM maps permit to identify numerous subgrain boundaries; the misorientation of some of them is indicated on the figure.

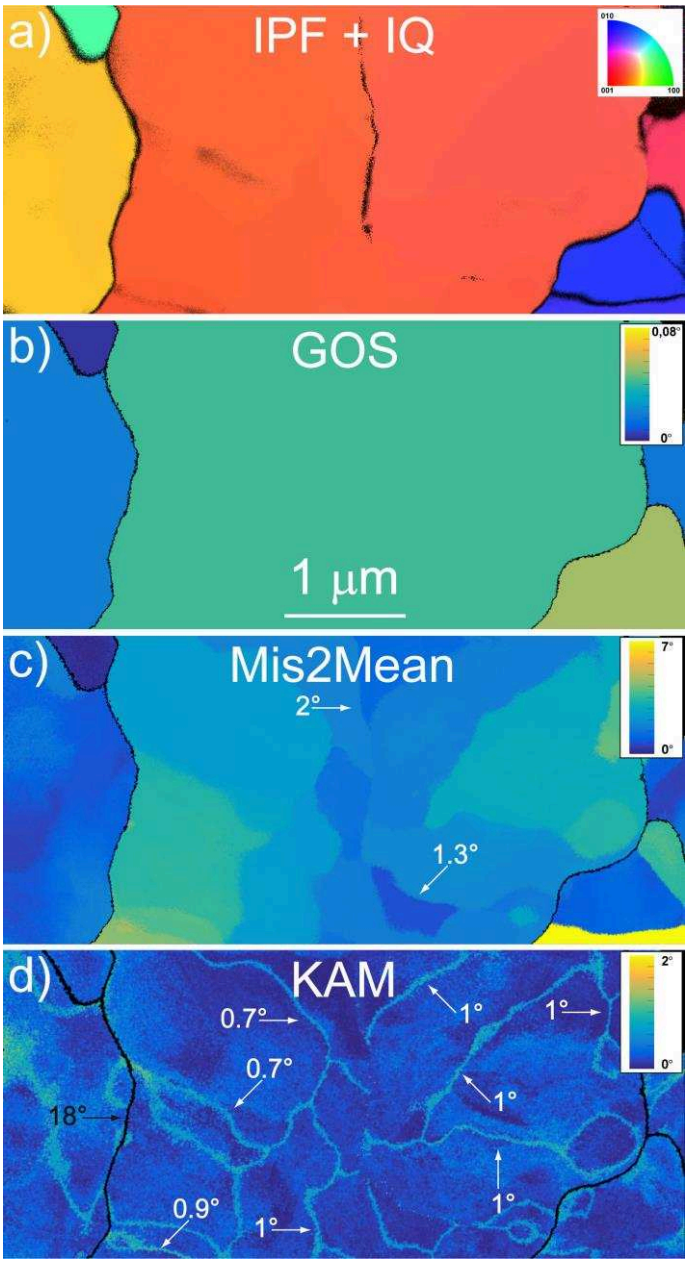

Figure 5. Morphology of the grains and grain boundaries in CMT16-13 deformed at 1473 K. (**a**) Inverse pole figure (IPF) corresponding to the direction normal to the figure superimposed with the indexation quality IQ (see eq. (1) and main text). (**b**) GOS map (**c**) Mis2Mean map, from 0° to 7°. (**d**) KAM map (3rd neighbours), from 0° to 2°. GROD and

KAM maps permit to identify numerous subgrain boundaries; the misorientation of some of them is indicated on the figure.

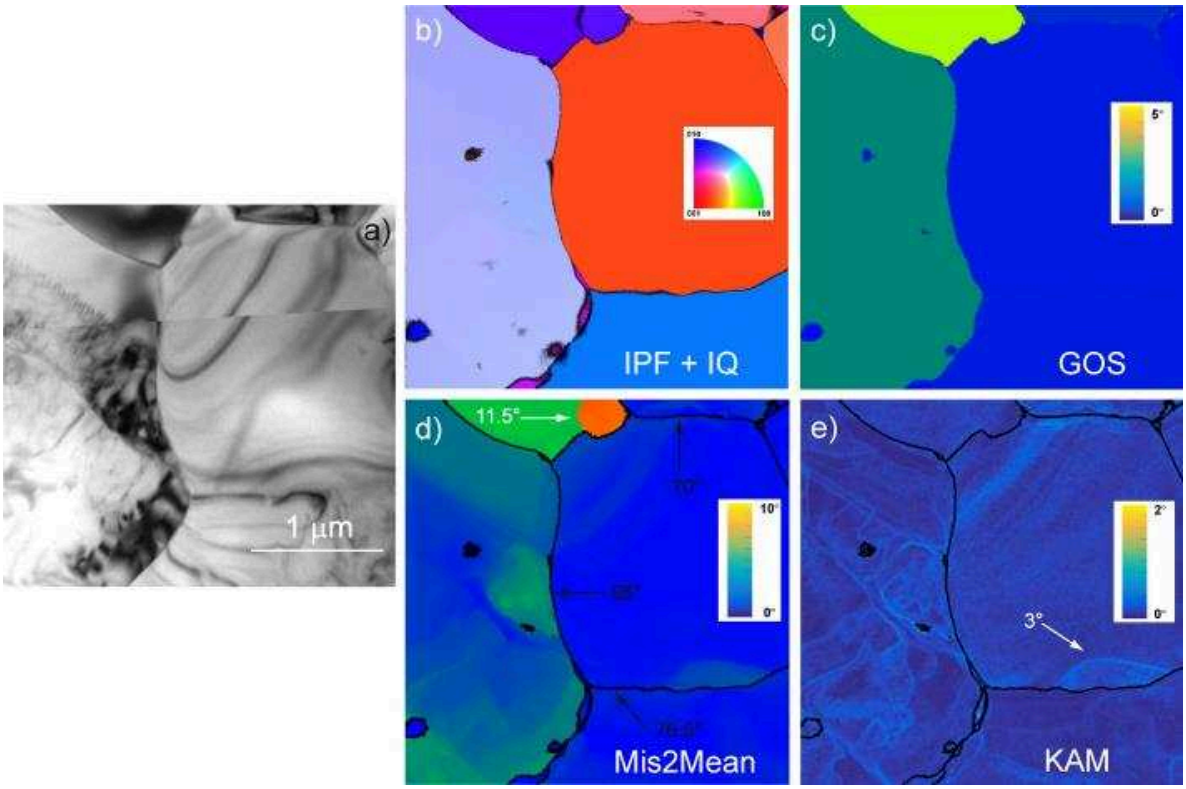

Figure 6. Morphology of the grains and grain boundaries in CMT16-9 deformed at 1473 K. (**a**) Conventional multi-beam TEM bright-field. (**b**) Inverse pole figure (IPF) corresponding to the direction normal to the figure superimposed with the indexation quality IQ (see eq. (1) and main text). (**c**) GOS map (**d**) Mis2Mean map, from 0° to 10°. (**c**) KAM map (3rd neighbours), from 0° to 2°. Mis2Mean and KAM maps are consistent in indicating stored elastic energy where dislocation density is larger.

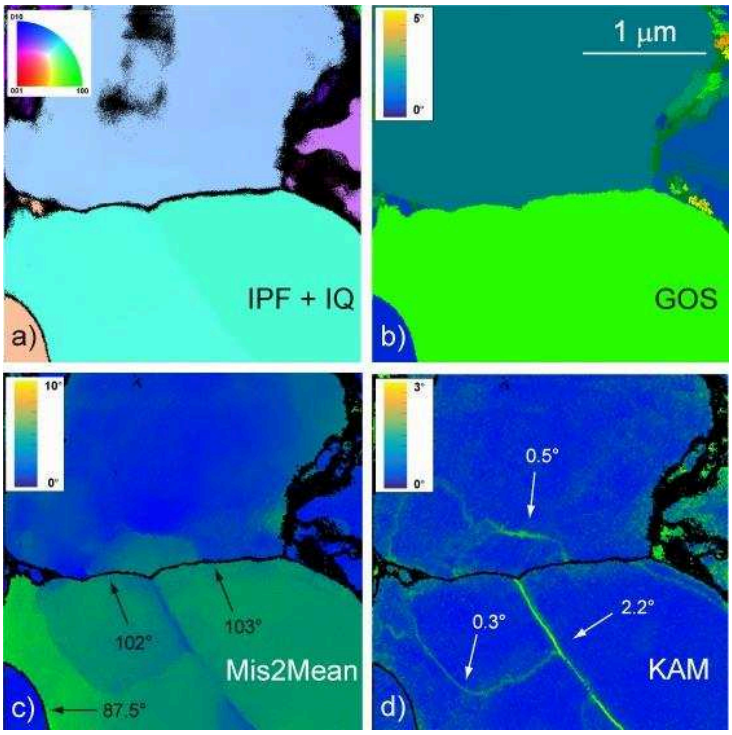

626 **Figure 7.** Morphology of the grains and grain boundaries in CMT16-9 deformed at 1473 K. (**a**)
627 Inverse pole figure (IPF) corresponding to the direction normal to the figure superimposed with
628 the indexation quality IQ (see eq. (1) and main text). (**b**) GOS map (**c**) Mis2Mean map, from
629 0° to 10°. (**d**) KAM map (3rd neighbours), from 0° to 3°. The pinning effect of the 2.2° subgrain
630 boundary on the 102-103° grain boundary is clearly visible.

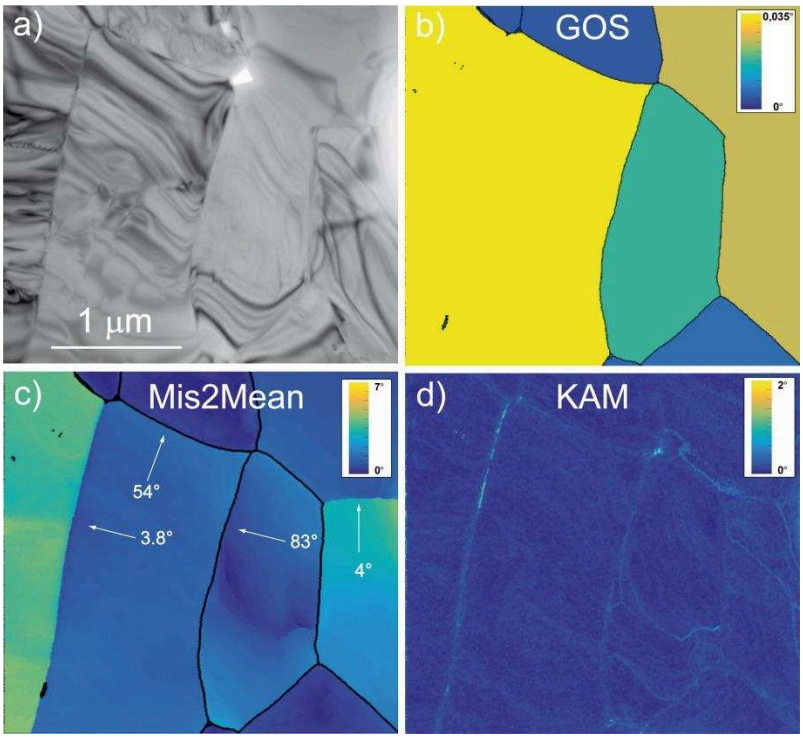

631 **Figure 8.** Morphology of the grains and grain boundaries in CMT16-8 deformed at 1273
632 K. **(a)** Conventional multi-beam TEM bright-field (**b**) GOS map (**c**) Mis2Mean map, from
633 0° to 7°. (**d**) KAM map (3rd neighbours), from 0° to 2°.

634

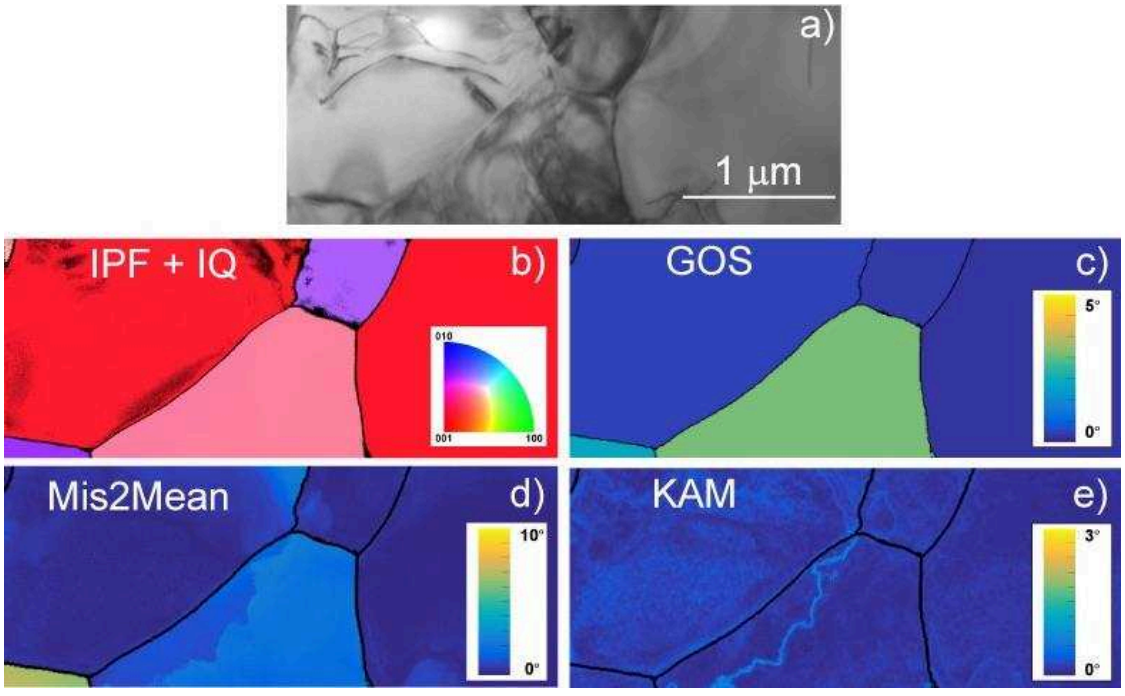

Figure 9. Morphology of the grains and grain boundaries in CMT16-4 deformed at 1273 K. (**a**) Conventional multi-beam TEM bright-field. (**b**) Inverse pole figure (IPF) corresponding to the direction normal to the figure superimposed with the indexation quality IQ (see eq. (1) and main text). (**c**) GOS map (**d**) Mis2Mean map, from 0° to 10°. (**e**) KAM map (3rd neighbours), from 0° to 3°.

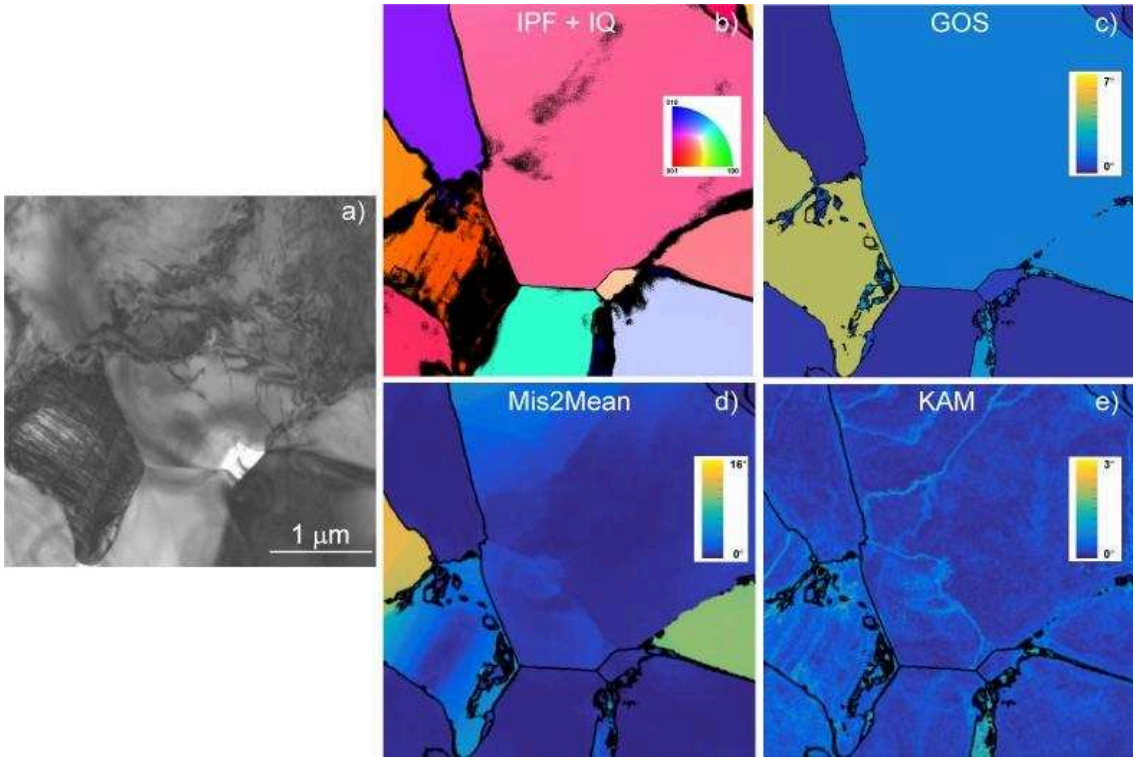

Figure 10. Morphology of the grains and grain boundaries in CMT16-4 deformed at 1473 K. (**a**) Conventional multi-beam TEM bright-field. (**b**) Inverse pole figure (IPF) corresponding to the direction normal to the figure superimposed with the indexation quality IQ (see eq. (1) and main text). (**c**) GOS map (**d**) Mis2Mean map, from 0° to 10°. (**e**) KAM map (3rd neighbours), from 0° to 3°.

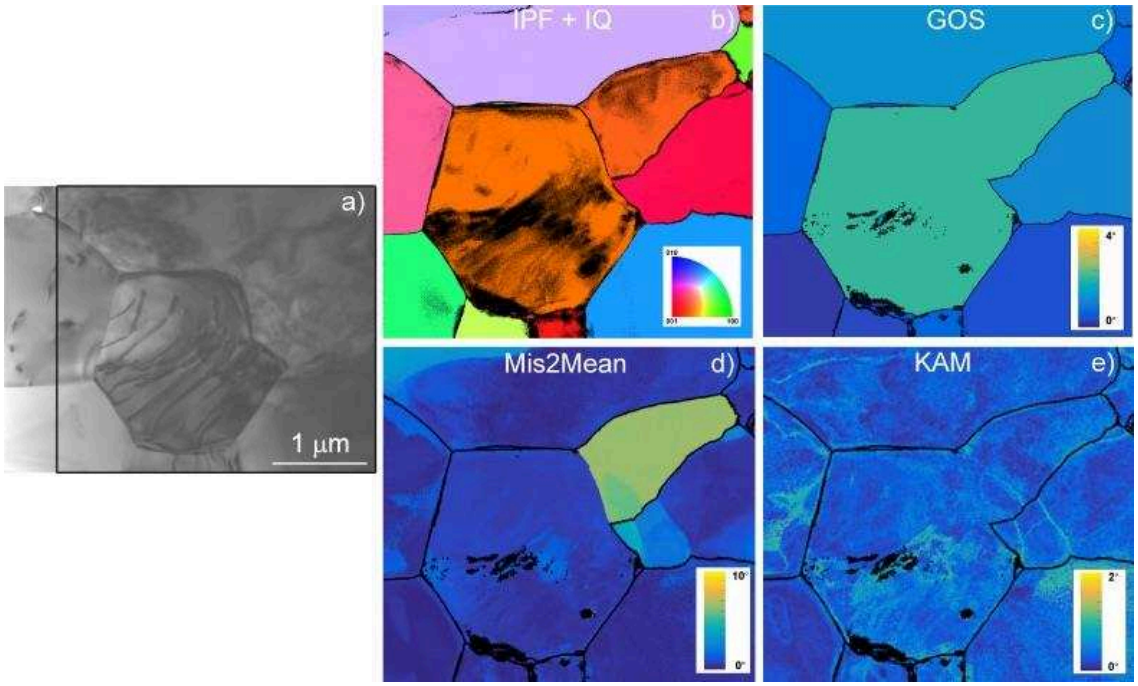

646 **Figure 11.** Morphology of the grains and grain boundaries in CMT16-4 deformed at 1473 K.
647 (**a**) Conventional multi-beam TEM bright-field. (**b**) Inverse pole figure (IPF) corresponding to
648 the direction normal to the figure superimposed with the indexation quality IQ (see eq. (1) and
649 main text). (**c**) GOS map (**d**) Mis2Mean map, from 0° to 10°. (**e**) KAM map (3rd neighbours),
650 from 0° to 2°.
651

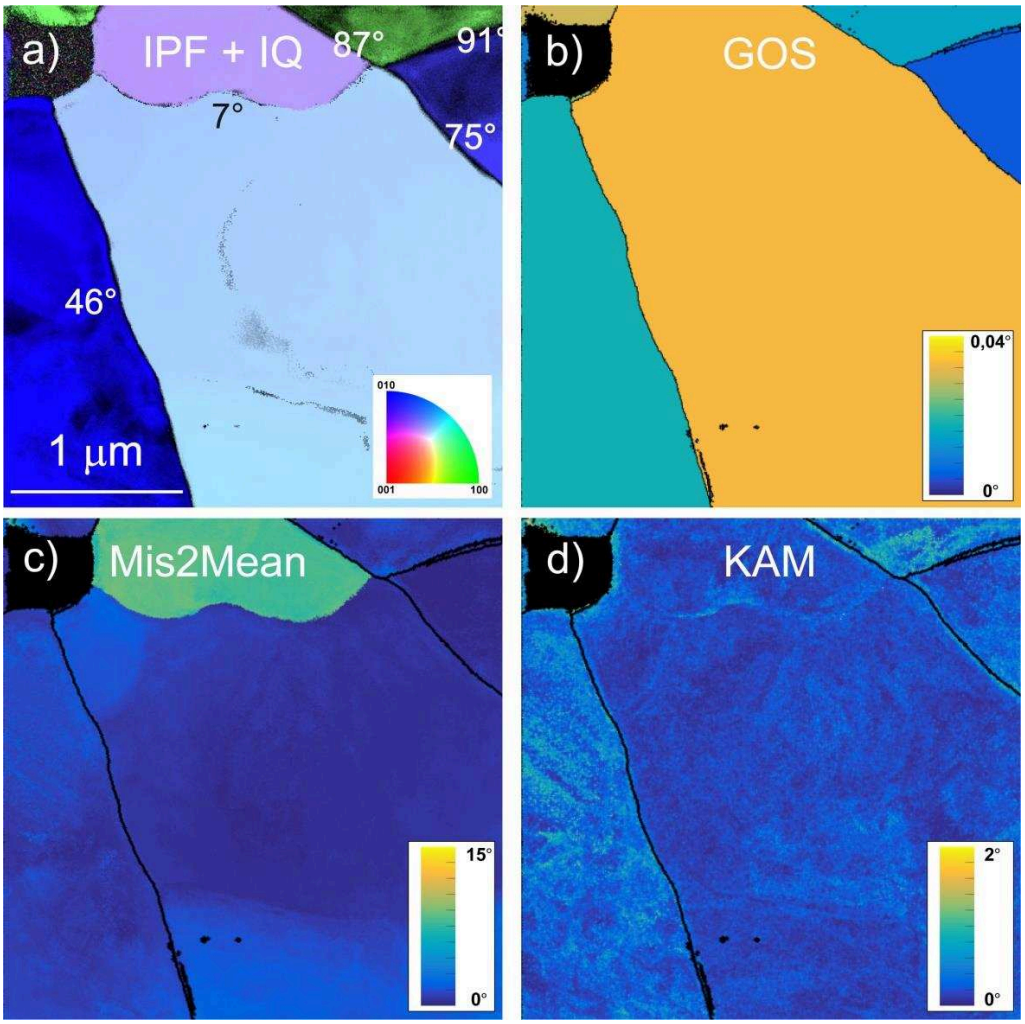

652 **Figure 12.** Morphology of the grains and grain boundaries in CMT16-8 deformed at 1273
653 K. (**a**) Inverse pole figure (IPF) corresponding to the vertical direction superimposed with
654 the indexation quality IQ (see eq (1) and main text).; (**b**) GOS map ; (**c**) Mis2Mean map,
655 from 0° to 15°, and (**d**) KAM map (3rd neighbours), from 0° to 2°.
656

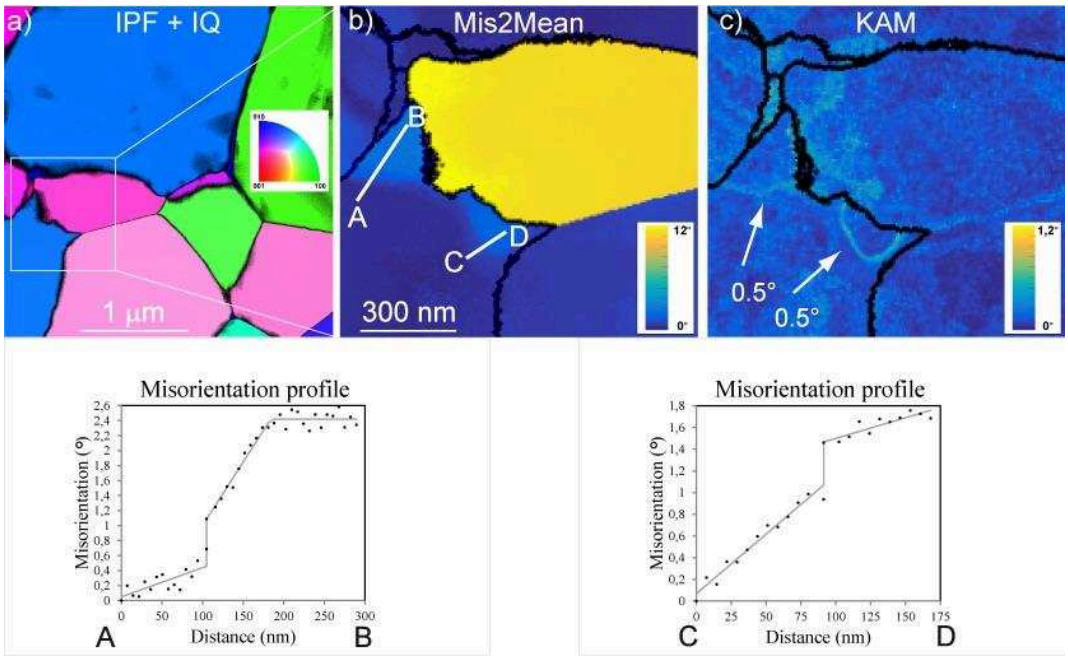

657 **Figure 13.** Morphology of the grains and grain boundaries in CMT16-8 deformed at 1273
658 K. (**a**) Inverse pole figure (IPF) corresponding to the direction normal to the figure
659 superimposed with the indexation quality IQ (equation (1)); (**b**) Mis2Mean map, from 0°
660 to 12°; (**c**) KAM map (3rd neighbours), from 0° to 1.2°; (d) and (e) show misorientation
661 profiles across subgrain boundaries from (b).

CONCLUSION GENERALE

Ce manuscrit rassemble plusieurs caractérisations par diffraction électronique en balayage (avec ou sans précession) de la microstructure, et de la plasticité d'échantillons provenant de la croûte terrestre jusqu'au manteau inférieur. A partir des cartographies d'orientations obtenues en MET à l'aide du dispositif ACOM-TEM, nous appliquons les différentes techniques habituellement employées dans le cadre de la diffraction des électrons rétrodiffusés. Nous utilisons les désorientations locales intragranulaires comme proxy à la déformation et nous les relions aux densités de dislocations. Ce travail met en avant les potentialités qu'offre la SPED, pour l'étude de la déformation plastique des minéraux. Cette technique récente et en pleine évolution, présente des avantages, mais aussi quelques inconvénients (cf. chapitre 2). La résolution spatiale et le faible temps d'exposition lors du balayage permettent de mettre en évidence des mécanismes de déformations nouveaux dans certains minéraux (par exemple, la déformation par bandes de cisaillement dans la bridgmanite). La caractérisation des défauts dans des échantillons sensibles à l'irradiation électronique est également possible. Par ailleurs, en microscopie conventionnelle, travailler sur des échantillons présentant une grande densité de dislocations ($\rho > 10^{15}$ m^{-2}) est très difficile. La SPED permet de dépasser cette limitation.

Rappels des principaux résultats

La SPED nous a permis de proposer une approche qui vient compléter celles utilisées d'ordinaire en MET pour l'étude de la plasticité des phases du manteau terrestre. Concernant le manteau supérieur, l'olivine fait l'objet de très nombreuses études. Comprendre ses mécanismes de déformation fondamentaux est important pour modéliser la rhéologie du manteau supérieur. A titre d'exemple, il est montré dans les expériences de déformation (Demouchy et al., 2012, 2014) qu'en dessous de 1200°C l'olivine polycristalline présente un important durcissement dû à un stockage de l'énergie interne, ce qui conduit à la rupture. La poursuite de la déformation n'est possible que si la microstructure peut évoluer de façon à dissiper cette énergie interne stockée. Parmi les différents mécanismes permettant une évolution de la microstructure durant la déformation, on distingue la recristallisation. Nous avons acquis des cartes d'orientations sur des échantillons de forstérite (pôle magnésien de l'olivine) fortement déformés ; nous nous sommes servis des désorientations locales pour mettre en lumière la différence de densité de dislocations entre grains; celles-ci ont permis de révéler des mécanismes de restauration et de recristallisation. La microstructure comportait plusieurs évidences de joints et de sous joints ondulés, qui sont interprétées dans littérature comme des signes de migration. Par comparaison entre la tension de surface des joints courbés (avec des rayons de courbures variant entre 100 et 500 nm) et la force motrice due au stockage des dislocations, nous avons conclu que l'élément moteur dominant à 1100° C pour la migration des joints est la tension de surface. Ce résultat est directement relié au pas de mesure : en diffraction des électrons rétrodiffusés, pour un balayage à 50 nm de pas, ces

courbures sont pratiquement invisibles. A 40% de déformation, nous avons observé de la recristallisation dynamique (transformation des sous grains en grains) et discontinue. Les nouveaux grains sont formés par une augmentation progressive de la désorientation. Ces grains recristallisés ont des orientations proches de celles des grains parents. Suite à ces observations, nous avons proposé le « bulging » (germination par gonflement) comme potentiel mécanisme de formation des nouveaux grains. Par comparaison de la microstructure obtenue à celle des échantillons naturels, nous postulons que les mécanismes de recristallisation mis en évidence dans cette étude sont également actifs dans les échantillons naturels. Nous avons ensuite poursuivi notre étude de déformation sur les minéraux de la zone de transition ; la viscosité dans cette zone du manteau terrestre fait l'objet jusqu'à nos jours de très longs débats(Fukao et al., 2009; Liu & Zhong, 2016). Etudier expérimentalement la rhéologie des phases qui constituent cette zone (ringwoodite et wadsleyite), permet de fournir une première approche à cette question. Ce qui reste un challenge à cause des conditions physiques qui y règnent. Les récents développements des dispositifs (« D-DIA apparatus » et « Rotational Drickamer Apparatus ») permettant d'atteindre les températures et pressions de la zone de transition, rendent aujourd'hui possible l'étude de ces phases. Dans notre étude par SPED du comportement plastique d'un agrégat de ringwoodite et de wadsleyite (cf. chapitre 3), déformé en D-DIA à 17.3 GPa et 1700 K, nous ne trouvons aucun contraste significatif dans la réponse plastique des deux phases (les distributions de désorientations locales sont assez similaires), hormis un mécanisme de restauration plus facilement activée dans la wadsleyite. Ce résultat est obtenu grâce aux gradients locaux de désorientations qui nous servent d'approximant à la déformation. La comparaison des gradients locaux de désorientation est possible dans ce cas car les mécanismes de déformations des deux phases sont assez proches. La caractérisation des mécanismes de déformation plastique des phases du manteau inférieur a été possible grâce à l'étude expérimentale menée à Yale par Girard et al. (2016). Mise à part cette étude, à notre connaissance, aucun échantillon de bridgmanite et ferropériclase n'avait encore été déformé dans les conditions du manteau inférieur. Les analyses des mécanismes de déformation plastique par MET ont présenté quelques difficultés : la première est liée au fait que la bridgmanite est très instable en conditions ambiantes, et la seconde vient du fait que le ferropériclase est très déformé, avec des densités de dislocations très élevées, qui sont d'ordinaire un obstacle à toute caractérisation en MET. L'étude simultanée de ces deux phases ayant des mécanismes de déformations différents est donc impossible par les méthodes de microscopie conventionnelle. Une fois encore, le couplage entre la diffraction électronique à balayage et les développements de l'EBSD a permis d'avoir un regard neuf sur la façon dont se déforment ces phases du manteau inférieur. Dans la bridgmanite, la déformation se fait par cisaillements localisés de lamelles amorphes, tandis que les grains de ferropericlase s'allongent et se fractionnent, subissant de forts taux de déformation. La déformation plastique du ferropériclase a été évaluée de manière semi-quantitative en comparant les distributions de désorientations et, contrairement aux précédentes études, n'a montré aucun signe de recristallisation.

Perspectives

Au cours de cette thèse, la SPED a permis de poser les fondations d'une approche nouvelle dans l'étude de la plasticité des phases du manteau. Elle bénéficie d'une excellente résolution spatiale (de 1 à 10 nm en fonction de la qualité du filament), ce qui permet d'étudier des désorientations locales résultant de l'activité des dislocations. Cependant, la résolution angulaire, de l'ordre du demi-degré, reste limitée par la qualité de l'indexation. Un des challenges serait donc d'améliorer la qualité des templates pour améliorer la résolution angulaire. Une meilleure résolution angulaire permettrait de caractériser des défauts comme les disclinaisons. Par ailleurs, nous avons caractérisé la migration des joints de grains et la recristallisation par SPED. Une manière de poursuivre cette étude serait d'y associer les cartes de déformations (Rottmann & Hemker, 2018) ce qui permettrait de rendre compte (quantitativement) du niveau d'énergie élastique mis en jeu lors de la migration. Aussi, les mécanismes de création de nouveaux grains restent mal compris. La mesure des champs de déformations créées par des dislocations isolées dans un matériau polycristallins et le développement des dispositifs de déformation *in situ* offrent de nouvelles possibilités dans l'étude des phénomènes de migrations.

BIBLIOGRAPHIE

Arsenlis, A., & Parks, D. M. (1999). Crystallographic aspects of geometrically-necessary and statistically-stored dislocation density. *Acta Materialia*, *47*(5), 1597–1611.

Ashby, M. F. (1970). The deformation of plastically non-homegeneous materials. *Philosophical Magazine*, *21*(October 2012), 37–41.

Bachmann, F., Hielscher, R., & Schaeben, H. (2010). Texture Analysis with MTEX – Free and Open Source Software Toolbox. *Solid State Phenomena*, *160*, 63–68. https://doi.org/10.4028/www.scientific.net/SSP.160.63

Bachmann, F., Hielscher, R., & Schaeben, H. (2011). Grain detection from 2d and 3d EBSD data-Specification of the MTEX algorithm. *Ultramicroscopy*, *111*(12), 1720–1733. https://doi.org/10.1016/j.ultramic.2011.08.002

Beausir, B., & Fressengeas, C. (2013). Disclination densities from EBSD orientation mapping. *International Journal of Solids and Structures*, *50*(1), 137–146. https://doi.org/10.1016/j.ijsolstr.2012.09.016

Bollinger, C., Marquardt, K., & Ferreira, F. (2019). Intragranular plasticity vs. grain boundary sliding (GBS) in forsterite: Microstructural evidence at high pressures (3.5–5.0 GPa). *American Mineralogist: Journal of Earth and Planetary Materials*, *104*(2), 220–231.

Bunge, H. J. (1993). Texture Analysis in Materials Science: Mathematical Methods. https://doi.org/9781483278391

Carter, N. L. (1976). Steady state flow of rocks. *Reviews of Geophysics*. https://doi.org/10.1029/RG014i003p00301

Cockayne, D. J. H., Ray, I. L. F., & Whelan, M. J. (1969). Investigations of dislocation strain fields using weak beams. *Philosophical Magazine*. https://doi.org/10.1080/14786436908228210

Demouchy, S., Tommasi, A., Barou, F., Mainprice, D., & Cordier, P. (2012). Deformation of olivine in torsion under hydrous conditions. *Physics of the Earth and Planetary Interiors*, *202–203*, 56–70. https://doi.org/10.1016/j.pepi.2012.05.001

Demouchy, S., Mussi, A., Barou, F., Tommasi, A., & Cordier, P. (2014). Viscoplasticity of polycrystalline olivine experimentally deformed at high pressure and 900°C. *Tectonophysics*, *623*, 123–135. https://doi.org/10.1016/j.tecto.2014.03.022

Field, D. P., Trivedi, P. B., Wright, S. I., & Kumar, M. (2005). Analysis of local orientation gradients in deformed single crystals. In *Ultramicroscopy*. https://doi.org/10.1016/j.ultramic.2004.11.016

Fukao, Y., Obayashi, M., Nakakuki, T., & Group, D. S. P. (2009). Stagnant slab: a review. *Annual Review of Earth and Planetary Sciences*, *37*, 19–46.

Fundenberger, J. J., Morawiec, A., Bouzy, E., & Lecomte, J. S. (2003). System for creating orientation maps using TEM. *Materials Chemistry and Physics*, *81*(2–3), 535–537.

https://doi.org/10.1016/S0254-0584(03)00068-3

Girard, J., Amulele, G., Farla, R., Mohiuddin, A., & Karato, S. -i. (2016). Shear deformation of bridgmanite and magnesiowustite aggregates at lower mantle conditions. *Science*, *351*(6269), 144–147. https://doi.org/10.1126/science.aad3113

Hansen, L. N., Zimmerman, M. E., & Kohlstedt, D. L. (2011a). Grain boundary sliding in San Carlos olivine : Flow law parameters and crystallographic - preferred orientation. *Journal of Geophysical Research*, *116*(May), 1–16. https://doi.org/10.1029/2011JB008220

Hansen, L. N., Zimmerman, M. E., & Kohlstedt, D. L. (2011b). Grain boundary sliding in San Carlos olivine: Flow law parameters and crystallographic-preferred orientation. *Journal of Geophysical Research: Solid Earth*, *116*(8), 1–16. https://doi.org/10.1029/2011JB008220

Hirsch, P. B., Howie, A., & Whelan, M. J. (1960). A Kinematical Theory of Diffraction Contrast of Electron Transmission Microscope Images of Dislocations and other Defects. *Philosophical Transactions of the Royal Society A: Mathematical, Physical and Engineering Sciences*. https://doi.org/10.1098/rsta.1960.0013

Kawazoe, T., Nishihara, Y., Ohuchi, T., Miyajima, N., Maruyama, G., Higo, Y., et al. (2016). Creep strength of ringwoodite measured at pressure–temperature conditions of the lower part of the mantle transition zone using a deformation–DIA apparatus. *Earth and Planetary Science Letters*, *454*, 10–19. https://doi.org/10.1016/j.epsl.2016.08.011

Kiss, Á. K., Rauch, E. F., & Lábár, J. L. (2016). Highlighting material structure with transmission electron diffraction correlation coefficient maps. *Ultramicroscopy*, *163*, 31–37. https://doi.org/10.1016/j.ultramic.2016.01.006

Liu, X., & Zhong, S. (2016). Constraining mantle viscosity structure for a thermochemical mantle using the geoid observation. *Geochemistry, Geophysics, Geosystems*, *17*(3), 895–913.

Mainprice, D., Bachmann, F., Hielscher, R., Schaeben, H., & Lloyd, G. E. (2015). Calculating anisotropic piezoelectric properties from texture data using the <tt>MTEX</tt> open source package. *Geological Society, London, Special Publications*, *409*(1), 223–249. https://doi.org/10.1144/SP409.2

Milne, G. a, Mitrovica, J. X., & Forte, A. M. (1998). The sensitivity of glacial isostatic adjustment predictions to a low-viscosity layer at the base of the upper mantle. *Earth and Planetary Science Letters*. https://doi.org/10.1016/S0012-821X(97)00191-X

Mitrovica, J. X., & Forte, A. M. (2004). A new inference of mantle viscosity based upon joint inversion of convection and glacial isostatic adjustment data. *Earth and Planetary Science Letters*. https://doi.org/10.1016/j.epsl.2004.06.005

Morniroli, J.-P. (1998). *Diffraction électronique en faisceau convergent à grand angle (LACBED)* Paris, Société Française des Microscopies.

Mussi, A., Cordier, P., & Frost, D. J. (2012). Crystal defects in dense hydrous magnesium silicate phase A deformed at high pressure: characterization by transmission electron microscopy. *European Journal of Mineralogy*, *24*(3), 429–438. https://doi.org/10.1127/0935-1221/2011/0024-2126

Mussi, A., Cordier, P., Ghosh, S., Garvik, N., Nzogang, B. C., Carrez, P., & Garruchet, S. (2016). Transmission electron microscopy of dislocations in cementite deformed at high pressure and high temperature. *Philosophical Magazine*, *96*(17), 1773–1789. https://doi.org/10.1080/14786435.2016.1177670

Nye, J. F. (1953). Some geometrical relations in dislocated crystals. *Acta Metallurgica*, *1*(2), 153–162. https://doi.org/10.1016/0001-6160(53)90054-6

Own, C. (2005). *System Design and Verification of the Precession Electron Diffraction Technique. (Doctoral dissertation). Retrieved from http://www.numis.northwestern.edu/Research/Current/precession.shtml Evanstorn,Illinois:Northwestern University*.

Pantleon, W. (2008). Resolving the geometrically necessary dislocation content by conventional electron backscattering diffraction. *Scripta Materialia*, *58*(11), 994–997. https://doi.org/10.1016/j.scriptamat.2008.01.050

Pfiffner, O. A., & Ramsay, J. G. (1982). Constraints on geological strain rates; arguments from finite strain states of naturally deformed rocks. *Journal of Geophysical Research*. https://doi.org/10.1029/JB087iB01p00311

Rauch, E. and Dupuy, L. (2005). Rapid spot diffraction patterns identification through template matching. *Archives of Metallurgy and Materials*, *50*(1), 87–99.

Rauch, E. F., & Véron, M. (2014). Virtual dark-field images reconstructed from electron diffraction patterns. *The European Physical Journal Applied Physics*, *66*(1), 10701. https://doi.org/10.1051/epjap/2014130556

Rauch, E. F., & Véron, M. (2014). Automated crystal orientation and phase mapping in TEM. *Materials Characterization*, *98*(December), 1–9. https://doi.org/10.1016/j.matchar.2014.08.010

Rottmann, P. F., & Hemker, K. J. (2018). Nanoscale elastic strain mapping of polycrystalline materials. *Materials Research Letters*, *6*(4), 249–254. https://doi.org/10.1080/21663831.2018.1436609

Schwarzer, R. A., & Sukkau, J. (1998). Automated Crystal Orientation Mapping (ACOM) with a Computer-Controlled TEM by Interpreting Transmission Kikuchi Patterns. *Materials Science Forum*, *273–275*(July), 215–222. https://doi.org/10.4028/www.scientific.net/MSF.273-275.215

Thieme, M., Demouchy, S., Mainprice, D., Barou, F., & Cordier, P. (2018). Stress evolution and associated microstructure during transient creep of olivine at 1000–1200 °C. *Physics of the Earth and Planetary Interiors*, *278*(March), 34–46. https://doi.org/10.1016/j.pepi.2018.03.002

Villert, S., Maurice, C., Wyon, C., & Fortunier, R. (2009). Accuracy assessment of elastic strain measurement by EBSD. *Journal of Microscopy*. https://doi.org/10.1111/j.1365-2818.2009.03120.x

Vincent, R., & Midgley, P. A. (1994). Double conical beam-rocking system for measurement of

integrated electron diffraction intensities. *Ultramicroscopy, 53(3), 271-282.* https://doi.org/10.1016/0304-3991(94)90039-6

Wang, Y., Durham, W. B., Getting, I. C., Weidner, D. J., & Durham, W. B. (2003). The deformation-DIA : A new apparatus for high temperature triaxial deformation to pressures up to 15 GPa The deformation-DIA : A new apparatus for high temperature triaxial deformation to pressures up to 15 GPa. *Review of Scientific Instruments*, *74*(2003). https://doi.org/10.1063/1.1570948

Wilkinson, A. J., Meaden, G., & Dingley, D. J. (2006). High resolution mapping of strains and rotations using electron backscatter diffraction. *Materials Science and Technology*, *22*(11), 1271–1278. https://doi.org/10.1179/174328406X130966

Williams, D. B., & Carter, C. B. (2009). *Transmission Electron Microscopy: A Textbook for Materials Science*. *Materials Science*. https://doi.org/10.1007/978-1-61779-415-5_23